The Effect of Strontium Substitution on Apatite-Wollastonite Glass-Ceramics

William Oliver Maxwell Vickers

Submitted in accordance with the requirements for the degree of
Doctor of Philosophy

The University of Leeds
School of Mechanical Engineering

August 2013

The candidate confirms that the work submitted is his/her own and that appropriate credit has been given where reference has been made to the work of others.

Acknowledgements

Firstly I would like to say a huge thank you to my three supervisors, David Wood, Paul Genever and Xuebin Yang who's academic advice and guidance have got me to where I am. You have all been both excellent mentors and valued friends.

I would like to thank all the technical support team who have aided me in my research. There are a selection of people that I feel deserve an individual thank you: Nigel Bubb for his help in getting me started in the lab and for all the time he has spent developing my scientific brain (I sometimes worry that I may be turning into him!), Jackie Hudson for allowing me to use the SEM for days at a time and for all the advice she has given me throughout the years, Tim Comyn for the hours spent training me on Rietveld analysis (and for giving me a job), (Aunty) Claire Godfrey for bringing order to my disorder and to Adam Steel and Julie McDermott for booking me onto trains and planes to travel the country and world.

I have made so many friends during my time at Leeds and York and would like to say thank you to all my co-workers at the LDI and BTR and to everyone on the DTC. In particular Jihad, Niki and Eirini, we have been through it all together and I hope that we will stay friends for life. I would like to say thank you to Charles, Abbie, Jack, Jake and Dave for providing me with plenty of parties and mixes to distract me from work. Though I may not have been out clubbing with you recently I feel that we have had more than enough fun times to make up for it and I promise you will see more of me now the work is done.

Thank you to Selena for putting up with my lack of holidays and haircuts. I know I said I would finish a year ago but it's finally done and you can enjoy not having a student for a boyfriend!

It goes without saying that I am most grateful to my Mum and Dad for being there for me throughout my studies. You have witnessed firsthand the highs and lows of a Ph.D. and have always been quick to offer emotional (and financial) support. Your encouragement if ever I became despondent has kept me going. There is no doubt in my mind that without you I would not have completed this work and so I dedicate this thesis to you.

Abstract

The aim of this work was to synthesise novel strontium containing glass-ceramics based on the apatite-wollastonite system. Parent glasses were formed via the melt quench route with strontium being substituted for calcium according to: $35.4SiO_2$•$7.1P_2O_5$•$0.4CaF_2$•7.1MgO• (49.9-X)CaO•XSrO, where X = 6.2, 12.5, 18.7 or 24.9. Glass frits were ground and sieved and size distribution shown to be constant. Successful substitution of strontium into the parent glass was confirmed with energy dispersive x-ray (EDX) analysis, x-ray diffraction (XRD) and density measurements Glass rods were successfully cast for all the compositions tested. The x-ray attenuation of the material increased with increasing strontium substitution in line with theoretical values.

Differential scanning calorimetry (DSC) revealed two major exotherms, T_{P1} and T_{P2}. T_{P1} moved to lower temperatures with increasing strontium substitution while T_{P2} moved to higher temperatures. XRD and Rietveld refinement identified T_{P1} as corresponding to fluorapatite and T_{P2} as to wollastonite, both phases took in strontium following substitution. Pseudowollastonite formed at higher strontium contents. The weight percentage of wollastonite decreased with increasing strontium substitution. Scanning electron microscopy (SEM) and EDX revealed the bulk morphology and composition of the material's phases.

Porous scaffolds were formed by sintering the parent glasses in carbon moulds. Increasing strontium substitution shifted sintering from a solid state mechanism towards liquid phase resulting in a loss of porosity. In all but the highest substitution, the flexural strength decreased with increasing strontium.

Simulated body fluid (SBF) testing indicated an increase in solution pH with increasing strontium substitution and a shift in the ability of the material to form a surface apatite layer. Human bone mesenchymal stem cells (hMSCs) were able to attach, expand and differentiate on the materials. Strontium doping was shown to significantly affect the osteogenic capacity of apatite-wollastonite glass-ceramic.

Table of Contents

List of Figures

List of Tables

List of Abbreviations

Abbreviation	Full Name
μ	Mass Absorption Coefficient
A	Linear Absorption Coefficient
ALP	Alkaline Phosphatase
amax/min	Maximum/Minimum Average Radii
AMO	Amorphous
A_N	Nucleation Rate Constant
Ap	Apatite
APS	Amorphous Phase Separation
A-W	Apatite-Wollastonite
b	Breadth
BMP	Bone Morphogenic Protein
BMU	Basic Multicellular Unit
BO	Bridging Oxygen
BSA	Bovine Serum Albumen
BSE	Back Scattered Electron
C	Constant
CaSR	Calcium Sensing Rreceptor
C_C	Cell Suspension Concentration
Conc	Concentration
CT	Computed Tomography
d	Size/Distance
D	Size Band Midpoint
DMEM	Dulbecco's Modified Eagle Medium
DNA	Deoxyribonucleic Acid
DSC	Differential Scanning Calorimetry
DTA	Differential Thermal Analysis

E	Activation Energy
E_c	Excitation Energy
ECM	Extra Cellular Matrix
EDTA	Ethylenediaminetetraaceticacid
EDX	Energy Dispersive X-Ray Analysis
EXP	Experimental
F	Force
FA	Fluorapatite
FBS	Foetal Bovine Serum
FITC	Fluorescein Isothiocyanate
FTIR	Fourier Transform Infrared
h	Height
HA	Hydroxyapatite
HCA	Hydroxy/Carbonate apatite
HMDS	Hexamethyldisilazane
hMSC	Human Mesenchymal Stem Cell
HSC	Hematopoetic Stem Cell
I	X-Ray Intensity
I_0	Incident X-Ray Intensity
I_c	Steady State Nucleation Rate
ICDD	International Centre for Diffraction Data
KX	Donor Cell Identifier X
l	Head Spacing
LSP	Liquid Phase Sintering
m	Gradient
MAPK	Mitogen Activated Protein Kinase
MAS-NMR	Magic Angle Spinning Nuclear Magnetic Resonance
M_r	Molar Mass

MSC	Mesenchymal Stem Cell
n	Number
NBO	Non-Bridging Oxygen
NC	Network Connectivity
N_C	Number of Cells
NF	Network Former
NFATc	Calcineurin/Nuclear Factor of Activated Tc
NFκB	Nuclear Factor κB
ø	Heating Rate
OPG	Osteoprotegrin
P/B ZAF	Peak-to-Background ZAF
PBS	Phosphate Buffered Saline
PDF	Powder Diffraction File
PE	Phycoerythrin
PGA	Polyglycolide
PLA	Polylactic
PLC	Phospholipase C
PLGA	Copoly Lactic Acid/Glycolic Acid
pNPP	p-Nitrophenyl Phosphate
PsWol	Pseudo Wollastonite
PTH	Parathyroid Hormone
Q^n	Coordination Distribution
R	Gas Constant
r	Radius
r*	Critical Atomic Radius
R^2	Coefficient of Determination
R_a	Anion Radius
RANK	Receptor Activator of Nuclear Factor κ-B
RANKL	Receptor Activator of Nuclear Factor κ-B Ligand

R_c	Cation Radius
RNA	Ribonucleic Acid
R_p	R-Profile
R_{wp}	Weighted R-Profile
S_A	Nominal Surface Area
SBF	Simulated Body Fluid
SCMS	Strontium Calcium Magnesium Silicate
SDEV	Standard Deviation
SE	Secondary Electron
SEM	Scanning Electron Microscopy
Sil	Silicate
SrFA	Strontium Fluorapatite/Fluorstophite
STD	Standard
STD	Standard
T	Temperature
TCP	Tricalcium Phosphate
TE	Tris-EDTA
T_g	Glass Transition Temperature
THEO	Theoretical
T_m	Melting Temperature
T_{OX}	Temperature of Crystallisation Onset X
T_{PX}	Temperature of Crystallisation Peak X
U	Rate of Crystal Growth
U	Strain Broadening Factor
V	Volume
V_C	Volume of Cell Suspension
V_m	Crystal Molar Volume
V_s	Volume of SBF
$v\Delta G_v$	Volume Free Energy

W	Size Broadening Factor
w	Width
Wol-2M	Wollastonite-2M
Wt	Weight/Mass
XRD	X-Ray Diffraction
γ_{XX}	Interface Energy Vectors
ΔG	Bulk Free Gibbs Energy
ΔG^*	Change in Gibbs Free Energy
ΔG_a	Kinetic Barrier
ΔG_a	Activation Free Energy
ΔG_{het}^*	Heterogeneous Nucleation Thermodynamic Barrier
ε	Strain
λ	Glass/Crystal Interface Size
λ	Wavelength
ρ	Density
σ	Interfacial Energy
σ_{flex}	Flexural Strength
μ	Mass Absorption Coefficient
A	Linear Absorption Coefficient
ALP	Alkaline Phosphatase
amax/min	Maximum/Minimum Average Radii
AMO	Amorphous
A_N	Nucleation Rate Constant
Ap	Apatite
APS	Amorphous Phase Separation
A-W	Apatite-Wollastonite

b	Breadth
BMP	Bone Morphogenic Protein
BMU	Basic Multicellular Unit
BO	Bridging Oxygen
BSA	Bovine Serum Albumen
BSE	Back Scattered Electron
C	Constant
C_C	Cell Suspension Concentration
Conc	Concentration
CT	Computed Tomography
d	Size/Distance
D	Size Band Midpoint
DMEM	Dulbecco's Modified Eagle Medium
DNA	Deoxyribonucleic Acid
DSC	Differential Scanning Calorimetry
DTA	Differential Thermal Analysis
E	Activation Energy
E_c	Excitation Energy
ECM	Extra Cellular Matrix
EDTA	Ethylenediaminetetraaceticacid
EDX	Energy Dispersive X-Ray Analysis
EXP	Experimental
F	Force

FA	Fluorapatite
FBS	Foetal Bovine Serum
FITC	Fluorescein Isothiocyanate
FTIR	Fourier Transform Infrared
h	Height
HA	Hydroxyapatite
HCA	Hydroxy/Carbonate apatite
HMDS	Hexamethyldisilazane
hMSC	Human Mesenchymal Stem Cell
HSC	Hematopoetic Stem Cell
I	X-Ray Intensity
I_0	Incident X-Ray Intensity
I_c	Steady State Nucleation Rate
ICDD	International Centre for Diffraction Data
KX	Donor Cell Identifier X
l	Head Spacing
LSP	Liquid Phase Sintering
m	Gradient
MAS-NMR	Magic Angle Spinning Nuclear Magnetic Resonance
M_r	Molar Mass
MSC	Mesenchymal Stem Cell
n	Number
NBO	Non-Bridging Oxygen

NC	Network Connectivity
N_C	Number of Cells
NF	Network Former
ø	Heating Rate
P/B ZAF	Peak-to-Background ZAF
PBS	Phosphate Buffered Saline
PDF	Powder Diffraction File
PE	Phycoerythrin
PGA	Polyglycolide
PLA	Polylactic
PLGA	Copoly Lactic Acid/Glycolic Acid
pNPP	p-Nitrophenyl Phosphate
PsWol	Pseudo Wollastonite
PTH	Parathyroid Hormone
Q^n	Coordination Distribution
R	Gas Constant
r	Radius
r*	Critical Atomic Radius
R^2	Coefficient of Determination
R_a	Anion Radius
R_c	Cation Radius
RNA	Ribonucleic Acid
R_p	R-Profile

R_{wp}	Weighted R-Profile
S_A	Nominal Surface Area
SBF	Simulated Body Fluid
SCMS	Strontium Calcium Magnesium Silicate
SDEV	Standard Deviation
SE	Secondary Electron
SEM	Scanning Electron Microscopy
Sil	Silicate
SrFA	Strontium Fluorapatite/Fluorstophite
STD	Standard
STD	Standard
T	Temperature
TCP	Tricalcium Phosphate
TE	Tris-EDTA
T_g	Glass Transition Temperature
THEO	Theoretical
T_m	Melting Temperature
T_{OX}	Temperature of Crystallisation Onset X
T_{PX}	Temperature of Crystallisation Peak X
U	Rate of Crystal Growth
U	Strain Broadening Factor
V	Volume
V_C	Volume of Cell Suspension

V_m	Crystal Molar Volume
V_s	Volume of SBF
$v\Delta G_v$	Volume Free Energy
W	Size Broadening Factor
w	Width
Wol-2M	Wollastonite-2M
Wt	Weight/Mass
XRD	X-Ray Diffraction
γ_{XX}	Interface Energy Vectors
ΔG	Bulk Free Gibbs Energy
ΔG^*	Change in Gibbs Free Energy
ΔG_a	Kinetic Barrier
ΔG_a	Activation Free Energy
ΔG_{het}^*	Heterogeneous Nucleation Thermodynamic Barrier
ε	Strain
λ	Glass/Crystal Interface Size
λ	Wavelength
ρ	Density
σ	Interfacial Energy
σ_{flex}	Flexural Strength

Chapter 1
Introduction

Bone has a remarkable ability to heal but in cases where a defect may be too large or disease prevents healing, a surgical intervention is required. Bone transplantation/grafting is a recognised treatment for non-union fractures, bone loss due to tumours, congenital skeletal growth disorders and other bone defects that will not heal by themselves. In 2001, there were roughly 500,000 bone grafts in the US alone [1]. This value is set to rise due to advances in technology and healthcare along with an aging population [2]. The ideal graft material must be biocompatible, osteoinductive, osteoconductive, easy to use and cost effective [1]. Allogeneic bone grafts, collected from tissue donors, are a common source of transplanted bone. Banks of allogeneic donor tissue can be built up, though storage methods such as freezing can alter the materials properties. Allogeneic grafts also carry a risk of immunorejection or disease transferral [3]. Xenogeneic scaffolds, such as Bio-Oss, are utilised in dentistry to increases bone mass for implants. Autogenic bone grafts are the current gold standard. However, availability and donor site morbidity limit the technique [3]. This is emphasised by a Cochrane Collaboration systematic review following which it was determined that autografts were more successful in healing bone defects than allografts; but the method was over complicated due to graft harvesting [4]. Tissue engineering offers an alternative source of autologous bone and as well as novel methods of promoting bone formation and regeneration.

Tissue engineering is defined by Langer and Vacanti as:

"An interdisciplinary filed that applies the principles of engineering and life sciences toward the development of biological substitutes that restore, maintain, or improve tissue function or a whole organ" [5].

Tissue engineers utilise a combination of cells, scaffolds, growth factors and mechanical stimulation to promote tissue formation *in vitro* and *in vivo*. In order to tissue engineer bone, its anatomy and physiology must first be understood.

1.1 Bone

1.1.1 Anatomy

Bone is a composite, designed to support the body structurally, whilst acting as a calcium store and "factory" for the production of blood cells. There are two forms of skeletal bone: dense cortical and spongy cancellous. Their structure is highly hierarchical [6]. Cortical bone is composed of cylindrical oseteons where-as cancellous bone is formed from trabecular struts, figure 1. The bone matrix of the two structural organisations is composed of mineral and organic phases as well as water. The organic phase is 90% collagen I by weight [7], other collagen forms may be present, for example, collagens II and X in the metaphysis during growth [8]. Also contained in the organic phase are non-collagenous proteins such as osteopontin, osteocalcin and osteonectin [9], as well as various other glycoproteins. The mineral phase is composed of hydroxyapatite, $Ca_{10}(PO_4)_6(OH)_2$, a calcium phosphate. The mineral hydroxyapatite forms crystals of varying size [10] that lie inside and outside collagenous phases [11], thus forming a strong, interwoven, composite.

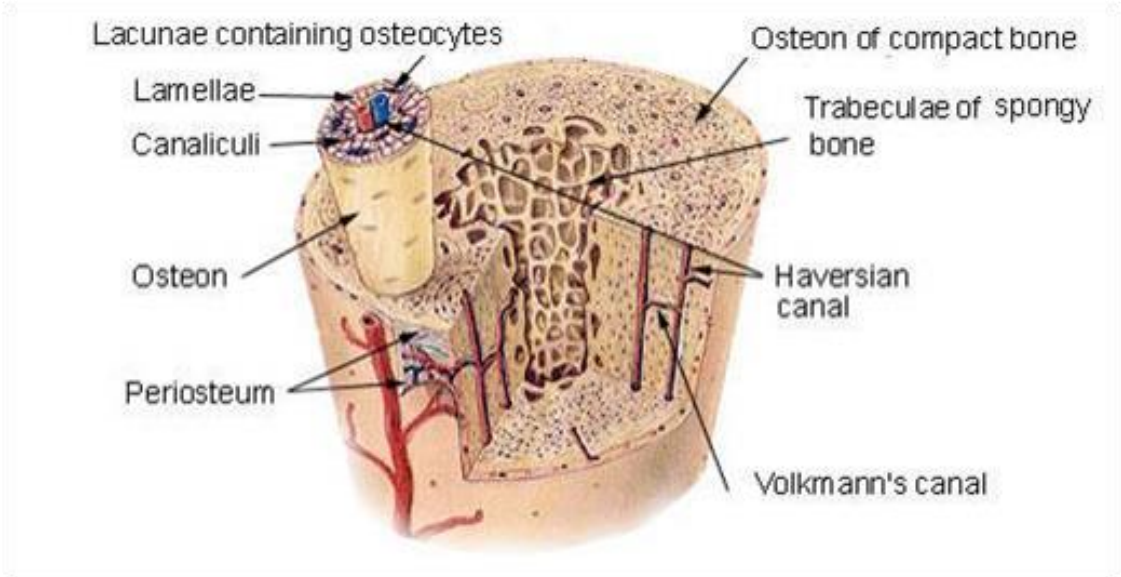

Figure 1: The structure of cancellous and cortical components of a human long bone, reproduced with permission [12].

The bone matrix is maintained and remodelled by four main cell types: osteoclasts, osteoprogenitors, osteoblasts and osteocytes. Osteoclasts are multinuclear cells formed form the fusion of multiple monocytes; phagocytic white blood cells derived

from hematopoietic stem cells (HSCs) [13]. Osteoclasts are involved in the dissolution of bone: osteolysis, via the secretion of acids and proteolytic enzymes [13]. Ostoeprogenitor cells, differentiated from multipotent mesenchymal stem cells (MSCs), are adult stem cells that divide and mature into osteoblasts [14]. Osteoblasts are responsible for new bone formation, osteogenesis, via the calcification of collagen osteoids. Osteoclast and osteoblasts together form a basic multicellular unit (BMU). The balance of activity of the two cell types is essential for bone mass maintenance. When osteoblasts become fully surrounded by new bone, most undergo apoptosis, the remaining become quiescent and differentiate into ostocytes or bone lining cells. Osteocytes are found in lacunae between lamellae (calcified matrix) sheets, linked via cytoplasmic extensions within canaliculi channels [15]. Their role is to detect damage to the bone matrix, then stimulate osteoblasts and osteoclasts to respond accordingly [16].

1.1.2 Mechanical Properties

The mechanical properties of bone lay between that of its mineral and collagenous components. This however produces highly anisotropic mechanical properties. Bone is much stronger in compression than tension due to the formation of micro-cracks during tension. The strength (yield stress) of cortical bone in compression is 117-216MPa compared to 78.8-151MPa under tension [17]. Also, due to the longitudinal alignment of the osteons, bone is much stronger when tested along its long axis, see figure 2. This is in part due to the trapping of cracks by lamella and osteon cement lines [18]. The strength in compression and tension decreases to 106-133MPa and 51-56MPa [17], respectively, when bone samples are tested in the transverse direction. The bend strength of bone varies with sample and test method choice but is given with the range of 30-90MPa [19]. The modulus and strength of bone increases with mineral content and apparent density [18, 20]. The modulus of cortical bone has been given as 17.2GPa compared to 6.13GPa for cancellous bone [17]. The modulus of cancellous bone can be directly related to apparent density via a power law [17]. The trabeculae of cancellous bone are arranged in a fashion that best distributes applied forces, contributing to bone's anisotropic properties.

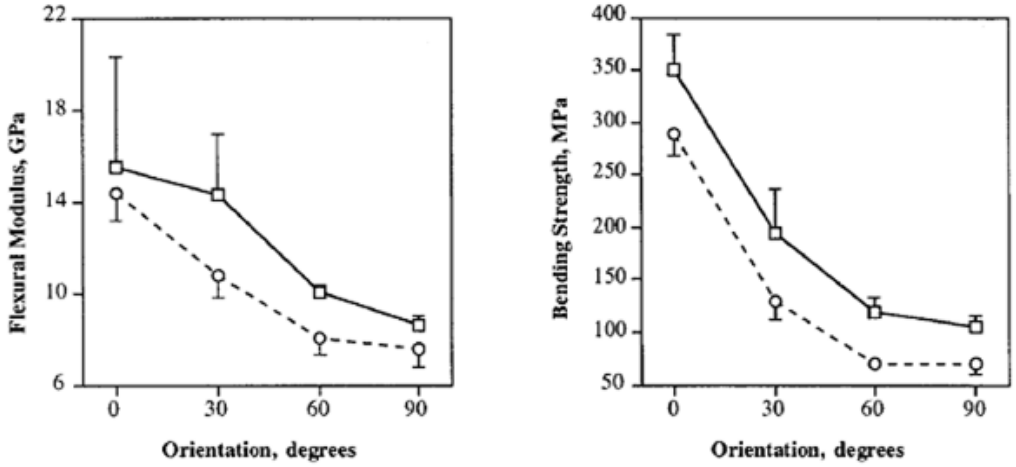

Figure 2: The effect of bone orientation on its modulus and flexural strength, as calculated via a 3-point bend test. All angles are given with respect to the long axis of the bone samples, reproduced with permission [21].

1.1.3 Bone Growth

1.1.3.1 Development

Bone matrix formation occurs in two forms during development: intramembranous ossification, whereby bone develops from mesenchymal or dermal tissue, and endochondral ossification, bone replacing an existing cartilage model [22]. Intramembranous ossification involves an initial condensation of the mesenchyme and is the mechanism by which the flat bones of the skull form [23]. Bone signalling factors, predominantly bone morphogenic proteins (BMPs), initiate the transformation of bone marrow stem cells into differentiated osteoblasts then secrete the organic collagen bone matrix. This mineral is then subsequently mineralised and the bone growth proceeds with the recruitment of more cells and the deposition of more bone. Endochondral formation takes place primarily in long bones and is responsible for both their formation and growth. Unlike in intramembranous ossification, the condensed mesenchymal cells differentiate into chondroblasts, which deposit a cartilage matrix. Chondroblasts embedded in cartilage are known as chondrocytes. Mesenchymal cells around the periphery form the perichondrium and differentiate into osteoblasts. The cartilage matrix is then calcified and bone is formed [22].

1.1.3.2 Increasing Length

Throughout childhood, bones elongate via the migration of osteoblasts to the epiphyses (the end of the bone). Ossification of a cartilaginous plate, the epiphyseal plate, between the epiphyses and diaphysis (shaft) then occurs. The bone continues to extend due to growth of the cartilaginous plate exceeding the rate of ossification [24]. Growth stops during puberty when accelerated ossification exceeds cartilage expansion.

1.1.3.3 Increasing Diameter

Bone diameter increases via formation without resorption, this is known as bone modelling and occurs on the outer/periosteal surface of the bone. On the inner surface of the bone, the endosteal surface, bone modelling proceeds as the removal of bone without replacement. In this manner, the marrow cavity grows as the bone increases in width [25]. Bone removal of the marrow cavity occurs at a reduced rate compared to radial growth [26], thus increasing the thickness of the cortical and cancellous bone walls.

1.1.4 Bone Remodelling

Bone remodelling is controlled by endocrine signalling, such as oestrogen, parathyroid hormone (PTH) and calcitonin; as well as auto- and paracrine signalling, for example: sclerostin [16], Wnt and RANK pathways [27]. Microcracks due to loading may also disrupt osteocyte extensions, leading to their death and triggering the formation of osteoclasts and osteoblasts [27]. Remodelling occurs differently in trabecular and cancellous bone, though both processes involve the removal and subsequent deposition of matrix by an active BMU. Cortical remodelling involves the formation of a cutting cone by osteoclasts, creating a tunnel roughly 2,000μm long and 150-200μm wide [27]. This is followed by osteoblastic bone deposition, replacing the bone removed by osteoclasts with concentric, new layers. Via this process, the BMU forms a new osteon with Haversian canal [28], as observed in cortical bone. In cancellous remodelling, the BMU moves across the surface of a trabeculae, cutting a trench 40-60μm in depth [27], before filling it in with fresh bone. This results in the formation of a “hemi-osteon” [29].

1.1.5 Bone Healing

Bone fractures heal via two methods - primary or secondary healing:

Primary bone healing occurs when two faces of a fracture remain in contact. Oscteocytes form cutting cones through the fracture, these are then remodelled and the fracture is secured. Any gaps between the fracture surfaces are quickly filled with hematoma containing osteoblasts that deposit new bone in the defect [30].

Secondary bone healing occurs when there is a fragmented fracture and progresses along the following sequence [30]:

Inflammation → Granulation → Callus mineralisation → Callus remodelling → Concurrent remodelling

1.2 Mesenchymal Stem Cells (MSCs)

"Mesenchymal stem cell" (MSC) is a broad term that covers multipotent stem cells that have the capacity to divide asymmetrically and give rise to multiple cell phenotypes of the mesoderm. This includes osteoblasts, chondrocytes, adipocytes [31], tenocytes [32] and cardio- and skeletal- myocytes [33]. They have been isolated from various tissues in the body, but most commonly from the bone marrow stromal stem cell niche. Other locations that MSCs have been isolated include dental pulp [34], adipose tissue [35], dermis [36], skeletal muscle [37] and prenatal tissues such as amniotic fluid [38] and umbilical cord blood [39].

It is due to their osteogenic potential and occurrence throughout the body that MSCs are the most commonly utilised cells for bone tissue engineering. Though osteogenically differentiated MSCs, osteoblasts, can be isolated directly from the body, they have been shown to undergo a massive reduction in deoxyribonucleic acid (DNA), ribonucleic acid (RNA) and protein synthesis with age, dropping to bellow half maximum activity after 15 doublings [40], reducing their long term bone forming capacity. Also, their somatic, differentiated, phenotype prevents prolonged expansion *in vivo* due to progressive shorting of telomeres [41].

1.2.1 Identification of Mesenchymal Stem Cells

1.2.1.1 Flow Cytometry

One of the major problems encountered in the use of MSCs has been the development of specific cell markers. MSCs in culture express many markers, such as CD105 (SH2), CD 73 (SH3 and SH4), CD166, CD29, CD44, CD90, and STRO-1 [42]. They also test negative for antigens to the CD14, CD34, CD45 and HLA-DR antibodies; of which the epitopes are enriched on the surface of hematopoietic stem cells [42]. The markers listed are however non-specific and different groups utilise different markers [33], adding to the confusing general terminology of "mesenchymal stem cell". The surface markers can be detected by staining with specific antibodies containing fluorochromes or target sites for secondary, labelled antibodies. The labelled cells can then be counted or sorted into purified populations using flow cytometry or fluorescence activated cell sorting (FACS).

1.2.1.2 *In vitro* Differentiation

MSCs can be identified in culture via their potency (capability to differentiate into different cell phenotypes). Cells are placed in a variety of media in order to differentiate them into the lineages of choice. Table 1 displays examples of supplements utilised to initiate differentiation. Different laboratories may follow different protocols, as can be seen in the variation in concentrations between the two osteogenic supplements, contributing to the difficulties in defining mesenchymal stem cells. Dexamethasone is a catabolic steroid and its use in varying concentrations will alter the metabolism of the cells.

Table 1: Examples of MSC differentiation supplements.

Differentiation Supplement	Content	Author
Osteogenic	$1x10^{-5}$ M dexamethalone (dex), 0.2 M β-glycerophosphate, $5x01^{-3}$ M ascorbic acid	Lennon, 2006 [43]
Osteogenic	$1x10^{-7}$ M dex, 0.01 M β-glycerophosphate, $5x01^{-5}$ M ascorbic acid	Roura, 2006 [44]
Adipogenic	1x10-6M aex, 5x10-4M misobutylmethylxanthine, 10μg/ml insulin, 1x10-4M indomethacin	Roura, 2006 [44]
Myogenic	1x10-5M 5-azacytidine (5-AZ)	Roura, 2006 [44]

The ability of the cells to differentiate in the presence of the supplements is measured via a variety of assays. Successful osteogenic differentiation can be observed via the production of alkaline phosphatase (easily detected via an ALP assay), increased mineralisation (via von Kassa and Alizarin red staining and a calcium assay) and also visually as the cells become more rounded and mineralised nodules may be present [43]. The formation of adipogenic cells is observed with the use of a Nile/oil red stain. Myogenic cells can be identified by the formation of inter-cellular gap junctions (measured by observing the movement of marked particles between neighbouring cells), Ca^{2+} oscillations (associated with muscle contraction) and the presence of sarcomeric proteins. Fluorescent histochemical stains can also be used. Examples of differentiated and un-differentiated MSCs are shown in figure 3.

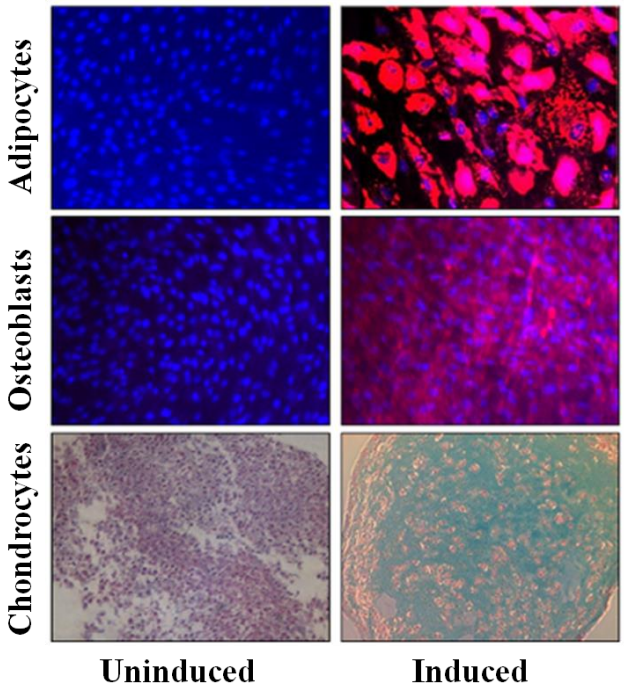

Figure 3: MSCs (left) and differentiation induced MSCs (right) labelled with fluorescent histochemical stains. Adipocytes: Blue = Hoechst nuclear stain, Red = AdipoRed. Osteoblasts: Blue = Hoechst nuclear stain, Red = Alkaline Phosphatase, Chondrocytes: Blue = mucins, Red = nuclei, reproduced with permission [45].

1.2.2 MSC Immunoregulation

Allogenic MSCs can be utilised *in vivo* due to their ability to constrict T-cell proliferation [46]. This is done by complex interactions, both cell-cell and via soluble factors, that hold T-cells in G_0 phase. This helps reduce rejection of allogenically implanted MSCs. It must be noted, however, that this characteristic may favour tumour growth *in vivo* [47]. It is suggested that MSC's immunoprivileged ability decreases as the stem cells become further differentiated [47].

1.2.3 MSC Aging

MSCs osteogenic potential decreases with age [44]. MSCs from older patients have the same length telomeres and lipofuscin biomarker build up as those from younger subjects [44], thus the reduction in potential may be due to oxidative damage or senescence of supporting cells [33].

1.3 Bone Tissue Engineering Scaffolds

Scaffolds are utilised to provide support and direction for new bone formation. Bioactive biomaterials that are used for bone scaffolds vary depending on the site in which the material is to be used. Polymers may be used in low load applications, such as the calvarium and pallet whereas inorganic ceramics are favoured for load bearing applications. The rate of resorption of the material must be considered and balanced with the rate of bone formation to ensure that structural integrity of the scaffold is not lost once it is implanted. For some materials this can be done by varying the base composition or a composite of two or more phases may be used. The modulus of the material should be matched to that of the native tissue, this has been shown to help induce MSC differentiation down the osteogenic lineage [48, 49]. The porosity of the scaffold must be considered. Macroporosity (>50μm) is important to allow the penetration of cells into a scaffold. 1000μm is considered the minimum pore size for cortical bone ingrowth, pore sizes smaller than this fail to support osteoid formation and result in the deposition of fibrous tissue [50]. However, non-load bearing bone has been shown to form equally well in porosities smaller than 100μm than those greater [51]. A larger porosity facilitates cell proliferation and migration compared to smaller porosities as oxygen and nutrients can more readily diffuse in [52]. Microporosity (<10μm) plays a key role in osteoinduction. The increased surface roughness associated with high levels of microporosity provide a large surface area for new bone formation [53, 54].

1.3.1 Polymers

As mentioned, polymers may be used for bone tissue engineering in low-load applications. Natural polymers such as collagen and hyaluronic acid [55] provide binding sites for cells and are highly biocompatible. However, the use of natural materials, primarily sourced from animals, introduces a risk of disease transmission. Synthetic polymers such as polylactic acid (PLA) and polyglycolide (PGA) have been utilised. PLA and PGA degrade at different rate is the body and the composition of the two in a composite, copoly lactic acid/glycolic acid (PLGA), allows for tailored degradation rates. Synthetic polymers lack the binding sites required for cell attachment [56]. Hydrogels and peptides that gel in inside the body have attracted interest as injectable scaffolds [57].

1.3.2 Bioactive Glasses And Ceramics

Bioceramics and glasses are an attractive material for use in load bearing bone tissue engineering. The most common bioceramics are the calcium phosphates. These include hydroxyapatite (HA) [58], β-tricalcium phosphate (β-TCP), and α-tricalcium phosphate (α-TCP). HA is very stable however and will not readily absorb in the body. β-TCP and α-TCP are less stable and can be combined with HA to control degradation rates and allow for the formation of a bone bonding apatite layer on its surface. Bioactive glasses, such 45S5 [59], based around Ca and P containing silica glasses are also popular as they rapidly form apatite layers on their surface when implanted into the body. They are however relatively weak. Glass ceramics, consisting of a crystal phase within a glass, allow for enhanced mechanical properties while maintaining the bioactivity of the bioactive glasses. Examples of bioactive glass ceramics are apatite-wollastonite ($Ca_5(PO_4)_3F$ and $CaSiO_3$ in a $CaO{\cdot}MgO{\cdot}2SiO_2{\cdot}P_2O_5$ glass) [60-64] and apatite-mullite [65]. Apatite-wollastonite gets its strength from the apatite phase lying within a fibrous wollastonite phase that helps block crack propagation [66].

1.3.2.1 Strontium Containing Bioactive Glasses and Glass Ceramics

Strontium, like calcium, is a divalent cation. As strontium and calcium have the same charge and similar sizes they can often be substituted for each other in crystalline and amorphous structures. In recent years interest has grown in the substitution of strontium for calcium in bioactive calcium phosphate ceramics, glasses and glass-ceramics such as Bioglass 45S5 [67-70], hydroxyapatite [71, 72] and wollastonite [73]. The inclusion of strontium into bioactive calcium phosphates is of interest due to both its biological role and its contribution towards the materials chemistry, structure and physical properties.

Strontium is the active component of anti-osteoporotic drug strontium ranelate, two strontium ions bound to ranelic acid. Orally administered strontuim ranelate has been shown to increase bone mineral density and reduce fracture risk in osteoporotic women [74]. It does this by both up-regulating osteoblastic new bone formation and down-regulating osteoclastic bone resorption [75], a feature unique among other osteoporosis treatments such as anti-catabolic and pro-anabolic drugs. Suggested modes of action for the effect of strontium on osteoblast and osteoclast activity will

now briefly be examined. For bone mass to increase, the activity of osteoblasts must exceed that of osteoclasts. This can either be achieved by increasing the number of osteoblasts, increasing the rate of osteoblast activity, decreasing the number of osteoclasts or decreasing the rate of osteoclast activity. Strontium has been shown to work by a combination of all four routes.

Osteoblast are capable of inducing osteoclast differentiation by the expression of receptor activator of nuclear factor κ-B lignad (RANKL) which bind to receptor activator of nuclear factor κ-B (RANK) on osteoclast precursor cells, activating intracellular signalling that leads to differentiation into osteoclasts [76]. Osteoblasts may also express osteoprotegrin (OPG), a decoy protein that is capable of blocking the interaction of RANKL with the RANK receptor, thus inhibiting osteoclast differentiation. Strontium has been shown to increase osteoblast OPG expression and decrease RANKL expression, therefore reducing osteoclast differentiation. The result is decoupling of the relationship between osteoblast and osteoclast numbers, leading a relative reduction in osteoclast population.

Strontium has also been shown to interact with the calcium sensing receptor (CaSR) on both osteoblasts and osteoclasts. In the case of osteoclasts, the interaction effects both osteoclast activity and lifespan. Both calcium and strontium act as full agonists for the CaSR, with strontium having a lower affinity [77]. CaSR stimulation in osteoclast activates phospholipase C (PLC) activity which, via a signalling cascade, triggers the nuclear translation of nuclear factor κB (NFκB), resulting in apoptosis of the osteoclast and a reduction in osteoclast numbers [78]. Strontium interaction with the CaSR, compared to that of calcium, has been shown to alter the PLC activated signalling cascade [78], indication that strontium's effect on osteoclast bone resorption is also as a result of cellular activity and apoptosis control.

Strontium has been shown to enhance replication of pre-osteoblasts, reduce osteoblast apoptosis and increase *in vitro* nodule formation (an indication of osteoegenesis) [74]. Activation of the CaSR receptor by strontium in osteoblasts has been shown to increase osteoblast replication via up-regulation of mitogen activated protein kinase (MAPK) leading to increased osteoblast replication [79]. Another signally pathway that is key to the osteoblast response to strontium is the calcineurin/nuclear factor of activated Tc (NFATc) [80]. This pathway has been shown to be activated by strontium, resulting in increased osteoblast replication.

While it is clear that strontium plays a crucial role in bone metabolism, its role in the material properties of bioactive calcium phosphates should not be downplayed. The substitution of strontium into calcium phosphates has been shown to expand the crystal unit cells [71, 72] or glass networks [81, 82] due to the increase in ionic radii (1.00 to 1.18 Å [83]) between the two . This in turn alters the degradation of the material and subsequent ion release [67, 73, 84, 85], the ability of a glass to sinter and crystallise [86, 87], the ability of the material to form a surface apatite layer [73, 88, 89] and also the ability of the material to direct cell attachment and fate [71, 90, 91].

Strontium has been successfully substituted into glasses in the $CaO•P_2O_5•CaF_2•SiO_2•MgO$ system [86]. The glasses however had a higher magnesium content than A-W and when heated crystallised to form diopside and apatite containing glass-ceramics. To the writers knowledge, strontium has yet to be incorporated into the A-W parent glass.

1.4 Glass-Ceramic Theory

In order to be understand the processing of glass ceramics, the theory behind the material must first be understood, staring with the structure and formation of the glass.

1.4.1 Glass Formation

As a liquid is cooled slowly through its melting point, T_m, it may crystallise as constituent atoms, ions or molecules arrange into their equilibrium lattices.

However, some materials are capable of forming glasses if the liquid is cooled at a high enough rate. The composition of these glass-forming materials are usually based around a simple oxide, most commonly silica (SiO_2), for reasons that will be discussed later. As the rate of cooling increase, the time required for the liquid elements to establish their equilibrium configuration increases [92] as viscosity of the melt increases. This prevents the formation of crystal phases and the liquid becomes supercooled. The difference between the temperature of the supercooled liquid and T_m is dubbed undercooling. At sufficiently high levels of undercooling, there is insufficient time for elements to form the long-range structure indicative of crystal lattices. At the glass-transition point, T_g, the viscosity of the melt approaches

1014 poise [93] and ions become fixed, forming an X-ray amorphous glass showing only a short range ordered network [94].

Unlike slowly passing through T_m to form crystals, passage of a supercooled liquid through T_g does not result in a massive change in specific volume, see figure 4. This exemplifies a significant difference between the structure of the glass and crystal and shows similarities between the liquid and glass packing.

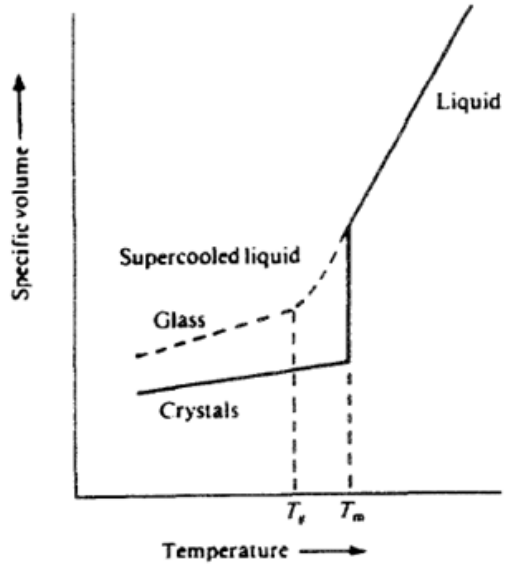

Figure 4: The change in specific volume as a function of temperature for theoretical glass, ceramic and crystal phases, reproduced with permission [94].

The conformational changes that occur during crystal and glass formation can also be observed via differential thermal analysis (DTA), figure 5. As crystals form at point Tm, a large exothermic peak is observed as elements settle into low energy configurations, this coincides with the drop in specific volume observed in figure 4. However, the supercooled liquid shows no latent heat evolution and no specific volume change as it passes through T_m, indicating elements are still in their liquid arrangement. At T_g, only a small peak is observed in the DTA trace, thus supporting the small gradient change observed in the figure 4 and indicating that the glass formed has a structure similar to that of a liquid [95].

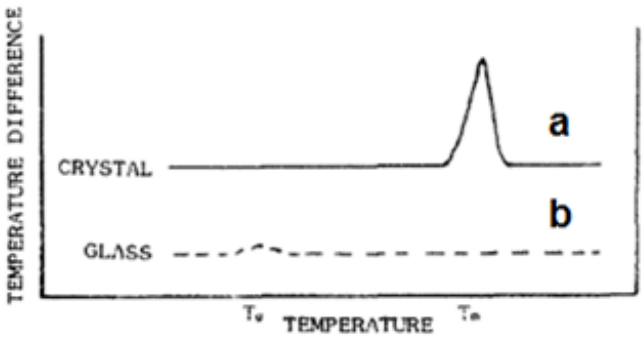

Figure 5: Theoretical DTA plot of (a) a crystal and (b) a glass as they undergo melting (T_m) and glass transition (T_g), reproduced with permission **[94]**.

Though glasses formed from a supercooled melt lack the long-range, repeating structure of their crystal forms, they retain similar interatomic forces, and co-ordinations [96]. This is most clearly observed in vitreous silica, where, in both its crystalline and amorphous states, each silicon ion is surrounded by four oxygen ions and each oxygen ion is surrounded by two silicon ions [93], forming a polyhedron. In the crystalline state, this polyhedron repeats in a regular manner, providing long-range order to the structure. However, in the amorphous state a continuous network of these polyhedra exist, but only short-range order is shown, see figure 6.

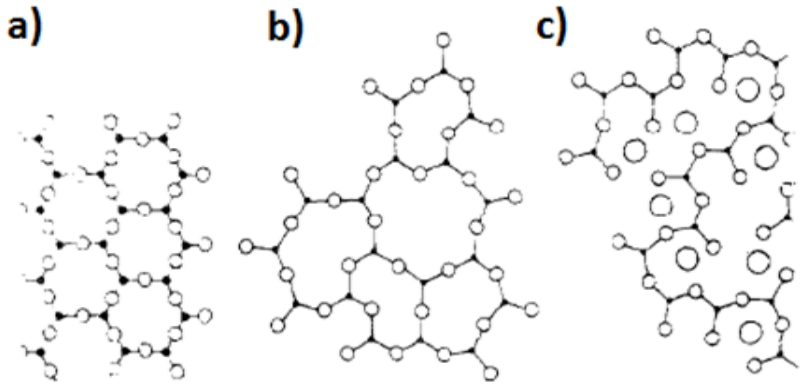

Figure 6: Silica in its a) crystalline state b) glassy state c) with non-bridging oxygen ions. Open circles indicate oxygen ions, black dots silicon ions and large circles are network modifiers, reproduced with permission [94].

In 1932, Zachariasen utilised studies of silica glass to establish a theory of glass structure [97]. The foundation of his work was a previous theory proposed by Goldschmidt (1926). Goldschmidt identified that for simple oxides there was a relationship between their glass forming capacity and the relative size of their cation in respect to the size of oxygen (anion) [96], in that only certain structures allow for

cations to be spaced in such a manner that they do not impose too great a repulsive charge on each other. Thus he determined that any oxide that conformed to equation 1 should theoretically be termed a glass former.

$$\frac{R_c}{R_a} \cong 0.3$$

Equation 1

Where R_c = the radius of the cation and R_a= the radius of the anion. Zachariasen expanded on Goldschmidt's work to develop four rules which predict if a single oxide is capable of forming a glass:

- Each oxygen must be linked to not more than two cations.
- The number of oxygen atoms that surround a cation must be low, ie. the coordination number must be 3 (triangular) or 4 (tetrahedral).
- The oxygen polyhedra are bonded to each other at their vertices and not at their edges or sides.
- At least three of the polyhedron vertices must be bonded to other polyhedral.

These rules predicted the following glass-forming oxides: SiO_2, GeO_2, B_2O_3, and P_2O_5, all of which are known as network formers. Other normally non-glass formers may substitute for network formers, such as Al_2O_3 substituting for silica, to form glass, these are referred to as intermediate glass components [98].

Network modifiers are glass components that occupy positions outside of the coordination polyhedra. As their name suggests, they modify the structure and properties of the network. Network modifiers are often alkalis and alkaline earth metals, such as CaO and Na_2O. Most network modifiers act as fluxes, lowering the liquidus temperature of the network while simultaneously reducing the viscosity [93]. Network modifiers work by depolymerising the network via the reduction of "bridging oxygens" that connect the tetrahedra at their vertices. The resultant "non-bridging oxygens" depolymerise the network to a degree by no longer contributing to cation-oxygen-cation bonds [98] and form the vertex of a tetrahedron, to which the network modifier is attached [96]. They also act as centres for chemical attack [93].

So why is the low energy crystalline state not always achieved in glass formers, even though the bonding patterns of the vitreous and crystalline states are so similar? The answer lies in the ability of the bonds of a glass former to be distorted by small amounts from their preferred orientations without the expenditure of large amounts of energy. This results in deformed bond angles and lengths that disrupt the long-range order of the crystal and thus it may be denoted as amorphous. The distributed bond lengths and angles require different energies to break, thus glasses do not have a well-defined melting point, unlike crystals where an equal amount of energy is required for breakage of all bonds [93]. Quenched glasses contain high concentrations of vacancies, dislocations, broken bonds and electron imperfection as a result of the disrupted lattice.

1.4.2 Crystallisation

The controlled crystallisation of a glass can be utilised to impart enhanced properties on the material, such as: increased machinabillity and toughness, high temperature stability, controlled expansion and biocompatibility [99]. A partial transformation of the glass to a crystal leads to the formation of a glass-ceramic, a material that shares the properties of the base glass and the crystal phases formed.

Crystallisation results in a drastic change in the atomic arrangement of small, localised volumes that form an interface between the parent glass and crystallised fraction. Crystallisation occurs in two stages: nucleation and growth.

Crystal nucleation is the formation of small, stable crystal phases within the parent glass. This may occur either randomly throughout the bulk of the parent glass (homogenous nucleation) or preferred sites (heterogenous nucleation). The formation of nuclei is best understood by examining the balance of the negative free energy transformation that occurs when a metastable glass rearranges to a stable crystal and the positive free energy that is required for the formation of a new interface.

The largest free energy change, ΔG^* occurs at a nuclei radius of r^*. This is known as the critical radius, any nuclei smaller than r^* will have to reduce in size to reduce the free energy change, however any nuclei larger than r^* will increase in size with a reduction in free energy and is thus thermodynamically stable.

Thus the rate of steady state nucleation per unit volume per unit time, I_c, equation 2, depends on the thermodynamic barrier ΔG^* that must be first overcome to form a nuclei with radius greater than r*. It also depends on the free energy required for the transport of molecules from the base glass, across the interface to the growing nuclei (the kinetic barrier), ΔG_a. ΔG^* can be defined with respects to the interfacial energy, σ, the bulk free energy of the liquid-to-crystal transformation, ΔG (per mol), the molar volume of the crystal phase, V_m, and assuming that all nuclei are spherical and the crystal phase formed has the same composition as the parent glass [100], equation 3.

$$I_c = A_N exp\left[\frac{-(\Delta G_a + \Delta G^*)}{kT}\right]$$

Equation 2

$$\Delta G^* = \frac{16\pi\sigma^2 {V_m}^2}{3\Delta G^2}$$

Equation 3

A_N is a constant while ΔG^* decreases with decreasing temperature while ΔG_a is considered to be temperature independent. Equations 2 and 3 dictate that optimum homogenous nucleation occurs at a specific temperature.

Though equations 2 and 3 are useful in the description of a system who's crystal and glass phases share the same composition, the case of crystallisation of two phases from a single glass is more complicated. Consider the two phase system which precipitates crystal phases α and β. The precipitation of a phase will result in a reduction in free energy that acts as a driving force for crystallisation, ΔG. During crystallisation from a liquid, ΔG is greatest when the composition of the precipitate is the same as the liquid [100]. However, for a solid state transformation the free-energy-composition relationship is broadened and ΔG will now be influenced by the interfacial energy and kinetic barrier and thus ΔG may not be a maximum when the two compositions are the same [101], dictating the first phase that will crystallise.

Nucleation may occur preferentially at specific sites within the glass; this is known as heterogeneous nucleation. Interfaces in the parent material, ie. the material's free surface (surface nucleation) or the surface of precipitates (bulk nucleation), are

favoured for heterogeneous nucleation as they reduce the thermodynamic barrier which must be overcome [95].

The principle behind this reduction in energy can be seen by examining the wettability of a nucleation site, ie. how easily the crystal may spread over the site, figure 7. Resolving the interface energies, γ_{NC} and γ_{CL} in figure 7 gives γ_{NL}, where N, L and C represent the nucleating site, liquid and crystal, respectively, equation 4 Thus the contact angle, θ, determines wettability and can be utilised to determine the thermodynamic barrier of heterogeneous nucleation, ΔG_{het}*, equation 5 [95].

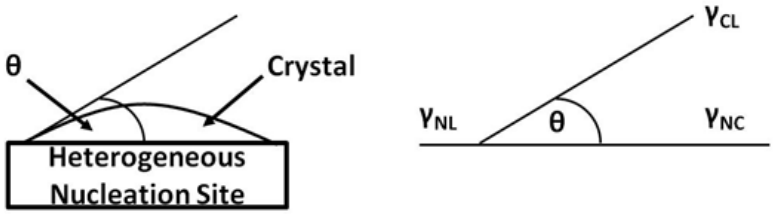

Figure 7: Heterogeneous nucleation wetting/contact angle and interface vectors, modified with permission [94].

$$\gamma_{NL} = \gamma_{NC} + \gamma_{CL} \cos\theta$$

Equation 4

$$\Delta G_{het}{}^{*} = \Delta G^{*} \left(\frac{(2 + cos\theta)(1 - cos\theta)^2}{4} \right)$$

Equation 5

1.4.3 Nucleating Agents

Nucleating agents work by either precipitating out of the parent glass during a heat treatment (as is the case with many metallic nucleating agents, eg. Au, Ag, Pt and Pd) or by the induction of amorphous phase separation (APS), if multiple phases are more stable than one [102], leading to the formation of an interface between the two glasses [95] and skewed concentration distributions [101]. Phase separation occurring above the liquidus produces two stable phases that remain after cooling; if the two phases exist bellow the liquidus then metastable states will occur that will form a single phase upon rapid cooling but that can be recovered with the appropriate heat treatment [102]. Nucleating agents may also alter homogenous nucleation by increasing ΔG, reducing σ or by increasing the diffusion rate [101].

Many non-metallic nucleating agents exist and are mainly oxides such as TiO_2 and ZrO_2. The process by which non-metallic nucleating agents promote crystallisation is poorly understood, but it is known that agents are specific to certain glasses [100]. Apatite containing glass-ceramics utilise P_2O_5 and fluorides as a nucleating agents where they reduce ΔG^* and promote APS [101].

The formation of critical nuclei leads to crystal growth. The controlling factor in crystal growth is the free energy required for the movement of elements from either the glass to the crystal or vice versa. It has already been stated that the arrangement of the crystal phase possesses a lower free energy than the glass phase. Figure 8 symbolises the activation energies that must be overcome for the movement of an element between the glass and crystal phases. $v\Delta G_v$ refers to the volume free energy, ΔG_a the activation free energy and λ the size of the glass and crystal interface over which elements must diffuse.

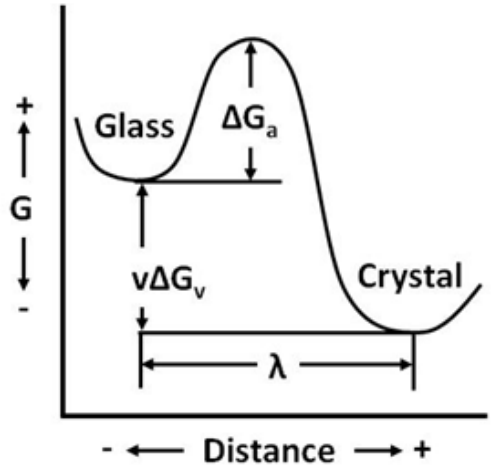

Figure 8: a) schematic free energy diagram for the growth of a crystal across an interface b) schematic of the arrangement of atoms during the phase transformation, modified with permission [103].

It is clear that $\Delta G_a + v\Delta G_v$ is greater than $v\Delta Gv$ and thus there is more restriction to the flux of elements to the glass than to the crystal, leading to crystal growth [95]. The rate of growth, the difference between the flux of elements from the glass-to-crystal and crystal-to-glass, U, is defined in equation 6, where v_0 is the attempted jump frequency of the elements [95].

$$U = \frac{v\Delta G_v}{kT} v_0 exp\left(-\frac{\Delta G_a}{kT}\right)$$

Equation 6

1.4.4 Heat Treatments

Heat treatments can be used to tightly control the final grain structure of a glass ceramic. As seen, both the formation of nuclei and the growth of crystal are highly dependent on temperature. The temperature ranges at which nucleation and growth occur vary dependent on the system. In some systems, there may be a broad overlap between the two, in this case a single heat treatment may be appropriate to maximise both the number of nuclei and the rate of crystal growth. In other systems the nucleation and growth temperature ranges may be spaced apart and in this case a two stage heat treatment is required: an initial dwell stage for nucleation and a second higher temperature dwell to ensure rapid crystal growth, figure 9.

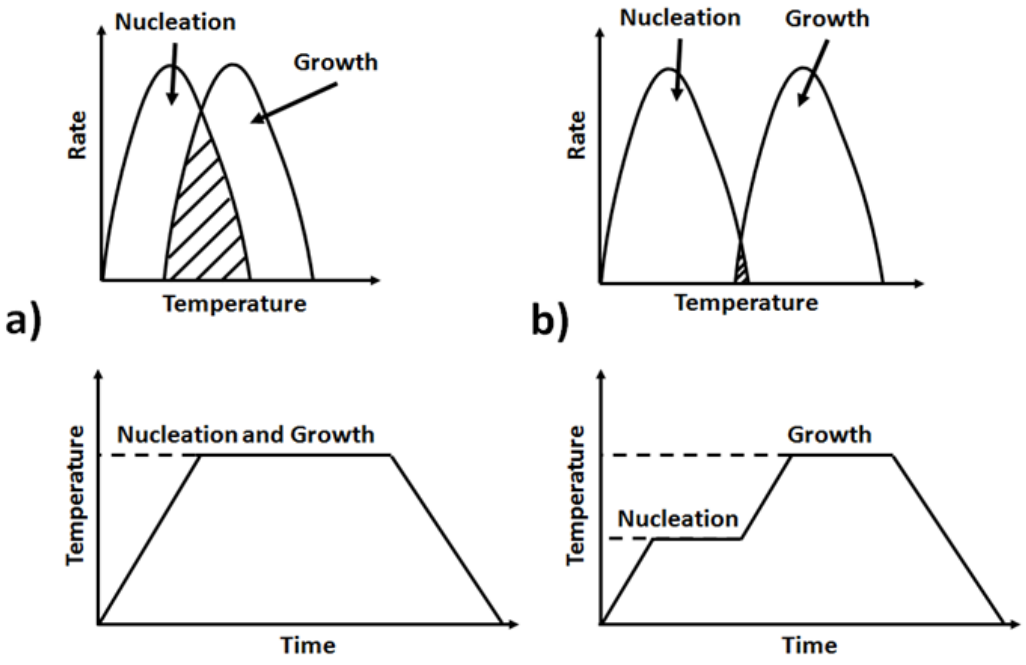

Figure 9: Nucleation and growth regions and appropriate heat treatment regimes for (a) overlapping curves (b) sparsely overlapping, modified with permission [94].

The effect of different nucleation processes must also be considered when designing a heat treatment. Bulk or surface nucleation may be favoured dependent on the heat treatment, as seen in figure 10. The two processes can be differentiated utilising

differential thermal analysis. Bulk nucleation produces a sharp peak where-as surface nucleation produces a much boarder one [104].

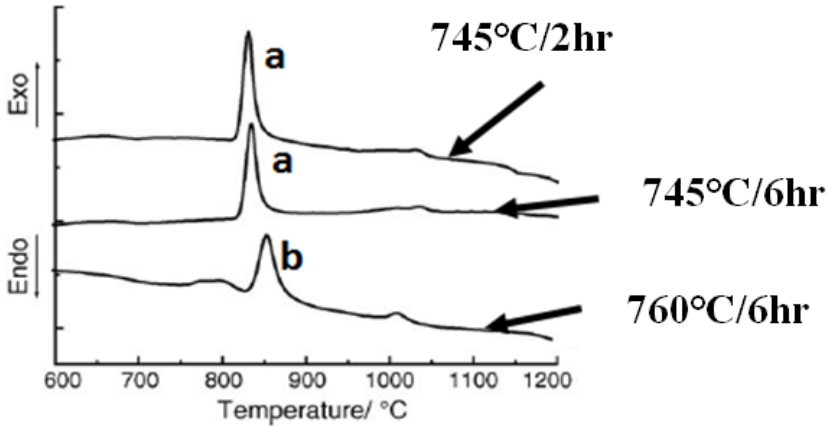

Figure 10: Bulk (a) and surface (b) nucleation in an Li_2O-Al_2O_3-SiO_2 glass following different heat treatments, modified with permission [104].

The size of the particles being heat treated will also determine the type of nucleation present. Surface nucleation favours smaller particles. In the case of apatite-wollastonite, the crystallisation of the surface nucleating wollastonite phase is shifted to a higher temperature when larger particles are used, figure 11

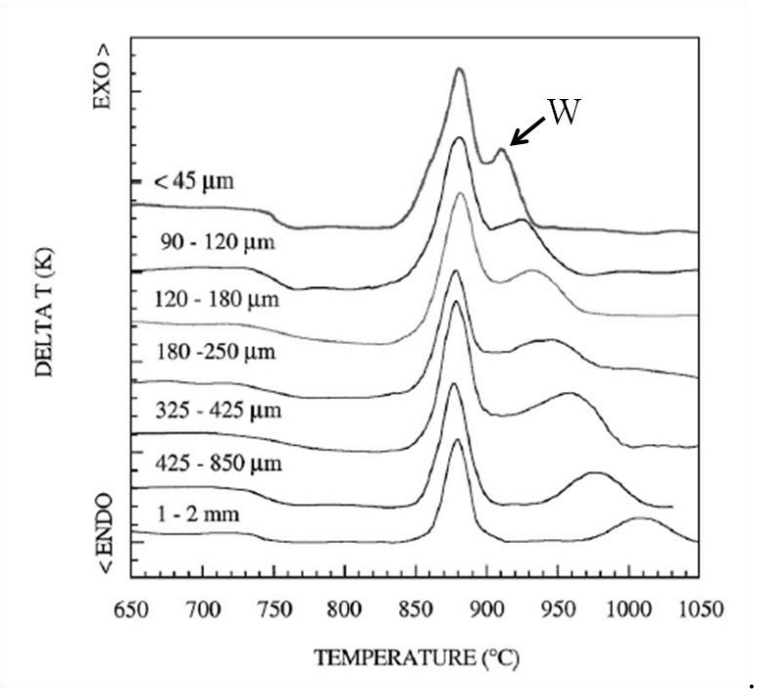

Figure 11: DTA showing the shift in the wollastonite peak (W) between different particle sizes for a 5K.min^{-1} heating rate, reproduced with permission [60].

When more than one phase is to be crystallised the phenomenon of amorphous phase separation and the preference for either surface or bulk nucleation can be utilised to ensure the crystallisation of both phases [105]. The combined optimum nucleation temperature for the two crystallising phases can be determined via DTA by plotting the variation between the crystallisation temperature during constant heating with the crystallisation temperature following a holding period at an assumed nucleation temperature, figure 12. The largest temperature shift observed is taken as the optimum nucleation temperature [62].

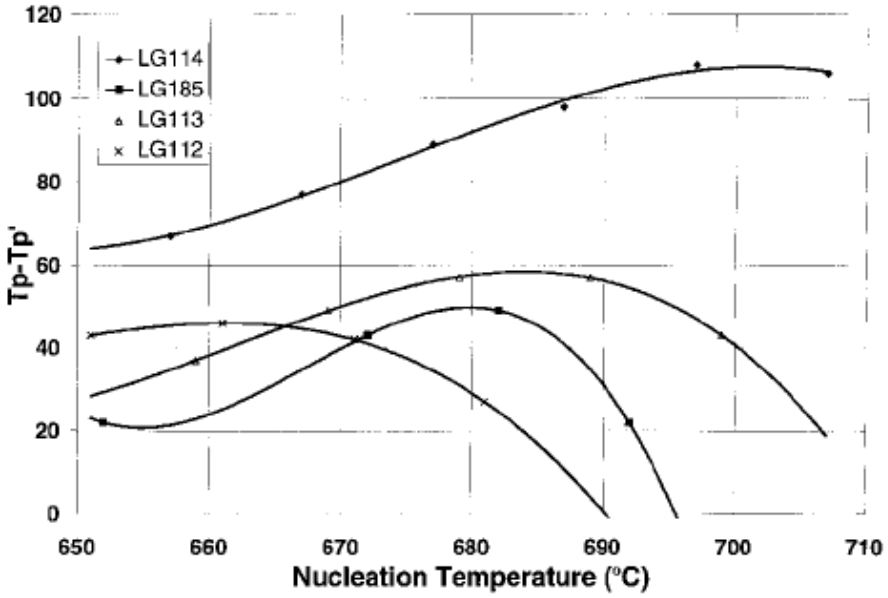

Figure 12: Optimum nucleation temperature calculation for apatite and mullite containing glass-ceramics calculated from DTA data, reproduced with permission [106].

Crystallisation heat treatments can be combined with a sintering heat treatment to allow for a single stage treatment in the formation of porous glass-ceramics from a glass powder.

1.5 Sintering

Heat treatment of the powders not only triggers crystallisation but also fusion of the particulates and densification of the final material. Sintering not only determines the strength of the bonds between the sintered particles (and thus the bulk material) but also the size of the pores of the material.

Sintering is performed at temperatures well below the melting point of the material at a temperature determined by the material composition and particle size. The driving force for sintering is the reduction in interfaces and contact angles in the material as well as the secondary elimination of grain boundary area, thus sintering is faster when smaller particles are used since diffusion distances are smaller and curvature induced stresses are greater [107]. Two main types of sintering can occur: solid state sintering and liquid phase sintering.

1.5.1 Solid State Sintering

A simple model to display solid state sintering is that of two spheres, diameter D, contacting at a single point, figure 13. Following initial contact, sintering progresses in three stages: early stage neck growth, late stage neck growth and finally a fully coalesced particle with diameter 1.26D [108]. During the early stage, pores between the particles remain interconnected but as necking progresses pores become smaller and smoother. The final stage results in the closure of pores. Any gasses that may have been evolved during the sintering process may be trapped, preserving the pore and impeding densification.

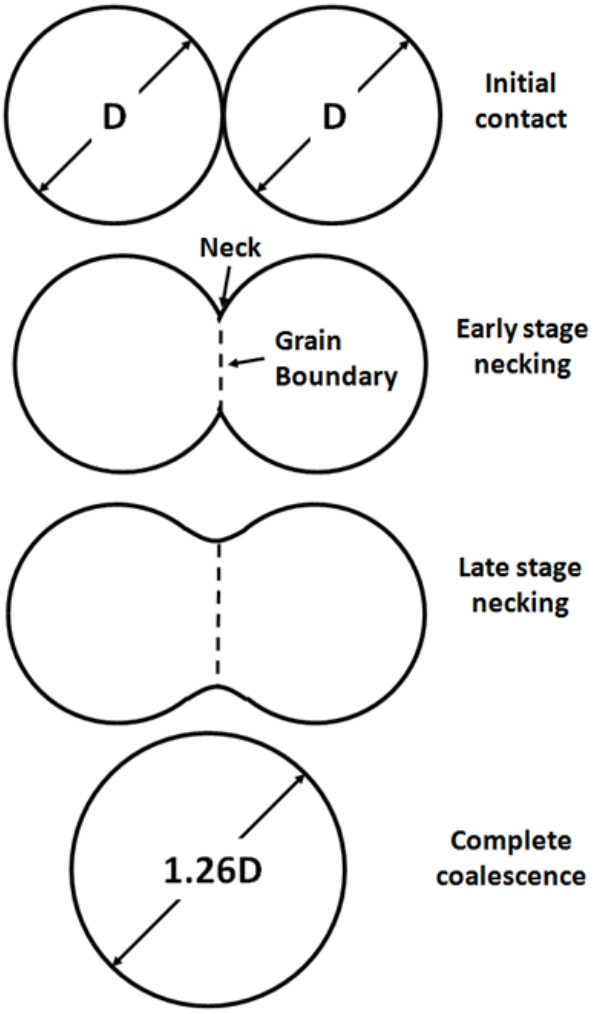

Figure 13: Sintering necking of two theoretical spherical particles, modified with permission [107].

The transport mechanism by which necking occurs can be visualised by considering pores as large accumulations of vacancies. Vacancy and mass transport occurs via two main mechanisms: surface transport and bulk transport.

Surface transport occurs at lower temperatures and results in necking with minimal densification due to mass transport occurring at the particle surface. It involves surface diffusion and evaporation-condensation. Bulk transport occurs at higher temperatures than surface transport [108]. It results in the transport of mass from within the particles to the necking region, causing densification. Bulk transport mechanisms include volume diffusion, grain boundary diffusion, plastic flow and viscous flow. Viscous flow is the favoured mechanism in glasses where-as crystalline materials favour grain boundary diffusion, volume diffusion and stress-induced plastic flow (though the role of the latter decreases with sintering time as stresses and dislocations are removed) [108].

1.5.2 Liquid Phase Sintering

Liquid phase sintering (LPS) utilises the formation of a liquid phase during sintering of alloys that melt over a large temperature range or composite [108]. LPS is associated with faster diffusion rates than solid state sintering. During LPS, the solid phase is usually soluble in the liquid phase formed, this allows for high levels of wetting and good contact between the two components. This also leads to enhanced densification as capillary action draws the solid phase particles together [107]. In a single component system, solid state sintering precedes LPS. But as temperatures increase, LPS takes over. A low melting point component can be added to a powder mix to form a composite to enhance LPS and further promote densification.

Liquid phase sintering can be used for the binding a solid particles using free-form fabrication methods such as selective laser sintering. This method has successfully been used to create porous apatite-wollastonite scaffolds [62].

1.5.3 Sintering Assessment

The level of sintering can be observed by looking at the shrinkage and deformation of the sample during or after heating. Hot stage microscopy allows for analysis of the structure of the sample as a function of temperature and is useful in relating shrinkages to thermodynamic events such as glass transitions and crystallisation [109]. Linear shrinkage can be measured by comparing the dimensions of the material pre- and post-sintering [110]. Further visual analysis can be performed using scanning electron microscopy (SEM), which is useful for observing the final structure of the material, with changes in particle morphology and the formation of necks being easily assessed visually [61, 110]. This can be performed on either the material surface or on cross-sections to map the pore sizes and distributions. In glasses, the phase that may form during sintering can also be observed using SEM [110] and their composition mapped using energy dispersive x-ray analysis (EDX) [111]. Crystalline phases that form in the material can be identified and quantified using XRD.

Incomplete sintering leaves behind residual porosity. The post sintering porosity is often reported as a density and is calculated from a direct measurement of the material mass and volume. The volume can be determined by filling the open pores

with paraffin oil and submerging the material in water to record to the volume increase [108]. The pores of the material can either be open, those that are connected to the surface, or closed pores, those that are sealed within the material. The Archimedes method can be used to measure open porosity and subsequently combined with the density to calculate the actually porosity that incorporates closed pores [112]. The material is weighed dried, weighed after fluid impregnation then weighed in water and the resulting value used to calculate the porosity. The Archimedes method is most suited to large geometries and so alternative methods are often used for smaller samples. Other impregnation techniques include mercury or liquid extrusion porosimetry and nitrogen pycnometry which can provide micro-porosity distributions and material densities, respectively, by loading and unloading the selected medium into the material and measuring the difference is forces required to do so [113].

Micro computed tomography x-ray imaging allows for the construction of 3D models that represent the porous material. The technique is non-invasive and can be combined with custom algorithms to provide values for the different pore features such as size distribution and interconnectivity [113].

The level of sintering of a material can also be determined using mechanical measurements. The more sintered a material, the stronger it will be. Pores reduce the effective cross-section of the material and thus its strength [108, 114]. The compressive strength and flexural strength are most commonly recorded for porous ceramics and glasses with the BS ISO 6872-2008, testing of dental ceramics specifying a 3- or 4-point bend test should be used [115]. The mechanical strength is also influenced by many other factors including crystallite composition, grain size, impurity levels, flaws and pore characteristics. The heat treatment applied to induce sintering will affect all these factors and so measurement of the mechanical strength of the material remains a successfully technique to determine the success of a sintering process [108].

1.6 Thesis Aims and Objectives

It is well known that the substitution of strontium into calcium phosphate systems has been shown to up-regulate osteoblast activity and down-regulate osteoclast activity, increasing the rate of neo-bone formation while also influencing the

material's processing and physical properties. While strontium substitution into the Bioglass 45S family of glasses is well documented, its substitution into the more mechanically and biologically stable apatite-wollastonite glass-ceramic is as of yet un-reported.

1.6.1 Overall Aim

The overall aim of this piece of work was to form a bioactive glass-ceramic based on the substitution of strontium into apatite-wollastonite glass-ceramic.

To achieve this a range of glasses were formed based on the molar substitution of strontium for calcium into the apatite-wollastonite parent glass. Their subsequent devitrification was investigated and utilised to form semi-crystalline glass-ceramics. The physical and biological properties of the developed materials was then investigated with respect to their application as bone replacement materials.

1.6.2 Objectives

The work can be broken down into four main objectives, presented as single chapters and subsequently discussed as a whole:

Chapter 2: The ability of the novel compositions to form an amorphous glass was investigated and control of the processing assessed.

Chapter 3: The thermodynamic and physical characterisation of the materials' devitrification was performed and utilised to produce a controlled heat treatment for the formation of strontium containing glass-ceramics.

Chapter 4: The ability of the strontium containing materials to be sinter was then assessed and the combined processing knowledge subsequently applied to form porous glass-ceramics who's mechanical and physical properties was characterised.

Chapter 5: *In vitro* testing assessed the capacity of the materials to form a surface apatite layer in a biologically relevant solution and also their ability to direct human mesenchymal stem cell attachment, growth and differentiation.

Chapter 2: Glass Powder Production

2.1 Introduction

Apatite-wollastonite glass-ceramic is formed from the controlled devitrification of an amorphous parent glass. In this work, the parent glass was produced via the melt quench route. Heating of the mixed oxide precursors to above their melting points followed by rapid quenching into a water bath allows for the solidification of the metastable glass without the formation of crystal nuclei. Strontium was substituted for calcium at molar ratios into the apatite-wollastonite composition reported by Kokubo [116] and Xiao [62] and the glass forming ability of the compositions was tested prior to devitrification studies.

The aim of this work was to determine if strontium had successfully been substituted into the glass network, retaining its amorphous structure, and to ensure that processing had produced powders with a regular morphology and size distribution. The subsequent devitrification studies were performed via differential scanning calorimetry (DSC). The DSC output is strongly influenced by particle size and thus consistent particle size distributions were essential. A scanning electron microscope (SEM) and dynamic light scattering were used to observe the morphology and size of the particles. The incorporation of strontium into the material was observed via the energy dispersive x-ray analysis (EDX) probe of an SEM and the amorphous nature observed via powder x-ray diffraction.

2.2 Experimental Methodologies

2.2.1 Glass Production

2.2.1.1 Glass Melt Quench

The apatite-wollastonite parent glass composition was that used by Xiao 2008 [62] and first reported by Kokubo in 1991 [116] to which gradual substitutions of strontium for calcium were made. Relative molar and weight ratios of the glass components are shown in table 2.

Table 2: Molar composition of the 0 Mol % strontium feedstock.

Reagent	MgO	CaO	SiO_2	P_2O_5	CaF_2
Mr	40.304	56.079	60.084	141.943	78.076
Molar%	7.1	49.9	35.4	7.1	0.4
Weight%	4.6	44.7	34.0	16.2	0.5

The mass of reagents required for a 200g batch were calculated. Whilst most of the reagents are available in the forms stated above, calcium oxide (CaO) is not stable in air and will spontaneously react with carbon dioxide (CO_2) to form calcium carbonate ($CaCO_3$). During production of the glass, calcium carbonate is used as a precursor reagent to calcium oxide as it is stable at room temperature in an air atmosphere and undergoes thermal decomposition at temperatures above 825°C, releasing one molecule of carbon dioxide and one molecule of calcium oxide per molecule of calcium carbonate, a process known as calcination, equation 7.

$$CaCO_3 \xrightarrow{Heat} CaO + CO_2$$

Equation 7

Thus, one mole of calcium carbonate is required to produce one mole of calcium oxide. The mass required for a 200g batch of glass can be easily calculated from the relative atomic masses of the two reagents.

$$Mass\ of\ CaO\ required = 2 \times Weight\% = 2 \times 44.7 = 89.4g$$

$$No.moles\ of\ CaO = \frac{Mass}{M_r} = \frac{89.4}{56.079} = 1.5942mol$$

$$\therefore Mass\ of\ 1.5942mol\ CaCO_3 = No.Mols \times M_r = 1.5942 \times 100.088 = 159.6g$$

The final reagent composition of a 200g batch of 0 Mol % strontium glass is shown in table 3.

Table 3: Final composition of the 0 Mol % strontium feedstock.

Reagent	MgO	$CaCO_2$	SiO_2	P_2O_5	CaF_2
Supplier	VWR International	VWR International	Tilcon Sands	Sigma-Aldrich	VWR International
Mass (g)	9.2	159.6	68.0	32.5	1.0

The reagents were weighed to the nearest 0.1g (Sartorius Roughing Balance, PT3100) into a mixing container. A steel agitation bar was added and the reagents were mixed for 1 hour. The powder mix was then transferred to a slip cast alumina crucible (Elite Thermal Systems) and agitated to promote powder densification and release trapped air. The crucible and powder were subsequently placed in a larger mullite crucible (Dyson Thermo), half filled with calcined alumina powder (VWR) and covered with a lid. The mullite crucible was included to contain any molten flux should the alumina crucible fail. The crucibles containing the powder mix were then pre-heated at $10K.min^{-1}$ to 500°C and held at this temperature for 15 minutes (Elite BCF 13/12-2416 furnace). They were then transferred to a second furnace (Pyrotherm 1600°C), pre-heated to 1400°C. The temperature of the furnace was then immediately increased to 1450°C and the powders were left to melt for two hours. The addition of alumina to the mullite crucible and an initial low temperature heat soak were used to minimise the thermal shock experienced by the crucible thus increasing the batch yield.

Following melting, the liquid flux was shock quenched into a cold water bath. The formed glass cracked into small frits soon after solidification due to stresses induced from the bulk cooling slower than the surface. The solidified glass was then sucked from the base of the bath using a pump (Clarke CPE 110) and passed through a 36µm sieve pan (Fisher Scientific). The glass frits were then placed in a drying cabinet for 24 hours to dry and allow for any residual stresses to be resolved.

2.2.1.2 Novel Compositions

Strontium (Sr^{2+}) was substituted in to the glass feedstock in place of calcium (Ca^{2+}). Strontium oxide (SrO) was chosen as the source of Sr^{2+} ions, replacing calcium oxide (CaO). Substitutions were calculated on a molar basis to produce glasses with compositions $35.4SiO_2$•$7.1P_2O_5$•$0.4CaF_2$•7.1MgO• (49.9-X)CaO•XSrO, where X = 6.2, 12.5, 18.7 or 24.9. Strontium carbonate ($SrCO_3$) was used as a precursor and was reduced, as with $CaCO_3$, in a calcination reaction, equation 8.

$$SrCO_3 \xrightarrow{Heat} SrO + CO_2$$

Equation 8

The mass of each reagent required, Wt, can be calculated utilising the relative molecular mass, M_r, equation 9.

$$Wt = M_r\left(\frac{Mol\%}{100}\right)$$

Equation 9

And the mass percentage of each reagent, Wt%, calculated from the total mass, equation10.

$$Wt\%_{Reagent} = \frac{Wt_{Reagent}}{\sum Wt}$$

Equation 10

The molar ratio was varied as opposed to the weight ratio to ensure that the composition of the glass did not vary with respects to the remaining elements. Four novel Sr containing compositions were proposed, the formulations of which are shown in tables 4 to 7.

Table 4: 3.12 Mol % strontium composition.

Reagent	MgO	$CaCO_3$	$SrCO_3$	SiO_2	P_2O_5	CaF_2
Mr	40.304	100.086	147.628	60.084	141.943	78.076
Molar%	7.1	43.7	6.2	35.4	7.1	0.4
Weight%	4.4	37.3	9.9	32.5	15.5	0.5

Table 5: 6.24 Mol % strontium composition.

Reagent	MgO	$CaCO_3$	$SrCO_3$	SiO_2	P_2O_5	CaF_2
Mr	40.304	100.086	147.628	60.084	141.943	78.076
Molar%	7.1	37.4	12.5	35.4	7.1	0.4
Weight%	4.2	30.6	18.9	31.1	14.8	0.5

Table 6: 9.35 Mol % strontium composition.

Reagent	MgO	$CaCO_3$	$SrCO_3$	SiO_2	P_2O_5	CaF_2
Mr	40.304	100.086	147.628	60.084	141.943	78.076
Molar%	7.1	31.2	18.7	35.4	7.1	0.4
Weight%	4.0	24.5	27.1	29.8	14.2	0.4

Table 7: 12.47 Mol % strontium composition.

Reagent	MgO	$CaCO_3$	$SrCO_3$	SiO_2	P_2O_5	CaF_2
Mr	40.304	100.086	147.628	60.084	141.943	78.076
Molar%	7.1	24.9	24.9	35.4	7.1	0.4
Weight%	3.9	18.8	34.7	28.6	13.6	0.4

2.2.1.3 Powder Formation

After drying, glass frits were ground. Though reagents were calculated to produce 200g of glass, some flux remained in the crucibles following pouring. Roughly 165±5g of frit were ground each time to ensure particle size distributions remained constant between batches. Though the addition of strontium to the glasses should increase the density of the frits and thus using the same volume would have been more appropriate, this was not possible at this stage of processing. Powders were ground in a puck mill (Gy-Ro Mill) for 2 minutes. The resulting powders were then sorted according to size using a sieve stack (Octagon Digital). An amplitude of 6 was used for 90 minutes to ensure thorough sorting of the size fractions. BSI410/1986 certified sieves in sizes 45µm, 90µm, 125µm, 1mm and 2mm were

used (Fisher Scientific) sorting particles into <45µm, 45-90µm, 90-125µm, 125µm-1mm, 1-2mm and >2mm size fractions.

2.2.2 Glass Powder Characterisation

Powder characterisation was performed on the 45-90µm particle size fraction. This fraction was used due to its successful use previously in the formation of apatite-wollastonite porous bone scaffolds [62, 117].

2.2.2.1 Scanning Electron Microscopy / Energy Dispersive X-Ray Analysis

In this work, all SEM images were taken on a Hitachi S3400N variable pressure SEM with either the secondary electron or back scattered detectors using the native software. Glass powders were attached to an aluminium stub via a conducting carbon patch. All samples were gold sputtered (Agar Auto Sputter Coater) to provide a conducting surface layer 6nm thick. Images were taken at an accelerating voltage of 10keV and 50µA probe current. Particle size analysis of the SEM images was done using ImageJ software. Energy dispersive x-ray analysis was performed using a Bruker XFlash detector and analysed with Quantax analysis software. An accelerating voltage of 10keV was used for all EDX measurements. The accelerating voltage used must be greater than twice the highest excitation energy, E_c, of any element present in order to obtain adequate intensities. Calcium was the element with the highest excitation energy, with an E_c of 3.692keV (for theKα1 electron), and so an accelerating voltage of 10keV was suitable. Quantifications were taken from three different shards for each composition and an average taken. A peak-to-background ZAF evaluation (P/B-ZAF) algorithm was used for the elemental quantification. Elemental identification was done utilising a preset list of expected elements (Ca, Sr, Mg, Si, P, O and F) plus automatic identification. The Bremsstrahlung background was automatically calculated. A Bayes deconvolution was used for line overlap separation. Standard samples, provided by MAC mciro analysis consultants, of $CaSiO_3$, $CaMg(CO_3)_2$ and CaPO were analysed to determine the accuracy of the semi-quantitative analysis.

2.2.2.2 Laser Scattering Particle Size Analysis

Particle size analysis was also performed via laser light scattering using a Malvern Mastersizer 2000. The system was first cleaned before a background reading was

taken. A slurry of roughly 1wt% glass particles in water was first made up. An additional dispersing agent was not required. The slurry was then passed through the light scattering laser and optics using a Hydro S (Malvern) small volume sample dispersion unit. A generic glass bead refractive index of 1.520 was assigned to the particles while the dispersant, water, had a refractive index of 1.330. A constant stirring rate of 1800rpm was used. 10 readings were taken per material and the average calculated and reported.

2.2.2.3 X-Ray Diffraction

X-ray powder diffraction was performed on the 45-90μm glass particles using a Philips X'Pert diffractometer with a spinning disc attachment and recorded using the X'Pert Data Collector software. A CuKα x-ray source was used. A 15x15mm fixed incident beam mask was used. Roughly 0.5g of glass powder was placed in the sample holders per scan. A step size of 0.0334225°, dwell of 3.18 seconds and disc rotation speed of 4 seconds were used to scan between the range of 10-70°2θ.

2.2.3 Radio Density

Radio density refers to the attenuation of electromagnetic radiation as it passes through a material. The attenuation of x-rays through a material is the underlying principle behind clinical x-ray radiography and computed tomography (CT) imaging techniques. An increase in the attenuation and thus radio density of an implant will aid in the postoperative identification of the device and monitoring of degradation/absorption. The replacement of calcium with strontium will have an effect on the radio density of the material. The x-ray intensity (I) decays exponentially when transmitted through a dense material and can be related to the incident x-ray intensity, I_0, the material linear absorption coefficient, A (cm^{-1}), and the material thickness, d (cm) by the Beer-Lambert law, equation 11 [118].

$$I = I_0 e^{-Ad}$$

Equation 11

The linear absorption coefficient is derived from the mass absorption coefficient, μ (cm^2/g), and density of the material, ρ (g/cm^3), equation 12 [118].

$$A = \mu\rho$$

Equation 12

Thus the density of the material also plays a crucial role in the attenuation of x-rays through a material, equation 13 [118].

$$I = I_0 e^{-\mu\rho d}$$

Equation 13

Equation 13 can be re-arranged to calculate the mass absorption co-efficient, equation 14.

$$\mu = \frac{ln\left(\frac{I}{I_0}\right)}{-\rho d}$$

Equation 14

Thus, the mass absorption coefficient of a material can calculated by measuring the intensity of an x-ray beam before (I_0) and after (I) passing through the material if the density (ρ) and thickness (d) of the material are known.

The density of the glasses was measured using a helium pycnometer and a clinical x-ray device, digital film and image reconstruction system were used to take x-ray radiographs of 100% dense samples of Sr substituted glasses. 100% dense samples were utilised to ensure that thickness measurements of the samples were a true measure of the amount of material with which the x-rays had interacted.

2.2.3.1 Density Determination

The density of the glass was first measured using a Micromeritics Accupyc 1330 helium pycnometer. The pycnometer was calibrated using standard steel spheres. 1±0.25g of glass was analysed per composition. The pycnometer automatically repeats the density measurement until 5 results with a standard deviation of less than 0.02 are recorded and reports the average. The mass attenuation coefficient could then be calculated using equation 12.

2.2.3.2 Glass Rod Formation

To produce 100% dense samples 65g of glass 125µm-1mm particle size fractions were ground for 10s in a puck mill (Gy-Ro-Mill) and then packed into a slip cast alumina crucible (Elite Thermal Systems) and agitated. Re-grinding of the powder produced a wider range of particle sizes thus improving particle packing with the aim of minimising bubble formation from trapped air during melting. The powder containing crucibles were then placed in larger mulite crucibles (Dyson Thermal) and heat-shock protected using a bed of calcined alumina (VWR). The crucibles were then preheated to 500°C at 10K.min^{-1} (Elite BCF 13/12-2416 furnace) and held at this temperature for 5 minute before being transferred to a furnace pre-heated to 1400°C (Pyrotherm 1600°C). The furnace temperature was immediately increased to 1450°C and the samples heated for 90 minutes. The temperature of the furnace was then increased to 1500°C for 30 minutes to help reduce the viscosity of the melt when pouring. The molten glass was then poured into a carbon mould, pre-heated to 750°C, and placed in a furnace at 750°C and allowed to cool at the furnace rate. After cooling, the rods were removed from the moulds and visually inspected for trapped bubbles and signs of crystallisation.

2.2.3.3 Dense Disc Formation

Discs, roughly 4mm thick, were cut from the glass rods using an abrasive cutter (Brillant 220) and diamond saw blade (Beneteo-121097). A disc speed of 1200rpm and feed rate of 3mm.min^{-1} were used. The cutting surface was then polished flat using P1200 grade grinding paper (Hermes). The thickness of the samples was then measured using vernier callipers.

The discs were placed on a digital radiographic plate (Kodak CS7600 size 1) and clinical radiographs were taken (Philips Oralix X-ray head) at 65kVp, 7.5mA and a 15mm aluminium filter with a 2 second exposure. The films were then digitally scanned using a Carestream CS7600 system and viewed using the native software. The resulting images were loaded into ImageJ software. The image was assigned a 32 bit grey scale, inverted and then the pixel intensity was read at 3 points on each disc and an average taken. Care was taken to ensure that sections of disc that may contain bubbles were not used for intensity measurements. The intensity (I) was

then calculated as a percentage of the fully exposed film (I_0). The relative linear absorption coefficient could then be calculated using equation 11.

2.3 Glass Production Results

2.3.1 Mastersizer Results

The laser diffraction particle size analysis results for the 45-90μm fraction glass compositions are shown in figure 14. In all compositions the grinding process has produced powders composed of a regular distribution of particle sizes. Each graph is composed from 10 runs, the results of which have been layered. It is clear to see that the sampling method used is highly repeatable as almost exactly the same particle size distribution was recorded for each subsequent run.

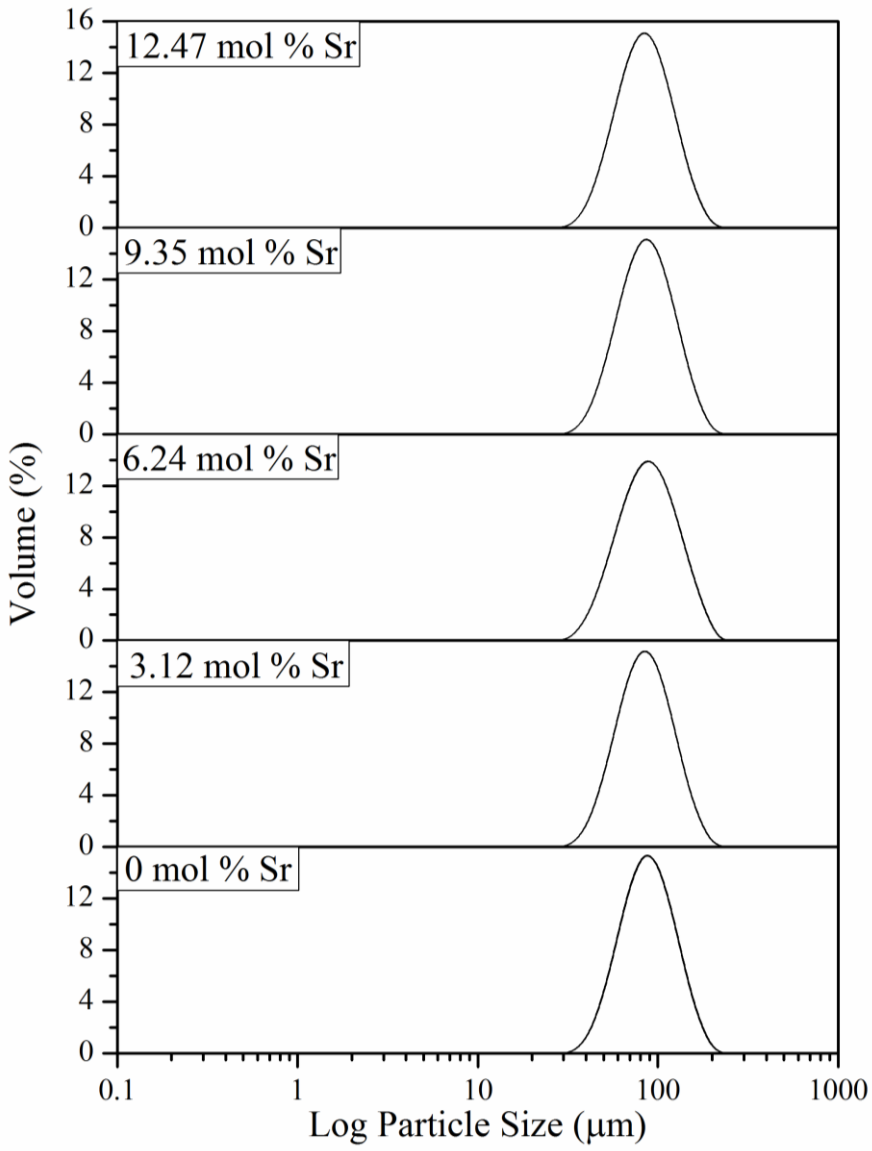

Figure 14: Mastersizer 2000 results for 45-90μm particle fractions of novel strontium containing glasses. Each graph contains the layered results of 10 runs indicating excellent repeatability.

The output of the Mastersizer 2000 is expressed as a series of size bands that are optimised to match the detector geometry and optical configuration, for example the 79.43 to 91.20 band. The midpoint of the bands must be calculated in order to determine distribution parameters. The midpoint, D, of the bands is calculated as the geometric mean of the size band limits as opposed to the arithmetic mean, see equation 15, where d is the particle size of partition i. The frequency curves of the size distribution data are all plotted using the geometrical midpoint. A comparison of the histogram and frequency curve plots for composition 0 Mol % strontium is shown in figure 15.

$$D_{geometric} = \sqrt{d_i d_{i+1}}$$

$$D_{arithmetic} = \frac{d_i d_{i+1}}{2}$$

Equation 15

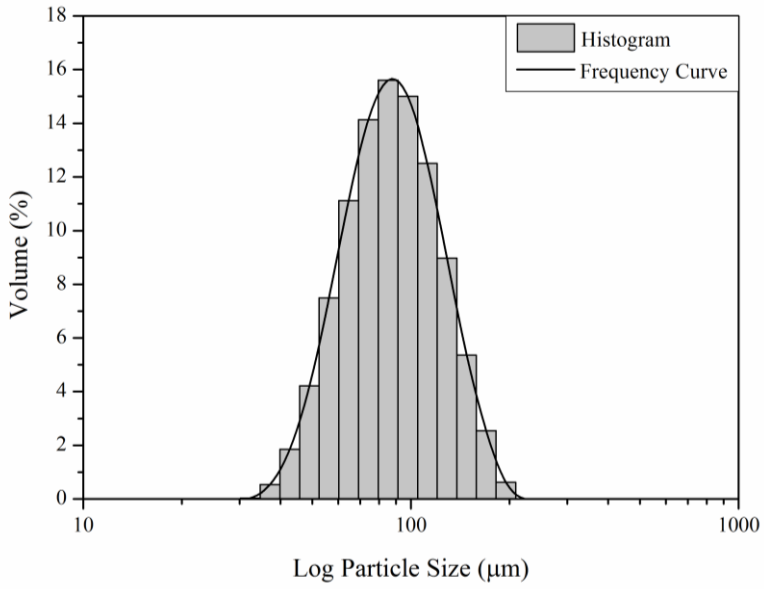

Figure 15: The size distribution histogram and frequency curve according to volume percentage for glass composition 0 Mol % strontium.

The 10 results recorded for each sample were then averaged and compared, figure 16. The particle size distribution ranges from the 26.30-30.20μm to the 208.9296-239.88μm size bands. No particles were detected outside of this range. The particle size is the diameter of a spherical particle that would produce laser scattering equivalent to the analysed particle. The peak particle size for all compositions lay within the 79.43-91.20 μm band. The 3.25 Mol % strontium composition had a flatter distribution producing a lower peak volume percentage. For the 6.24 Mol % Sr composition a volume percentage of 0.0288 % was detected in the 208.93-239.88μm range.

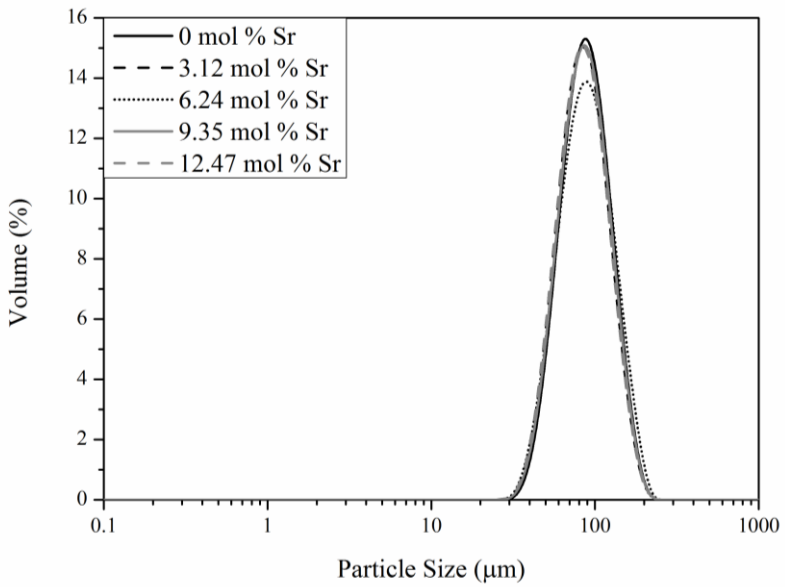

Figure 16: The average particle size distribution of the 45-90μm fraction glass powders.

The Mastersizer 2000 outputs all data as a volume percentage but this can be converted to a number percentage using equation 16[119], where i=1,2, ····· n, z_i is the particle diameter, V_i the volume percentage and N_i the number volume.

$$P_i = \frac{V_i}{(z_i)^3}$$

$$s = \sum_{i=1}^{n} P_i$$

$$N_i = \frac{P_i}{s} \times 100$$

Equation 16

The particle size range, peak particle size, the mean particle size according to particle number and the mean particle size according to the particle volume percentage for the glass compositions tested are summarised in table 8.

Table 8: Summary of the laser diffraction results for the 45-90µm size fraction of the different glass compositions.

Strontium Content (Mol %)	Minimum Particle Size Band (µm)	Maximum Particle Size Band (µm)	Peak Particle Size Band (µm)	Mean Particle Size (µm)	
				Number Weighted	Volume Weighted
0.00	30.20-34.67	181.97-208.93	79.43-91.20	66.70	91.94
3.12	26.30-30.20	181.97-208.93	79.43-91.20	64.09	89.08
6.24	26.30-30.20	208.93-239.88	79.43-91.20	63.68	93.32
9.35	30.20-34.67	181.97-208.93	79.43-91.20	65.04	90.62
12.47	26.30-30.20	181.97-208.93	79.43-91.20	63.46	88.50

The mean particle size weighted to volume sits within the range of 91 ± 2.5 µm for all compositions while the particle size weighted to particle number was lower at 65 ± 1.75 µm. The 6.24 Mol % Sr composition produced the highest volume weighted mean of 93.32 µm though had a relatively low number weighted mean of 63.68 µm. This is highlighted in figure 17 where composition 6.24 Mol % strontium is shown to have a higher volume of large particles and also higher number of small particles compared to composition containing 0 Mol % Sr, which is a good representation of the remaining compositions.

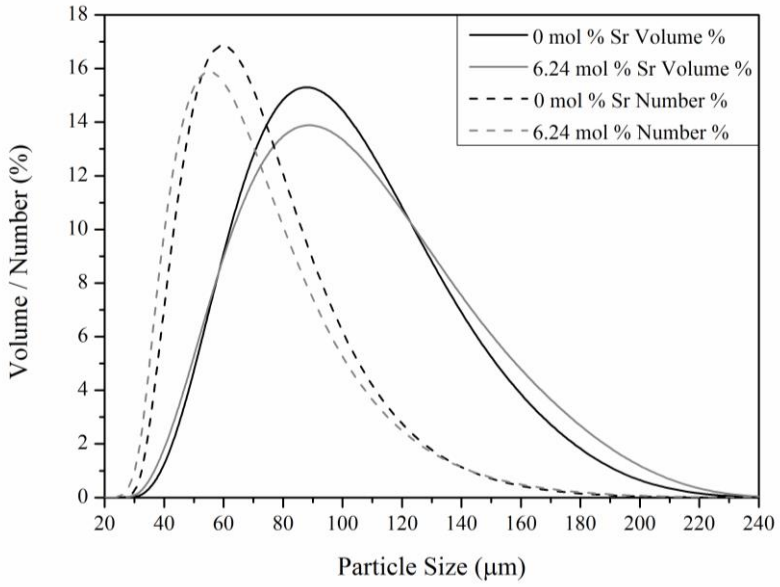

Figure 17: The particle size distribution for the 45-90µm fraction according to particle number and volume percentage for compositions 0 Mol % strontium and 6.24 Mol % strontium.

It can be seen in figure 17 that the distribution is not normally distributed about a linear axis and is instead skewed towards lower particle sizes. The distribution

according to volume is skewed less to lower sizes than that according to number due to volume being weighted towards larger particles.

2.3.2 Scanning Electron Microscope Results

From figure 18 it can be seen that the all compositions produced irregularly shaped, sharp edged, shards that are typical of a brittle glass or ceramic.

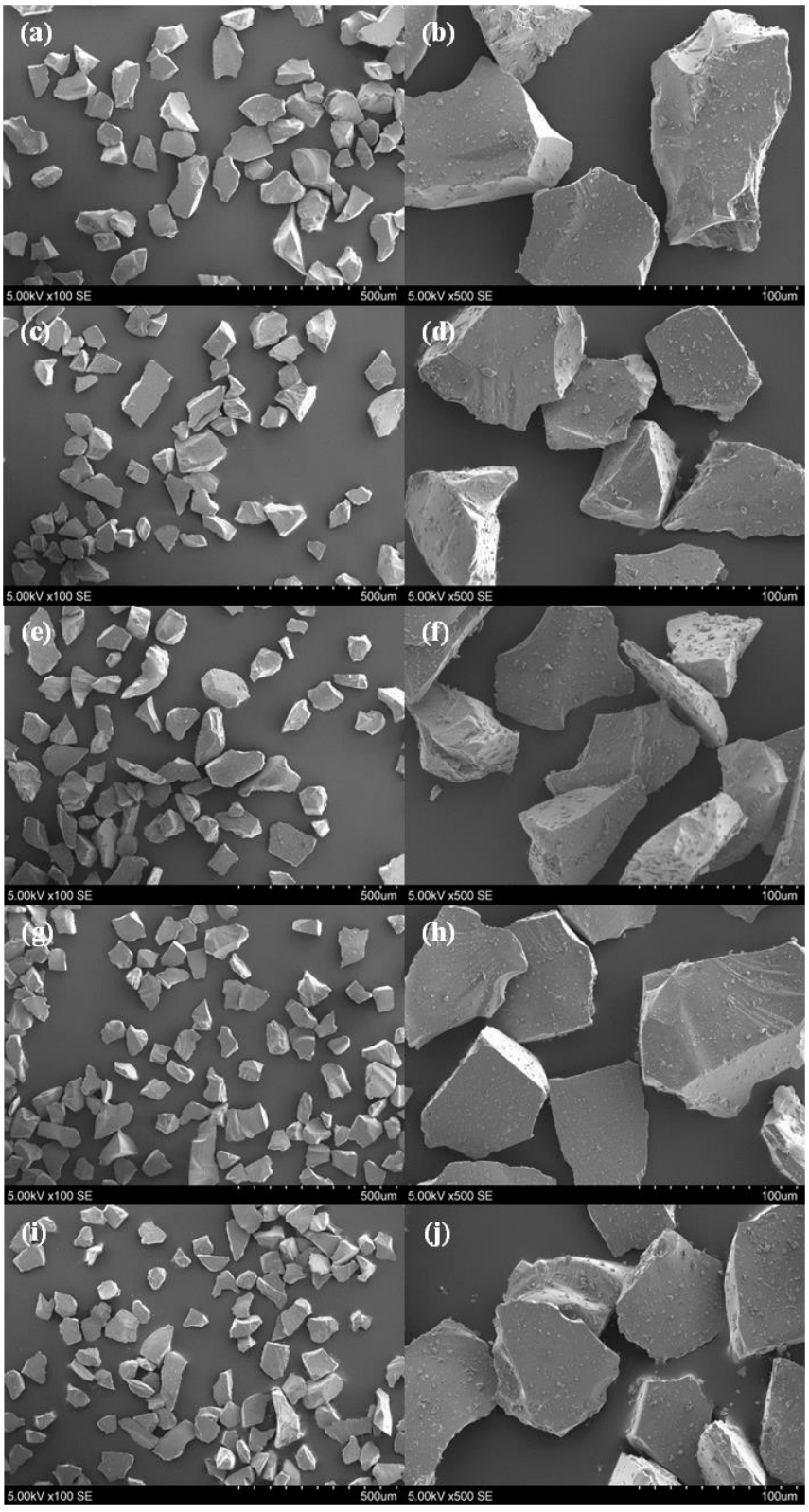

Figure 18: SEM secondary electron images taken at 100x and 500x magnification of 45-90 µm particle fraction for compositions (a-b) 0 Mol % Sr (c-d) 3.12 Mol % Sr (e-f) 6.24 Mol % Sr (g-h) 9.35 Mol % Sr and (i-j) 12.47 Mol % Sr. Submicron particles can be seen on the larger shards.

Although irregular in shape, the size of the particles in figure 18 are consistent. Though some particles exceed 90µm in one dimension, their other visible dimension is below it. An attempt was made to characterise the dimensions of the particles using image analysis software but this was not possible due to the image being two-dimensional and particle surfaces lying outside of the plane of the image. Submicron particles can be seen on the surface of the larger glass shards. This is consistent throughout all the glass compositions.

2.3.3 EDX Results of the Glass Particles

Tables 9 to 13 show the experimental and theoretical elemental compositions of the glass powders as recorded via EDX. The values given are an average of sampling points from three different particles per sample. Low levels (<1%) of aluminium were detected in all of the glasses, though they were small enough not to skew the percentage contents of the remaining elements.

Table 9: Experimental (EXP) and theoretical (THEO) EDX results for composition 0 Mol % strontium of the 45-90µm fraction glass powder, the standard deviations are shown (±).

0 Mol % Sr	Atomic Composition (Mol %)											
	Ca			Sr			Mg			Si		
EXP	22.01	±	0.93	0.00	±	0.00	2.70	±	0.10	11.12	±	0.70
THEO	25.08	±	0.00	0.00	±	0.00	3.57	±	0.00	11.81	±	0.00
	O			F			P			Al		
EXP	60.03	±	1.44	0.72	±	0.08	3.20	±	0.09	0.22	±	0.08
THEO	57.23	±	0.00	0.27	±	0.00	2.04	±	0.00	0.00	±	0.00

Table 10: Experimental (EXP) and theoretical (THEO) EDX results for composition 3.12 Mol % strontium of the 45-90µm fraction glass powder, the standard deviations are shown (±).

3.12 Mol % Sr	Atomic Composition (Mol %)											
	Ca			Sr			Mg			Si		
EXP	19.07	±	1.37	2.91	±	0.31	2.69	±	0.22	10.45	±	1.08
THEO	21.96	±	0.00	3.12	±	0.00	3.57	±	0.00	11.81	±	0.00
	O			F			P			Al		
EXP	60.04	±	3.08	0.78	±	0.06	3.23	±	0.41	0.84	±	0.35
THEO	57.23	±	0.00	0.27	±	0.00	2.04	±	0.00	0.00	±	0.00

Table 11: Experimental (EXP) and theoretical (THEO) EDX results for composition 6.24 Mol % strontium of the 45-90µm fraction glass powder, the standard deviations are shown (±).

6.24 Mol % Sr	Atomic Composition (Mol %)											
	Ca			Sr			Mg			Si		
EXP	17.03	±	1.38	6.39	±	0.61	2.56	±	0.31	11.12	±	0.77
THEO	18.84	±	0.00	6.24	±	0.00	3.57	±	0.00	11.81	±	0.00
	O			F			P			Al		
EXP	58.59	±	1.47	0.79	±	0.13	3.08	±	0.43	0.44	±	0.37
THEO	57.23	±	0.00	0.27	±	0.00	2.04	±	0.00	0.00	±	0.00

Table 12: Experimental (EXP) and theoretical (THEO) EDX results for composition 9.35 Mol % strontium of the 45-90µm fraction glass powder, the standard deviations are shown (±).

9.35 Mol % Sr	Atomic Composition (Mol %)											
	Ca			Sr			Mg			Si		
EXP	13.65	±	0.90	8.40	±	0.49	2.92	±	0.43	10.37	±	1.28
THEO	15.72	±	0.00	9.35	±	0.00	3.57	±	0.00	11.81	±	0.00
	O			F			P			Al		
EXP	60.32	±	2.27	0.37	±	0.26	3.27	±	0.23	0.71	±	0.34
THEO	57.23	±	0.00	0.27	±	0.00	2.04	±	0.00	0.00	±	0.00

Table 13: Experimental (EXP) and theoretical (THEO) EDX results for composition 12.47 Mol % strontium of the 45-90µm fraction glass powder, the standard deviations are shown (±).

12.47 Mol % Sr	Atomic Composition (Mol %)											
	Ca			Sr			Mg			Si		
EXP	11.57	±	0.97	12.65	±	0.85	2.78	±	0.22	10.63	±	1.14
THEO	12.61	±	0.00	12.47	±	0.00	3.57	±	0.00	11.81	±	0.00
	O			F			P			Al		
EXP	58.11	±	3.51	0.69	±	0.05	3.28	±	0.22	0.29	±	0.09
THEO	57.23	±	0.00	0.27	±	0.00	2.04	±	0.00	0.00	±	0.00

From tables 9 to 13 it can be seen that the experimental results are a close match to the theoretical values. The experimental values for Mg and F are consistently below that which would be expected while P is higher. Though Mg, F and P are within 1% of the predicted values, their overall contributions are low and thus represents a

large percentage error. This trend is repeated for all elements in the different compositions.

Standard samples of $CaSiO_3$, $CaMg(CO_3)_2$ and CaPO were quantified using EDX configured with the same settings used for the glass powders, table 14. The trend seen in the glass compositions was repeated in the standards with Mg under reading and P over reading.

Table 14: Experimental and theoretical EDX values for $CaSiO_3$, $CaMg(CO_3)_2$ and CaPO standards including standard deviations (±).

	Atomic Content (Mol %)			
	Ca	P	Mg	Si
$CaSiO_3$				
THEO	19.31 ± 0.50	- ± -	- ± -	19.75 ± 0.81
EXP	19.97 ± 0.00	- ± -	- ± -	19.77 ± 0.00
$CaMg(CO_3)_2$				
THEO	10.61 ± 0.21	- ± -	8.04 ± 0.25	- ± -
EXP	10.40 ± 0.00	- ± -	8.81 ± 0.00	- ± -
CaPO				
THEO	21.07 ± 0.80	16.98 ± 0.73	- ± -	- ± -
EXP	23.32 ± 0.00	15.15 ± 0.00	- ± -	- ± -

The experimental and theoretical calcium to strontium ratios for the different compositions are shown in table 15. The experimental Ca/Sr ratios are a close match to the theoretical values in all the novel strontium containing compositions.

Table 15: Calcium to strontium ratios for the experimental and theoretical glass compositions. Standard deviations (±) are shown.

Composition	Ca/Sr Mol % Ratio	
	Experimental	Theoretical
0 Mol % Sr	N/A	N/A
3.12 Mol % Sr	6.55 ± 0.85	7.04
6.24 Mol % Sr	2.66 ± 0.33	3.02
9.35 Mol % Sr	1.63 ± 0.14	1.68
12.47 Mol % Sr	0.91 ± 0.10	1.01

2.3.4 X-Ray Diffraction Results

The x-ray diffraction (XRD) traces for the glass powders are shown in figure 19. All samples display a broad peak centred around 30°2θ. This peak is often referred to as the amorphous hump or amorphous halo and indicates that the material sampled is x-ray amorphous. There are no sharp peaks present in any of the glasses that would indicate the presence of crystalline phases.

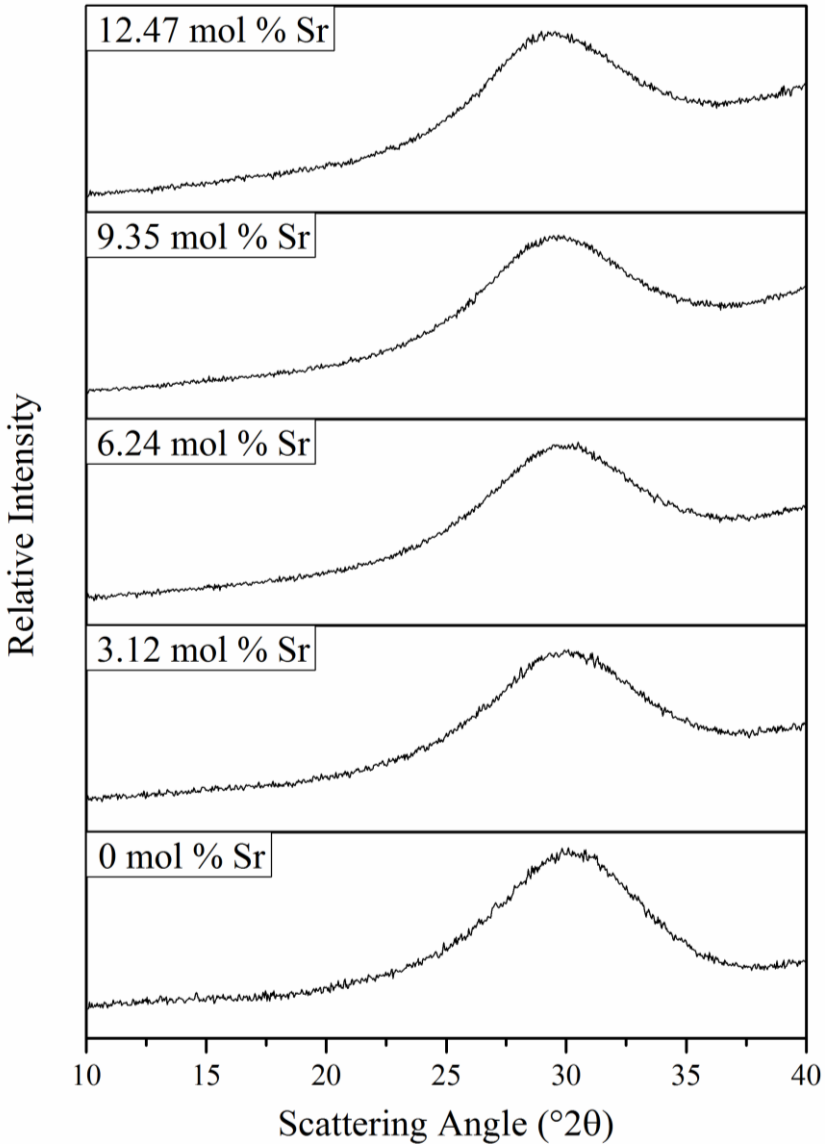

Figure 19: The x-ray diffraction traces for the glass compositions tested.

The XRD traces were converted from °2θ to d-spacing (nm) utilising the wavelength of the x-ray source, λ (1.5418nm for Cu K α), and equation 17, taken from Bragg's Law. An asymmetric double sigmoid peak was fitted to each of the XRD amorphous humps using Origin graphing software and the peak position calculated,

table 16. The quality of the fit was reported using the adjusted R^2 output and the accuracy of the peak value represented by the standard error of the parameter.

$$d = \frac{\lambda}{2\,sin\left(\frac{2\theta}{2}\right)}$$

Equation 17

Table 16: The output of the asymmetric double sigmoid peak fitting to the glass powder XRD traces.

Strontium Content (Mol %)	d-spacing (nm)	Standard Error	Adj. R^2
0	0.2944	$1.57x10^{-04}$	0.989
3.12	0.2982	$2.82x10^{-04}$	0.993
6.24	0.2992	$9.00x10^{-05}$	0.994
9.35	0.3012	$9.20x10^{-05}$	0.993
12.47	0.3025	$1.23x10^{-04}$	0.993

A good fit was achieved for all the glass powders showing that they could be well represented using the asymmetric double sigmoid function. The low standard errors represent a parameter with which a small variation in would result in a curve that fits the data much worse. The low standard error and good fit allow for accurate calculation of the peak position. The peak shifts to a higher d-spacing with increasing levels of strontium substitution, this is highlighted in figure 20. The average increase in d-spacing was 0.0020nm per 3.12 Mol % strontium substitution.

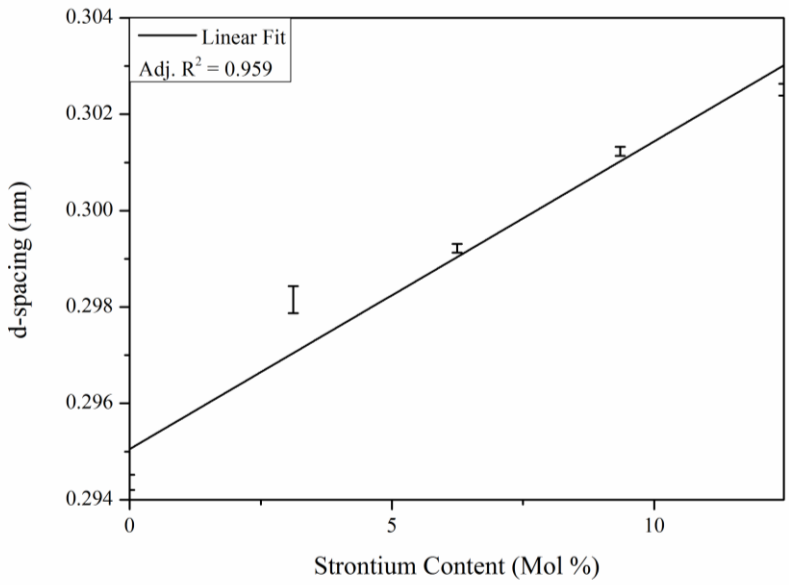

Figure 20: The effect of increasing strontium substitution on the d-spacing of the amorphous peak.

2.3.5 Density Results

The densities of the glass powders are shown in table 17. The density of the sample increased with increasing strontium substitution. The average increase in density was 0.1029 $g.cm^{-2}$ per 3.12 Mol % substitution of strontium. The increase was shown to be linear, with a fit producing an adjusted R^2 value of 0.996, see figure 21.

Table 17: The effect of strontium substitution on the density of the glass powders.

Strontium Content (Mol %)	Density ($g.cm^{-2}$)	Standard Deviation ($g.cm^{-2}$)
0	2.9325	0.0075
3.12	3.0447	0.0199
6.24	3.1322	0.0123
9.35	3.2536	0.039
12.47	3.3442	0.0044

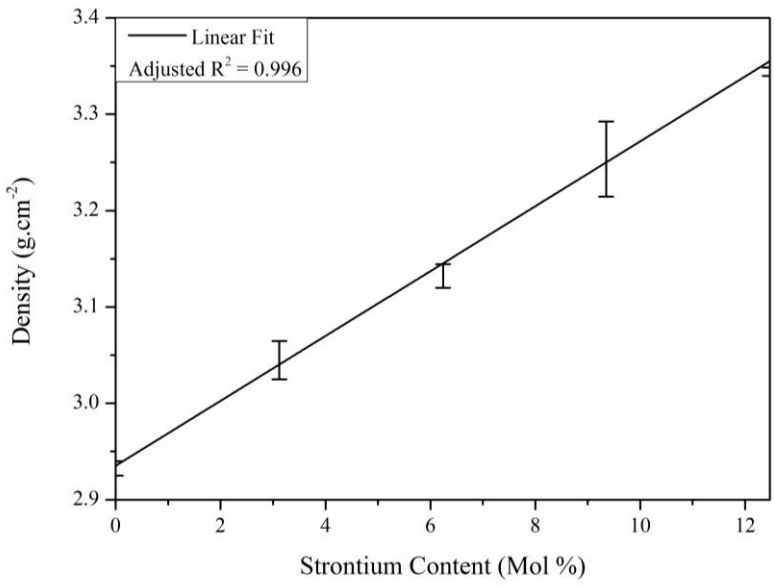

Figure 21: The effect of strontium substitution on the density of glass particles.

2.3.6 Casting Glass Rods

Initially glass rods were cast using a mould of 20mm diameter and a melt temperature of 1450°C but this failed to produce visibly crystal free rods. The mould diameter was subsequently reduced to 15mm and the temperature of the furnace increased to 1500°C for the last 30 minutes of melting. This allowed for the casting of glass rods that contained no visible crystals and a minimal amount of bubbles, see figure 22. While bubbles were present in the glass they had not nucleated crystals and formed mainly in the centre of the rods providing bubble free regions for subsequent x-ray attenuation readings.

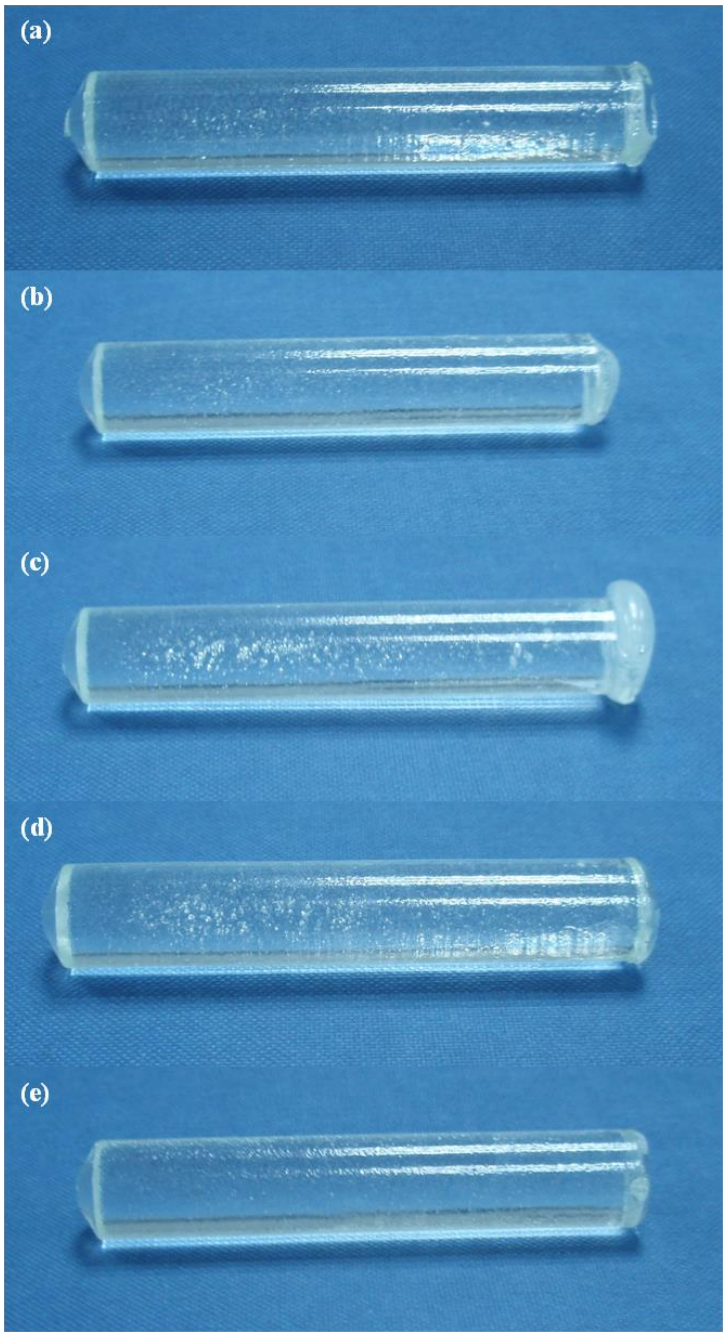

Figure 22: Glass rods cast from glasses with strontium substitutions of (a) 0 Mol % Sr (b) 3.12 Mol % Sr (c) 6.24 Mol % Sr (d) 9.35 Mol % Sr and (e) 12.47 Mol % Sr. Small bubbles can be seen in the centre of the rods but no crystals are visible.

2.3.7 X-Ray Attenuation

Figure 23 shows the initial radiograph of the glass discs alongside the inverted image and the sites from which pixel intensity readings were taken. Visually it is clear that there was a discernible difference between the brightness of the samples with increasing strontium substitutions. Darkening of the initial radiograph represents exposure of the film to x-rays. Therefore the darker the film, the greater

the number of x-rays that have passed through the material. As each x-ray that reaches the film will cause an increase in the darkening of the film at that point, the overall darkening can be used as a measure of the intensity of the x-ray beam that has passed through the sample. In the inverted image the opposite is true, the more white the image, the greater the number of x-rays that have passed through the sample to the film and thus the greater the intensity of the x-ray beam. Bubbles are visible in the centre of 6.24 Mol % sample.

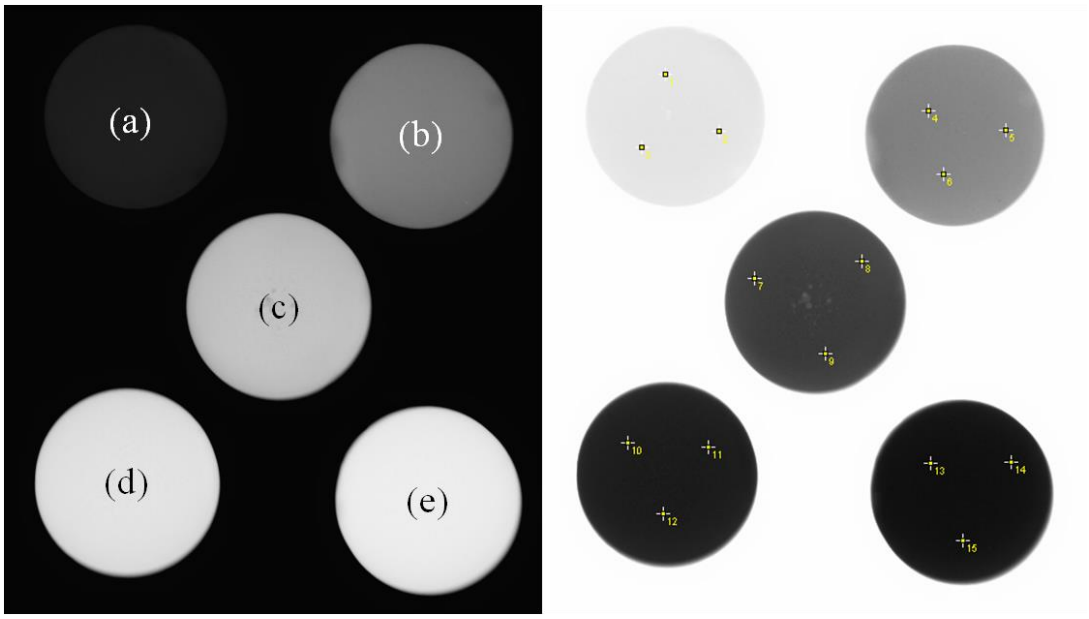

Figure 23: The initial radiographic (left) and inverted radiographic (right) images of the glass discs. The discs are positioned the same on each image with (a) 0 Mol % Sr (b) 3.12 Mol % Sr (c) 6.24 Mol % Sr (d) 9.35 Mol % Sr and (e) 12.47 Mol % Sr. The points from which pixel intensities were taken are shown on the inverted image.

The pixel intensity is a measure of how white (on a 32-bit gray scale) a point on the image is with whitest being 255 and the least white 0. An area with high pixel intensity represents a high x-ray beam intensity.

The average pixel intensities taken from figure 23, the average disc thickness and the calculated linear attenuation increases are shown in table 18. The pixel intensity decreases with increasing strontium substitutions indicating an increase in attenuation.

Table 18: The parameters involved in the calculation of the increase in linear attenuation. Standard deviations (±) are shown.

Sr Content (Mol %)	Average Pixel Intensity	Average Thickness (cm)	Linear Attenuation Increase (cm^{-1})
0	228.0 ± 1.7	$0.3656 \pm 1.8*10^{-6}$	0.000 ± 0.0000
3.12	131.0 ± 2.0	$0.3621 \pm 3.2*10^{-5}$	1.531 ± 0.0087
6.24	62.7 ± 3.51	$0.3622 \pm 1.5*10^{-5}$	3.565 ± 0.0162
9.35	27.3 ± 2.52	$0.3610 \pm 4.7*10^{-5}$	5.877 ± 0.0468
12.47	15.7 ± 0.577	$0.3617 \pm 4.9*10^{-6}$	7.403 ± 0.0168

The effect of strontium substitution on the transmitted intensity (I/I_0) relative to the 0 Mol % strontium composition (I_0) is shown in figure 24. The relative intensity decreases at a non-linear rate and is best modelled with a 2nd order polynomial fit.

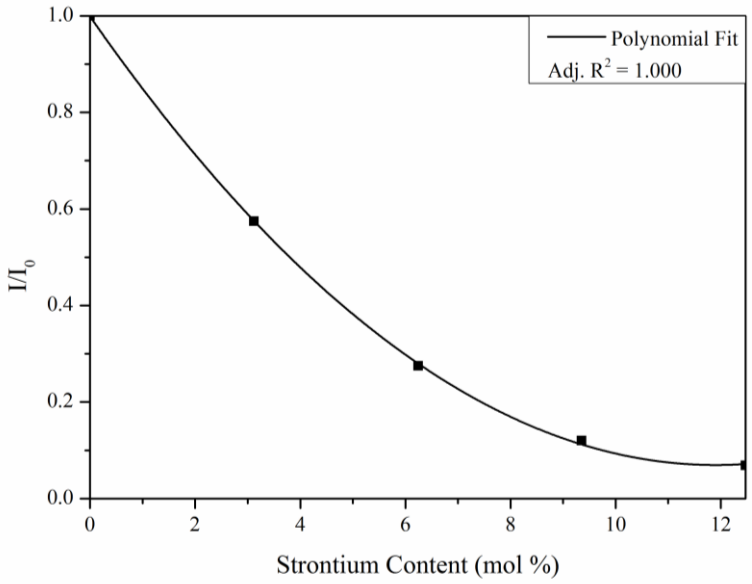

Figure 24: The effect of strontium substitution on the transmitted x-ray intensity relative to the 0 Mol % strontium glass.

The linear attenuation was calculated from the transmitted intensity and the sample thickness using the Beer-Lambert law, equation 11. It can be seen that the linear attenuation increases linearly with increasing strontium substitutions, figure 25.

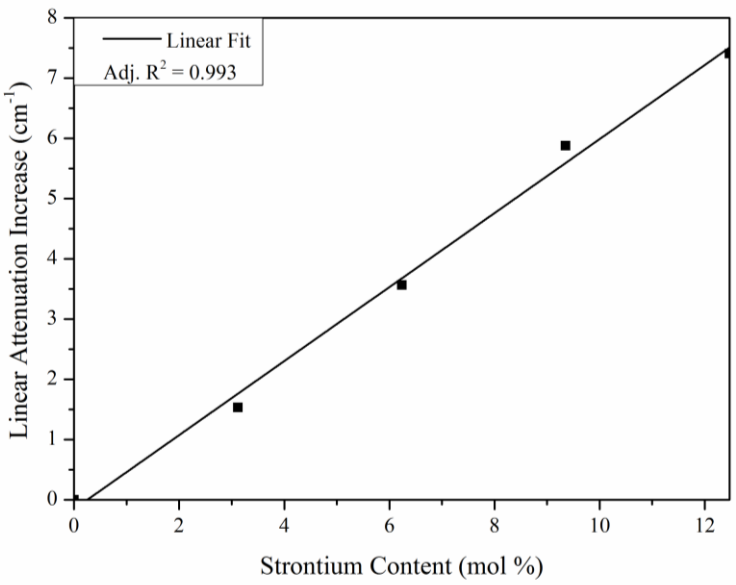

Figure 25: The linear attenuation increase with increasing strontium substitutions.

The theoretical mass attenuations of the novel strontium compositions were calculated from elemental mass attenuation coefficients on the NIST website [120] for excitation voltages of 60, 50 and 40 keV. Bulk material mass attenuations were calculated using equation 18 where w is the weight percentage and μ the mass attenuation coefficient for element i. A 2nd order polynomial was fit to the theoretical data, with each producing an adjusted R^2 of 1, figure 26. The gradient of the fitted curve increased as the excitation energy decreased. The experimental mass attenuation coefficient increases were calculated by dividing the linear increases by the experimentally determined densities in table 17. The calculated values are shown in table 19. A second order polynomial fit of the data produced an adjusted R^2 of 0.990. The experimental data lay within the theoretical values for 50 and 40 keV, figure 26. The experimental linear attenuation increase, densities and mass attenuation coefficients are summarised in table 20.

$$\mu = \sum_i w_i . \mu_i$$

Equation 18

Table 19: Theoretical mass attenuations at different excitation voltages.

Strontium Content (Mol %)	Mass Attenuation at Different Excitation Energies ($cm^2.g^{-1}$)		
	40 keV	50 keV	60 keV
0	0.9984	0.5922	0.4102
3.12	1.9006	1.0752	0.6978
6.24	2.7038	1.5053	0.9539
9.35	3.4236	1.8907	1.1834
12.47	4.0722	2.2380	1.3902

Table 20: The effect of strontium on the linear attenuation, density and mass attenuation of the glass compositions. Standard deviations (±) are shown.

Sr Content (Mol %)	Increase in Linear Attenuation (cm^{-1})	Denisty ($g.cm^{-2}$)	Increase in Mass Attenuation ($cm^2.g^{-1}$)
0	0.000 ± 0.0000	2.9325 ± 0.0075	0.000 ± 0.0000
3.12	1.531 ± 0.0087	3.0447 ± 0.0199	0.503 ± 0.0044
6.24	3.565 ± 0.0162	3.1322 ± 0.0123	1.138 ± 0.0068
9.35	5.877 ± 0.0468	3.2536 ± 0.0390	1.806 ± 0.0260
12.47	7.403 ± 0.0168	3.3442 ± 0.0044	2.214 ± 0.0058

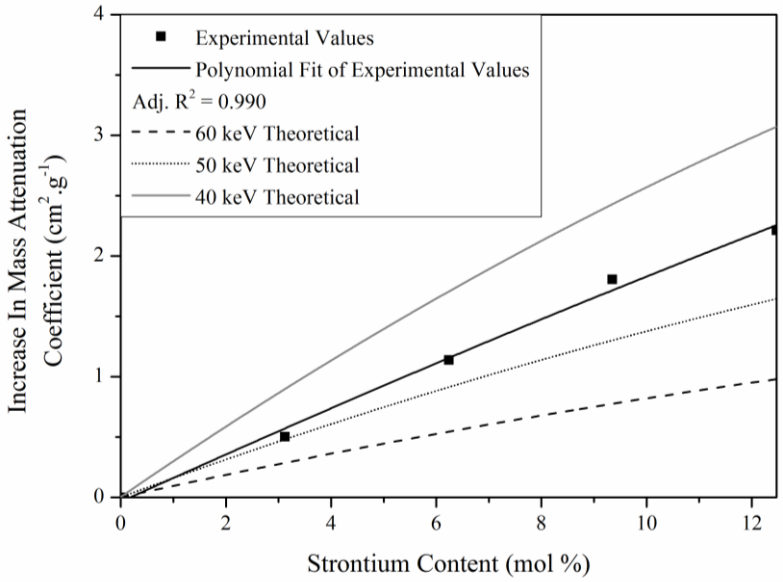

Figure 26: The increase in the experimental mass attenuation coefficient with subsequent substitutions of strontium. Polynomial fits of the theoretical mass attenuations for 60, 50 and 40 keV are also shown.

2.4 Discussion

The aim of this first section of work was to determine if a strontium containing glass could be formed and to confirm that the processing route used produced powders with consistent size distributions and geometries. Subsequent work looking at crystallisation, sintering and mechanical testing relies on a consistent particle size. Crystallisation of wollastonite from the apatite-wollastonite parent glass is a surface nucleation process [60] and as such is affected by the surface area to volume ratio of the powder. The results from the Mastersizer 2000 show excellent repeatability for individual powders. A comparable distribution was achieved for the all the glass powders tested. Though the 6.24 Mol % strontium powder had a slightly flatter distribution, it was skewed by very few larger volume particles. Its peak size band and mean according to number all lay within the range of the other powders.

The maximum particle size of all the distributions is greater than the 90µm diameter that would be expected from a 90µm sieve. This is because the particle sizes given by the Mastersizer are the diameters of an equivalent sphere that would have the same volume as the particle tested. From the SEM images it can be seen that the analysed particles are not spheres. The simplest representation of the particles would be as cuboids. The peak particle size band according to volume was 79.43-91.20µm, the geometric mid-point of this range is 85.11µm, a sphere of this diameter would have the same volume as a cube of 68.60µm. Thus the peak particle size is within the limits expected of the 45µm and 90µm sieves used.

A sphere of diameter 111.66µm would produce a cube of 90µm edge length, the largest cube that would fit through the 90µm sieve. An average of 29 % of the volume and 6 % of the number of particles fell into a size band larger than this. Very few particles exceeded this size though the volume of particles exceeding it is much larger, due to the volume ratio being skewed towards larger particle sizes. Sieves sort particles according to the second largest dimension, as such a rectangular cubic particle could have two dimensions of 90µm and one much larger and still pass through the sieve. This is visible in the SEM images, where a single dimension of the larger particles is seen to exceed 90µm. The maximum size band for the 6.24 Mol % strontium composition was 208.93-239.88µm with a mid-point of 223.87µm and 181.97-208.93µm with a midpoint of 194.98µm, larger than the theoretical maximum particle size. If we assume that the maximum value for the

two smallest dimensions is 90µm, then the largest dimension recorded must be 725.27µm in order to produce a cuboid with the equivalent volume. There was no evidence of particles this size in any of the SEM images taken. The inconsistency between the Mastersizer and SEM results could be down to errors in the assumptions made. Firstly, an assumed refractive index was assigned to the particles (1.520, that as for glass beads), however, a weighted residual of below 1% was achieved for all samples, suggesting this was a good representation of the data [121]. The Mastersizer assumes that the particles would scatter the laser light in the same manner as the equivalent sphere. This would not be the case for the irregular particles analysed and scattering would be enhanced for the wide angle (larger particle size) detectors [122]. The Mastersizer takes measurement of a particle cross-section and assumes the volume from it. This requires the particles to be randomly oriented to ensure all dimensions of a sample are measured. Particles with a high aspect ratio, as is the case with the larger particles, may align with the flow, causing the longer dimension to dominate and the particle size being given relative to the cross-section of the largest face [122].

The midpoint of the minimum size band (26.30-30.20µm) is 28.81µm, a plate like particle of this volume could have two dimensions of 45µm (too large to pass through a 45µm sieve) and a smaller dimension of 6.19µm. The submicron particles seen on the SEM images are not present in the Mastersizer data. Some of the particles are below the size range of the Mastersizer (0.5µm) but others are at least 1µm in diameter. A dispersant was not used and so the particles may have remained attached to the larger particles. Also, the output of the Mastersizer is in volume %, these particles would have produced such a small volume that they may not have been recorded and as such would not have been visible even after conversion to a distribution according to number.

It has been shown that the Mastersizer data does not indicate the true size of the glass powders. It does however show that the processing method used produced glass powders with the same particle size distributions, crucial for comparison in later experiments, such as differential scanning calorimetry. This is also emphasised by the SEM images of the glass powders.

The EDX results of the glass particles show a strong agreement between the experimental and theoretical results, suggesting that the substitution of calcium with

strontium had been successful. A good match for the calcium to strontium ratio was achieved for all the compositions tested. The mismatch for the values of Mg, F and P are each out by less than 1%, this is well within the error range to be expected of a semi-quantitative EDX setup. The standards analysed also produced Mg and P values that were below and over (respectively) their predicted values. The difference was much less than that recorded on the glass particles but this is what would be expected for the highly polished and precisely prepared standard materials. The calcium in the experimental standard was not always under the predicted value, as in the glass compositions, the variations observed are due to different matrix effects in the materials and the inability of the peak-to-background ZAF algorithm to fully model them.

The EDX analysis was performed on particles and so is prone to effects not seen when analysing a flat polished surface. The angle with which the particle is scanned can strongly affect the ratios of an element due to the particle absorption effect. This is most pronounced in elements with emissions under 4 keV [123]. This could explain why oxygen is over read in all the samples. Oxygen is not always measured directly from an EDX spectra and is sometimes calculated from the ratio of oxides, though in this instance a close match was achieved using the spectra only. The experimentally recorded value for F has a large experimental error. This is due to it being present in very small amounts. Also, fluorine has a very low photon energy and is thus difficult to quantify. The small levels of aluminium detected are likely to be from the alumina crucibles used for the glass melting. The quantities are very small and will not have an influence on the properties of the glass.

X-ray diffraction analysis revealed the broad peaks or humps centred around 30 °2θ that are indicative of an x-ray amorphous glass. The hump appears due to the glass network having a short range order [94] with bonds that vary around the peak d-spacing. All the samples tested were seen to be x-ray amorphous, and thus a glass had been formed in all cases. Goel has previously synthesised glasses in the same system, though with a higher molecular content of MgO and lower total molecular percentage of CaO and SrO. The amorphous halo was visible in the their results, with a peak centred around 30 °2θ [86]. The peak shift to a smaller °2θ/larger d-spacing is a result of the larger ionic radii of strontium compared to calcium, reducing the interaction between the divalent cations and the non-bridging oxygens

in the network [81, 124]. This behaviour has also been reported by Lotfibakhshaiesh [125] and Fredholm [81] in bioactive glasses substituted with strontium. Substituting strontium for calcium in phosphosilicate glasses has been shown to have no effect on the co-ordination of the silicate tetrahedra which remain predominately networked with two bridging oxygens [81, 86]. The average peak shift recorded was 0.0020 nm per 3.12 Mol % strontium substitution. Both strontium and calcium are thought to have a coordination of 6 within the glass network [126], as such would have ionic radii of 0.1nm for calcium and 0.118nm for strontium [83], thus an increase in radius of 0.018nm. Using equation 19, where r is the ionic radius and x the molar ratio, the theoretical increase in ionic radii with each 3.12 Mol % strontium substitution is 0.0022nm, an excellent match to the experimental data.

$$\Delta d = (r_{Sr} - r_{Ca}) * \left(\frac{x_{Sr}}{x_{Sr} + x_{Ca}}\right)$$

Equation 19

The mass and x-ray densities of the material were investigated to further confirm the successful substitution of strontium and to investigate the application of the material as a radiographic contrast medium. The linear increase in the density of the glasses with increasing strontium occurred as well as a recorded increase in the bond length of the glass. Strontium has a larger ionic radius than calcium but is also more dense. Strontium has a higher atomic number (Z) than calcium (30 to 20, respectively) but crucially a smaller atomic number to mass ratio (0.43369 to 0.49903), due to the inclusion of extra neutrons. This makes strontium more dense than calcium (2.540g/cm^3 to 1.550g/cm^3, respectively). Similar densities were reported by Kansal et. al. [127] and Galliano et. al. [126] for other phosphosilicate glasses with divalent cation concentrations close to those reported here.

To the writers knowledge, casting of apatite-wollastonite parent glass rods has not previously been reported [61]. Though initial attempts failed, the increase in melt temperature and reduction in rod diameter proved successful. The use of a smaller diameter mould will help reduce temperature gradients across the glass as it cools, minimising the chance of crystal nucleation. A higher temperature results in a lower viscosity melt, this helps in attaining a smooth pour which not only minimise bubble

formation but also reduces contamination of the rod with insoluble impurities that would almost certainly initiate crystallisation upon cooling.

The intensity measured from the radiographs is actually a measure of the blackening of the film, known as radio density. The exposure time used produced a good radiographic density in the samples but over exposed the bare film [128], meaning that measurements had to be made relevant to the 0 Mol % strontium glass and not the air (intensity prior to passing through any glass). A relatively long exposure time of 2 seconds was used. A 0.25 second dose would be more clinically relevant. A 100% dense material was required in order to correctly measure the linear attenuation coefficient and the thickness was limited by the ability to machine thin sections of the glass rod. As such, a long exposure was required to ensure contrast between the materials.

The linear increase that is observed is the result of a number of interactions between the x-rays and the material. Two interactions dominate at the low energies used: the photoelectric effect and the Compton effect. The photoelectric effect is a pure absorption interaction where high energy photoelectrons are emitted from a material following their interaction with and absorption of energy from an incoming X-ray photon. The Compton effect is an absorption and scattering effect as a result of inelastic scattering from a free charged particle. It results in a decrease in the energy of the x-ray photon [128]. The remaining two interactions are Rayleigh scattering and pair production, but these are insignificant at the energies examined. Thus the observed increase in the linear attenuation is a result of an increase in the interaction of the x-ray beam and the material as the average atomic number of the material increases. The number of interactions is dependent on the number of atoms per volume of a material. Normalisation of the linear attenuation to the density of the material allows for determination of the mass attenuation coefficient.

The theoretical mass attenuations increased non-linearly with strontium substitutions. This was due to the substitutions being calculated according to molar percentage and the mass attenuation from the weight percentage. While the molar ratios of everything but calcium and strontium remain constant, the weight ratio of all the elements changes with each substitution. The theoretical mass attenuation decreases with increasing x-ray energy as a result of the contribution of the photoelectric effect becoming smaller and Compton scattering increasing [118].

The head of the x-ray device has a rating of 65kVp, this means that the peak x-ray energy is 65keV but the true x-ray energy will be a range of values below this. A 1.5mm aluminium filter on the x-ray head removes some of the low energy x-rays producing the equivalent to a monoenergetic beam of a third or half of the kVp [118, 129]. The samples tested will also attenuate the low energy x-rays, a process known as beam hardening. All the experimental attenuations are calculated using the intensity of the 0 Mol % strontium glass as the initial beam intensity, this effectively adds another filter to the beam and so the average energy will be higher still. The experimental values sit between the 40 keV and 50 keV theoretical calculations, indicating both successful measurement of the attenuation increase and also the successful substitution of strontium into the material.

Cortical bone has a theoretical mass attenuation of 0.314 $cm^2.g^{-1}$ [120], much less than the theoretical value of the glasses tested. The increase in mass attenuation increases the contrast of the material on a radiographic image. This is useful for non-invasive postoperative monitoring of an implant. On a two-dimensional radiograph the interface between the implant and bone may be obscured by the x-ray dense material however the loss of definition that occurs with remodelling of the implant will be more noticeable with increasing attenuation [130]. Computed tomography (CT) can be used to better view the placement of an implant and also the interface between the body tissue and prosthesis. High attenuating devices, such as metal prosthesis, can be difficult to image on CT due to low levels of x-rays passing through the material and creating a void in a slice image. This produces a star like artefact when back projecting and forming the complete CT image [131]. Another artefact that metal implants can induce is beam hardening due to attenuation of low energy x-rays by the high attenuator, which subsequently effects the beam interaction with softer tissues [132]. This produces problems when reconstructing the slices taken at multiple angles. Titanium implants have been shown to be easier to image using CT than stainless steel and cobalt chrome implants due to their lower mass attenuations [133]. As can be seen from table 21 only the attenuation 12.47 Mol % strontium glass is equal to or exceeds that of iron and cobalt (the main constituent of common orthopaedic implants) while compositions 0 and 3.12 Mol % strontium have a lower attenuation than titanium making them more suitable implant materials for CT imaging.

Table 21: Theoretical mass attenuations for bone and orthopaedic metals [120].

Material	40 keV	50 keV	60 keV
Cortical Bone	0.6655	0.4242	0.314
Titanium (Ti)	2.214	1.213	0.766
Iron (Fe)	3.629	1.958	1.205
Cobalt (Cr)	3.981	2.144	1.314

Chapter 3: Crystallisation

3.1 Introduction

The aim of this section was to characterise devitrification of the strontium containing glasses. The glasses formed are metastable and given an adequate input of energy will first nucleate and then grow crystals. The formation of crystals within the bulk glass is crucial in determining the bulk mechanical properties, sinterability and biocompatibility of the material. The particle size and heating rate used for devitrification are known to influence the crystal phases formed in apatite-wollastonite glass ceramic and so both were investigated. The temperature to which the parent glass is heated also influences the phases that are formed, this was investigated by heating all samples to the same temperature and also by heating of individual compositions according to regimes defined by the crystallisation temperatures.

The first step in the characterisation is determining under what conditions crystals form in the material. The effect of heating on devitrification was assessed using differential scanning calorimetry (DSC). The effect on the thermodynamic events of strontium substitution into the parent glass was analysed via DSC at different heating rates and for different particle sizes. Whilst the DSC provides information on crystallisation temperatures, it does not provide any information about the phases that have formed. X-ray diffraction (XRD) and the International Centre for Diffraction Data (ICDD) database were used to identify the phases formed in the glasses following heating with quantification performed via a Rietveld refinement. Surfaces of the devitrified glass-ceramics were analysed via SEM and EDX to observe the morphology and composition of any crystals that were visible on the surface of the material.

3.2 Experimental Methodologies

3.2.1 Differential Scanning Calorimetry

All DSC experiments were performed on a Netsch DSC 404 F3 with a PC running the Proteus data collection and analysis software. The DSC was calibrated using

indium, zinc, aluminium and gold standard materials. Matched platinum-rhodium crucibles with lids were used. All DSC pans were cleaned by soaking in hydrofluoric acid for 24 hours followed by 30 minutes sonication in an ultrasonic bath and 2 hours in boiling ultrapure water before being dried thoroughly. All experiments were performed in an air atmosphere and a protective nitrogen gas flow. A mass of 20±0.2mg of sample was used each time and the differential calculated against an empty pan. All of the five compositions tested in chapter 2 were analysed. The effect of heating rate on the glass was assessed using the 45-90µm particle fraction and heating rates of 2, 5, 10 and 15 $K.min^{-1}$. The effect of particle size on devitrification of the glass was analysed by using the <45µm, 45-90µm and 1-2mm size fractions with a constant heating rate of 10 $K.min^{-1}$. The position of the glass transition temperature and exothermic peaks were measured using Proteus Analysis. The glass transition was determined using the inbuilt glass transition function and thermal event peaks and onsets were determined using the complex peak function. The activation energy for crystallisation was calculated from multiple DTA curves, performed at the different heating rates, using the Kissinger equation, equation 20 [134].

$$ln\left(\frac{\emptyset}{T_P^2}\right) = -\frac{E}{RT_P} + C$$

Equation 20

Where ø is the heating rate (K/min), R the gas constant (J/K Mol), Tp the crystallisation peak temperature (K), E the activation energy (KJ/Mol) and C a constant. The gradient of the line produced by plotting $ln(ø/T_P^2)$ versus $1000/T_p$ gives E.

3.2.2 X-Ray Diffraction (XRD)

1g of each of the 45-90µm powders were heated (in an Elite BCF 13/12-2416 furnace) to temperatures T_{O1}-15, T_{P1}+10, T_{P2}+10 and 1050°C at a constant rate of $10K.min^{-1}$ and held at that temperature for 2 hours. The powders were then ground using a (Gy-Ro Mill) for 2 seconds. 10 Wt % of calcined alumina (Fisher Scientific) was added to each sample as an internal standard and thoroughly mixed in using an agate pestle and mortar. Samples were scanned using a Philips X'Pert run at 40kV and 40mA outputs logged using the X'Pert Data Collector software. A 15x15mm

fixed incident beam mask was used. A step size of 0.0334225°, dwell of 3.18 seconds and disc rotation speed of 4 seconds were used to scan between the range of 10-70°2θ. All analysis of the XRD pattern was done using HighScore Plus software. An ultra-low background off-cut silicon sample holder was used. The diffraction peaks were then matched to powder diffraction files (PDF) contained within the ICDD database using HighScore software. A search match was run on the diffraction data using the elemental restrictions determined from previous EDX of the parent glasses. A Rietveld refinement was then run on the powders. Figure 27 shows the systematic protocol used for the refinement, the matched phases were added into the refinement and it was then applied to all samples. The most intense peaks were first matched and refined and then the residual peaks were matched and refined using the same method. Any factor that did not lead to convergence or produced impossible values (Peak Shape 1 and size broadening factor W becoming negative) were removed. A refinement producing a weighted R-profile (R_{wp}) less than 10 was taken as a good fit.

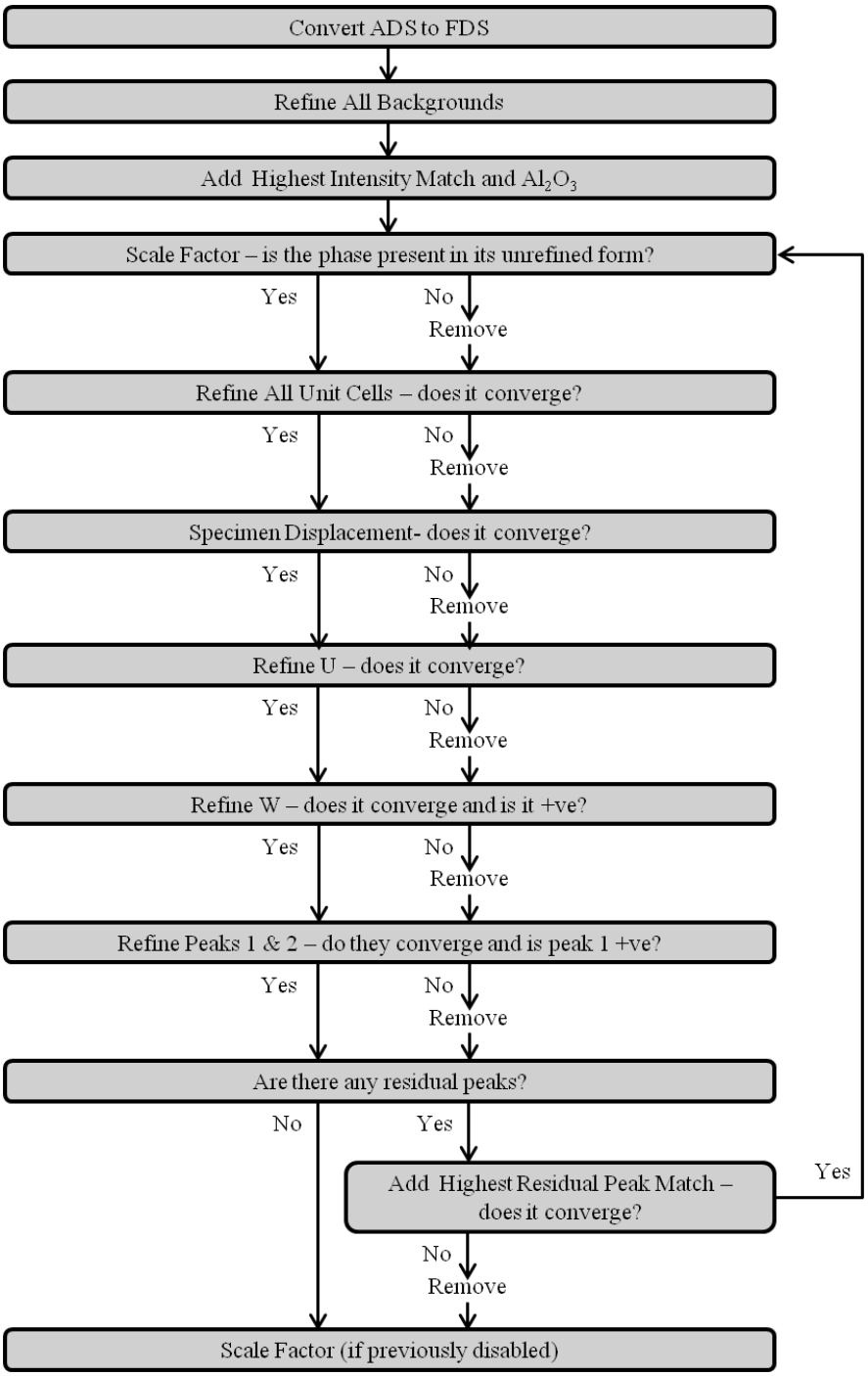

Figure 27: The initial Rietveld refinement strategy.

A silicon standard was scanned using the same equipment settings and the instrumental broadening calculated using PDF 04-016-4861. The instrumental values calculated were then used in all subsequent Rietveld refinements. For each phase the weight percentage (Wt %), unit cell dimensions, unit cell volume and size and strain broadening factors were reported along with the R-profile and weighted R-profile fits for the whole refinement. The known weight percentage of internal

standard, W_{STD}, and the experimental value, W_{EXP}, were used to calculate the weight percentage of the residual amorphous phase, W_{AMO}, equation 21.

$$W_{AMO} = \frac{1 - \left(\frac{W_{STD}}{W_{EXP}}\right)}{100 - W_{STD}}$$

Equation 21

3.2.3 Scanning Electron Microscopy (SEM)

0.25g of each of the 45-90µm glass fractions was heated in a furnace (Elite BCF 13/12-2416 furnace) to 1050°C at a constant heating rate of 10K.min^{-1} and held there for 2 hours before being cooled at the furnace rate. 1050°C was chosen as it exceeded the first exotherm for all the compositions tested while being low enough below the melting point to minimise dissolution of phases back into the melt. XRD had shown the secondary phase to form at this temperature for all compositions. Samples were then fixed to SEM aluminium stubs using carbon adhesive pads. Samples were sputtered with a 6nm gold coating. Samples were imaged using a Hitachi S3400N SEM with the native software and elemental analysis was performed using a Bruker XFlash detector and analysed with Quantax analysis software. Eneregy dispersive x-ray analysis (EDX) was performed using both a surface elemental map and point scans on specific crystal structures. Care was taken to ensure that EDX data was taken from as flat a surface as possible to ensure that the x-ray takeoff angle remained constant.

3.3 Crystallisation Results

3.3.1 DSC

The 45-90µm particle size fraction was first examined with a heating rate of 10K.min^{-1} to determine the effect of strontium substitution on the observable thermodynamic events, figure 28.

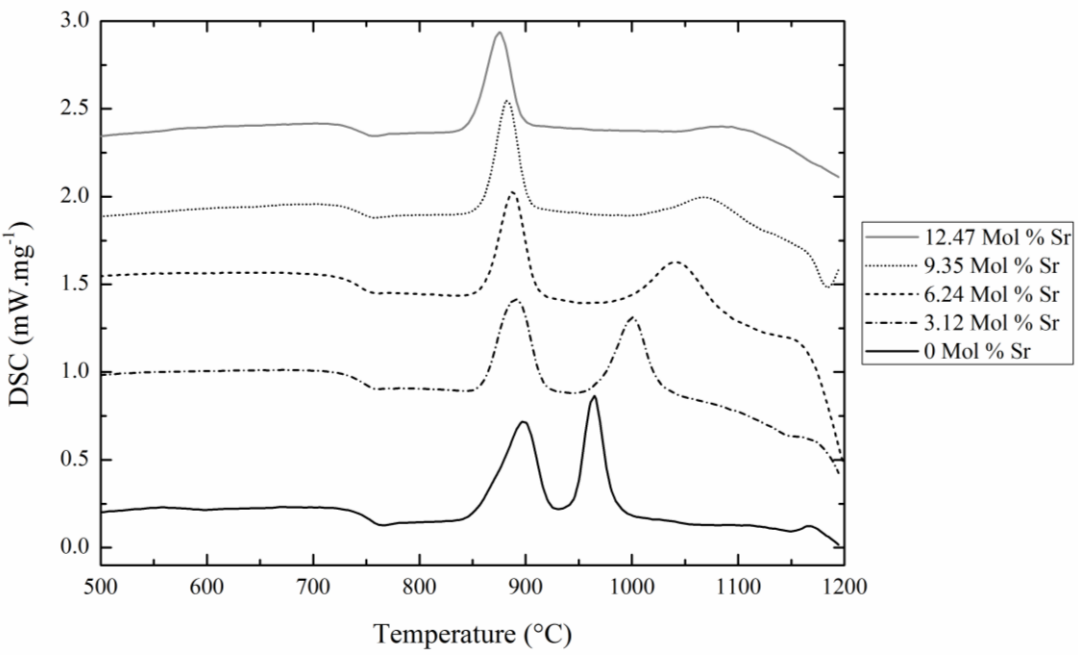

Figure 28: Offset DSC traces of the 45-90µm size fraction for glass compositions 0-12.47 Mol % strontium heated at 10K.min^{-1}.

Figure 29 highlights the main exothermic events that occurred in the samples, T_g = glass transition temperature, T_O = peak onset temperature T_P = peak temperature and T_m = melting point. The values of T_g, T_O and T_P are summarised in figure 30 and table 22 . T_m was not included as it was not possible to identify a definite point where melting had occurred in all samples.

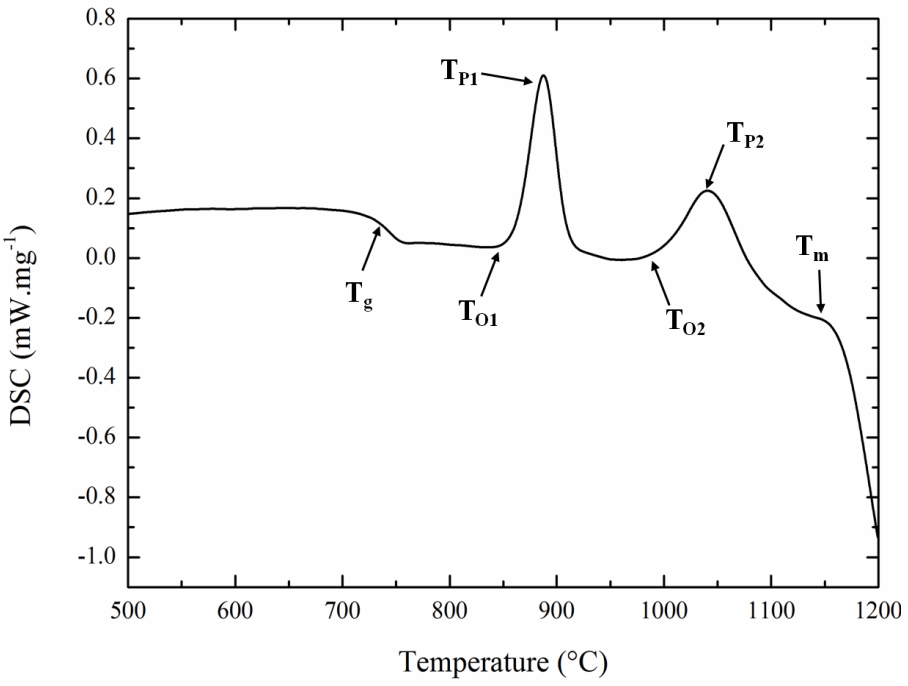

Figure 29: Examples of the thermodynamic events observed in the DSC traces.

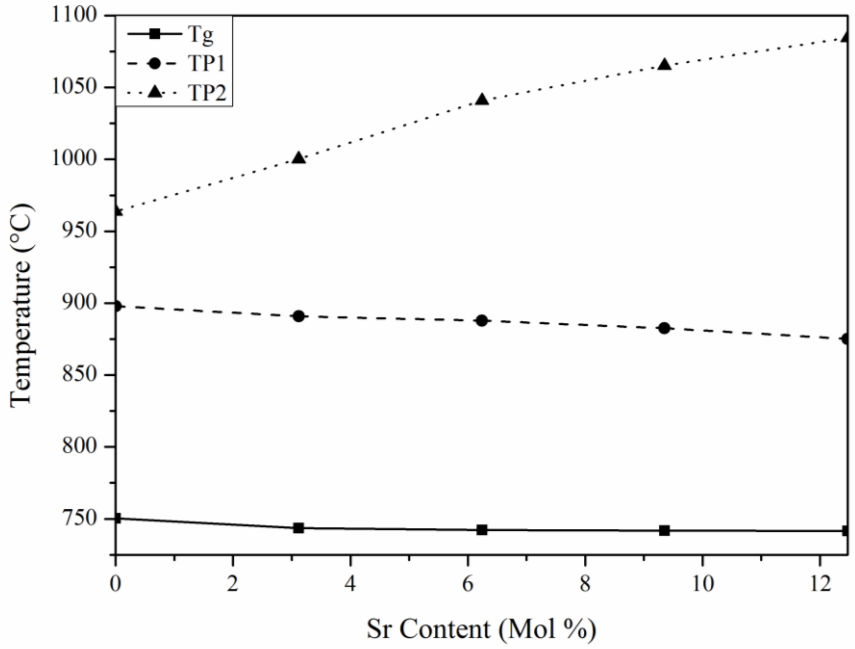

Figure 30: The major thermodynamic events observed in DSC traces of the 45-90 µm glass compositions heated at 10 $K.min^{-1}$.

Table 22: Summary of the thermodynamic events observed in DSC traces of the 45-90µm glass compositions heated at 10 $K.min^{-1}$.

Sr Content (Mol %)	T_g (°C)	T_{O1} (°C)	T_{P1} (°C)	T_{O2} (°C)	T_{P2} (°C)
0	750.4	856.7	898.0	947.9	963.8
3.12	743.6	860.7	890.9	970.9	1000.3
6.24	742.3	863.0	887.9	998.2	1040.9
9.35	741.8	861.4	882.6	1020.2	1065.2
12.47	741.5	849.4	875.1	1047.6	1084.5

Both T_g and T_{P1} occurred at lower temperatures with increasing strontium substitution into the parent glass. T_g decreased by only 9°C across the whole range of compositions tested while T_{P1} decreased by 22.9°C. An increase in T_{O1} was observed between compositions 0-6.24 Mol % strontium and then decreased for subsequent additions. An increase in both T_{O2} and T_{P2} was observed for all sequential substitutions of strontium, with T_{P2} increasing by 120.7°C for the compositional range of 0-12.47 Mol % strontium. Though a definite value could not be assigned to the melting point, the presence of the endothermic slope became more pronounced with increasing strontium substitution.

The effect of particle size on the thermodynamic events was then observed. The resulting DSC traces are shown in figure 31.

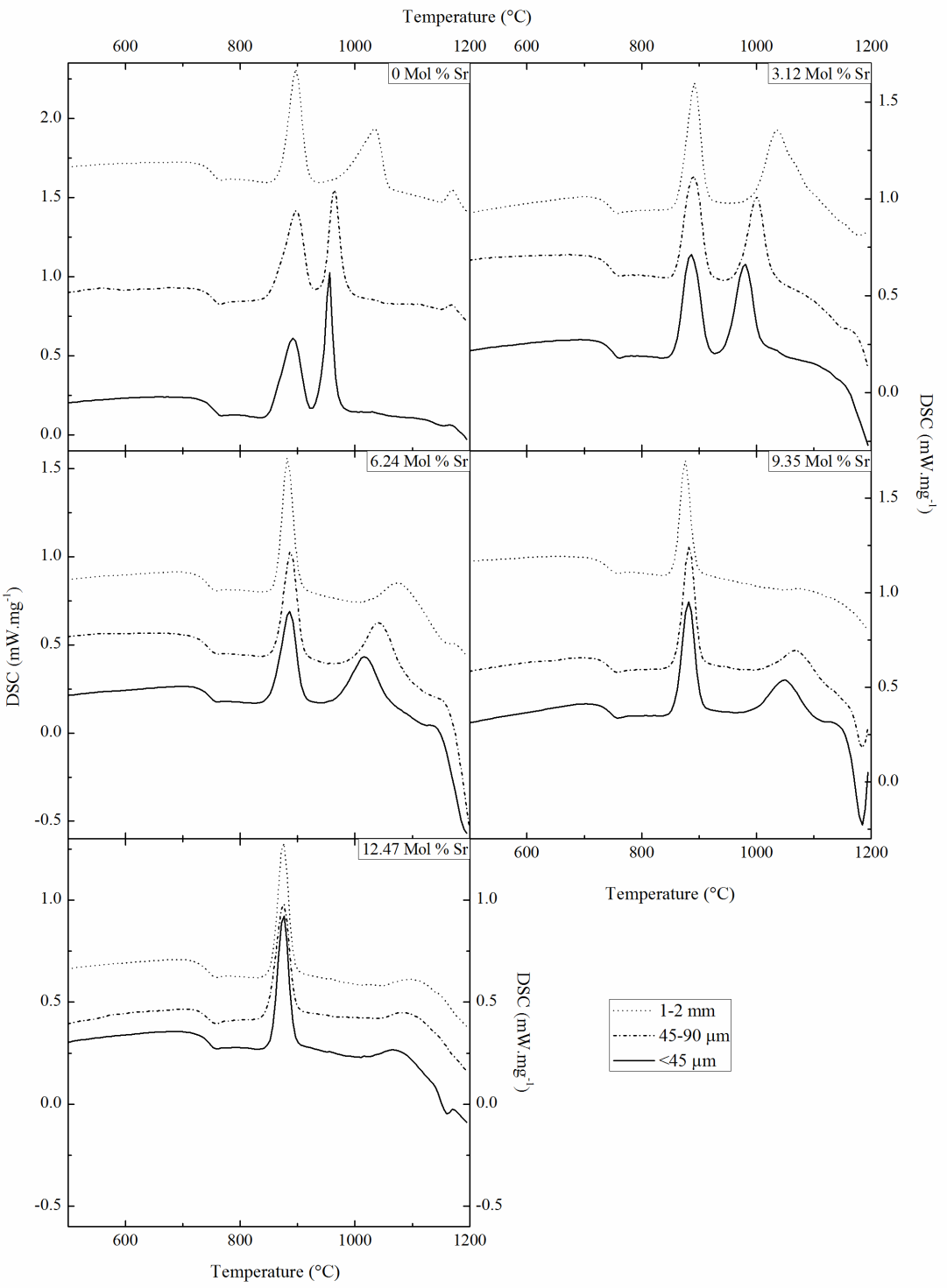

Figure 31: Comparison of offset DSC traces recorded for particle size fractions <45µm, 45-90µm and 1-2mm at a heating rate of 10K.min^{-1} for compositions 0-12.47 Mol % strontium.

T_g and T_{P1} varied by a maximum of 4.3°C and 6.7°C, respectively, over the whole range of particles tested. T_{P2} varied most for composition 0 Mol % strontium with an increase of 79.5°C between particle fractions <45µm and 1-2mm. The increase in peak temperature with increasing particle size became less pronounced with

increasing strontium substitution, but still produced a minimum increase of 29.3°C. Melting occurred at a higher temperature with increasing particle size. The change in T_{P1} and T_{P2} are summarised in figure 32 and the values of T_g, T_{P1} and T_{P2} shown in table 23.

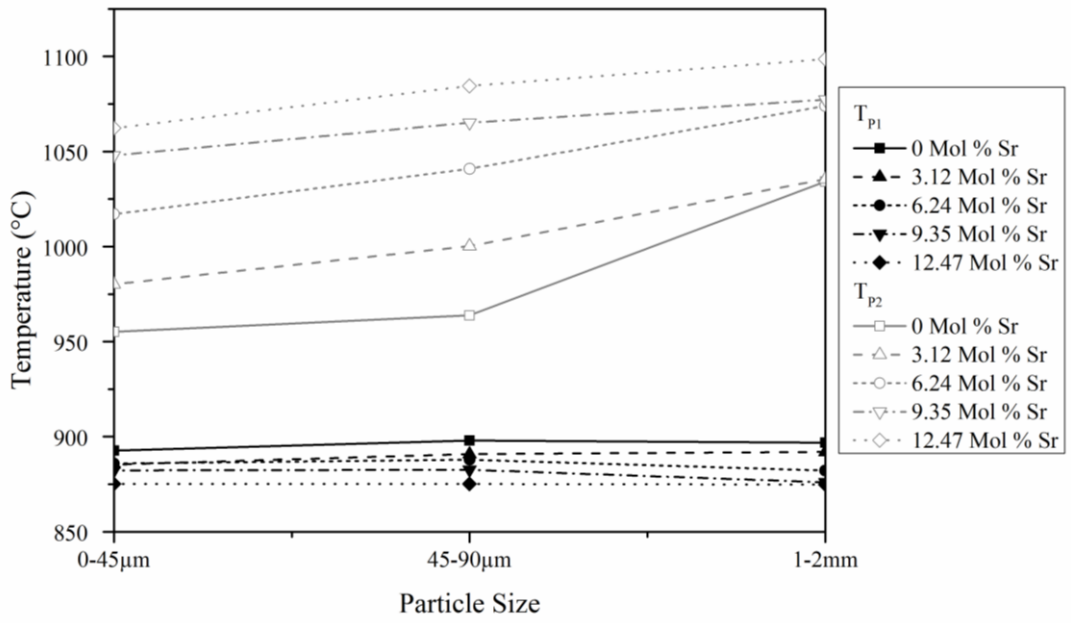

Figure 32: The effect of particle size on T_{P1} and T_{P2} for the glass compositions heated at 10 $K.min^{-1}$.

Table 23: The effect of particle size on T_{P1} and T_{P2} for the glass compositions heated at 10 $K.min^{-1}$.

Event	Size Fraction	Strontium Content (Mol %)				
		0	3.12	6.24	9.35	12.47
T_g (°C)	0-45µm	752.1	747.8	743.2	742.5	742.1
	45-90µm	750.4	743.6	742.3	741.8	741.5
	1-2mm	751.7	743.5	741.8	740.8	740.5
T_{P1} (°C)	0-45µm	892.7	885.3	885.9	882.3	875.2
	45-90µm	898	890.9	887.9	882.6	875.1
	1-2mm	896.9	892	882.2	876	874.8
T_{P2} (°C)	0-45µm	955.2	980.2	1017.1	1048	1062.3
	45-90µm	963.8	1000.3	1040.9	1065.2	1084.5
	1-2mm	1034.3	1035.5	1074	1077.3	1098.6

The effect of heating rate on the 45-90µm size fractions was then examined, figure 33.

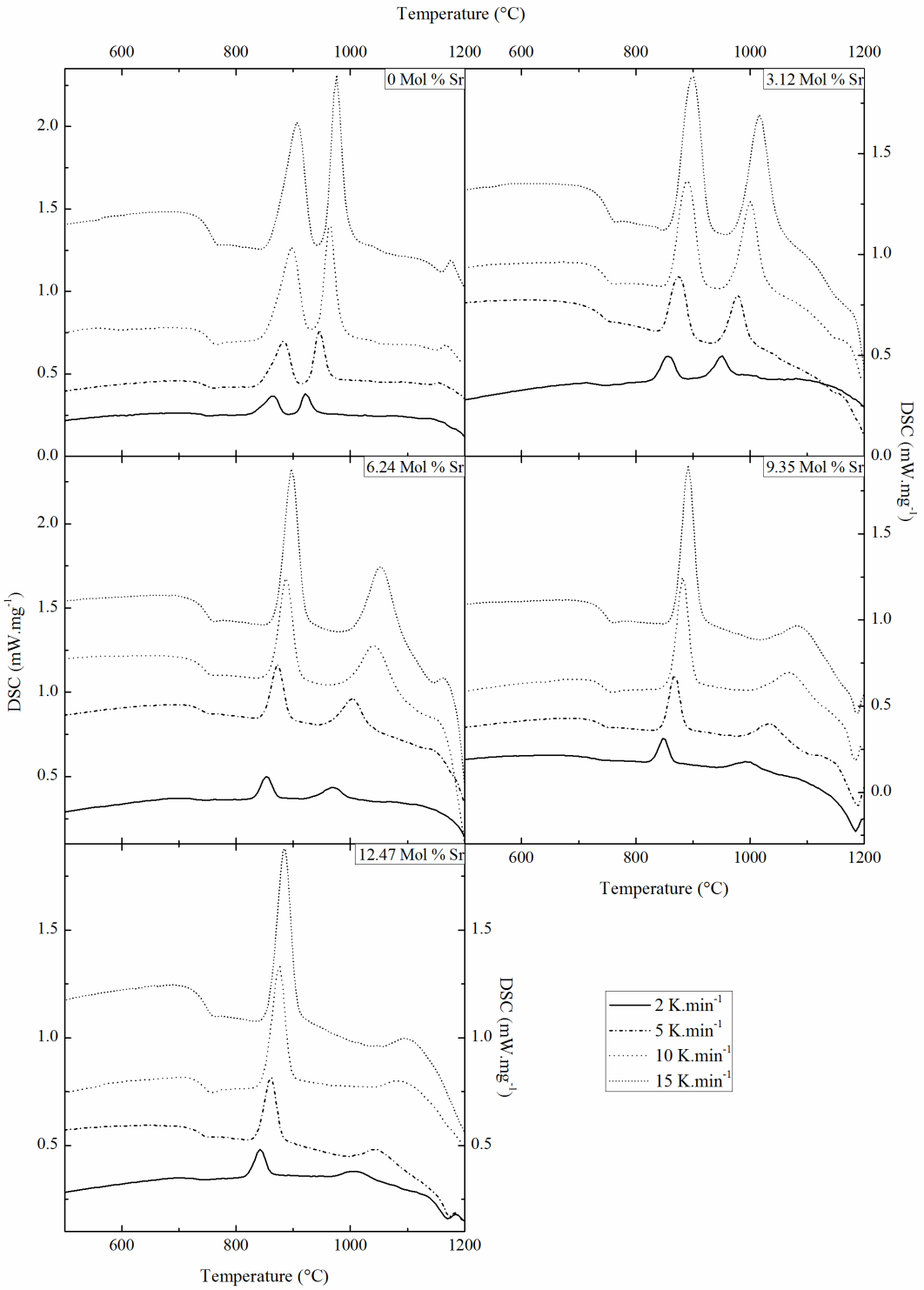

Figure 33: Comparison of offset DSC traces recorded at different heating rates for particle size fraction 45-90µm for compositions 0-12.47 Mol % strontium.

The height of the exothermic peaks increased with increasing heating rate. Both T_{P1} and T_{P2} shifted to higher temperatures with increasing heating rate. The position of the exothermic peaks at different heating rates was used to determine the activation energy via the Kissinger method. The derived graphs are shown in figure 34 and the

resulting gradients, m, adjusted R^2 values and activation energies, E, are shown in table 24.

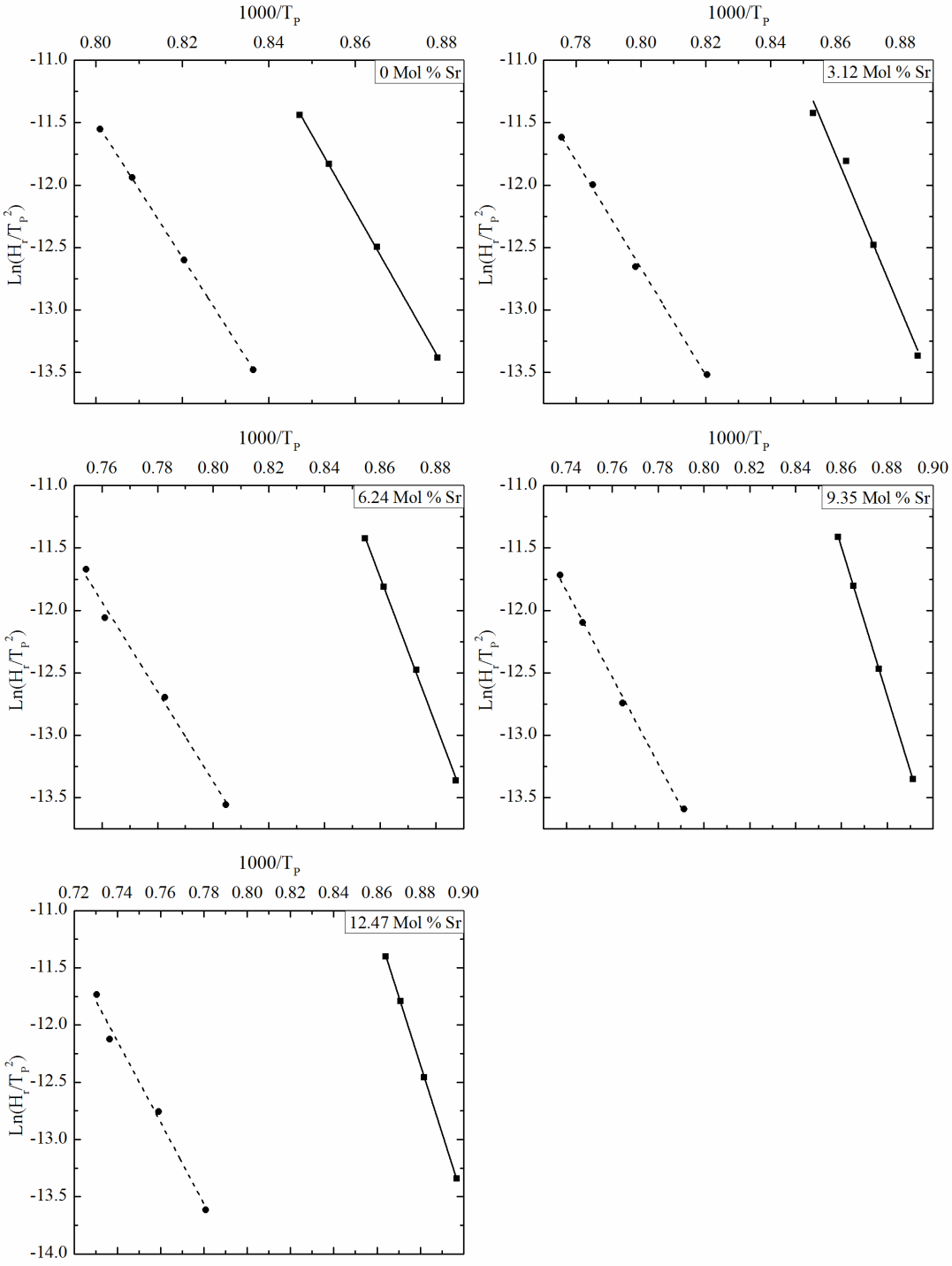

Figure 34: The Kissinger plots for 45-90µm size fractions of glass compositions 0-12.47 Mol % strontium heated at 2, 5, 10 and 15 $K.min^{-1}$.

Table 24: The gradient and activation energies for particle size fraction 45-90µm of compositions 0-12.47 Mol % strontium calculated using the Kissinger method.

Sr Content (Mol %)	Tp1			Tp2		
	m	Adj. R^2	E ($kJ.mol^{-1}$)	m	Adj. R^2	E ($kJ.mol^{-1}$)
0	-61.099	1.000	508.006	-54.572	1.000	453.737
3.12	-62.042	0.976	515.847	-42.932	0.996	356.957
6.24	-59.070	1.000	491.136	-35.994	0.989	299.271
9.35	-59.689	1.000	496.283	-34.606	0.997	287.731
12.47	-59.606	1.000	495.592	-35.537	0.985	295.471

All fits achieved an adjusted R^2 value of 0.97 or greater, indicating a good fit to the data. The calculated activation energy as a function of strontium content of the parent glass is shown in figure 35. T_{P1} was higher than T_{P2} for all compositions with a value of 499.5 ± 8.5 $kJ.mol^{-1}$. A large decrease, 154.45 $kJ.mol^{-1}$, was observed in T_{P2} between compositions 0 -6.24 Mol % strontium. Subsequent additions resulted in little change in activation energy, 293.5 ± 6 $kJ.mol^{-1}$ for the range 6.24-12.47 Mol % strontium.

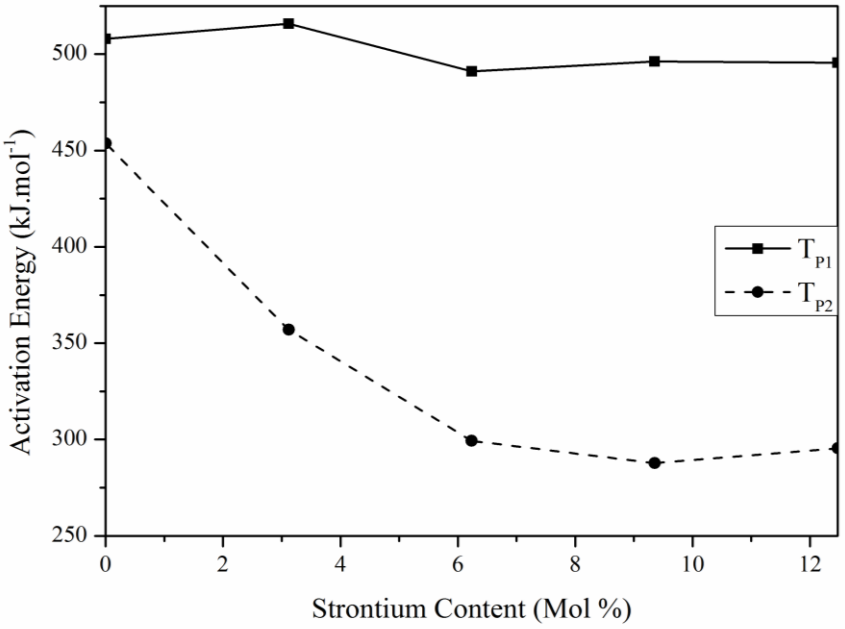

Figure 35: The effect of strontium substitution on the activation energy of thermodynamic events T_{P1} and T_{P2}.

3.3.2 X-Ray Diffraction / Rietveld

3.3.2.1 Phase Identification

The Rietveld refinement strategy was first applied to samples heated to 1050°C at 10Kmin^{-1} and held for 2 hours. The results are shown in figures 36 to 41 and tables 25 to 35 on pages 80 to 86. The data shows the observed data, the calculated fit, the calculated background, the position of matched peaks and the difference plot (observed-calculated).

3.3.2.1.1 0 Mol % Strontium

The most intense diffraction peaks were matched to an apatite phase. fluorapatite (FA), $Ca_5(PO_4)_3F$, ICDD: 04-009-4021. Following refinement of FA residual peaks were matched to a silicate, monoclinic wollastonite-2M (Wol-2M), $CaSiO_3$, ICDD: 04-009-5600. The completed refinement is shown in figure 36 with the results shown in tables 25 and 26. A good fit was achieved with a weighted R-profile of 7.688. The maximum peak intensity occurred at 31.6997°2θ and was matched to FA. The largest difference between the observed and calculated intensities occurred around the second most intense apatite peak at 31.9°2θ, with a ratio of 1:5 to the maximum peak intensity.

3.3.2.1.2 3.12 Mol % Strontium

Both FA and Wol-2M were successfully refined for composition 3.12 Mol % strontium, producing a weighted R-profile of 7.746, figure 37 and tables 27 and 28. The maximum peak intensity was at 31.4997°2θ and was matched to FA. Again the largest difference occurred around the second most intense apatite peak at 31.7°2θ with a ratio of 1:4 with the maximum intensity.

To reduce the size of the difference peaks, an alternative match for the apatite phase was found. Fluorstophite (SrFA), $Sr_{3.65}Ca_{1.35}(PO_4)_3F$, ICDD: 04-009-1806, was used instead of FA and the refinement re-run, figure 38 and tables 29 and 30. Though the ratio of the largest difference to the highest intensity was reduced to 1:5, the weighted R-profile increased to 8.063.

3.3.2.1.3 6.24 Mol % Strontium

Convergence was not achieved for the apatite phase using FA 04-009-4021 and so SrFA was used, figure 39 and tables 31 and 32. The silicate phase was successfully matched to Wol-2M with the final refinement producing a weighted R-profile of 4.928. The maximum peak intensity was at 31.3077°2θ and was matched to SrFA. The maximum difference was observed around 31.4°2θ and the difference to maximum ratio was 1:10.

3.3.2.1.4 9.35 Mol % Strontium

FA and Wol-2M were both successfully refined for composition 9.35 Mol % strontium producing a weighted R-profile fit of 4.335, figure 40 and tables 33 and 34. The maximum peak intensity, occurring at 31.2027, was matched to SrFA. The maximum difference occurred around 32.4°2θ, with the maximum difference to maximum height ratio of 1:15.

3.3.2.1.5 12.47 Mol % Strontium

SrFA and Wol-2M were both successfully refined for composition 12.46 Mol % strontium producing a weighted R-profile of 9.333, figure 41 and tables 35 and 36. The maximum peak intensity, matched to SrFA, occurred at 31.1697. The largest difference occurred at 31.2°2θ producing a ratio of the difference to the maximum intensity of 1:5.

A strong residual peak was observed around 45°2θ. An attempt was made to identify the phase producing the peak. Monoclinic pseudo wollastonite (PsWol), $CaSiO_3$, ICDD: 04-012-1776, was fitted but conflicted with Wol-2M. Wol-2M was removed and the residual peaks were matched to tetragonal strontium calcium magnesium silicate (SCMS), $SrCaMg(Si_3O_7)$, ICDD: 04-009-1844, resulting in a weighted R-profile of 5.461, figure 42 and tables 37 and 38. Though a good fit was achieved using PsWol and SCMS, there was an increase in the number of un-matched reference peaks, with 1 in 10 of the PsWol peaks failing to match. The ratio of the maximum difference to the peak intensity dropped to 1:4 in part due to the PsWol peaks overlapping strongly with the apatite peaks, producing large differences in intensity around the 31.2°2θ apatite peak. Multiple large, negative, differences were also observed.

Though a stronger fit was achieved using PsWol and SCMG in place of Wol-2M for composition 12.47 Mol % strontium, the increase in the intensity of the difference plot and the non-matching of multiple peaks meant the it's values were not included in subsequent analysis of weight percentages and unit cell volumes.

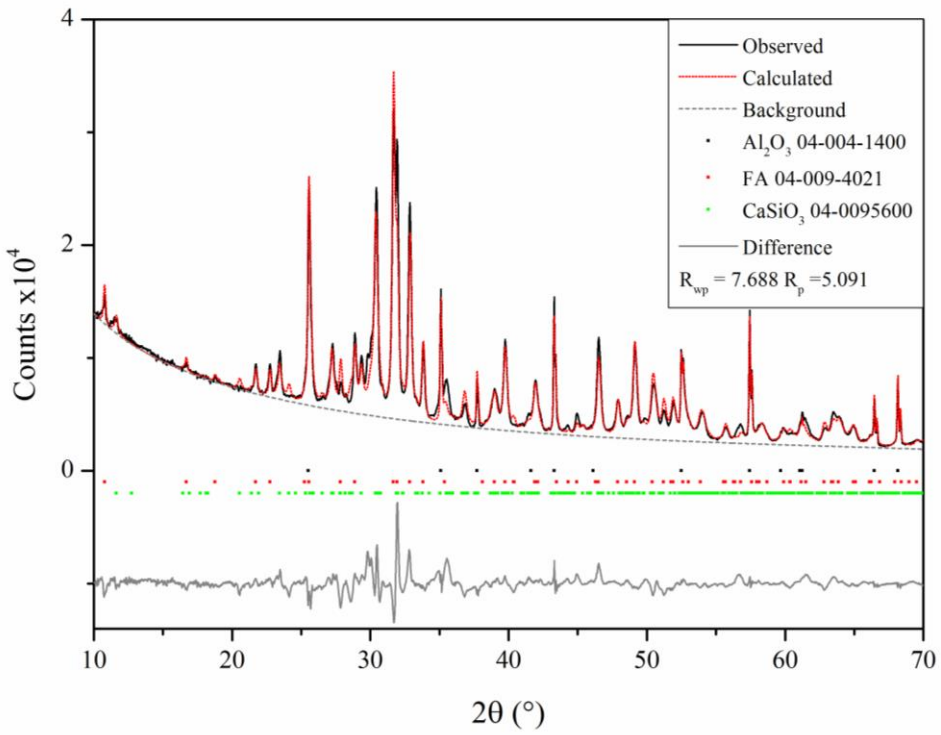

Figure 36: Rietveld refinement of 0 Mol % strontium heated at 10Kmin^{-1} to 1050°C and held for 2 hours.

Table 25: The unit cell dimensions and volume calculated using the developed Rietveld refinement for composition of 0 Mol % strontium heated at 10Kmin^{-1} to 1050°C and held for 2 hours. Standard deviations (SDEV) are shown.

Phase	Unit Cell Dimensions						Volume (nm^3)
	a (Å)	SDEV	b (Å)	SDEV	c (Å)	SDEV	
FA	9.422	0.001	9.422	0.001	6.947	0.001	534.000
Wol-2M	6.949	0.002	7.214	0.002	15.209	0.005	758.874
Amorphous	-	-	-	-	-	-	

Table 26: Refinement factors U and W and weight percentages calculated with the Rietveld refinement of 0 Mol % strontium heated at 10Kmin^{-1} to 1050°C and held for 2 hours. Standard deviations (SDEV) are shown.

Phase	Refinement Factors				Wt%
	U	SDEV	W	SDEV	
FA	0.1799	0.0518	0.032198	0.005501	33
Wol-2M	0.4438	0.2042	0.0592	0.0195	27
Amorphous	-	-	-	-	40

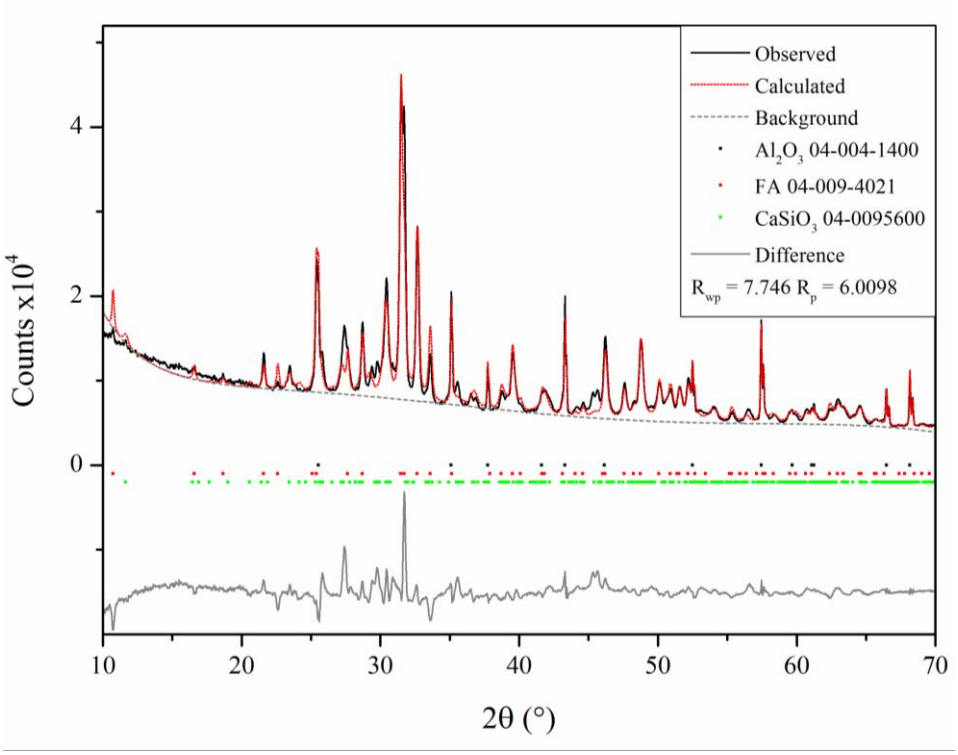

Figure 37: Rietveld refinement of 3.12 Mol % strontium heated at 10Kmin^{-1} to 1050°C and held for 2 hours.

Table 27: The unit cell dimensions and volume calculated using the developed Rietveld refinement for composition of 3.12 Mol % strontium heated at 10Kmin^{-1} to 1050°C and held for 2 hours. Standard deviations (SDEV) are shown.

Phase	Unit Cell Dimensions						Volume (nm^3)
	a (Å)	SDEV	b (Å)	SDEV	c (Å)	SDEV	
FA	9.481	0.001	9.481	0.001	7.003	0.001	545.167
Wol-2M	6.970	0.001	7.215	0.000	15.213	0.001	761.641
Amorphous	-	-	-	-	-	-	

Table 28: Refinement factors U and W and weight percentages calculated with the Rietveld refinement of 3.12 Mol % strontium heated at 10Kmin^{-1} to 1050°C and held for 2 hours. Standard deviations (SDEV) are shown.

Phase	Refinement Factors				Wt%
	U	SDEV	W	SDEV	
FA	0.2504	0.0678	0.0298	0.0065	39
Wol-2M	1.0240	0.3367	0.1415	0.0296	18
Amorphous	-	-	-	-	43

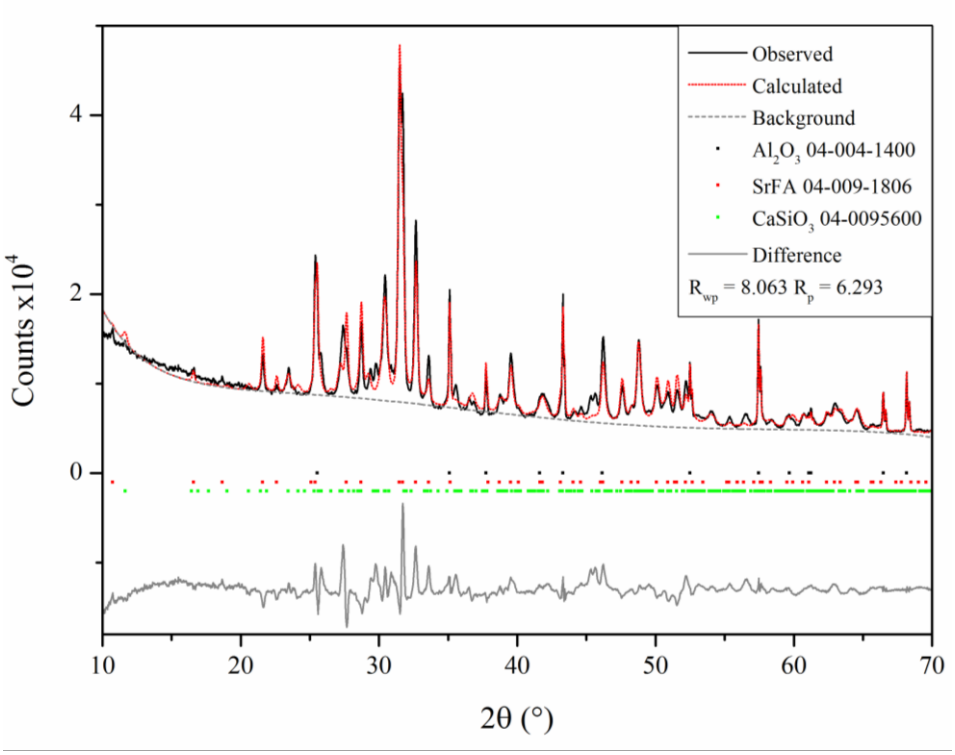

Figure 38, Rietveld refinement using SrFA of 3.12 Mol % strontium heated at 10Kmin^{-1} to 1050°C and held for 2 hours.

Table 29: The unit cell dimensions and volume calculated using the SrFa containing Rietveld refinement for composition of 3.12 Mol % strontium heated at 10Kmin^{-1} to 1050°C and held for 2 hours. Standard deviations (SDEV) are shown.

Phase	Unit Cell Dimensions						Volume (nm^3)
	a (Å)	SDEV	b (Å)	SDEV	c (Å)	SDEV	
SrFA	9.481	0.001	9.481	0.001	7.003	0.001	545.183
Wol-2M	6.970	0.001	7.215	0.000	15.212	0.001	761.636
Amorphous	-	-	-	-	-	-	

Table 30: Refinement factors U and W and weight percentages calculated with the SrFA containing Rietveld refinement of 3.12 Mol % strontium heated at 10Kmin^{-1} to 1050°C and held for 2 hours. Standard deviations (SDEV) are shown.

Phase	Refinement Factors				Wt%
	U	SDEV	W	SDEV	
SrFA	0.2504	0.0678	0.0298	0.0065	20
Wol-2M	1.1965	0.6114	0.1043	0.0489	16
Amorphous	-	-	-	-	64

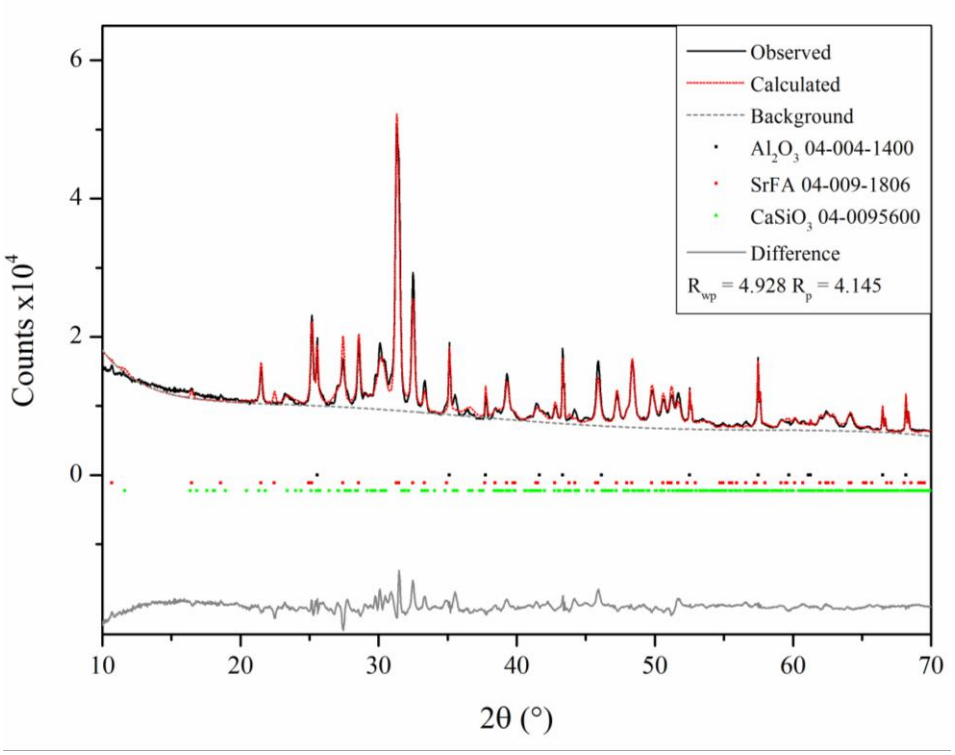

Figure 39: Rietveld refinement of 6.24 Mol % strontium heated at 10Kmin^{-1} to 1050°C and held for 2 hours.

Table 31: The unit cell dimensions and volume calculated using the developed Rietveld refinement for composition of 6.24 Mol % strontium heated at 10Kmin^{-1} to 1050°C and held for 2 hours. Standard deviations (SDEV) are shown.

Phase	Unit Cell Dimensions						Volume (nm^3)
	a (Å)	SDEV	b (Å)	SDEV	c (Å)	SDEV	
SrFA	9.536	0.001	9.536	0.001	7.067	0.001	556.456
Wol-2M	7.003	0.005	7.283	0.004	15.253	0.015	774.346
Amorphous	-	-	-	-	-	-	

Table 32: Refinement factors U and W and weight percentages calculated with the Rietveld refinement of 6.24 Mol % strontium heated at 10Kmin^{-1} to 1050°C and held for 2 hours. Standard deviations (SDEV) are shown.

Phase	Refinement Factors				Wt%
	U	SDEV	W	SDEV	
SrFA	0.2306	0.0457	0.0279	0.0045	23
Wol-2M	2.0021	0.8731	0.3365	0.0785	17
Amorphous	-	-	-	-	60

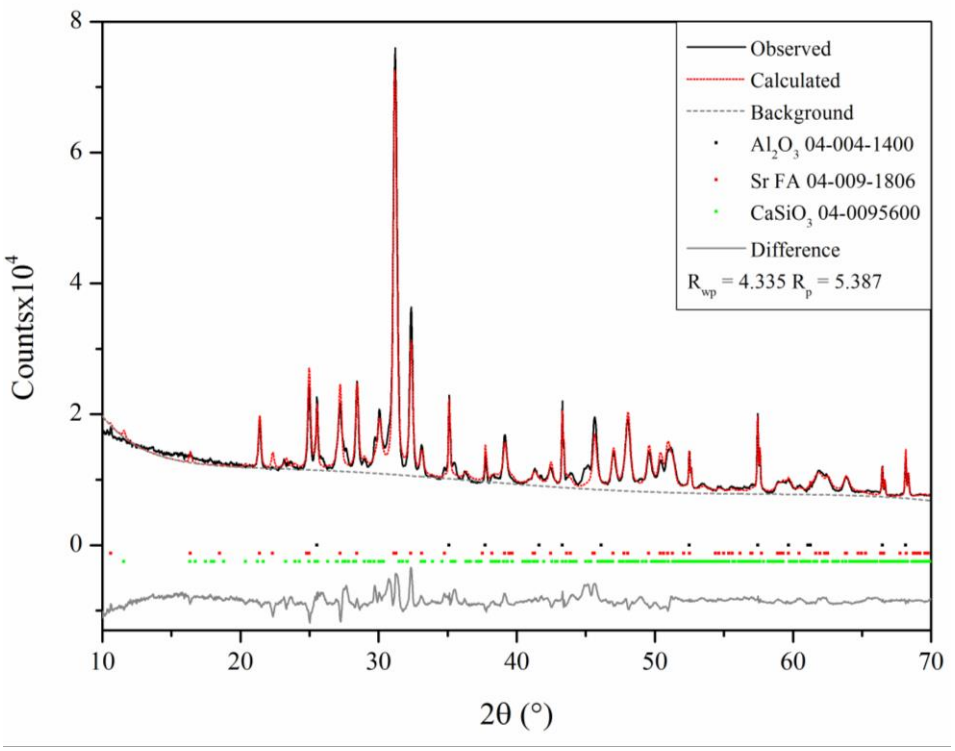

Figure 40: Rietveld refinement of 9.35 Mol % strontium heated at 10Kmin^{-1} to 1050°C and held for 2 hours.

Table 33: The unit cell dimensions and volume calculated using the developed Rietveld refinement for composition of 9.35 Mol % strontium heated at 10Kmin^{-1} to 1050°C and held for 2 hours. Standard deviations (SDEV) are shown.

Phase	Unit Cell Dimensions						Volume (nm^3)
	a (Å)	SDEV	b (Å)	SDEV	c (Å)	SDEV	
SrFA	9.569	0.001	9.569	0.001	7.117	0.001	564.387
Wol-2M	7.024	0.005	7.316	0.005	15.295	0.018	782.779
Amorphous	-	-	-	-	-	-	

Table 34: Refinement factors U and W and weight percentages calculated with the Rietveld refinement of 9.35 Mol % strontium heated at 10Kmin^{-1} to 1050°C and held for 2 hours. Standard deviations (SDEV) are shown.

Phase	Refinement Factors				Wt%
	U	SDEV	W	SDEV	
SrFA	0.3846	0.0581	0.0241	0.0051	27
Wol-2M	1.5636	0.8698	0.0222	0.0594	13
Amorphous	-	-	-	-	60

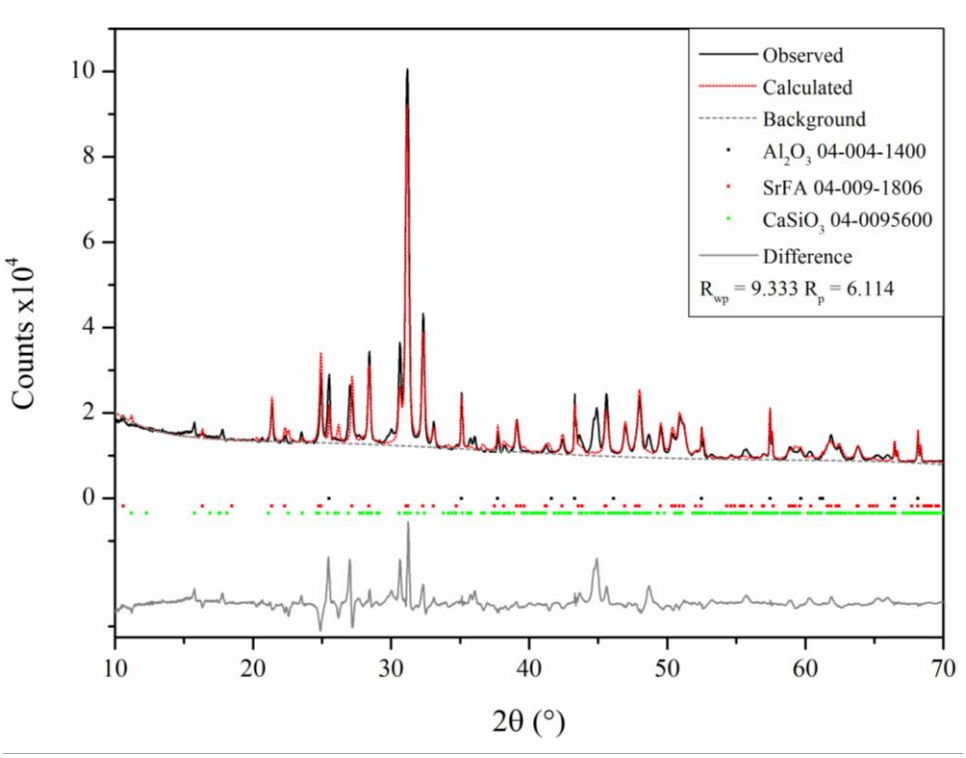

Figure 41: Rietveld refinement of 12.47 Mol % strontium heated at 10Kmin^{-1} to 1050°C and held for 2 hours.

Table 35: The unit cell dimensions and volume calculated using the developed Rietveld refinement for composition of 12.47 Mol % strontium heated at 10Kmin^{-1} to 1050°C and held for 2 hours. Standard deviations (SDEV) are shown.

Phase	Unit Cell Dimensions						Volume (nm^3)
	a (Å)	SDEV	b (Å)	SDEV	c (Å)	SDEV	
SrFA	9.574	0.001	9.574	0.001	7.127	0.001	565.722
Wol-2M	7.203	0.005	7.012	0.004	15.800	0.016	793.749
Amorphous	-	-	-	-	-	-	

Table 36: Refinement factors U and W and weight percentages calculated with the Rietveld refinement of 12.47 Mol % strontium heated at 10Kmin^{-1} to 1050°C and held for 2 hours. Standard deviations (SDEV) are shown.

Phase	Refinement Factors				Wt%
	U	SDEV	W	SDEV	
SrFA	0.2537	0.0768	0.0149	0.0068	30
Wol-2M	0.2846	0.4664	0.0144	0.0332	11
Amorphous	-	-	-	-	59

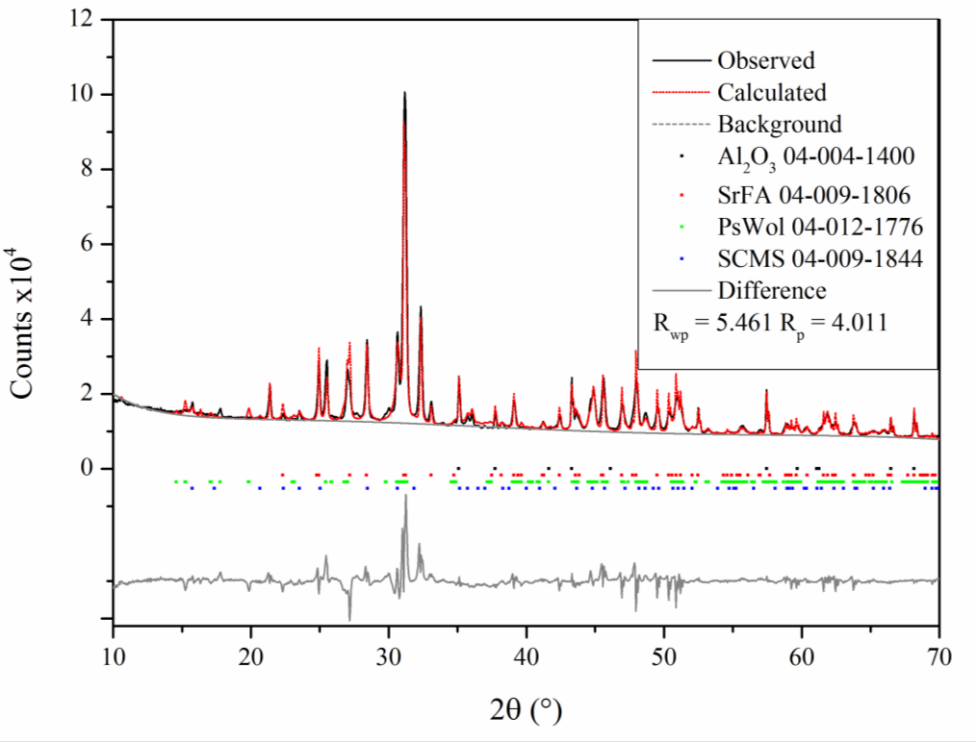

Figure 42: Rietveld refinement using PsWol and SCMS for the glass composition 12.47 Mol % strontium heated at 10Kmin^{-1} and held at 1050°C for two hours.

Table 37: The unit cell results of the Rietveld refinement using PsWol and SCMS for the 12.47 Mol % strontium composition heated at 10Kmin^{-1} and held at 1050°C for two hours. Standard deviations (SDEV) are shown.

Phase	Unit Cell Dimensions						Volume (nm^3)
	a (Å)	SDEV	b (Å)	SDEV	c (Å)	SDEV	
SrFA	9.576	0.001	9.576	0.001	7.126	0.001	565.873
PsWol	6.987	0.004	12.093	0.007	19.902	0.005	1681.523
SCMS	7.933	0.002	7.933	0.002	5.099	0.002	320.916
Amorphous	-	-	-	-	-	-	

Table 38: The refinement factor U and W and weight percentages calculated using the Rietveld refinement containing PsWol and SCMS for the 12.47 Mol % strontium composition heated at 10Kmin^{-1} and held at 1050°C for two hours. Standard deviations (SDEV) are shown.

Phase	Refinement Factors				Wt%
	U	SDEV	W	SDEV	
SrFA	0.3068	0.0383	0.0106	0.0035	34
PsWol	0.0074	0.0616	0.0301	0.0100	17
SCMS	0.3297	0.0000	0.3792	0.0000	11
Amorphous	-	-	-	-	38

3.3.2.2 Final Refinement Strategy

A summary of the refinement strategy including the matched phases is shown in figure 43.

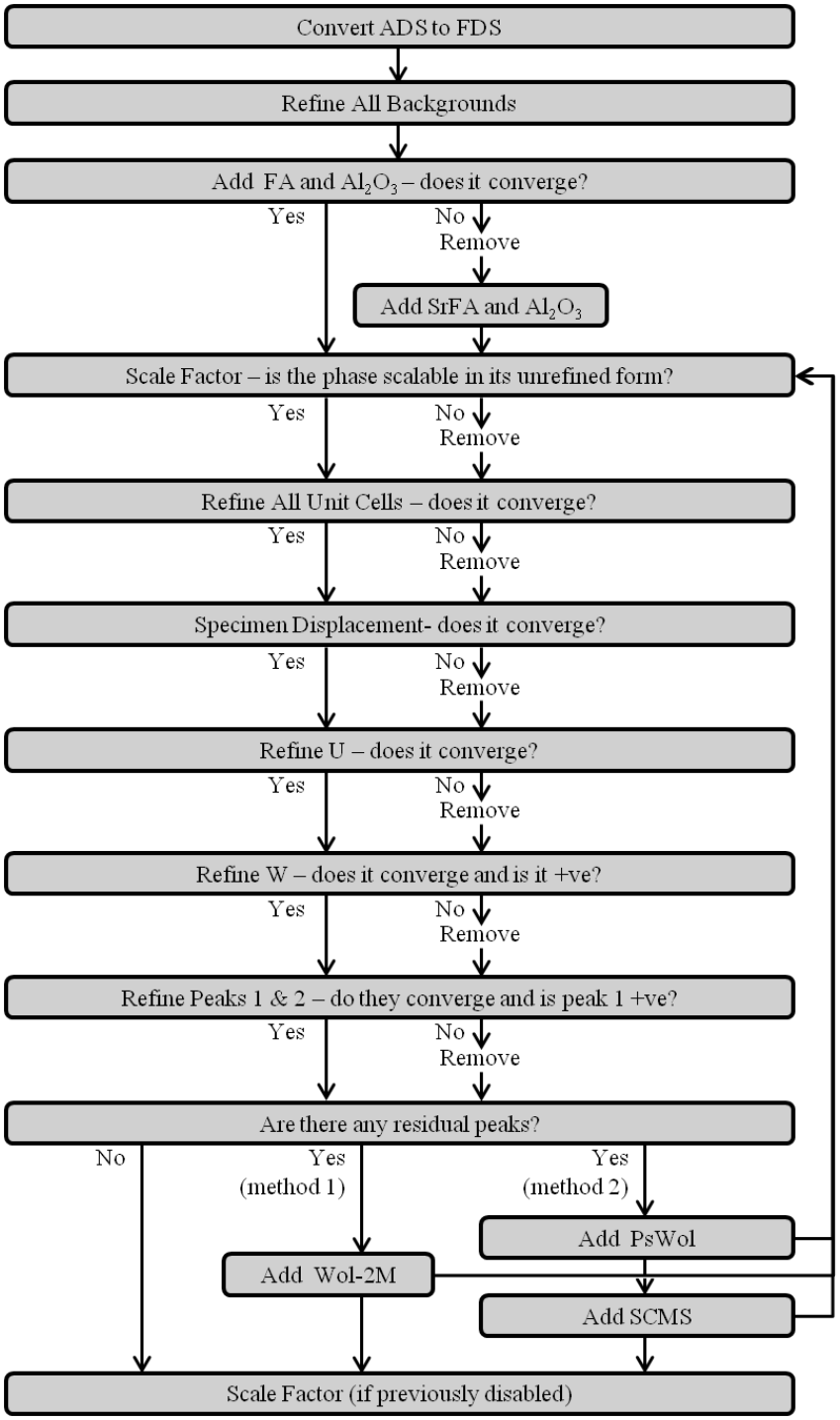

Figure 43: The final Rietveld refinement strategy including the phases identified. FA = Fluorapatite ICDD: 04-009-4021 SrFA = fluorstophite ICDD: 04-009-5600, Wol-2M = wollastonite 2M ICDD: 04-009-5600, PsWol = pseudo wollastonite ICDD: 04-012-1776 and SCMS = strontium magnesium calcium silicate ICDD: 04-0091844.

3.3.2.3 Phase Content Determination

The weight ratios for the glass-ceramics formed by a 2 hour hold at 1050°C and heating rate of 10K.min^{-1} are shown in figure 44.

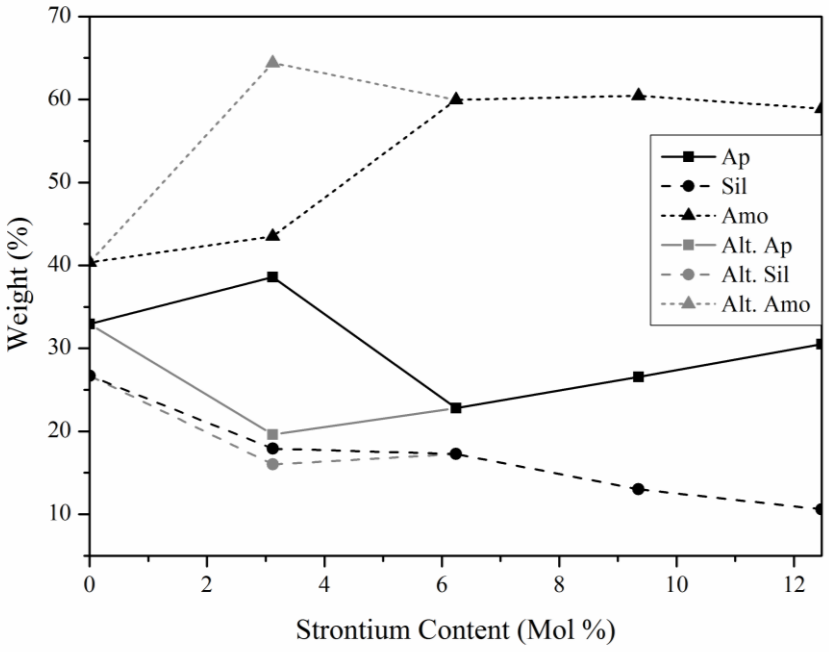

Figure 44: The variation in weight percentage of the phases present following a 2 hour hold at 1050°C with a heating rate of 10Kmin^{-1}. Ap = apatite phase, Sil = silicate phase, Amo = amorphous phase Alt. = alternative values determined using SrFA for composition 3.12 Mol % strontium.

For composition 0 Mol % strontium the amorphous content, calculated from the observed and known weight percentage of Al_2O_3, accounted for 40% of the weight of the material, apatite 33% and silicate 27%. An increase in the amorphous and apatite phases weight percentage was observed with the first substitution of strontium when refining using FA as well as a reduction in the weight percentage of the silicate phase. A large reduction in the apatite phase and a large increase in the amorphous phase weight percentages were observed when SrFA was utilised in place of FA for the refinement of composition 3.12 Mol % strontium. A small reduction in the quantity of the silicate phase was also observed. The refinement of 12.47 Mol % strontium using PsWol and SCMS, not included in figure 44, produced an increase in the total silicate phase present (PsWol + SCMS) compared to the refinement using Wol-2M, increasing from 11 to 28 Wt%. A small increase was also observed in the weight percentage of the apatite phase. A large reduction was observed in the amount of residual amorphous phase, dropping by 21 Wt%.

3.3.2.4 The Effect of Strontium Substitution on Unit Cell volume

From figures 45 and 46 it can be seen that the unit cell volume calculated using the Rietveld refinement of both the apatite and silicate phase increases with increasing strontium substitution into the parent glass.

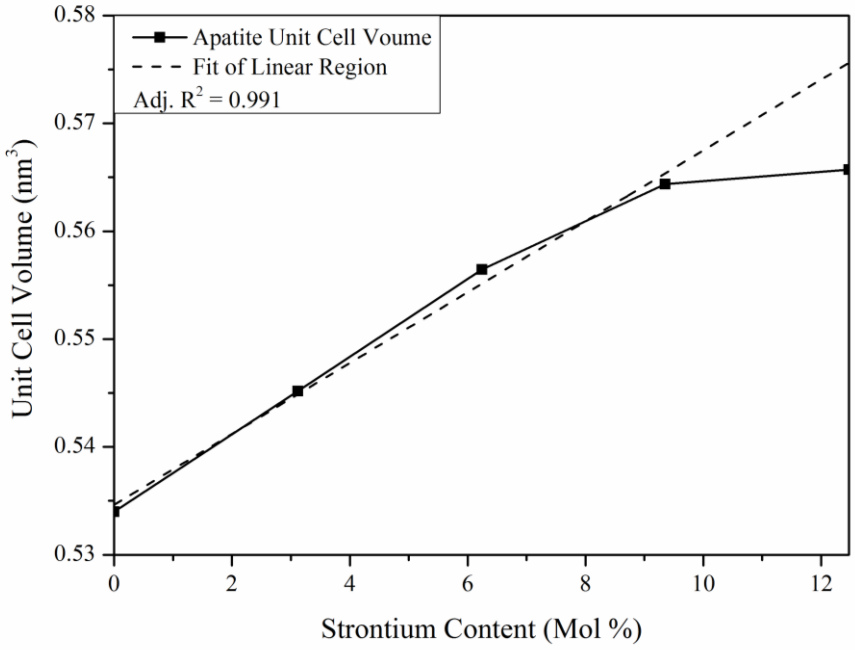

Figure 45: The effect of glass composition on the unit cell volume of the apatite phase formed during devitrification.

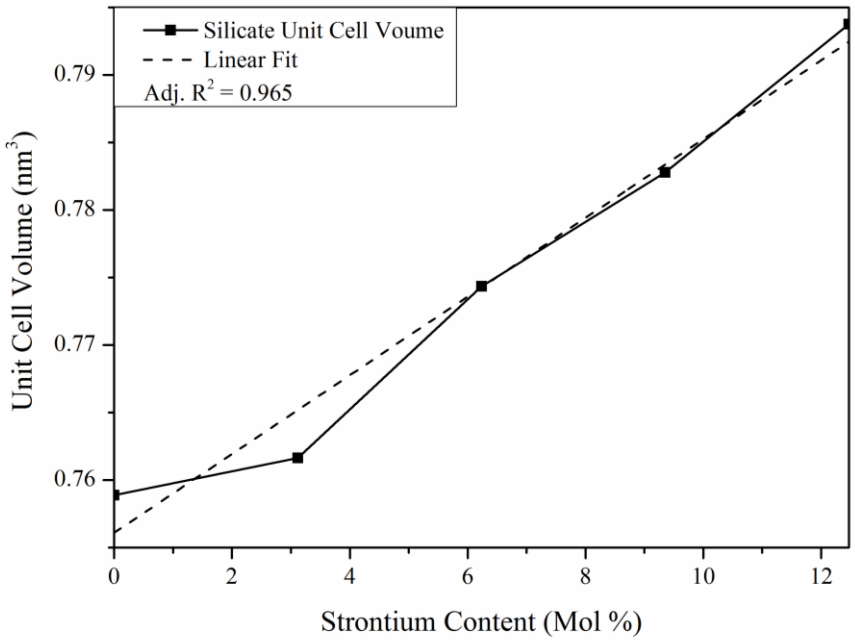

Figure 46: The effect of glass composition on the unit cell volume of the silicate phase formed during devitrification.

Figure 45 shows that the apatite unit cell volume increased linearly between compositions 0-9.35 Mol % strontium with an average increase of 0.010129 nm^3 per 3.12 Mol % strontium increase. A small increase of 0.00135 nm^3 was observed between compositions 9.35 and 12.47 Mol % strontium. A linear fit was achieved for the increase in the silicate phase unit cell volume with an average increase of 0.008719 nm^3 with each 3.12 Mol % strontium substitution.

For composition 3.12 Mol % strontium, utilising SrFA instead of FA produced unit cell volumes for the apatite and silicate phases that differed from the previously calculated by only $1.6x10^{-5}$ and $5x10^{-6}$ nm^3, respectively.

3.3.2.5 The Effect of Heating on Crystallisation

The Rietveld refinement strategy was then applied to powders that had been heated at $10Kmin^{-1}$ to T_{O1}-15°C, T_{P1}+10°C and T_{P2}+10°C and held at the respective temperature for 2 hours. The results are shown in figures 47-51 and tables 39-43.

3.3.2.5.1 0 Mol % Strontium

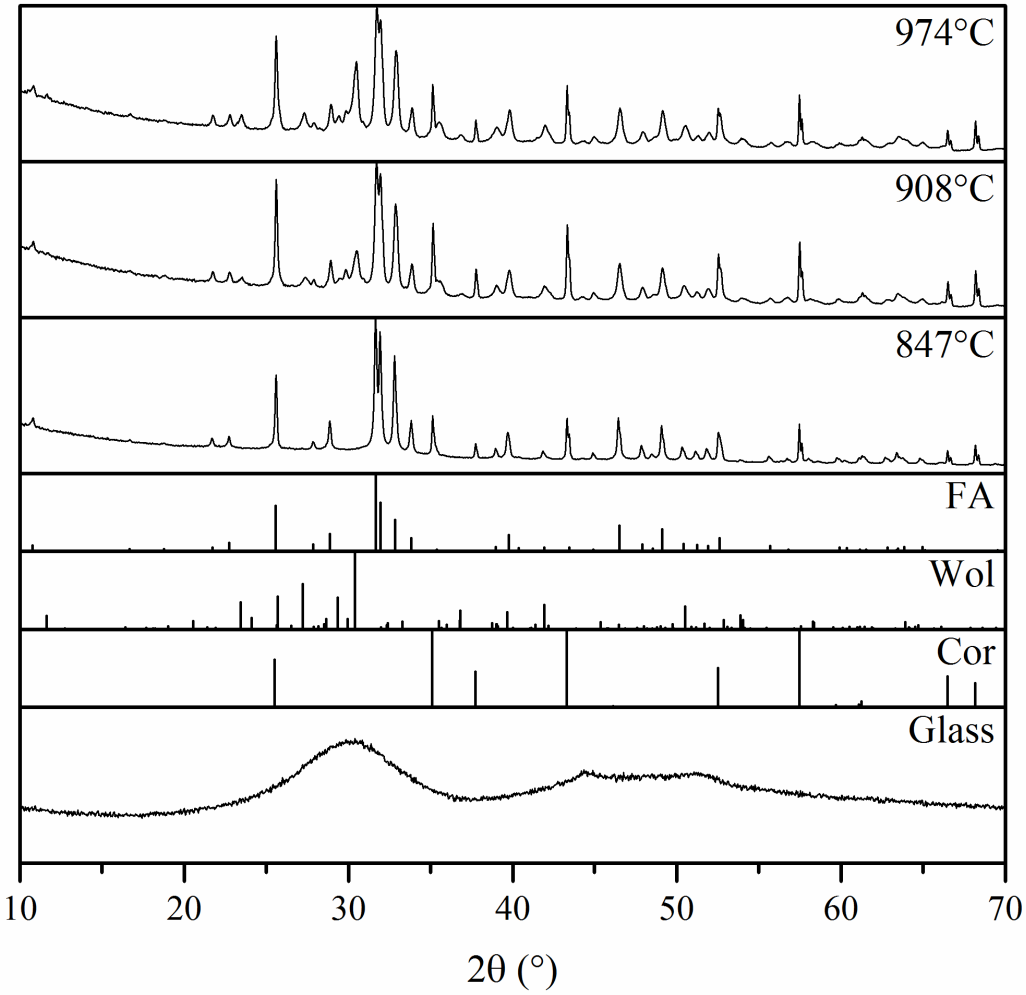

Figure 47: The effect of a 2 hour hold at increasing temperatures on the crystal phases formed in glass composition 0 Mol % strontium.

Table 39: The results of the Rietveld refinements shown in figure 47.

Temperature	Phase	Volume (nm^3)	Refinement Factor		Wt%
			U	W	
974 °C	FA	0.534332	0.2606	0.0350	33
	Wol-2M	0.759656	0.9281	0.0815	21
	Amorphous	-	-	-	46
908 °C	FA	0.535611	0.2037	0.0309	24
	Wol-2M	0.757900	1.0130	0.1321	10
	Amorphous	-	-	-	66
847 °C	FA	0.536881	0.0704	0.0134	37
	W-2M	-	-	-	0
	Amorphous	-	-	-	63

3.3.2.5.2 3.12 Mol % Strontium

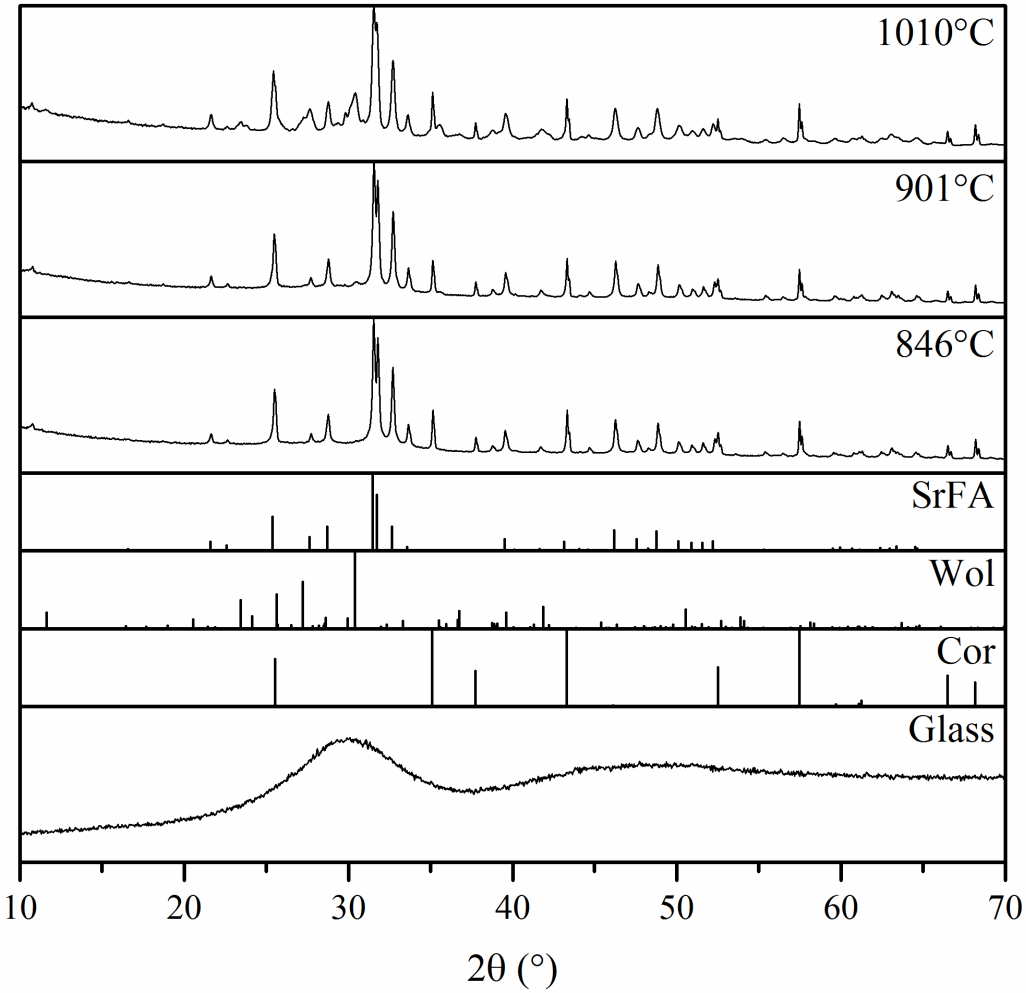

Figure 48: The effect of a 2 hour hold at increasing temperatures on the crystal phases formed in glass composition 3.12 Mol % strontium.

Table 40: The results of the Rietveld refinements shown in figure 48.

Temperature	Phase	Volume (nm^3)	Refinement Factor		Wt%
			U	W	
1010 °C	SrFA	0.544078	0.2705	0.0270	13
	Wol-2M	0.766470	2.3605	0.2864	24
	Amorphous	-	-	-	63
901 °C	SrFA	0.542739	0.0849	0.0147	21
	Wol-2M	0.765442	2.1106	0.1082	4
	Amorphous	-	-	-	75
846 °C	SrFA	0.543408	0.0931	0.0147	19
	Wol-2M	-	-	-	0
	Amorphous	-	-	-	81

3.3.2.5.3 6.24 Mol % Strontium

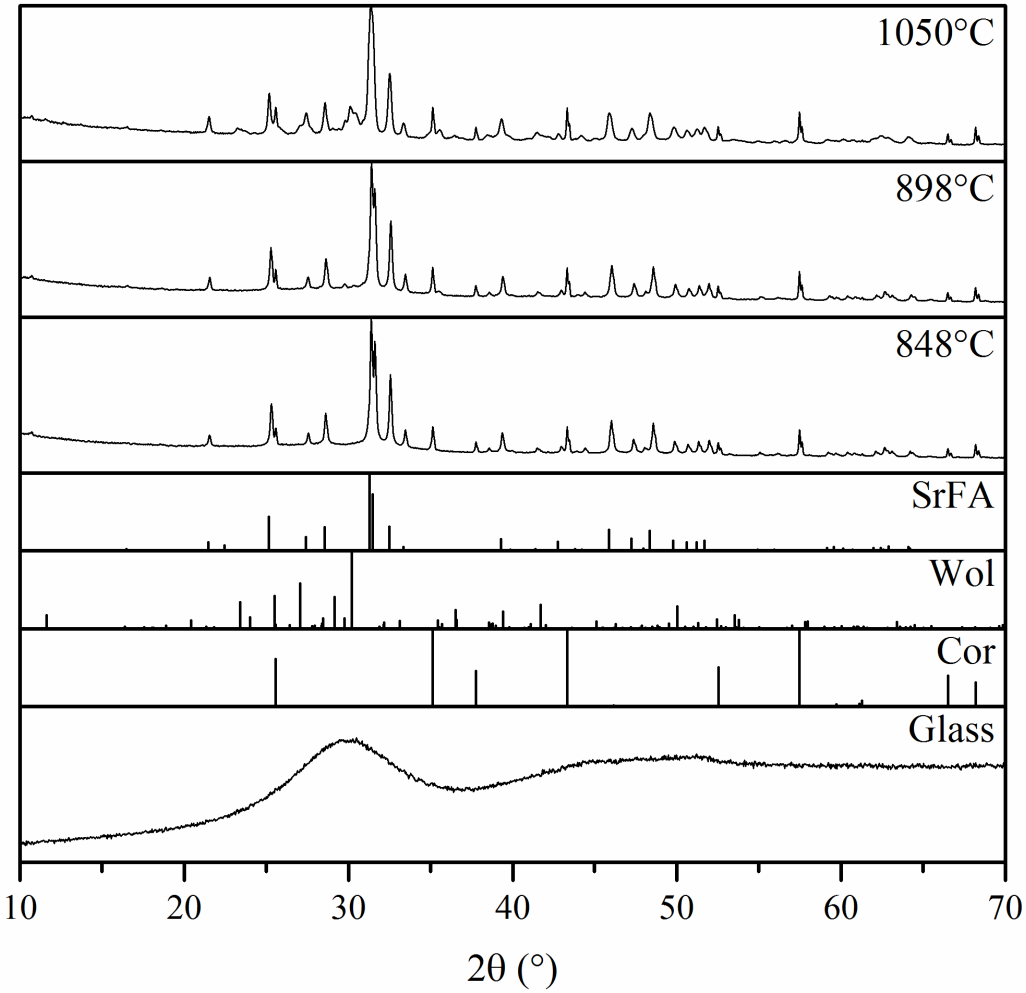

Figure 49: The effect of a 2 hour hold at increasing temperatures on the crystal phases formed in glass composition 6.24 Mol % strontium.

Table 41: The results of the Rietveld refinements shown in figure 49.

Temperature	Phase	Volume (nm^3)	Refinement Factor		Wt%
			U	W	
1050 °C	SrFA	0.556456	0.2306	0.0279	23
	Wol-2M	0.774346	0.8731	0.0785	17
	Amorphous	-	-	-	60
898 °C	SrFA	0.551194	0.0870	0.0147	25
	Wol-2M	0.778748	1.5396	0.6608	6
	Amorphous	-	-	-	69
848 °C	SrFA	0.552066	0.0864	0.0128	26
	Wol-2M	-	-	-	0
	Amorphous	-	-	-	74

3.3.2.5.4 9.35 Mol % Strontium

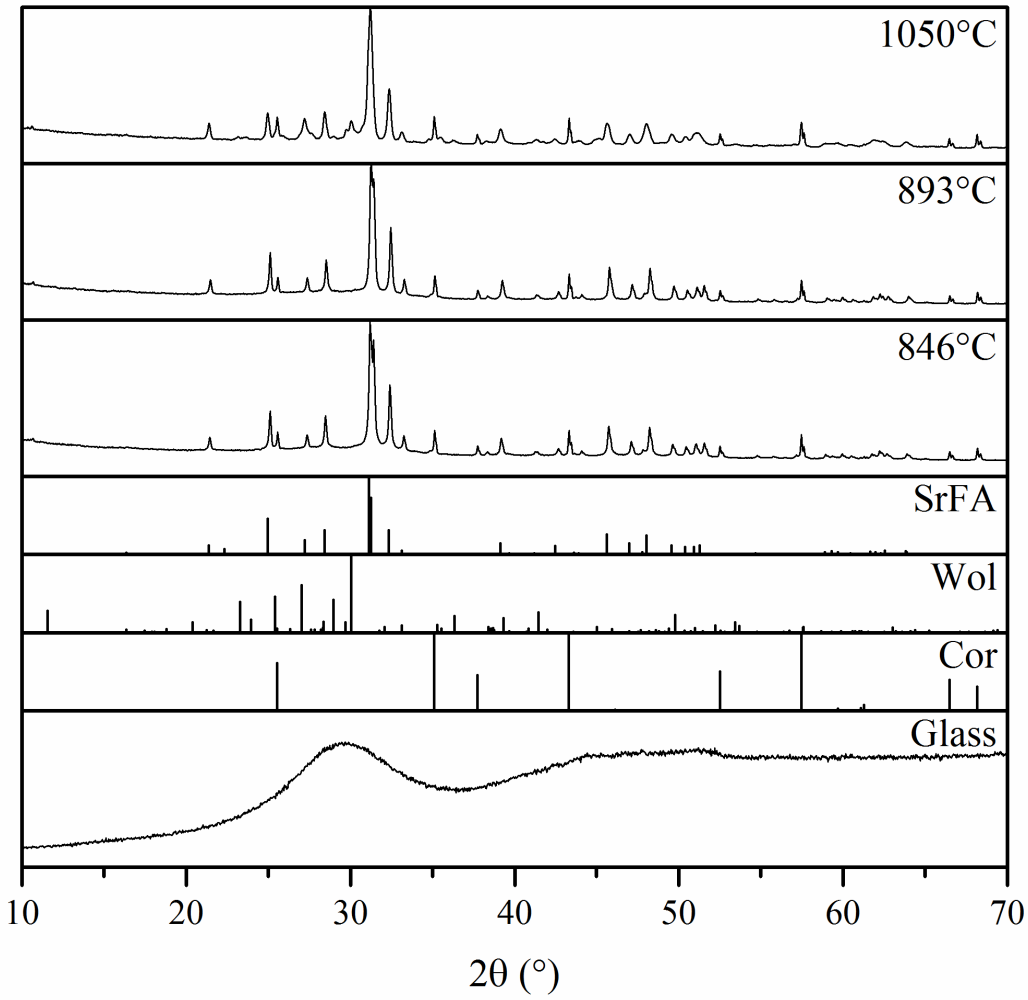

Figure 50: The effect of a 2 hour hold at increasing temperatures on the crystal phases formed in glass composition 9.35 Mol % strontium.

Table 42: The results of the Rietveld refinements shown in figure 50.

Temperature	Phase	Volume (nm3)	Refinement Factor		Wt%
			U	W	
1050 °C	SrFA	0.564387	0.3846	0.0241	27
	Wol-2M	0.782779	1.5636	0.0222	13
	Amorphous	-	-	-	60
893 °C	SrFA	0.559394	0.0547	0.0121	27
	Wol-2M	-	-	-	0
	Amorphous	-	-	-	73
846 °C	SrFA	0.560823	0.1001	0.0120	27
	Wol-2M	-	-	-	0
	Amorphous	-	-	-	73

3.3.2.5.5 12.47 Mol % Strontium

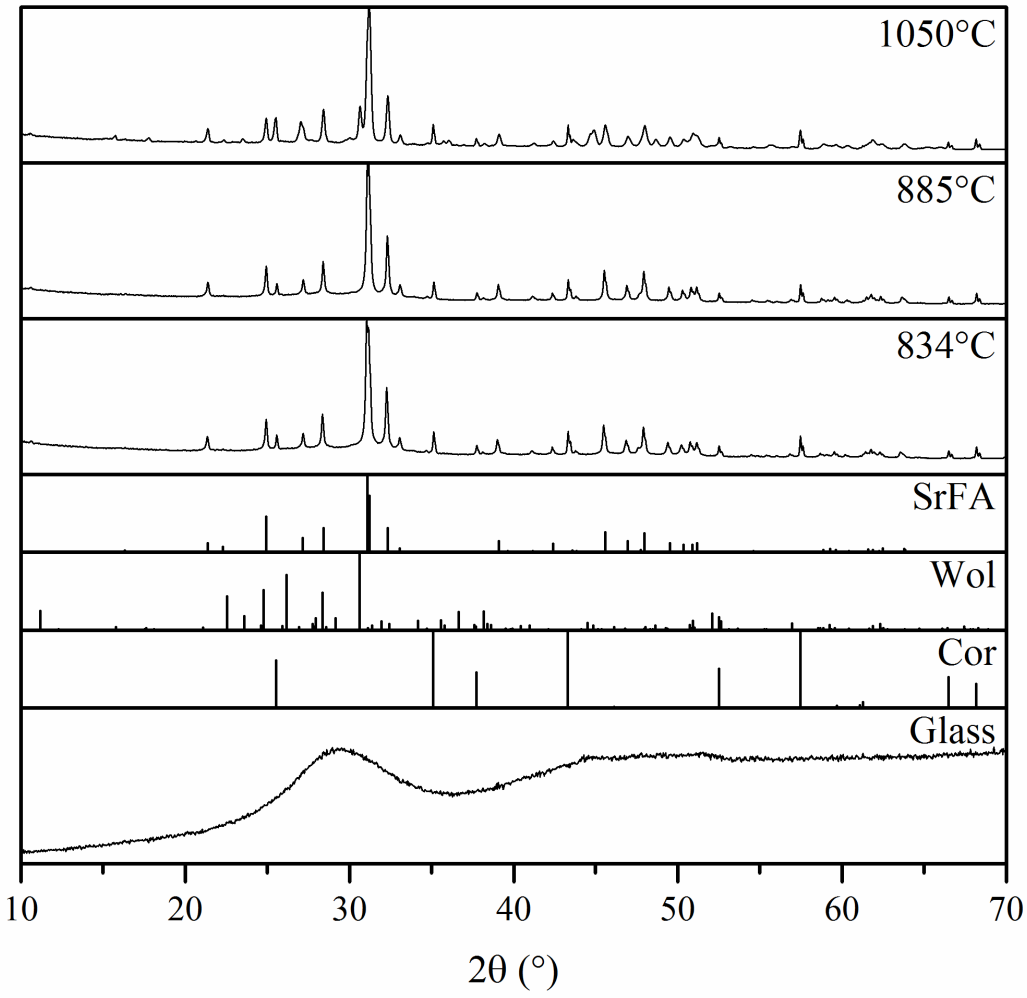

Figure 51: The effect of a 2 hour hold at increasing temperatures on the crystal phases formed in glass composition 12.47 Mol % strontium.

Table 43: The results of the Rietveld refinements shown in figure 51.

Temperature	Phase	Volume (nm^3)	Refinement Factor		Wt%
			U	W	
1050 °C	SrFA	0.565722	0.2537	0.0149	31
	Wol-2M	0.793749	0.2846	0.0144	10
	Amorphous				59
885 °C	SrFA	0.568975	0.0618	0.0107	31
	Wol-2M				0
	Amorphous				69
834 °C	SrFA	0.570183	0.0983	0.0117	29
	Wol-2M	-	-	-	0
	Amorphous	-	-	-	71

In all samples crystal peaks became visible following a 2 hour hold at T_{O1}-15. The matched peaks corresponded to the apatite phase. To aid comparison between strontium containing samples, SrFA and Wol-2M were used for all strontium containing samples. The hold temperature decreased with increasing strontium content. An initial drop in apatite weight percentage was observed with the first substitution of strontium followed by an increase with each subsequent substitution. In all samples no other crystalline phases were detected at T_{O1}-15 and the residual weight percentage was composed of an amorphous phase.

At T_{P1}+10 apatite was again detected but in compositions 0-6.24 Mol % strontium secondary peaks were observed which were matched to silicate phase Wol-2M. These peaks were most prominent in composition 0 Mol % strontium but were still detectable in the strontium containing materials. The amount of this phase decreased with strontium substitution but was higher in composition 6.24 than 3.12, 6 to 4 Wt% respectively. No secondary phase was detected in compositions 9.35 and 12.46 Mol % strontium. Compared to T_{O1}-15, there was a reduction in the weight percentage of the amorphous phase in all samples, apart from composition 0 Mol % strontium which showed a small increase from 63 to 66 Wt%. A reduction in the weight percentage of the apatite phase was also detected in this composition as the secondary phase formed. The weight percentage of the apatite phase varied by a maximum of 2 Wt% in the strontium containing compositions compared to the previous hold temperature.

At T_{P2}+10 both the apatite and silicate phase peaks were clearly visible in all the compositions tested. The weight percentage of the silicate phase increased in samples which had been shown to form it at lower temperatures. The weight percentage of the apatite phase increased by 9 Wt% in the 0 Mol % strontium composition but reduced by a maximum of 1 Wt% in the strontium containing samples when compared to the previous hold temperature. When comparing samples held at T_{P2}+10, the weight of the residual amorphous phase increased from 46 to 63 Wt% between compositions 0 and 3.12 Mol % strontium, respectively. Subsequent additions of strontium resulted in little change in amorphous phase weigh percentage with all samples coming within 60±3 Wt% of each other. The weight contribution of the silicate phase got smaller with increasing strontium substitution.

3.3.3 Surface Analysis

3.3.3.1 SEM

Samples heated at 10K.min^{-1} to 1050°C and held there for 2 hours were then imaged using a scanning electron microscope, figures 52-56 on pages 99 to 103.

3.3.3.1.1 0 Mol % Strontium

Small domains were observed on the surface of the material that appear to be interlocked with a small void visible in figure 52 (c). Brighter, whiter, seams can be seen to run throughout figure 52 (a) and (b). Though small variations in domain size can be observed, there are no visible changes in morphology. From the high magnification image, figure 52 (c), the larger structures appear to be formed from small crystallites of fibrous form.

3.3.3.1.2 3.12 Mol % Strontium

Three morphologically different phases are clearly visible in figure 53 (a) (labelled 1-3). Phase 2 appears brighter than phase 3 while phase 1 resides in boundaries between the two other phase and appears most bright. From figure 53 (b) it can be seen that phase 1 is composed from a phase exhibiting a homologous morphology of equant granular domains or crystals. There is no definable structure visible in phase 3. From figure 53 (c) it can be seen that phase 2 is composed of two different morphologies, small, equant, granular and larger elongated, branching crystals.

3.3.3.1.3 6.24 Mol % Strontium

From figure 54 three clearly define phases are again visible. Phases 1 and 2 appear to form on the surface of the material with phase 1 forming in the bulk. Phase 1 retains the equant granular structure observed in pervious structures but is more exposed than previously. Phase 2 forms long extensions which from figures 54 (b) and c are seen to run either parallel to each other or grow perpendicular from a central spine. Phase 1 is partially visible through phases 1 and 2 while no other surface morphologies are visible. Phase 3 is present in distinct regions on the surface of the material and forms as dendrites that appear to have grown outwards from a central point.

3.3.3.1.4 9.35 Mol % Strontium

Three different morphologies are clearly visible in figure 55 (a). Phase 1 retains the granular morphology observed in previous compositions. Phases 1 and 2 are yet more clearly defined than in previous samples and lie predominantly isolated from each other. Phase 2 presents thin extensions which are not seen to branch but extend from a single point, growing out in a manner comparable to spherulitic crystal growth. Phase 3 forms much broader extensions than phase 2 and appears much more angular. High magnification image 55 (c) shows that phase 2 has small voids between some of the domains. Regions of a similar morphology to phase 1 can be observed within phase 3, however the voids are not visible.

3.3.3.1.5 12.47 Mol % Strontium

In figure 56 the phases are yet more differentiated. Phase 2, while retaining its spherulitic growth, has become broader and has taken on an almost leaf like form with the large crystals having serrated edges. Phase 3 remains more angular than phase 2 with the crystals having flattened ends that finish perpendicular to the long axis of the crystal. A phase of similar morphology to phase 1 is visible within phase 3 at high magnification, figure 56 (c).

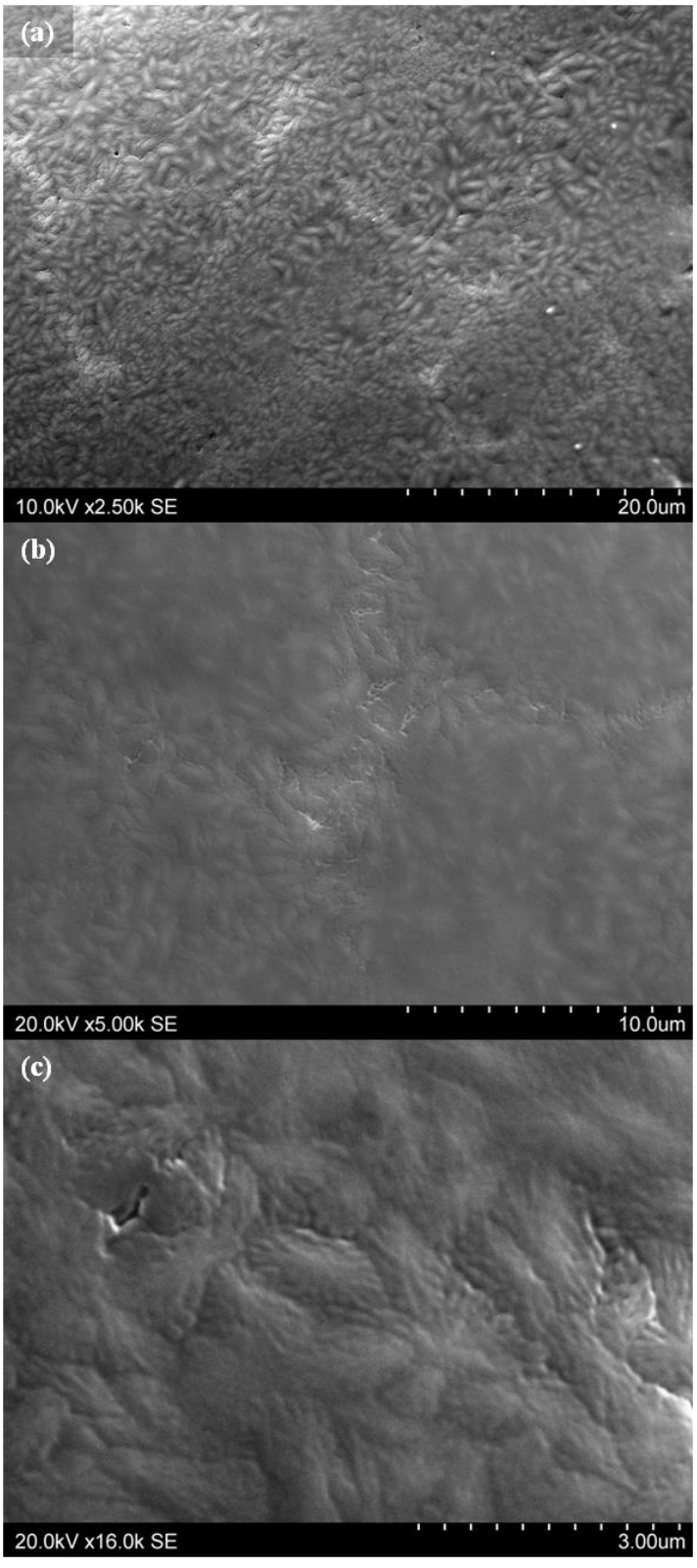

3

Figure 52: SEM SE images at different magnifications of composition 0 Mol % strontium following heat treatment.

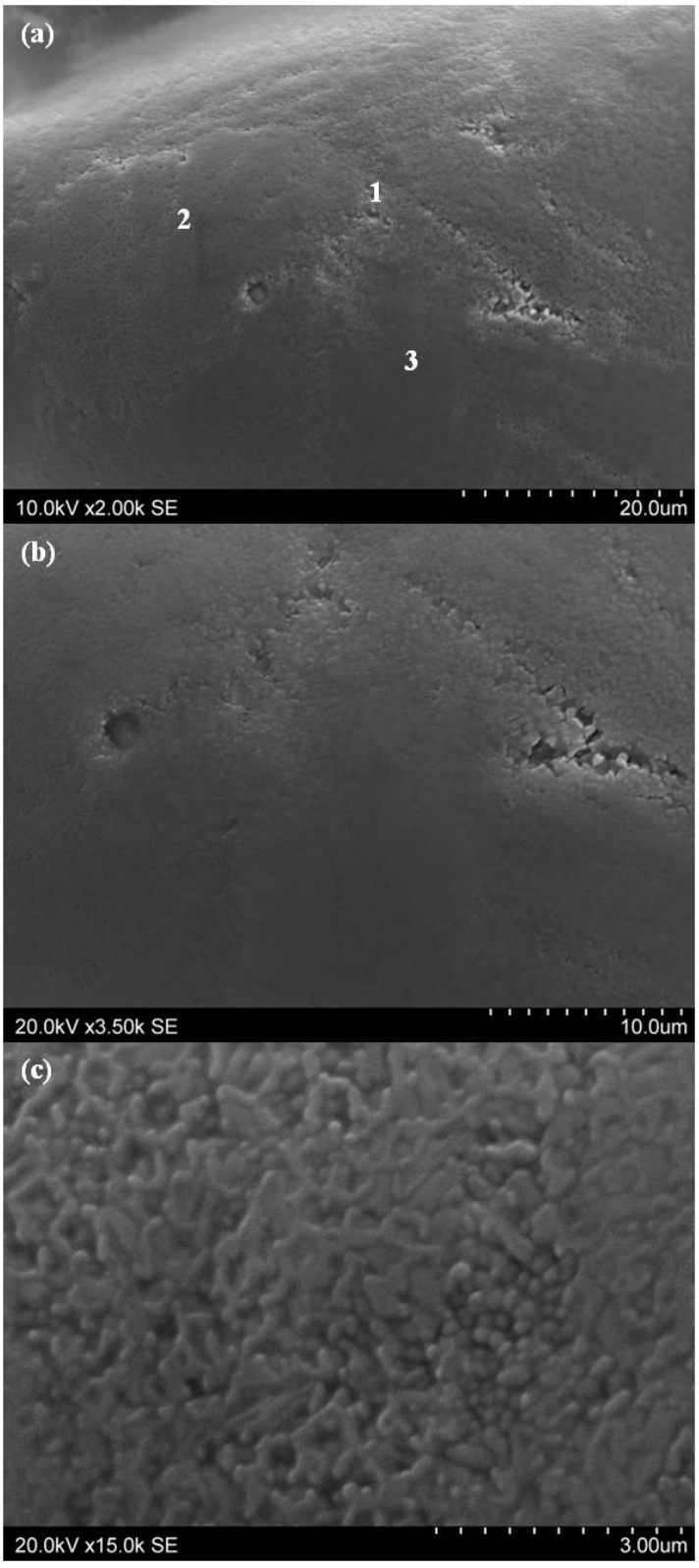

Figure 53: SEM SE images of composition 3.12 Mol % strontium following heat treatment with morphologically different regions labelled 1-3. (b) magnified area encompassing regions 1-3. (c) high magnification of region 2.

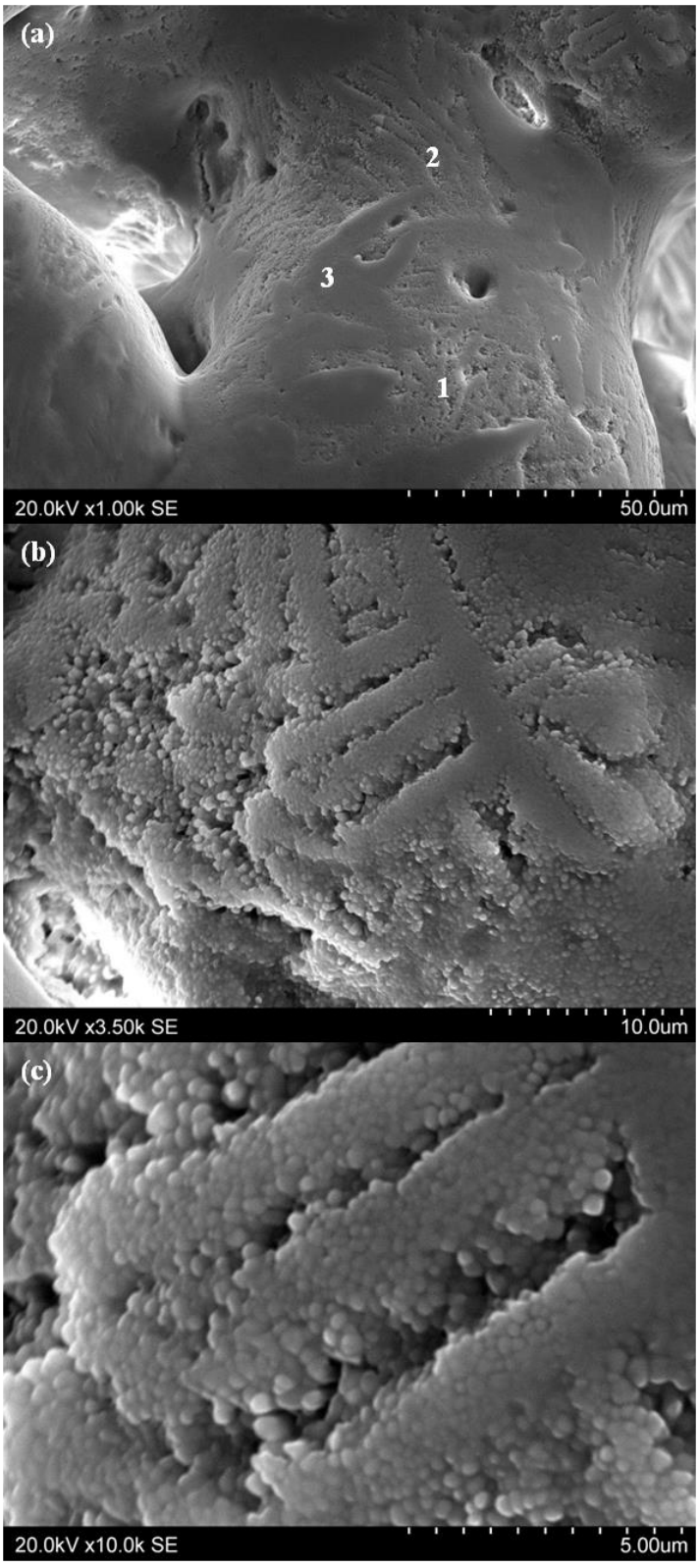

Figure 54: SEM SE images of composition 6.24 Mol % strontium following heat treatment with morphologically different regions labelled 1-3. (b and c) higher magnification images from the top right of (a).

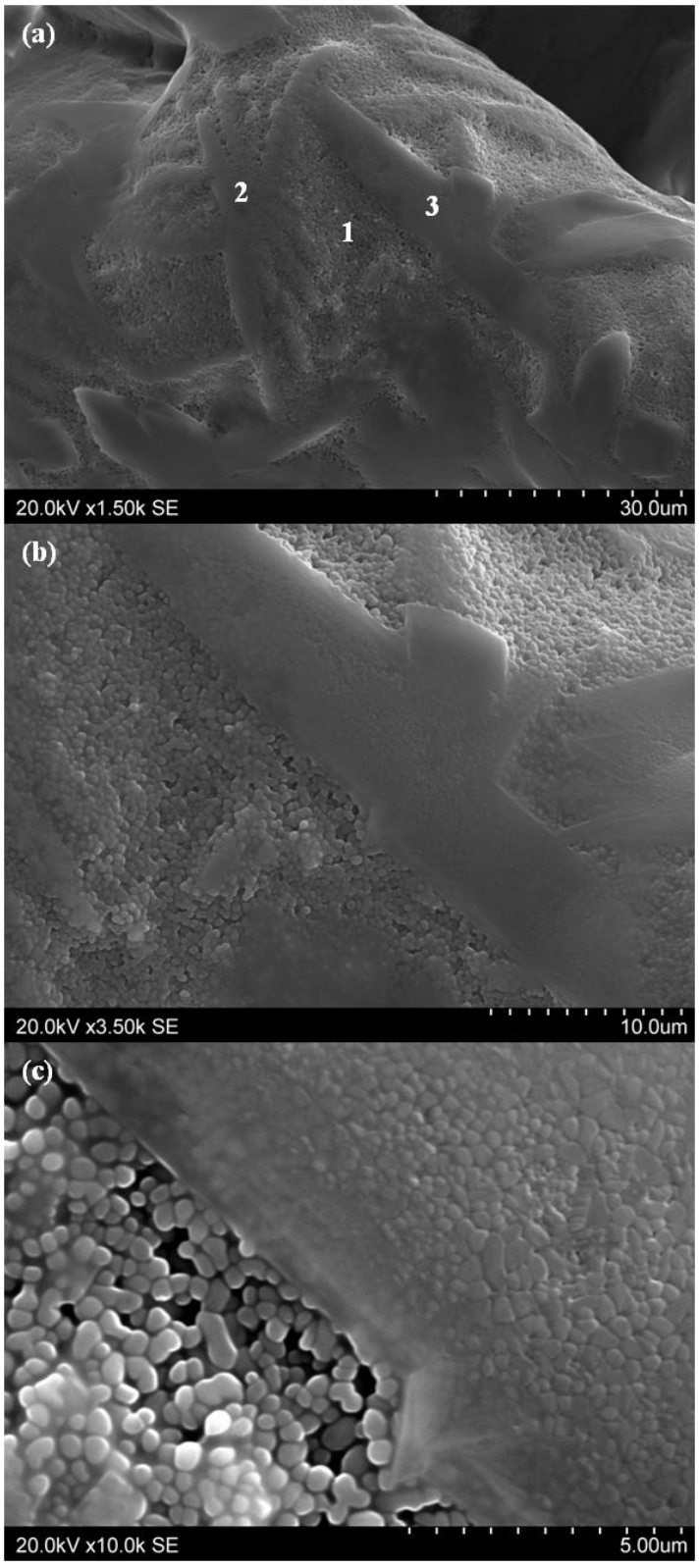

Figure 55: SEM SE images of composition 9.35 Mol % strontium following heat treatment with morphologically different regions labelled 1-3. (b and c) higher magnification images of region 3.

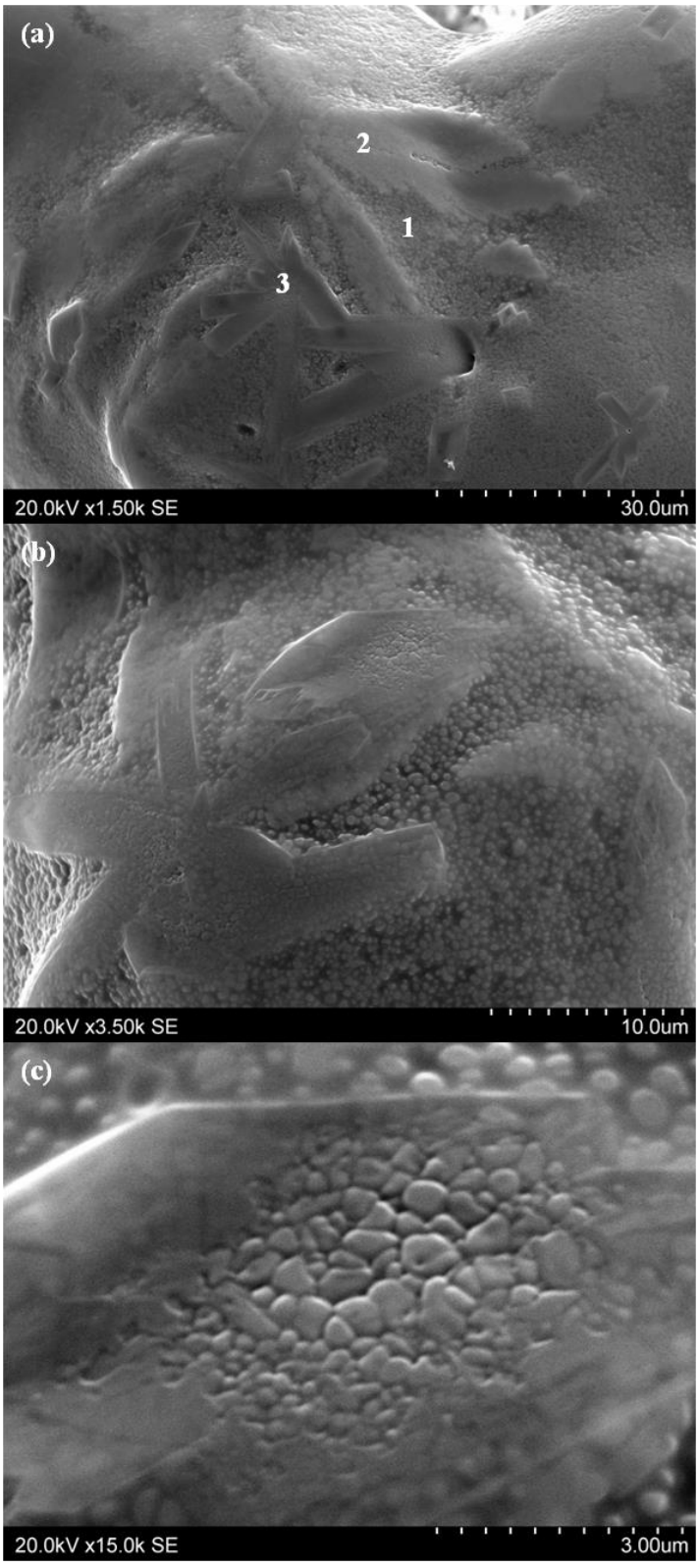

Figure 56: SEM SE images of composition 12.35 Mol % strontium following heat treatment with morphologically different regions labelled 1-3. (b and c) higher magnification examples from a second site on the powder.

3.3.3.2 EDX Maps

EDX map scans of the surface of the glass ceramics were run to determine any inhomogeneous elemental surface distributions, figures 57 to 61.

3.3.3.2.1 0 Mol % Strontium

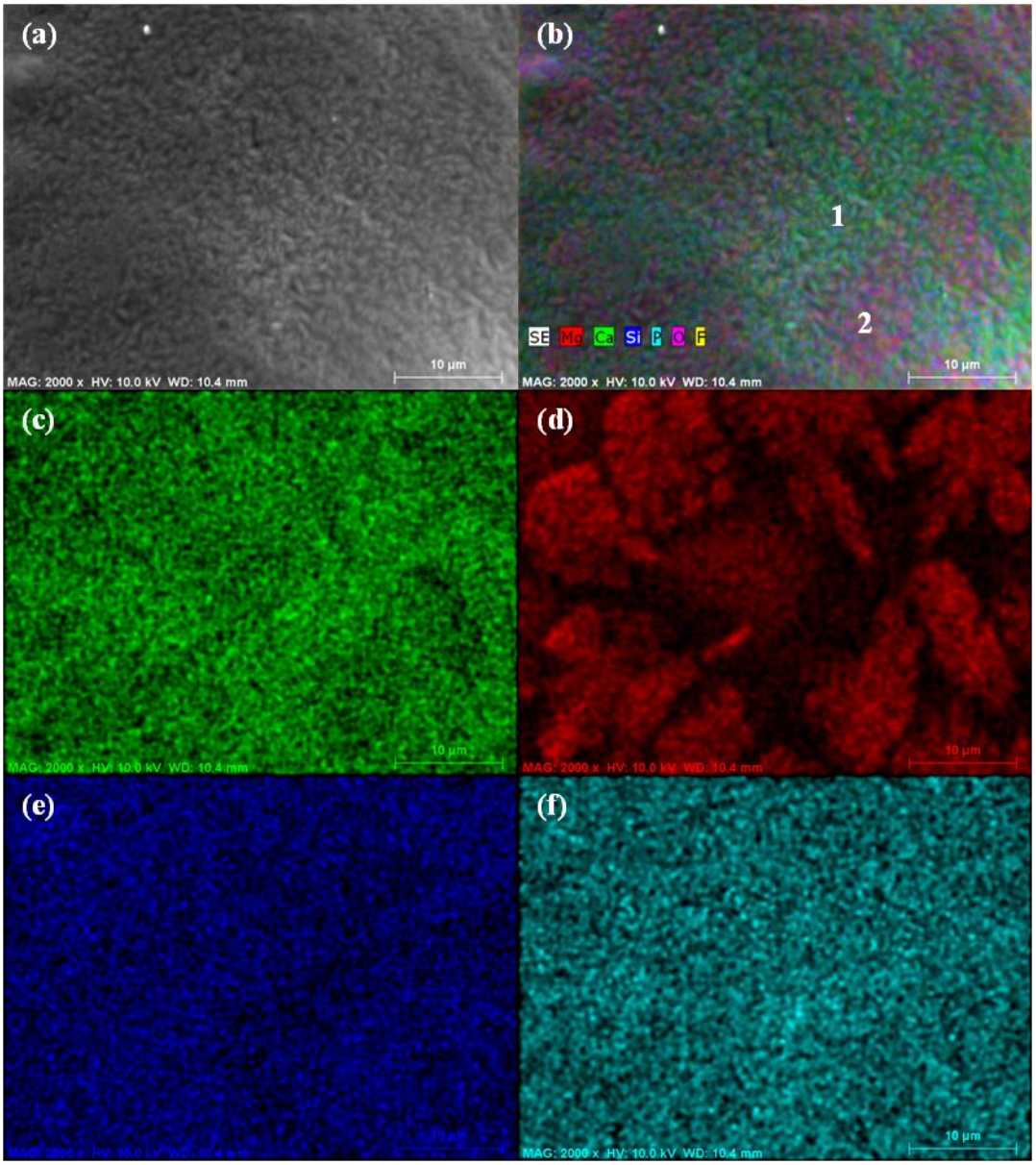

Figure 57: SEM and EDX images of the surface of composition 0 Mol % strontium following devitrification. (a) SE (b) SE + EDX map overlay (c) Ca (d) Mg (e) Si and (f) P.

3.3.3.2.2 3.12 Mol % Strontium

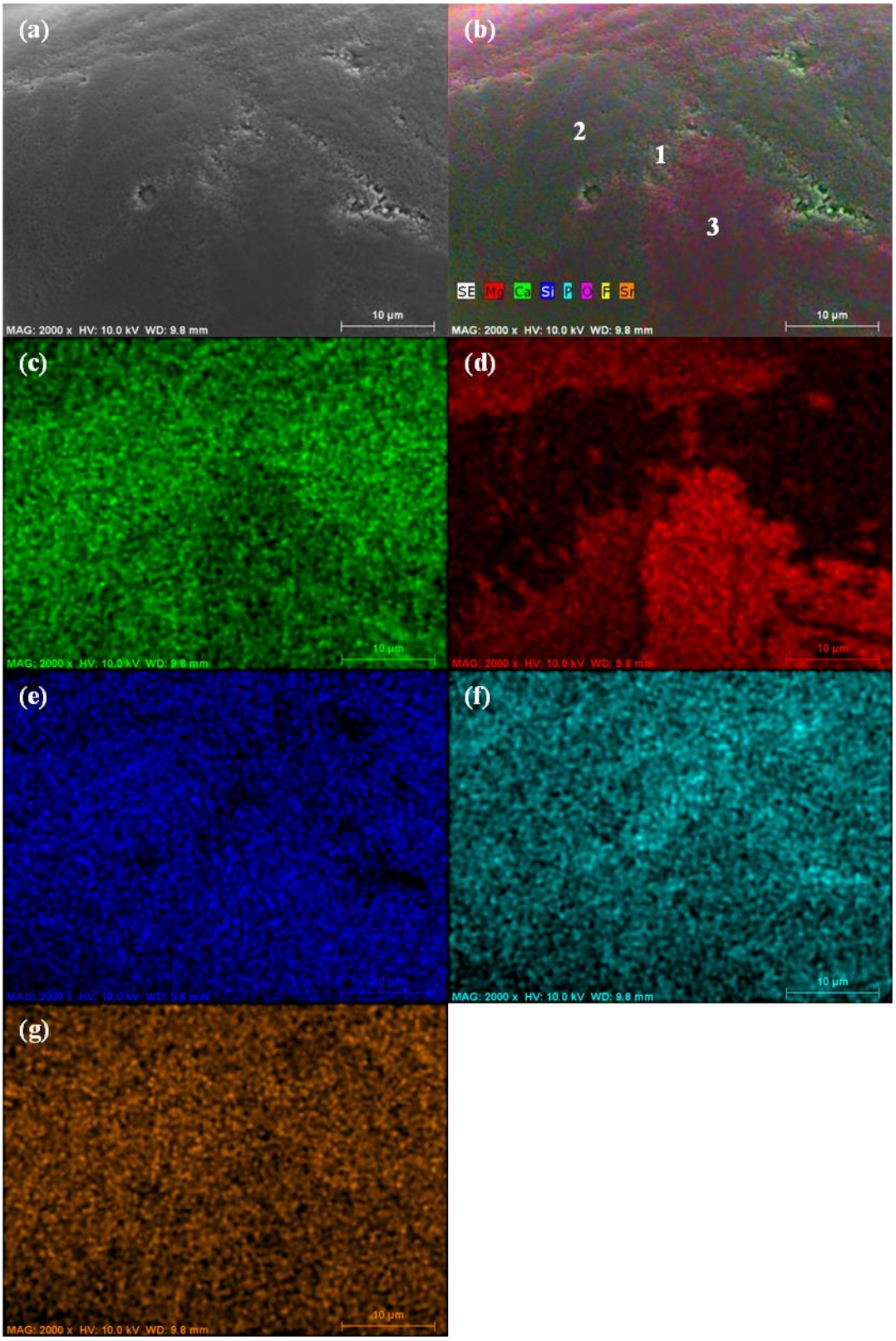

Figure 58: SEM and EDX images of the surface of composition 3.12 Mol % strontium following devitrification. (a) SE (b) SE + EDX map overlay (c) Ca (d) Mg (e) Si (f) P and (g) Sr.

3.3.3.2.3 6.24 Mol % Strontium

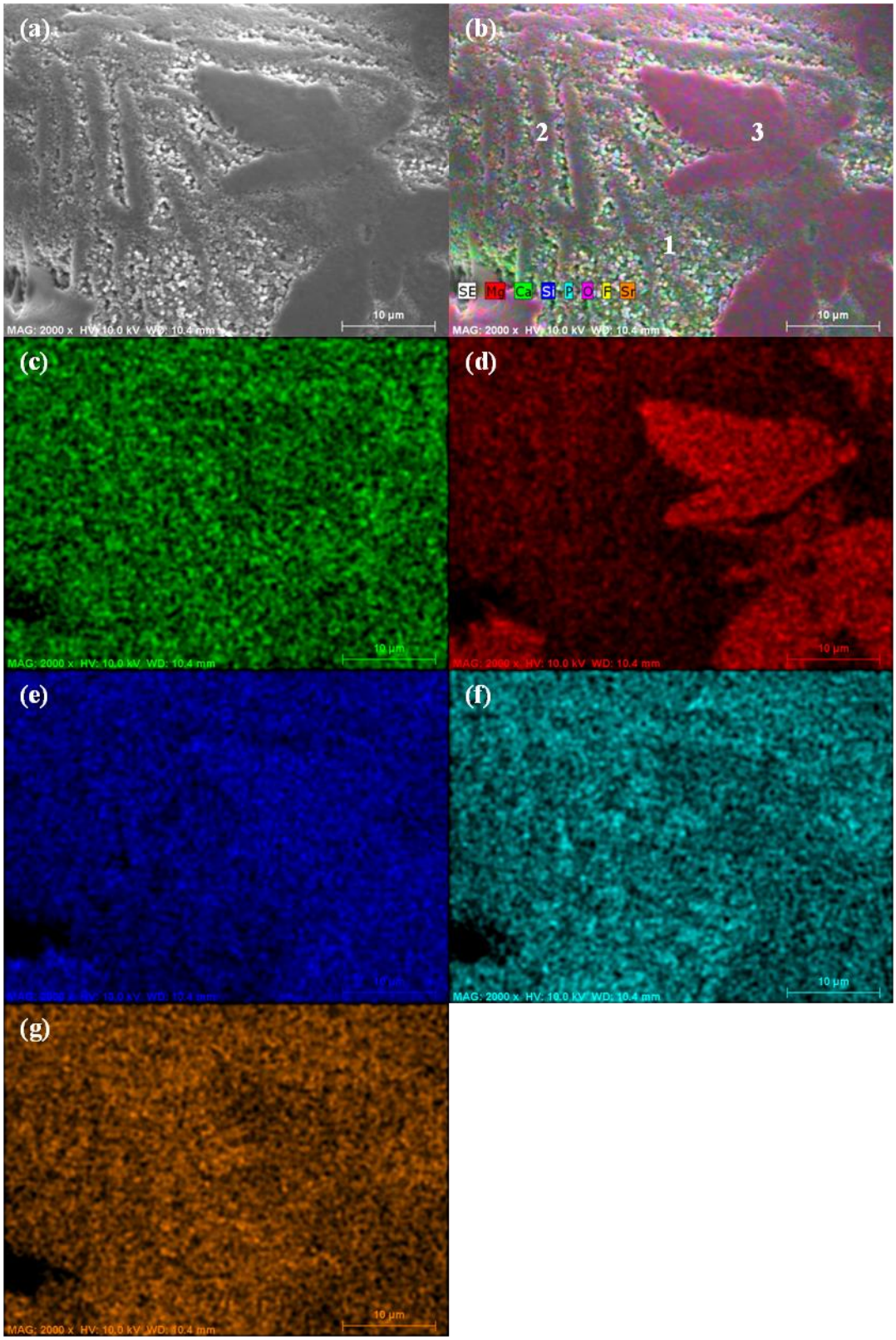

Figure 59: SEM and EDX images of the surface of composition 6.24 Mol % strontium following devitrification. (a) SE (b) SE + EDX map overlay (c) Ca (d) Mg (e) Si (f) P and (g) Sr.

3.3.3.2.4 9.35 Mol % Strontium

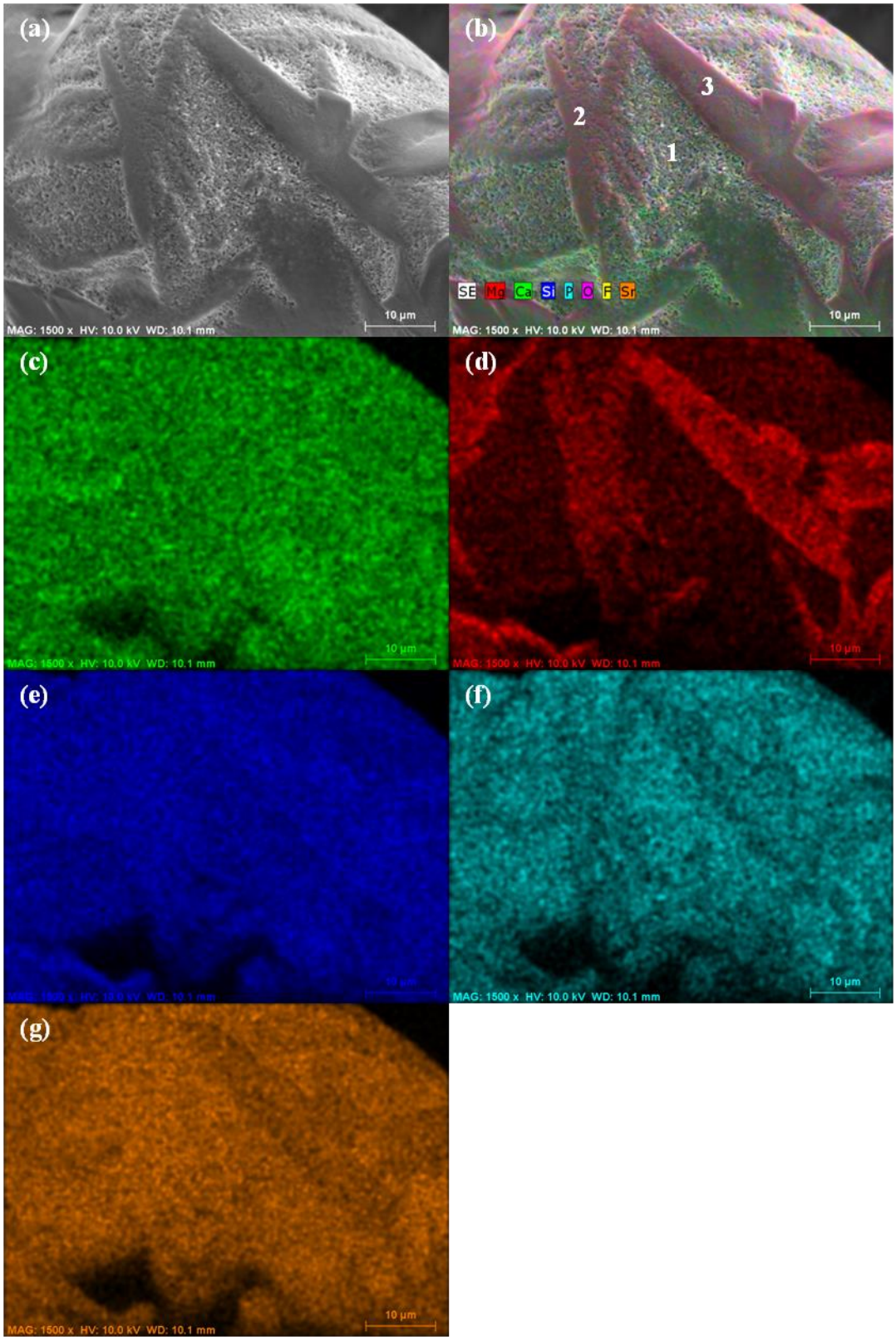

Figure 60: SEM and EDX images of the surface of composition 9.35 Mol % strontium following devitrification. (a) SE (b) SE + EDX map overlay (c) Ca (d) Mg (e) Si (f) P and (g) Sr.

3.3.3.2.5 12.47 Mol % Strontium

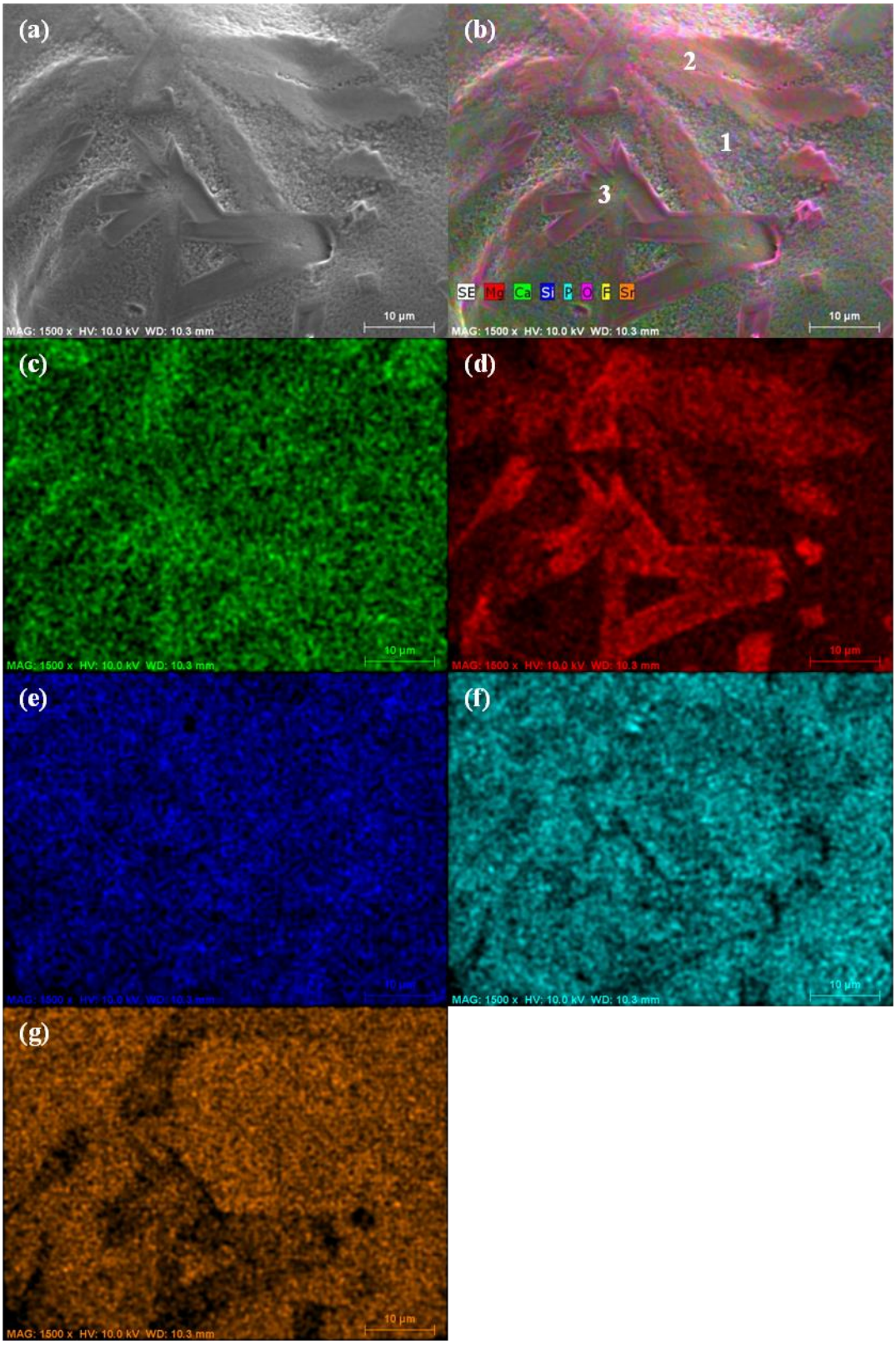

Figure 61: SEM and EDX images of the surface of composition 12.47 Mol % strontium following devitrification. (a) SE (b) SE + EDX map overlay (c) Ca (d) Mg (e) Si (f) P and (g) Sr.

From figure 57 (b) it is clear that there are definable regions of varying composition. The lighter areas of the SE image correspond to regions high in calcium while the darker regions are high in magnesium. The magnesium rich areas are high in silicon but low in phosphorous.

In figure 58 the three phases previously observed can be clearly defined according to their relevant calcium, magnesium, silicon and strontium contents. Phase 2 is high in calcium, silicon and strontium. Phase 3 is high in magnesium and silicon while showing relatively lower levels of strontium and calcium compared to phase 2. Phase 1 is rich in strontium, calcium and phosphorous. This is repeated for compositions 6.24, 9.35 and 12.46 Mol % strontium with the contrast between the phases increasing as the strontium content of the parent glass increases. Strontium is present in higher amounts in phases 1 and 2 than in phase 3. Magnesium is preferentially taken into phase 3 but is present in phase 2 at higher levels than in phase 1.

3.3.3.3 EDX Point Scans

Point scans were then performed on the individual phases. Phase 2 was designated silicate phase A and phase 3 silicate phase B. The location of the point scans are shown in figure 62. The main constituents on the silicate phases are shown in figures 64 and 65.

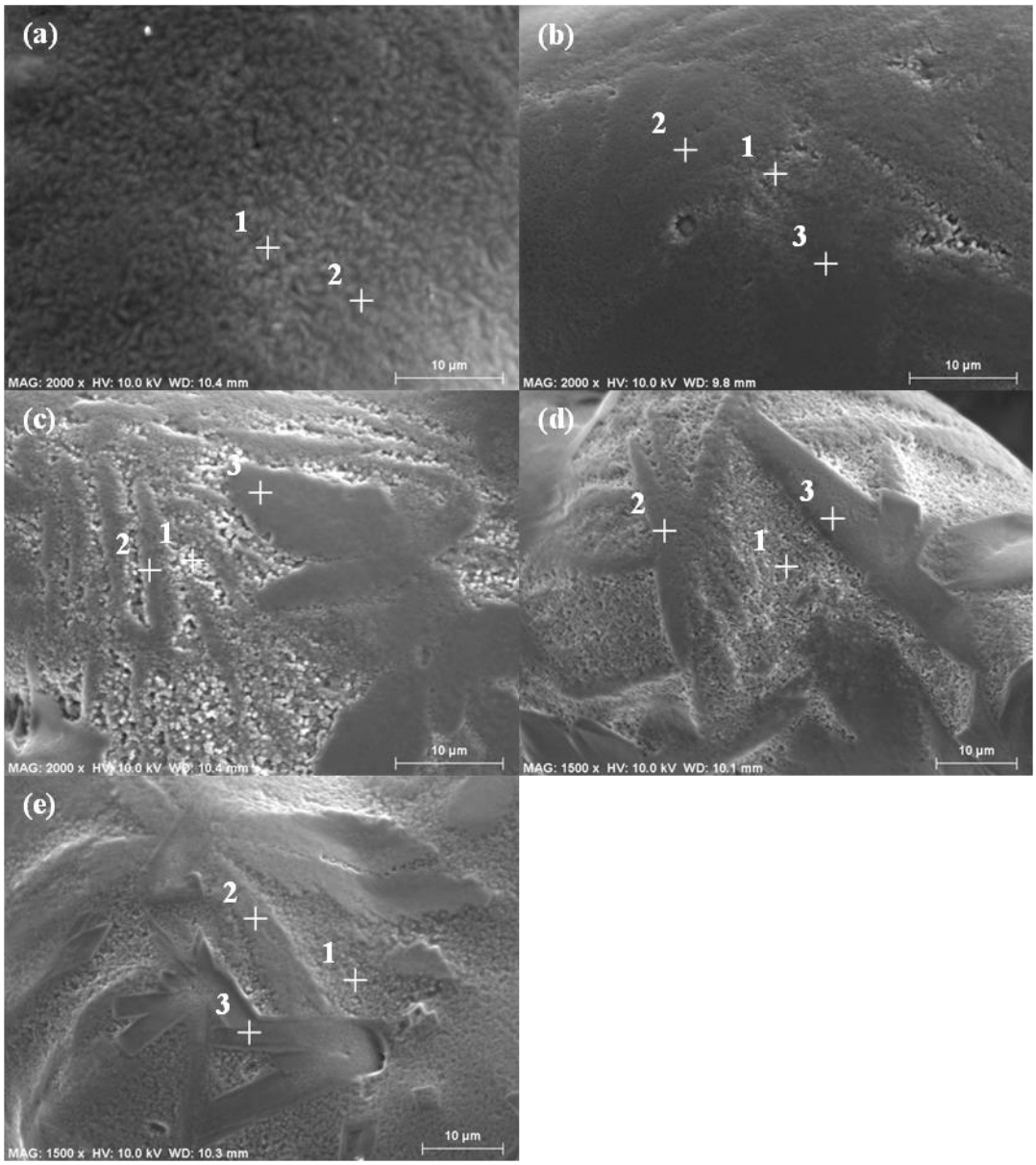

Figure 62: the site of EDX point scans on devitrified compositions (a) 0 Mol % strontium (b) 3.12 Mol % strontium (c) 6.24 Mol % strontium (d) 9.35 Mol % strontium and (e) 12.47 Mol % strontium.

Phase 1 was identified as an apatite due to its low silicon levels and high calcium and phosphate levels. Phases 2 and 3 were identified as silicates due to their relatively high silicon and low phosphorous levels. Phases 2 and 3 are subsequently referred to as silicate phase A and B, respectively.

Table 44: The results of the EDX point scans shown in figure 62.

Comp.	Phase	Composition (Mol %)						
		Ca	Sr	Mg	Si	O	F	P
0 Mol % Strontium	Apatite	17.72	0.00	0.63	9.04	66.10	0.87	5.65
	Silicate	16.37	0.00	1.65	12.16	65.10	0.76	3.97
3.12 Mol % Strontium	Apatite	14.93	2.53	0.53	8.86	66.29	1.05	5.82
	Silicate A	15.97	2.11	0.36	11.52	65.05	0.78	4.22
	Silicate B	13.83	1.62	3.36	12.57	63.60	0.66	4.36
6.24 Mol % Strontium	Apatite	13.15	6.13	0.85	9.17	63.35	0.32	7.03
	Silicate A	15.12	3.20	2.37	11.45	63.58	0.53	3.75
	Silicate B	11.03	2.72	3.55	12.04	66.42	0.52	3.73
9.35 Mol % Strontium	Apatite Phase	10.56	7.45	1.05	10.70	63.16	0.73	6.34
	Silicate A	9.04	7.17	2.66	12.29	64.37	0.26	4.21
	Silicate B	10.50	4.24	4.39	13.43	63.15	0.37	3.93
12.47 Mol % Strontium	Apatite Phase	6.73	8.05	1.79	10.61	66.01	1.02	5.79
	Silicate A	6.88	7.87	3.81	12.95	65.44	0.53	2.52
	Silicate B	8.70	5.48	4.42	13.70	63.62	0.25	3.84

Fluorine levels were below 1.05 Mol % in the apatite phase for all compositions tested. Figure 63 shows the variation in the EDX point scans of the apatite phase. Oxygen was not included as it is not accurately quantified via EDX. A 1.16 Mol % increase in magnesium levels was observed between compositions 0 and 12.47 Mol % strontium. The silicon levels remained constant for compositions 0 to 6.24 Mol % strontium and increased for compositions 9.35 and 12.47 Mol % strontium. Phosphorous levels increased between 0 and 6.24 Mol % strontium and decreased for subsequent compositions. The calcium levels decreased and the strontium levels increased in the apatite phase as the strontium content of the parent glass increased.

For composition 0 Mol % strontium, only one silicate phase (high silicon and low phosphorous) was identifiable. Figures 64 and 65 show the variations in the main elements detected following point scans of the silicate phases. It can be seen that the

silicon in both phases remained relatively constant, increasing by less than 1 Mol % between compositions 0 and 12.47 Mol % strontium. For the strontium containing compositions, two silicate phases were identified, silicate phases A and B. A drop in silicon was observed between compositions 0 and 3.12 Mol % strontium for silicate phase A while an increase was observed in silicate phase B. The phosphorous levels of the silicate phases decreased with increasing strontium substitution into the parent glass. In silicate phase A, the magnesium levels were much lower than silicate phase B. The strontium and calcium levels were higher in silicate phase A than silicate phase B. The calcium levels in both silicate phases A and B decreased and strontium levels increased as the strontium level of the parent glass was increased. In silicate phase A, the strontium levels exceed the calcium levels at composition 12.47 Mol % strontium; this was not the case for silicate phase B. Silicate phase A consistently contained more strontium than magnesium. This was the not case for silicate phase B for compositions 3.12 and 6.24 Mol % strontium but magnesium and strontium levels were the same for composition 9.35 Mol % strontium and strontium levels were higher for composition 12.47 Mol % strontium.

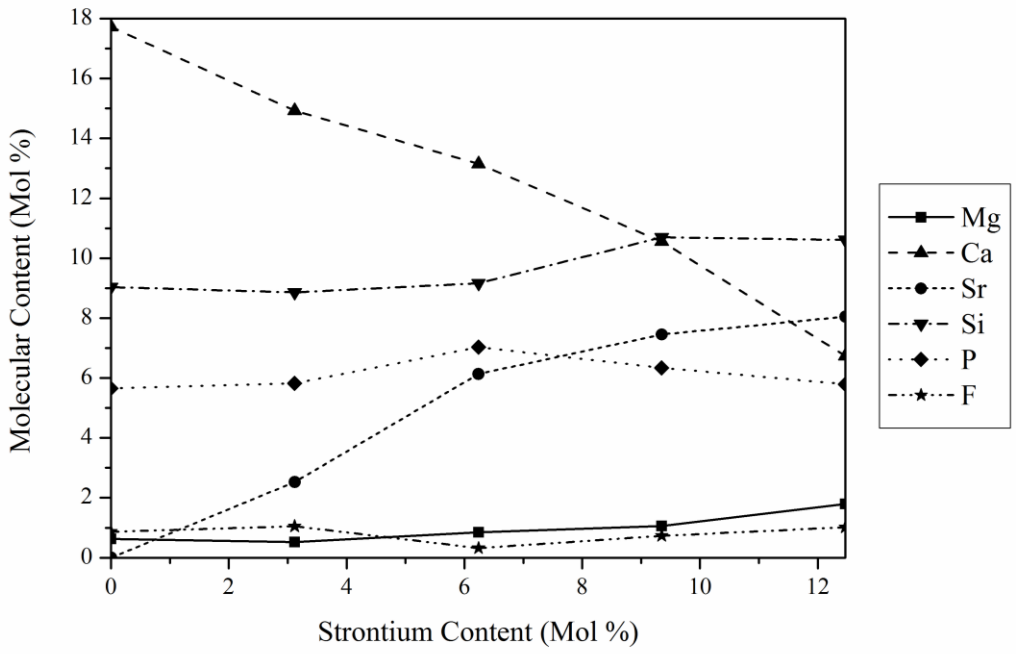

Figure 63: The effect of parent glass strontium content on the composition of the apatite phase measured using EDX.

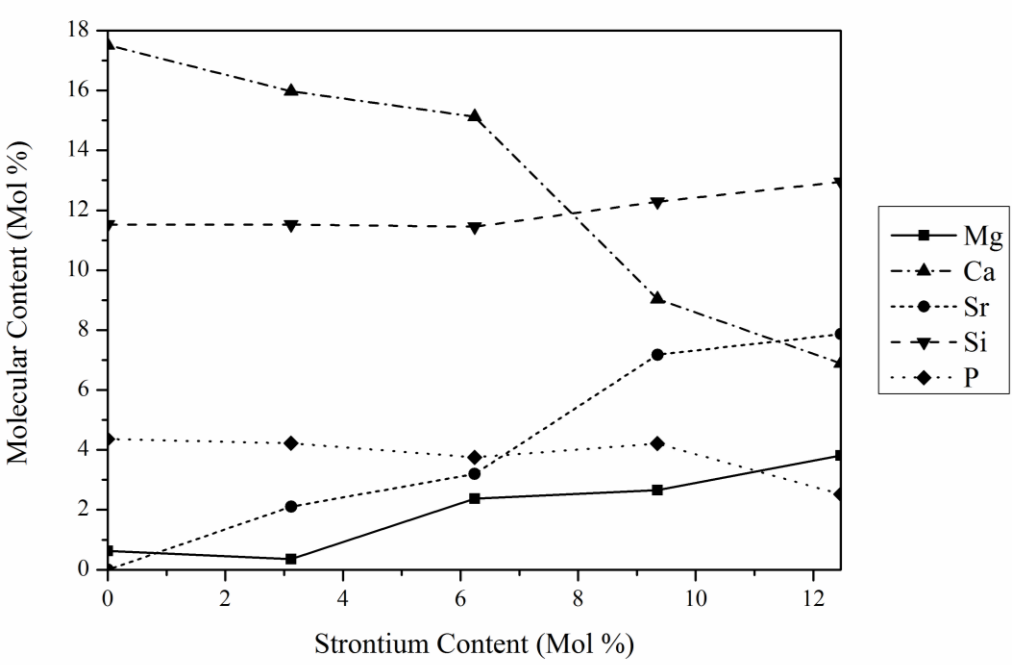

Figure 64: The effect of parent glass strontium content on the composition of silicate phase A measured using EDX.

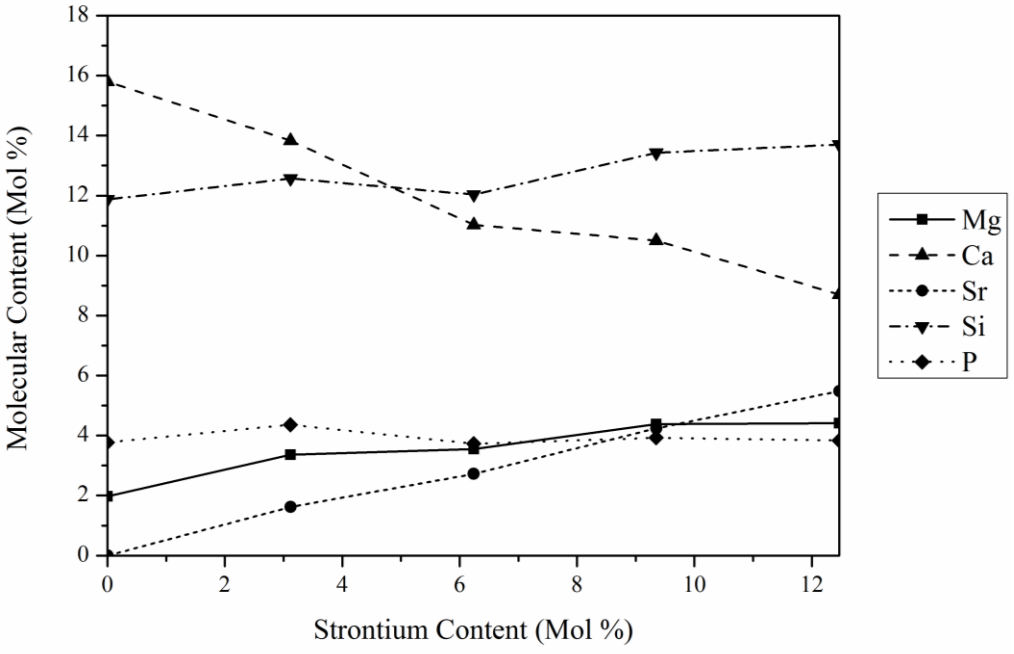

Figure 65: The effect of parent glass strontium content on the composition of silicate phase B measured using EDX.

A comparison of Mg, Ca and Sr content variation for the silicate phases is shown in figure 66. It can be seen that for compositions 3.12 to 12.47 Mol % strontium, strontium levels were consistently higher and magnesium levels lower in silicate phase A than silicate B. Calcium levels were higher for silicate phase A for

compositions 3.12 and 6.24 Mol % strontium but dropped lower than silicate phase B for compositions 9.35 and 12.47 Mol % strontium.

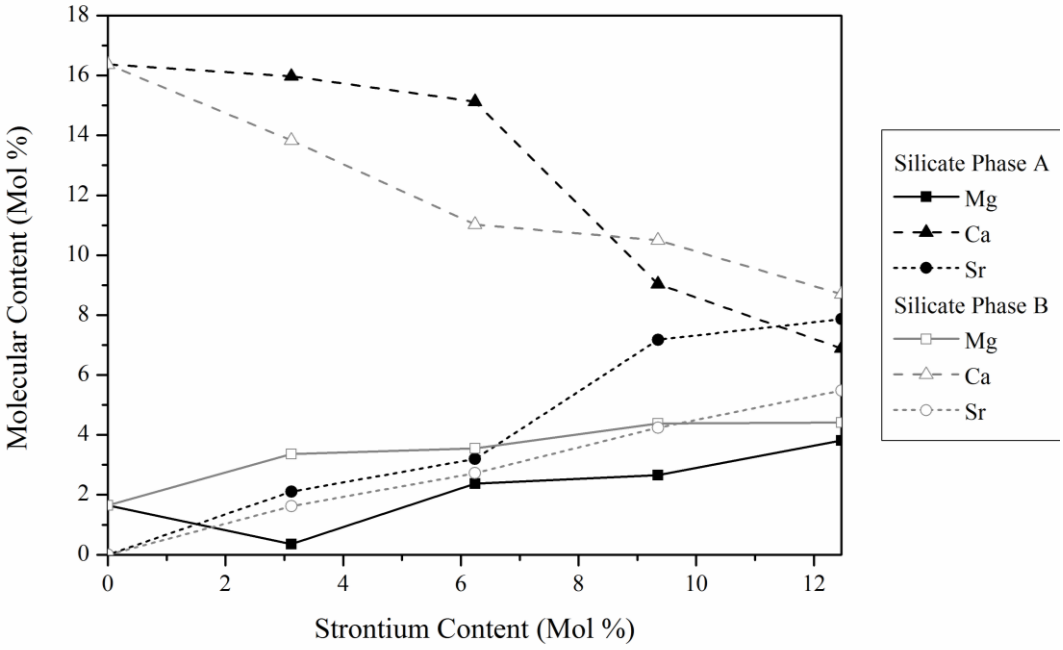

Figure 66: Comparison of the composition of silicate phases A and B at different parent glass strontium contents.

3.4 Discussion

The aim of this chapter was to determine what crystalline phases, if any, could be formed in the glass following a controlled heat treatment. Differential scanning calorimetry (DSC) was used to observe any thermodynamic events that occurred in the glass during heating. To best understand the process of devitrification of the glass, the thermodynamic events will be discussed in the order in which they occur, starting with the lowest temperature and finishing with the highest, before discussing the material as a whole.

The first event observed during heating is the glass transition temperature, T_g. The glass transition is an endothermic event where an amorphous or polymeric material transforms from a brittle material to a molten or rubber-like one. The glass transition recorded at 10K.min^{-1} for the 0 Mol % strontium composition was 750.4°C, this is in agreement with previously reported values for glasses with a similar composition. Kokubo [135] reported a T_g of 750°C for particles of 44µm average diameter when a heating rate of 5K.min^{-1} was used. Goel [86, 109] reported

a T_g within the range of 740-755°C for glasses composed of a higher magnesium to calcium ratio. Cannillo [110] reported a lower T_g of 719.85°C for the same glass composition formed via the melt quench route but with a smaller particle size of <38μm. Likitvanichkul [60] measured T_g of bulk glass rods using dialometric push rods at a heating rate of $3K.min^{-1}$ and recorded a value of 740°C. The addition of strontium into the parent glasses resulted in a reduction in the glass transition temperature. This was observed by Goel [86] in glasses in the same system, but with higher magnesium to calcium ratios, where a reduction in T_g from 745°C to 738°C was observed following a substitution of SrO for CaO up to a maximum of 3:1 Ca:Sr molar ratio. Hill [87] observed a reduction in T_g in a SiO2-Al2O3-P2O5-CaO-CaF2 system glass with additions of strontium. A maximum reduction of 34°C was observed with additions up to a 2:3 Ca:Sr molar ratio but an increase was observed for the 100 Mol % strontium composition. A reduction in T_g with strontium for calcium substitution in BioGlass 45S was also reported by, O'Donnel [69, 136], Salman [70], Fredholm [81] and Fujikura [68] where a reduction of 32°C was observed in T_g up to a 1:1 Ca:Sr molar ration and a further 30°C up to 100 Mol % strontium substitution for calcium. The reason for the reduction in T_g can be explained by looking at the connectivity of the glass network. Ray [137] proposed that glass could be treated as an inorganic polymer of oxygen (bridging-oxygens, BOs) cross-linked with network formers (NFs) with chains modified by cations and hydrogen that can break cross-links (producing non-bridging-oxygens, NBOs) or distort the network via expansion. This introduces the idea of network connectivity, NC, equation 22, which can be used to determine the stability of the network [136].

$$NC = \frac{No.BO - No.NBO}{No.NF}$$

Equation 22

The coordination distribution, Q^n, of $[SiO_4]^{4-}$ tetrahedrons can also be used to describe the polymerised state of the glass. One Q^n species consists of [81, 138]:

- One Si^{4+}
- n/2 BO
- (4-n) NBO

- (4-n) alkali metal ions or (4-n)/2 alkaline earth cations to equilibrate the electronic charge if NBOs are present.

Calcium and strontium ions each produce 2 NBOs, thus substituting Sr for Ca at a molar ratio will not produce a change in the network connectivity of the glass. They also present the same charge and so will not produce a change in the distribution of Q^n species in the glass. This was observed in the systems mentioned previously [68-70, 81, 86, 87, 136] where the effect of strontium on the network connectivity and silica coordination was observed using magic angle spinning nuclear magnetic resonance (MAS-NMR) and Fourier transform infrared (FTIR) spectroscopy. In all samples Sr was found to have no effect on the connectivity or Q^n distribution of the glass network. Equation 22 does not however take into account the distortion of the network due to variations in field strengths and charge-to-size ratios [85]. This was observed in the discussed glasses [68-70, 81, 86, 87, 136] and also in the novel compositions developed here (see chapter: Glass Production). The expansion of the network is a result of strontium ions being larger than calcium and this leads to a greater degree of distortion and a weaker network, due to weaker Sr-O bonds, producing a reduced barrier for transition resulting in a drop in the glass transition temperature [68, 81, 86, 125, 136].

The next thermodynamic event that occurs is an exothermic peak, indicating a crystallisation event. For composition 0 Mol % strontium, 45-90µm particles and a heating rate of $10K.min^{-1}$, the exotherm/crystallisation onset occurred at 856.7°C and peaked at 898.0°C. XRD of samples heated to T_O-15 indicate that the phase forming is an apatite with an activation energy calculated as $508.01kJ.mol^{-1}$. A match was achieved for fluorapatite (ICDD: 04-009-4021). This is in keeping with previous reports of the same system where the first exotherm was attributed the formation of apatite crystals. For particles <45µm in size and a heating rate of $5K.min^{-1}$, Kokubo [135, 139] recorded a peak temperature of 870°C and identified that this peak was attributed to the crystallisation of both fluorapatite and oxyapatite. A heating rate of $1K.min^{-1}$ and hold of 4 hours at 870°C produced a material that was 35% apatite and 65% glass by weight[139], comparable to the 0 Mol % strontium composition, which with a heating rate of $10K.min^{-1}$ and hold at 855°C for 2 hours was composed of 37% apatite and 63% glass. Calver [140] reported the formation of a fluorapatite/oxyapatite solid solution that had a peak at 887°C.

Cannillo [110] reported the formation of an oxyapatite phase with an activation energy of 385±11kJ.mol^{-1} and an onset at 863°C and peak at 886.85°C. Likitvanichkul [60] reported an apatite phase that formed with an activation energy of 514kJ.mol^{-1} and exothermic peak at 880°C. Magallanes-Perdomo [141] reported the formation of a calcium deficient apatite for samples heated to 900°C. The variation between the reported values is likely the result of different analysis methods such as mass of the sample, heating rate, particle size, atmosphere, use of DSC/DTA, quality of calibration and variations in the composition of the parent glass. The DSC used in this report was calibrated with 4 pure high temperature standards to ensure accuracy. A mass of 20±2mg was used for all samples to ensure peak temperatures were accurate. The temperature of the exothermic peak shifts with changing sample mass while onset remains constant [142]. In metals, the onset is a clear, well defined point. However, in these glass ceramics the onset is more gradual due to variations and distortions in bond lengths and as such the peak position is more often given despite its reliance on sample mass.

The position of the peak of the first exotherm reduced with increasing strontium substitution. This was seen following the substitution of strontium into apatite-mullite glass ceramics [87] where a reduction in T_{p1} (fluorapatite) was observed up to a 2:1 Ca:Sr substitution, an increase was seen following the next substitution to 2:3 Ca:Sr. The same behaviour was observed following the substitution of strontium into BioGlass [68, 81, 85]. However, in the case of BioGlass the first exotherm is attributed to the formation of both a sodium calcium silicate and sodium calcium phosphate phase and not an apatite. The addition of strontium had no effect of the formation of the sodium calcium silicate phase but suppressed the formation of the sodium phosphate phase [85]. It is proposed that the reason for the reduction in T_{p1} is due to the distortion and destabilisation of the glass network due to the larger Sr^{2+} ion. As with the glass transition, this results in less resistance to transition and the transformation to a crystalline state can progress more readily. It should be noted that very little change was observed in the activation energy of the formation of the apatite phase. An increase in the temperature of the first exotherm was observed by Goel [86] following the addition of strontium into a high magnesium A-W system. The exotherm corresponded to predominantly diopside ($CaMgSi_2O_6$) and also fluorapatite. Strontium was taken into the fluorapatite phase but not reported in the diopside phase and thus a reduction in the amount of

available calcium with increasing strontium substitution may force the nucleation/growth peak to a higher temperature.

XRD reveals that strontium was taken into the fluorapatite crystal structure of the novel materials tested. This resulted in a change in diffraction file being used between compositions 3.12-6.24 Mol % strontium from fluorapatite (FA) to strontium fluorapatite (SrFA), ICDD: 04-009-4021 to 04-009-1806 respectively. An increase in the intensity of the maximum fluorapatite peak was observed with increasing strontium content of the parent glass, suggesting incorporation of a more electron dense element The uptake of strontium produced a shift in peak position to lower °2θ/larger d-spacing, indicating expansion of the crystal planes. The Rietveld refinement of the crystal phases confirmed the expansion of the unit cell along both the a and c axis, resulting in a linear unit cell volume increase up to 9.35 Mol % strontium and only a small increase up to 12.47 Mol % strontium. It should be noted that successful refinements could be produced for composition 3.12 Mol % strontium using either FA or SrFA diffraction data with each producing the same unit cell volume, indicating accurate unit cell determination. The unit cell volume for the apatite phase formed in the 0 Mol % strontium composition had a unit cell volume of 534.00 nm^3, larger than the reference pattern, which presented a volume of 527.74nm^3, suggesting the crystals formed were not of a stoichiometric composition. Though the reference diffraction pattern had to be changed in order to allow for refinement, the linear change in unit cell volume with increasing strontium suggests the formation of a solid solution of fluorapatite and strontium fluorapatite and not two distinct phases, as predicted by Vegard's law [87]. The maximum unit cell volume measured was 564.39nm^3, if Vegard's law is obeyed and no magnesium or other elements are substituted into the system then the strontium fluorapatite crystals would have a calcium to strontium ratio close to that of the reference, 1.35:3.65 Ca:Sr. Similar observations were made by Hill [87] in apatite-mullite glass ceramics where the addition of strontium produced a solid solution in the fluorapatite phase with all calcium sites being fully replaced with strontium following 100 % substitution of strontium for calcium. The uptake of strontium into the FA phase was also observed in glass ceramics by Goel [86]. Sr incorporation into hydroxyapatite has been reported for crystals produced via a wet chemical route [71, 91] where, again, a shift towards smaller °2θ was observed with increasing strontium substitution. The Sr^{2+} ions have been shown to preferentially

occupy the CaII site in the hexagonal crystal structure. This matches the information in the reference diffraction pattern, see table 45.

Table 45: Position and site occupancy factors of ICDD: 04-009-1806 strontium calcium phosphate fluoride.

No.	Name	Element	Position			Site Occupancy Factor
			X	Y	Z	
1	O1	O	0.4886	0.1528	0.747	1
2	O2	O	0.5356	0.1212	0.23	1
3	F1	F	0	0	0.286	1
4	SR1	Sr	0.33333	0.66666	0	0.3
5	O3	O	0.329	0.257	0.091	1
6	SR2	Sr	0.2388	0.9853	0.2591	0.87
7	O4	O	0.356	0.264	0.434	1
8	CA1	Ca	0.33333	0.66666	0.5049	0.25
9	P1	P	0.4005	0.3708	0.263	1
10	CA2	Ca	0.33333	0.66666	0	0.7
11	CA3	Ca	0.2388	0.9853	0.2591	0.13
12	SR3	Sr	0.33333	0.66666	0.5049	0.75

The width of the first exotherm got smaller with increasing strontium substitution, this resulted in an onset that increases between composition 0-6.24 Mol % strontium before reducing between 6.24-12.47 Mol % strontium [60]. The broad peak for composition 0 Mol % strontium could suggest a surface nucleation process, however, the peak temperature did not vary much with particle size and so a bulk nucleation process is the likely mechanism. This is supported by the results of Kokubo [135] who showed the apatite phase to form via a bulk nucleation process. Hill observed that strontium substitution for calcium shifted apatite nucleation in apatite-mullite glass/glass-ceramics from a bulk to a surface nucleated process. No large change in nucleation was observed in the apatite peak temperature with changing particle size for any of the novel strontium containing glasses tested in this report.

A second exotherm is visible at temperatures above 940°C. Heating of the 0 Mol % strontium composition to T_{P1}+10 and T_{P2}+10 reveals that this peak was attributed to the crystallisation of wollastonite-2M, ICDD:04-009-5600, with an onset at 947.9°C and a peak of 963.8°C. The formation of monoclinic wollastonite-2M (Wol-2M) has been reported previously for the temperature range 900-1200°C [60, 88, 110,

111, 135, 140, 141]. The weight percentage of wollastonite increases between T_{P1}+10 and T_{P2}+10. The hold at T_{P1}+10 results in the formation of wollastonite at the expense of the apatite phase, with the glass weight percentage remaining the same as a hold at T_{O1}-15. Whereas a hold at T_{P2}+10 results in an increase in the overall crystallinity of the material and an increase in the wollastonite to fluorapatite ratio indicating that higher temperatures favours wollastonite formation. T_{P2} exotherms corresponding to wollastonite were reported as 912°C and 1008°C for <90µm powders and frits respectively, by Likitvanichkul [60], with an activation energy of 374±34kJ.mol^{-1} for the frits and 346±30kJ.mol^{-1} for the fine particles. This was below the activation energy reported for the first exotherm (514±57kJ.mol^{-1}), in keeping with the results for composition 0 Mol % strontium. Both Calver [140] and Cannillo [110] reported T_{P2}s of 927°C for fine particle powders with Calver [140] reporting an increase to 1025°C for frits. Cannillo reported an activation energy of 550±16kJ.mol^{-1}, higher than the activation energy for the apatite phase. The temperature of T_{P2} recorded for 0 Mol % strontium, 45-90µm size fraction was within the temperature ranges reported in the literature for fine particles and frits.

XRD showed expansion of the wollastonite structure following strontium substitution into the parent glass. A linear increase was observed in the unit cell volume, suggesting a solid solution forming. The unit cell volume ranged from 758.87 to 793.75 Å^3, smaller than or equal in size to the unit cell volume of the reference material, 794Å^3. This suggests that a smaller element may be substituted into the crystal structure, most likely magnesium, this will be examined further when the bulk material is discussed. The expansion of the network with increasing strontium suggests that a larger element is being taken into the structure. A residual peak around 45°2θ becomes more apparent with increasing strontium substitution. In the 12.47 Mol % strontium sample this was matched to pseudowollastonite, ICDD: 04-012-1776, a high temperature polymorph of wollastonite. Labelling of this form of wollastonite varies in the literature [71, 73, 143-145] but for the purpose of this work pseudowollastonite will refer to the form that produces powder diffraction peaks around 45°2θ and not around 30°2θ (as in the case of wollastonite-2M) and has been shown by Yang [146] to be a monoclinic crystal with C2/c symmetry. This behaviour has been observed in wollastonite crystals formed by a wet chemical and sol-gel routes [71, 73, 145]. Carrodegaus [145] showed that the

transformation from wollastonite-2M to pseudowollastonite occurred at temperatures above 1125°C and that the transformation was permanent in that the pseudowollastonite form was retained following cooling. Wu showed that the transformation temperature was reduced following the substitution of strontium for calcium. Wollastonite samples that did not contain strontium and were sintered at 1100°C were found to contain wollastonite-2M only, samples that contained 5% strontium or greater produced pseudowollastonite only and intermediary compositions produced a mixture of the two phases. A residual phase of strontium calcium magnesium silicate (SCMS) was found in the sample having fit pseudowollastonite to the XRD trace for 12.47 Mol % strontium. This phase was not found in samples that were fit with Wol-2M, however this does not mean that it wasn't present. Wol-2M may have been fit to the SCMS peaks and obscured any residuals. This may suggest that a solid solution is not forming in the material and in fact up to 3 distinct calcium silicates are forming in the material: wollastonite-2M, pseudowollastonite and the strontium calcium magnesium silicate.

A large increase in the temperature of T_{P2} was observed with strontium substitution. The increase was linear between 0-6.24 Mol % strontium and the rate of increase reduced between 6.32-12.47 Mol % strontium. The delay in onset is observed in the XRD results of samples heated to T_{P1}+10 where wollastonite-2M was detected in samples 0-6.24 Mol % strontium but not in samples 9.35 and 12.47 Mol % strontium. The activation energy reduces rapidly between 0-3.12 Mol % strontium and stabilises between 6.24-12.47 Mol % strontium. The change in activation energy suggests that the composition of the phases formed may be approaching a metasilicate eutectic point. The reduction in activation seems to contradict the increase in peak temperature with increasing strontium substitution. However, T_{P2} is an indication of the maximum rate of transformation and so will not always match trends in the activation energy due to the influence of other factors. An example being that the two phases do not form independently and so the formation of an initial phase will strongly influence the formation of subsequent phases. The increase in peak temperature may be due to the reduction in the onset temperature of the apatite phase. The increased crystallisation of the apatite phase will remove divalent cations from the residual glass. The glass will then be depleted with respects to Ca^{2+}/Sr^{2+}, providing a reduced reservoir from which to form the calcium silicate phase. This is supported by the observed change in peak shape: T_{P2} becomes

less intense and wider with increasing strontium substitution, indicating a loss of nuclei [147]. The loss of Ca^{2+}/Sr^{2+} from the glass network will also increase the viscosity of the amorphous phase further inhibiting subsequent transformations [148, 149].

For all compositions tested, the position of T_{P2} shifted to higher temperatures following an increase in particle size indicating a surface nucleation process. The exotherm also gets wider and not as intense/high as the particle size increases, indicating a loss of nuclei, again supporting a surface dominated nucleation process. Wollastonite is known to surface nucleate in apatite-wollastonite glass ceramics [60, 135, 139, 140, 150], an issue that has prevented the use of cast devices and limited its use to sintered powders. The addition of strontium reduces the shift observed between different particle sizes, but in all samples an increase of at least 29.3°C between <45µm and 1-2mm fractions indicates that T_{P2} was still surface nucleation dominated. The reduction in dependence on particle size may be due to an overall reduction in the number of nuclei, as observed by the change in peak profile, minimising the effect of surface nucleation site availability, which may have previously been a limiting factor.

Having examined the thermodynamic events individually it makes sense to consider them as a whole. Composition 0 Mol % strontium presents few surface details visible via SEM. High magnification images reveal small domains of interlocked crystals similar to that observed by Kokubo [135]. Magallanes-Perdomo observed more distinct domains, though these had been etched, which were composed of interlocked apatite and wollastonite crystals. The weight ratio of apaite:wollastonite:residual glass for composition 0 Mol % strontium heated at 10K.min-1 to 1050°C and held for 2 hours was 32.9:26.7:40.4. Kokubo [139] reported a ratio a 35:40:25 for samples held at 1050°C for 4 hours. The increase in crystallinity may be a result of the extended hold, while the ratio of crystal phases remains comparable to the values reported here. Magallanes-Perdomo [88] reported a ratio of 44.8:28.0:27.2, the increase in apatite phase compared to composition 0 Mol % strontium may be due to an extended 2 hour hold at 820°C (which would favour apatite nucleation) before the final 1 hour hold at 1100°C.

XRD revealed an increase in the ratio of apatite to silicate with increasing strontium substitution into the parent glass. It should be noted however that the refinement did

not take into account the variation in peak intensity that would occur with strontium substitution which would influence the quantifications. This is clearly visible for composition 3.12 Mol % strontium which was modelled using both fluorapatite and strontium fluorapatite references. The fluorapatite reference will have overestimated the apatite content where-as the strontium containing reference will have underestimated it. This also true for the silicate phase where the uptake of strontium in the crystal will cause its weight ratio to be over-estimated.

The addition of strontium resulted in the formation of more clearly defined surface structures. In composition 3.12 Mol % strontium a phosphorous rich and silicon depleted phase is visible, attributed to the strontium fluorapatite phase. Two silica rich phase are visible. One phase, depleted in magnesium, presents a structure similar to that observed by Magallanes-Perdomo, which was attributed, via transmission electron microscopy, to apatite and wollastonite crystals within a glass matrix. The second silicate phase is higher in magnesium and showed no visible surface features. The addition of strontium further separated out these phases with their boundaries becoming more and more distinct. The area of exposed apatite rich phase increases with increasing strontium substitution into the parent glass. This complements the XRD data which shows an increase in the ratio of apatite to silicate. The silicate phase has been shown to be predominately surface nucleating and so a reduction in its overall weight contribution is likely to result a loss the phase from the material surface, as observed. Silica is detected in the apatite phase, supporting Magallanes-Perdomo's [88, 89, 141] observation of distinct domains containing apatite, wollastonite and residual glass. The domains in the compositions tested do however look like the crystals that were formed by Kokubo in apatite glass ceramics containing no wollastonite [135]. Zhang [91] reported hydroxypatite crystals that grew in size with strontium substitution and their morphology and shape matches the crystals visible in compositions 6.32-12.47 Mol % strontium. The strontium content of the apatite rich phase increased with substitution, complementing the XRD results, while an increase in magnesium levels was also detected, suggesting magnesium may be taken into the structure to relieve stresses induced by the expansion on the unit cell by the larger strontium ions. From EDX of the two isolated silicate phases it is clear strontium is taken into both of their crystal structures. Phase A is definable from phase B by its lower magnesium content and more spherulitic morphology compared to phase 2's more rod like

shape. Phase A had an increased capacity to substitute strontium for calcium, a transformation which was accompanied by the uptake of magnesium, possibly to relax the induced lattice stresses. Phase B already contained a higher ratio of magnesium and this may have limited its ability to take on strontium. The increase in the presence of silicate phase B with increasing strontium coincides with an increase in the intensity of peaks attributed to pseudowollastonite. The crystals display the morphology and size of the pseudowollastonite crystals reported by Carrodeguas [145]. The range of silicate phase compositions is supported by the XRD results. Although for compositions 0-9.35 Mol % strontium only a single phase was matched to the silicate phase, a larger value of U was determined. U represents the peak broadening due to stress caused by compositional inhomogeneities. A value of <0.2 is usually expected but in the results reported here U exceeds 1.5. This can be explained by taking the compositional range of the silicate phase from the EDX data and using data from the ICDD database to calculate a theoretical value for U that would be produced by the measured compositional inhomogeneity. The powder diffraction files of quality Star or Index were found for monoclinic forms of $CaSiO_3$, $SrSiO_3$, $MgSiO_3$ and $MgCaSi_2O_6$ and the unit cell volume and number of elemental units were taken from the data, table 46. The average divalent cation radius was calculated utilising the ionic radii reported by Shannon [83] with all three cations having a coordination number of 6 [111]. The primitive volume was calculated (volume divided by number of units, Z) and plotted against the calculated average ionic radii and a linear regression fitted, figure 67.

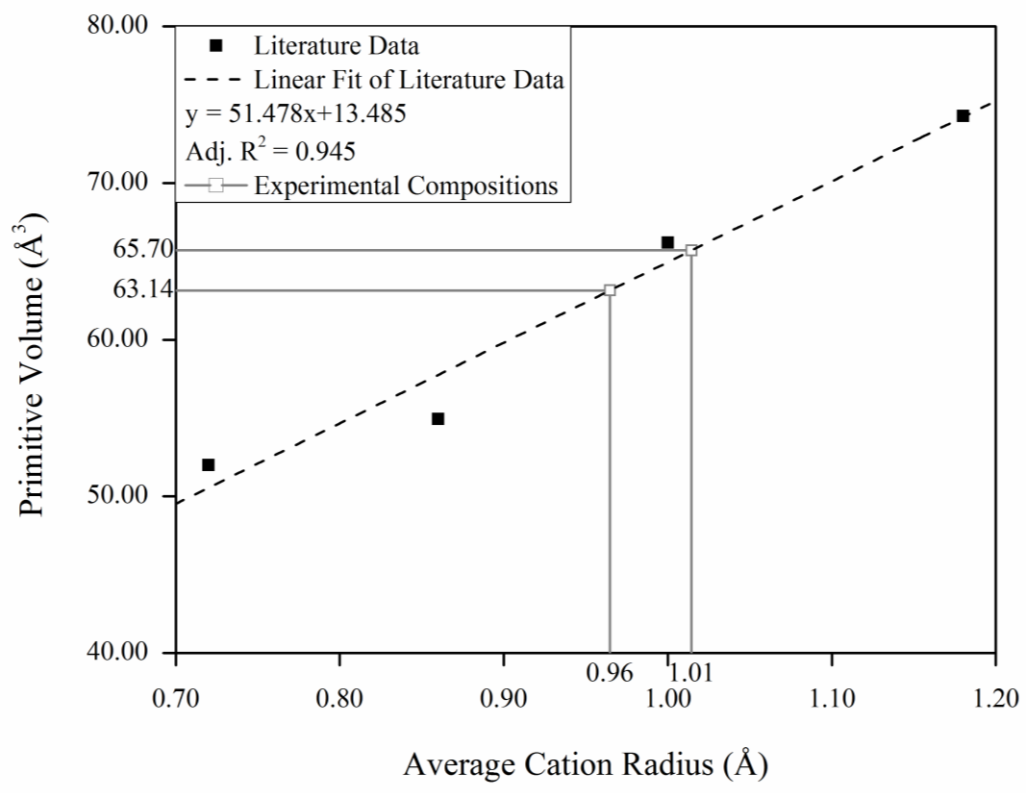

Figure 67: Calculation of the theoretical primitive volumes.

The EDX data of the silicate phases was then used to determine the range of compositions of $(xMg.yCa.zSr)SiO_3$,where x+y+z=1, that were present in the samples in the form of silicate phases A and B. Unit volumes were then calculated for the theoretical compositions using the average radii vs. unit volume fit and finally unit cell dimensions were determined (the cube root of the volume). These values were taken as the minimum (a_{min}) and maximum (a_{max}) values. The strain, ε, was then calculated using equation 23. The maximum reported strain was measured in composition 3.12 Mol % strontium and so will be examined here. The average strain was calculated as 0.662%, see table 47. A modified version of the Scherrer equation that assumes no broadening due to size can be used to determine the strain broadening parameter, U_{THEO}, utilising the instrumental strain broadening, U_{STD}, measured from a silicon standard, equation 24. A theoretical value of 3.190 was determined, the maximum value of U observed experimentally, U_{Obs}, was 3.199, this relatively high value is thus justified due to the large strains induced by the formation of phases with varying composition, as observed with EDX, see table 47 for a summary of the values used. A variation in the composition of the evolved phases can be explained by considering the environment in which they form. As crystals form in the glass they remove elements from it. This leaves regions of glass

depleted in these elements causing subsequent crystals to form with varying compositions and even form new phases.

$$y = \frac{a_{max} - a_{min}}{2}$$

$$x = \frac{a + a_{min}}{2}$$

$$\varepsilon = \left(\frac{y}{x}\right) * 100$$

Equation 23

$$\varepsilon = \frac{\sqrt{(U_{THEO} - U_{STD})}}{\left(\left(\frac{1}{100}\right)\left(\frac{180}{\pi}\right)4\left(\sqrt{(2\,ln\,2)}\right)\right)}$$

$$U_{THEO} = \left(\varepsilon\left(\frac{1}{100}\right)\left(\frac{180}{\pi}\right)4\left(\sqrt{(2\,ln\,2)}\right)\right)^2 + U_{STD}$$

Equation 24

Table 46: Calculation of the average ionic radius and primitive volumes of monoclinic cationic silicates from the literature.

ICDD Ref.	Grade	Comp.	Cation Ratio			Cell Volume ($Å^3$)	Z	Average Cation Ionic Radii (Å)	Primitive Volume ($Å^3$)
			Mg	Ca	Sr				
04-009-5600	S	$CaSiO_3$	0	1	0	794.34	12	1.00	66.20
00-034-0099	I	$SrSiO_3$	0	0	1	891.35	12	1.18	74.28
00-035-0610	S	$MgSiO_3$	1	0	0	415.9	8	0.72	51.99
00-019-0239	I	$MgCaSi_2O_3$	1	1	0	439.55	8	0.86	54.94

Table 47: The calculation of the strain and strain broadening factor for composition 3.12 Mol % strontium.

Phase	Element			Average Cation Ionic Radii (Å)	Primitive Volume ($Å^3$)	Estimated a (Å)
	Mg	Ca	Sr			
Silicate Phase A	0.4	16	2.1	1.01	65.70	4.035 (a_{max})
Silicate Phase B	3.4	13.8	1.6	0.96	63.14	3.982 (a_{min})

	y (Å)	x (Å)	ε (%)	U_{Std}	U_{Theo}	Max U_{Obs}
Results	0.027	4.009	0.662	0.009	3.190	3.199

Chapter 4: Scaffold Formation

4.1 Introduction

The previous chapters described the synthesis and devitrification of novel parent glasses and glass-ceramics, this chapter looks at the application of the material to form porous bone replacement scaffolds for tissue engineering. Bone replacements need to be porous to best mimic native bone and allow cellular in-growth but must also maintain a mechanical strength that is matched to their application. This section of work focuses on assessing the formability of the novel powders.

Porosity was achieved by the sintering of loose powders, with sintering being terminated prior to complete densification and the resulting loss of porosity. Porous bars were formed from the powders using graphite moulds. The level of sintering that occurred in the bars was assessed visually using SEM imaging of the surface of the bars and also their cross-sections. A bone replacement material must not only be biologically attractive but must also be mechanically strong, a property affected by both the macro-structure of the material and its compositional makeup. With this in mind, the degree of sintering and mechanical strength of the bars was assessed via a three-point bend test with the fracture surfaces examined via SEM and EDX.

4.2 Experimental Methodology

4.2.1 Sintering of Porous Bars

To form uniform structures, the 45-90μm glass particle fractions were transferred to carbon moulds and heat treated. The mould dimensions are shown in figure 68. Moulds were milled from rods of grade EE250 graphite (Tokai carbon). The moulds also included a 3mm thick lid machined from the same material. Both the mould and lid were cleaned prior to use with both a cloth and compressed air. To ensure repeatability, the moulds were filled using a layer by layer method with glass being swept across the surface and into the moulds until they were full. Lids were then placed on the moulds and the samples heat treated in a Elite BCF 13/12-2416 furnace with a heating rate of $10K.min^{-1}$ and a 2 hour hold at 1050°C.

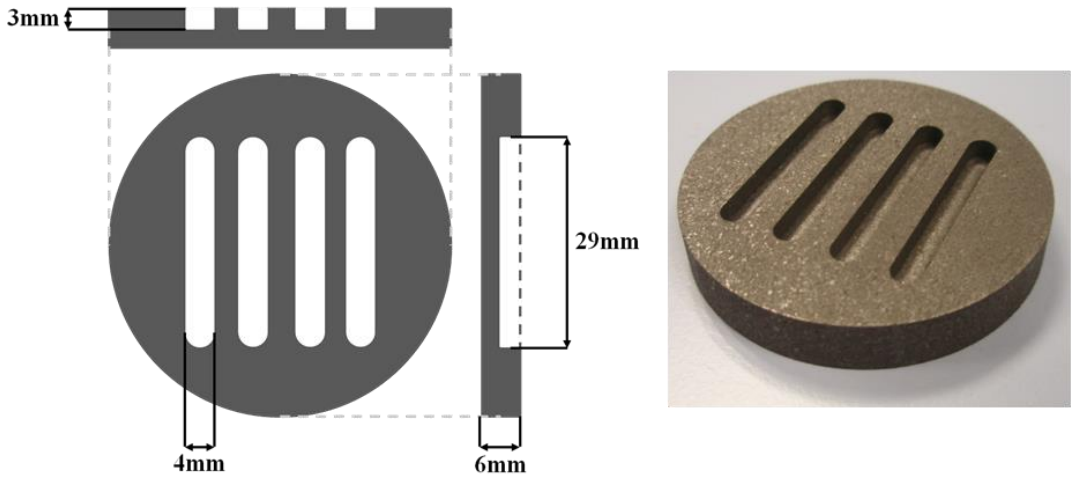

Figure 68: (left) schematic of the mould with dimensions marked and (right) photograph of the finished mould.

4.2.2 Scanning Electron Microscopy

The scaffolds were then cut into 3mm long sections using an Accutom with a diamond blade fitted. The native/outer surface and also the cross-section surfaces of the scaffolds were then imaged using a scanning electron microscope (Hitachi S3400N variable pressure SEM) using the proprietary software. All samples were secured to aluminium stubs using adhesive conducting carbon pads. Silver dag was applied to the edges of the samples to minimise charge build up and all samples were sputtered with a 6nm thick gold coating. The level of sintering was assessed by observation of the shape and morphology of the particles visible at the surface. The level of densification was measured from the cross-section images with residual pore size being measured using imageJ software.

4.2.3 3-point Bend Test

Sintered bars were mechanically tested using a Universal Testing Machine, Lloyd LR10K, with a 500N head. Test parameters were chosen to comply with BS ENISO 6872:EN, Dentistry – Ceramic materials [115]. The width and breadth of each bar was measured using a screw gauge micrometer. Measurements were made in the central 1/3rd of the samples, as this was where the samples were loaded and would be most likely to fail. Each measurement was made three times per sample and an average taken. A three point bend test was performed on the bars using a head diameter of 1.5mm, cross-head span of 15mm and head speed of 2mm.min^{-1}, see figure 69. Care was taken to ensure that the samples were correctly aligned.

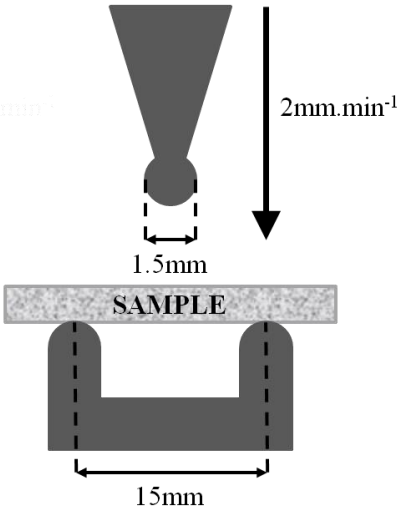

Figure 69: The 3-point bend test setup.

10 samples were tested per group (n=10). The fracture stress was calculated from the peak force. In instances where multiple fractures occurred, only the single highest value was recorded. The flexural strength (σ_{flex}) was then determined using equation 25, where F is the peak force, l the head spacing, w is the sample width (mould width) and b the breadth (mould depth).

$$\sigma_{flex} = \frac{3Fl}{2wb^2}$$

Equation 25

Statistical analysis was performed using SPSS software. The normality of the results was first determined using a Shapiro-Wilk test. Significant differences were then determined using an ANOVA test for normally distributed data. A post-hoc Tukey test was used for multiple comparisons when a significant difference was observed.

The fractured samples were then cut 2mm from the fracture surface using the Accutom with a diamond saw blade. The samples were then prepared for imaging using a Hitachi S3400N variable pressure SEM, as previously described. Fracture surfaces were also imaged using EDX, Bruker XFlash, and Quantax software, to observe any local compositional inhomogeneities.

4.3 Results

4.3.1 Bar Surface

Sintered porous bars were successfully formed from all glass compositions. Following heat treatment, the graphite mould outer surfaces had degraded but the inner surfaces had not. The bars were easily removed from the moulds post heat treatment. The moulds were not reused. The surfaces of the sintered bars were imaged using a scanning electron microscope, figures 70 and 71.

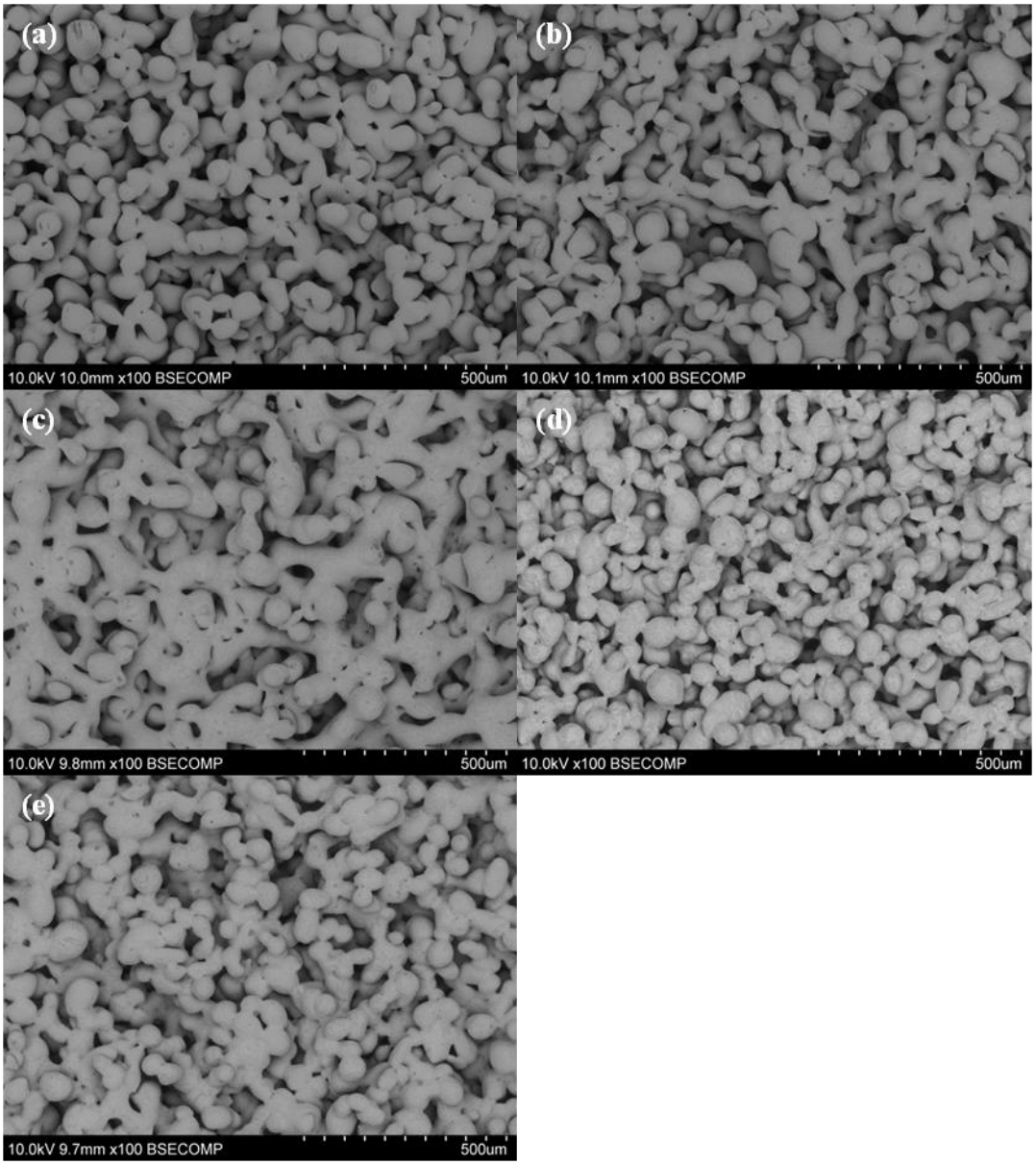

Figure 70: SEM backscattered electron images of the surface of the bars formed following a heating rate of 10K.min^{-1} and 2 hour hold at 1050°C. (a) 0 Mol % strontium (b) 3.12 Mol % strontium (c) 6.24 Mol % strontium (d) 9.35 Mol % strontium and (e) 12.47 Mol % strontium.

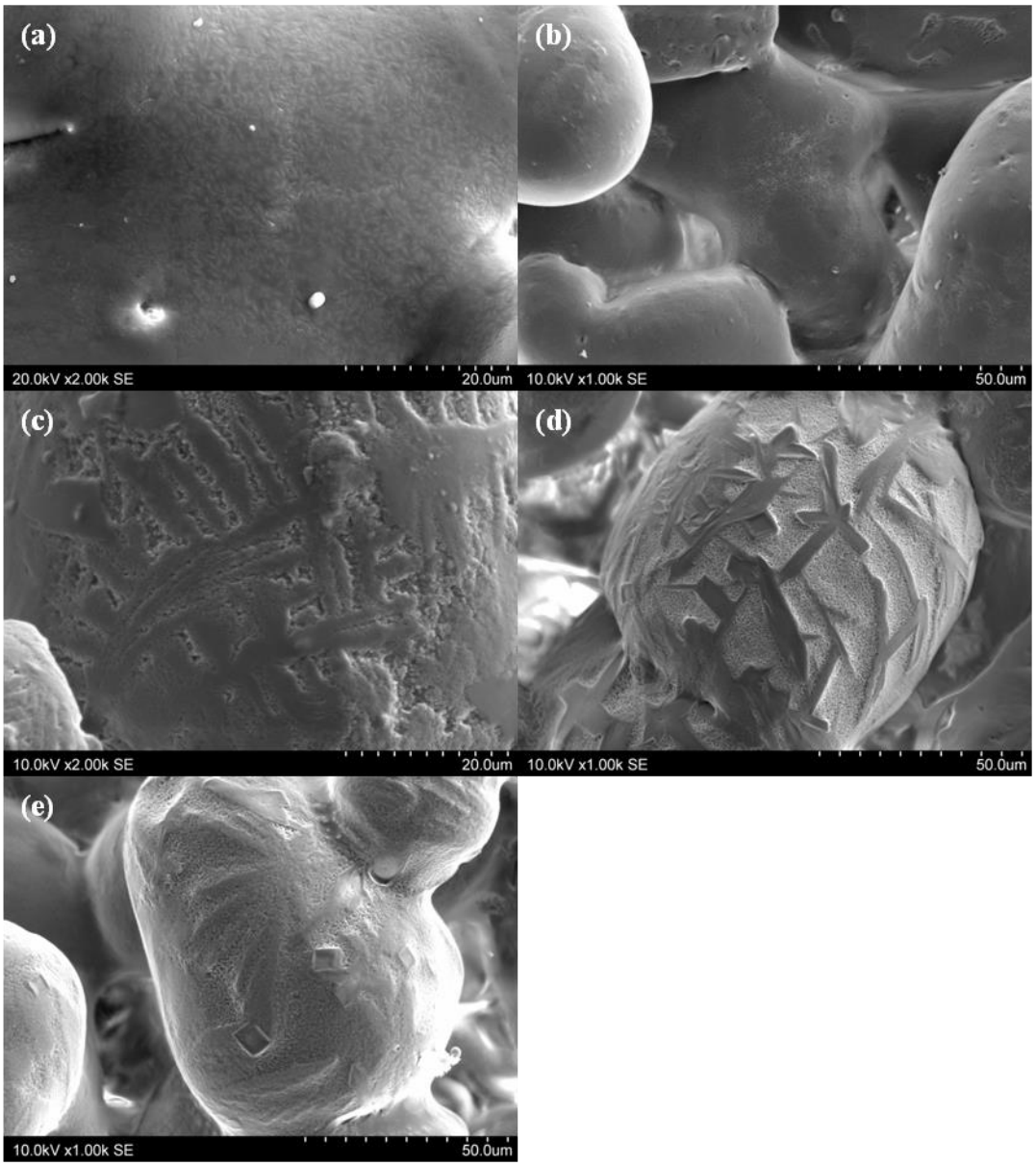

Figure 71: High magnification secondary electron images of the bar surfaces. (a) 0 Mol % strontium (b) 3.12 Mol % strontium (c) 6.24 Mol % strontium (d) 9.35 Mol % strontium and (e) 12.47 Mol % strontium.

From figure 70 it can be seen that a well sintered structure was achieved in all the compositions tested. The particles have clearly fused forming necks, and the angular structure of the glass particles has been lost with the particles becoming rounded. The sintering process has been terminated prior to complete densification and large micro pores are visible from the surface. Compositions 0-6.24 Mol % strontium produced a network that contains thicker necks than compositions 9.35 and 12.47 Mol % strontium. Composition 6.24 Mol % strontium has the thickest necks of all the samples. In compositions 9.35 and 12.47 Mol % strontium the

particles appeared more rounded than in the lower strontium containing compositions.

The high magnification images, figure 71, reveal that the surface architecture previously observed when the powders were heat treated without moulds has been retained. As with the previous samples, increasing the strontium content of the parent glass results in a breakdown of the surface, exposing what has previously been identified as apatite crystals. The surface nucleating silicate crystals are clearly definable in the higher strontium containing compositions and their prevalence decreases with increasing strontium substitution.

4.3.2 Bar Cross-Sections

Bars were cross-sectioned and imaged to better show the residual porosity, figures 72 and 73.

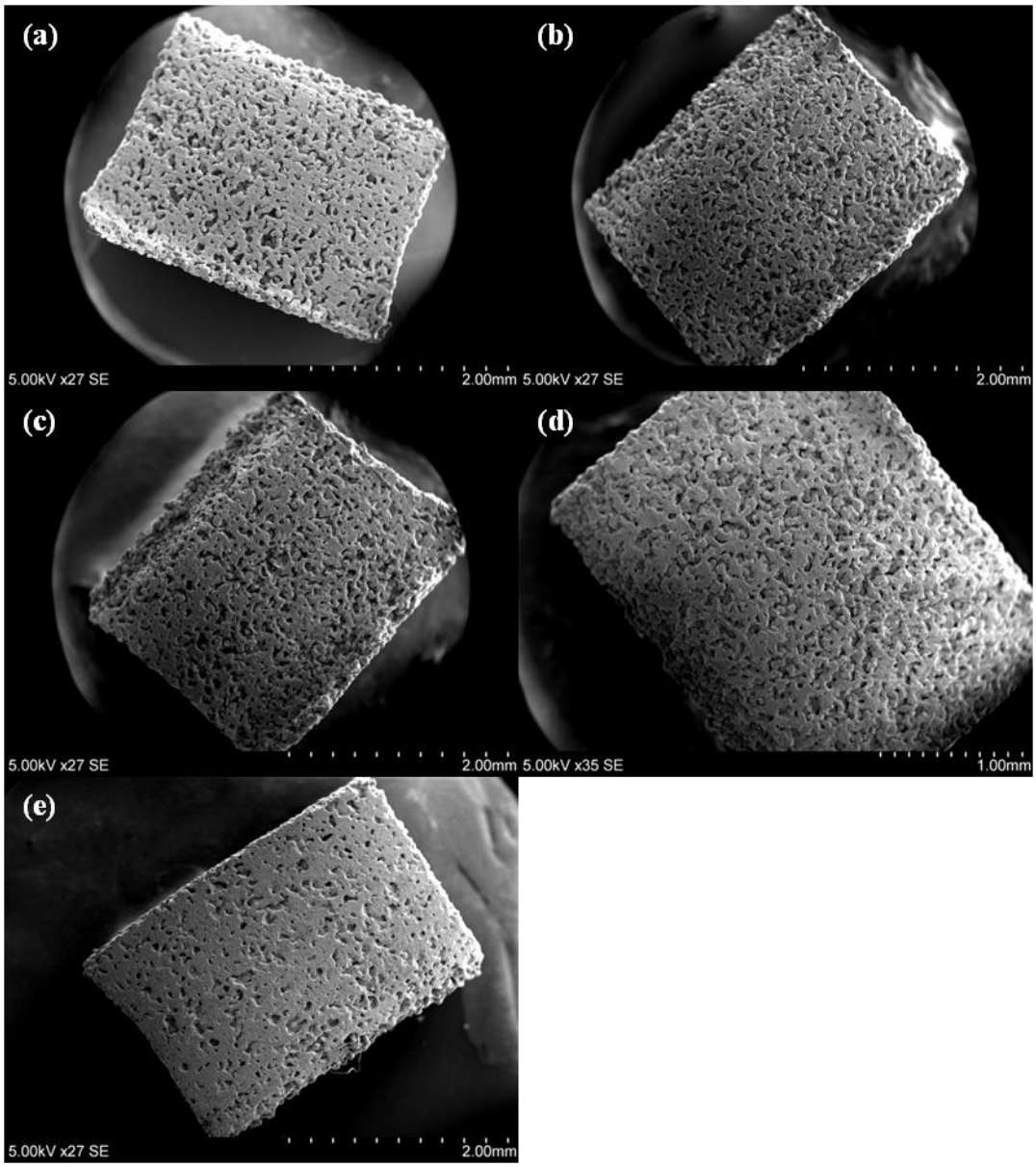

Figure 72: Low magnification SEM secondary electron images of the bar cross-sections. (a) 0 Mol % strontium (b) 3.12 Mol % strontium (c) 6.24 Mol % strontium (d) 9.35 Mol % strontium and (e) 12.47 Mol % strontium.

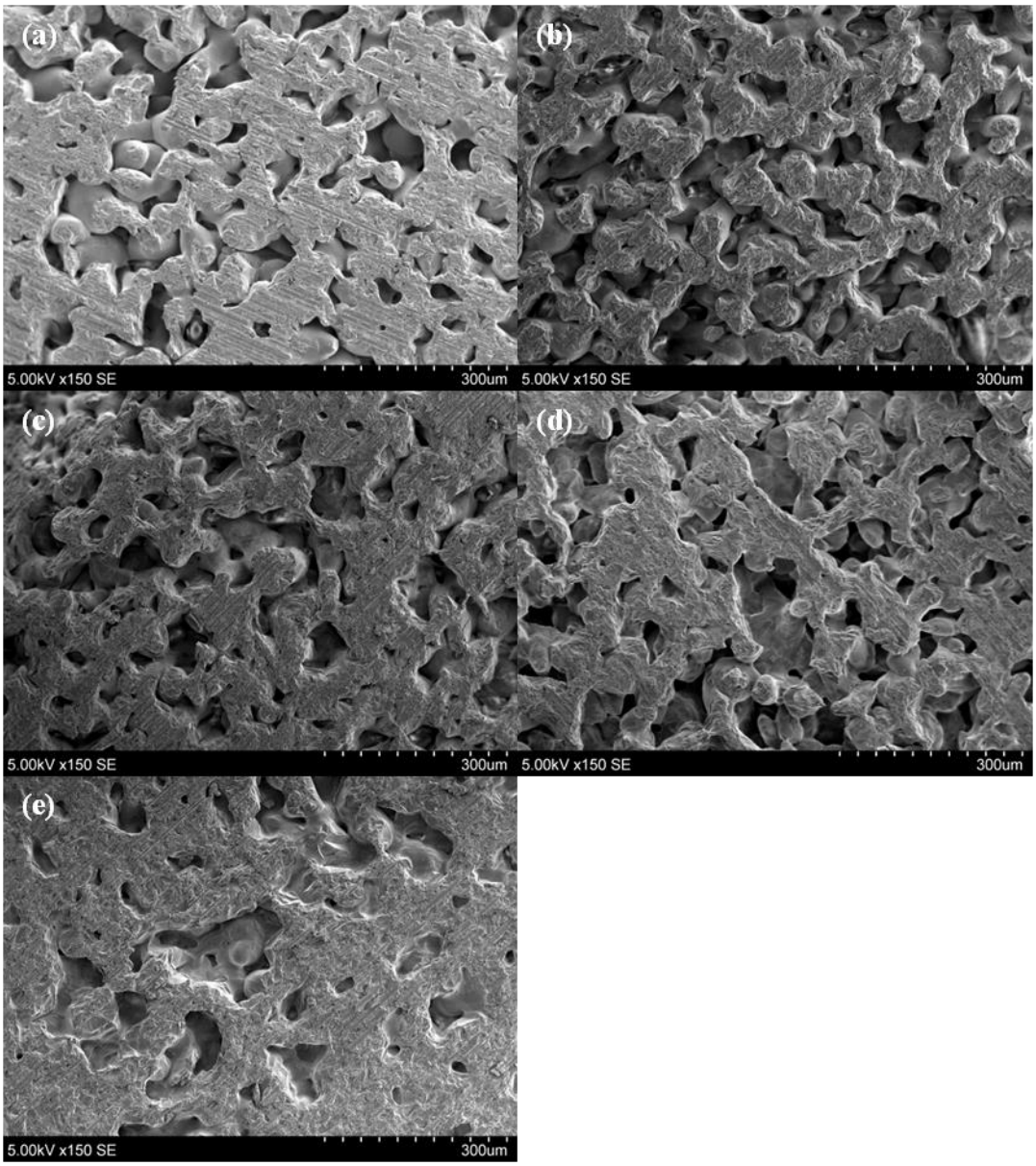

Figure 73: High magnification SEM secondary electron images of the bar cross-sections. (a) 0 Mol % strontium (b) 3.12 Mol % strontium (c) 6.24 Mol % strontium (d) 9.35 Mol % strontium and (e) 12.47 Mol % strontium.

From figure 72 it can be seen that residual pores were present throughout the bars. In all compositions the porosity was evenly distributed, with pores present at both the centre and the periphery of the cross sections. There was no discernible difference between the porosity of compositions 0-9.35 Mol % strontium. However there was a large decrease in the both the number and size of the pores in the 12.47 Mol % strontium sample. This is highlighted further in figure 73. Compositions 0-9.35 Mol % strontium were composed of pores of varying size and shape with areas of pore collapse that have formed a highly interconnected structure. From figure 73 (e), composition 12.47 Mol % strontium, it is clear that pores have

both shrunk and been occluded. The area occupied by material has increased dramatically and individual particles are no longer visible. An attempt was made to quantify the pore size distribution but this was not possible due to their irregular shape. In figure 74 it can be seen that the dimensions of the pores could not easily be described using a single measurement, as would be the case if they were spherical. The width of the pores ranged from a few microns up to 200µm. The interconnectivity is also highlighted in figure 74. The continuation of the interconnectivity throughout the materials was confirmed using a coloured ink. In samples 0-9.35 Mol % strontium, the ink was drawn up into the scaffolds and permeated the whole cross-section. In composition 12.47 Mol % strontium the ink remained on the scaffold surface, indicating that the porosity was not interconnected.

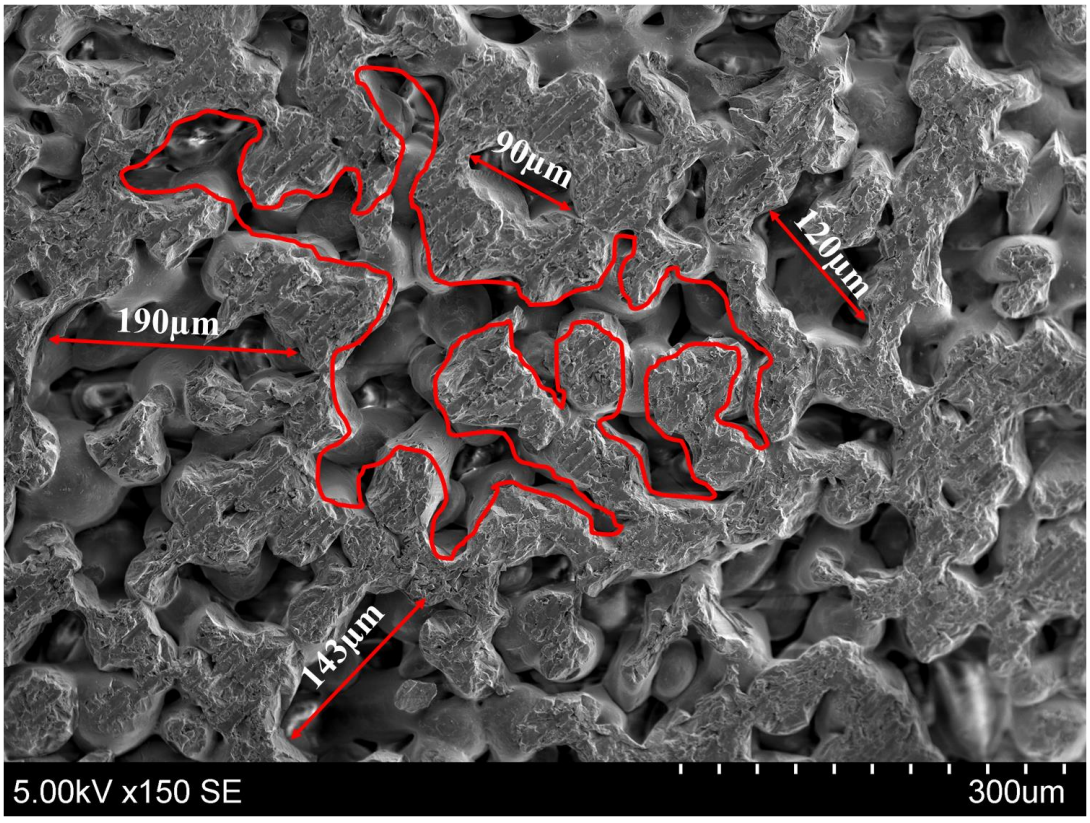

Figure 74: An example of the range of sizes and shapes of the pores present in the bar cross-sections. The red bordered area highlights an example of interconnected porosity.

The mechanical integrity of the bars was then tested using a 3-point flexural strength, figure 75 and tables 48 and 49, all errors are the standard deviations calculated directly from values or by the propagation of errors method. All groups were found to be normally distributed, according to both Shapiro-Wilks and

Kolmogorov-Smirnov methods. Statistical significance was then assessed using a one-way ANOVA analysis and the post-hoc Tukey method. Also included are the sizes of the sintering windows for the parent glasses. The sintering windows were calculated from the DSC results, see chapter 3, whereby the sintering window is defined as the difference in temperature between the first exotherm and the glass transition temperature (T_{P1}-T_g). The size of the sintering window decreased with increasing strontium levels, the rate of reduction increased with increasing strontium. A significant reduction in the flexural strength of the bars was observed between compositions 3.12-9.35 Mol % strontium. This coincided with a reduction in the sintering window. There was a significant difference between the flexural strength of compositions 6.24 and 9.35 Mol % strontium. Composition 12.47 Mol % strontium produced a flexural strength that was significantly higher than any of the compositions tested while at the same time had a sintering window that was 14.0°C smaller than the 0 Mol % strontium composition. The breadth and width of the samples increased for samples 3.12-9.35 Mol % strontium compared to composition 0 Mol % strontium. The breadth and width of composition 12.47 Mol % strontium was smaller than compositions 3.12-9.35 Mol % strontium but larger than composition 0 Mol % strontium.

4.3.3 3-Point Flexural Strength

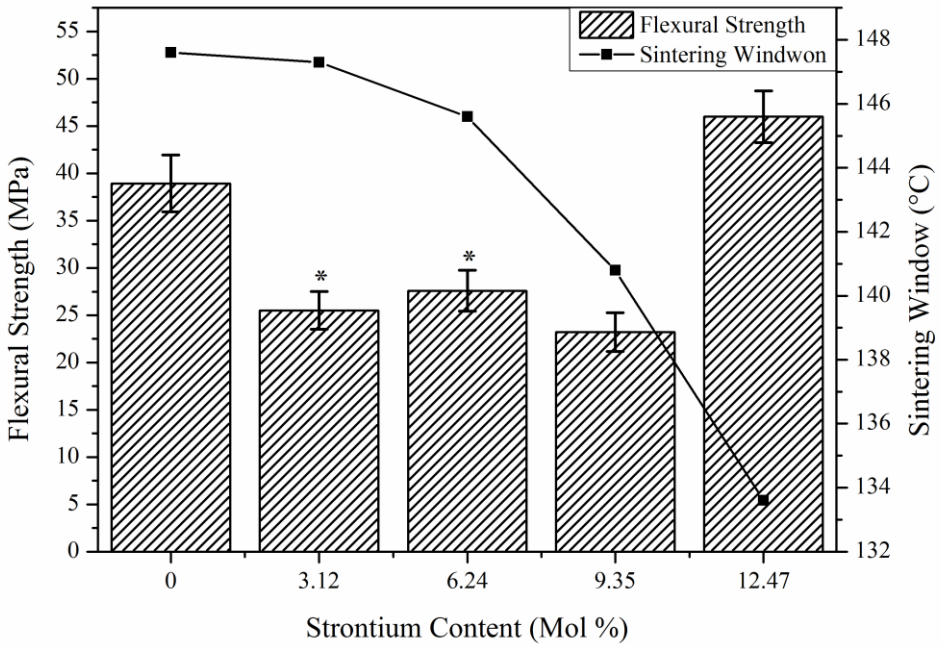

Figure 75: The effect of the parent glass strontium content on the width of the working window (T_{P1}-T_g) and the flexural strength of the devitrified and sintered bars, the error bars represent the standard deviations. n=10. * indicates samples that are not significantly different, p=0.05.

Table 48: The average bar width and breadths for the samples tested in figure 75. Standard deviations are shown (±).

Strontium Content (Mol %)	Average Width (mm)			Average Breadth (mm)		
0	3.281	±	0.034	2.291	±	0.055
3.12	3.449	±	0.031	2.604	±	0.041
6.24	3.335	±	0.031	2.532	±	0.058
9.35	3.623	±	0.023	2.682	±	0.054
12.47	3.386	±	0.051	2.331	±	0.034

Table 49: Numerical values shown in figure 75, the errors shown are the calculated standard deviations. Standard deviations are shown (±).

Strontium Content (Mol %)	Sintering Window (°C)	Average Force at Rupture (N)			Flexural Strength (MPa)		
0	147.6	29.81	±	2.05	38.94	±	3.01
3.12	147.3	26.51	±	1.99	25.51	±	2.01
6.24	145.6	26.23	±	1.85	27.59	±	2.16
9.35	140.8	26.89	±	2.24	23.22	±	2.05
12.47	133.6	37.59	±	2.02	45.99	±	2.73

4.3.4 Fracture Surfaces

4.3.4.1 Low Magnification SEM

The fracture surfaces of the bars were then investigated using scanning electron microscopy. Low magnification images were taken to provide on overall image of how the fracture had progressed through the material, figure76. All samples failed via a brittle mechanism. In compositions 0-9.35 Mol % strontium, where sintering had produced individual particles connected by necks, fracture had occurred through both the particles and the necks. The fracture surfaces are aligned, lying perpendicular to the length of the bar. The overall fracture surface is not perfectly flat and undulations are visible. In composition 12.47 Mol % strontium, where individual particles are not so clearly defined, fracture has occurred through the material in a single plane.

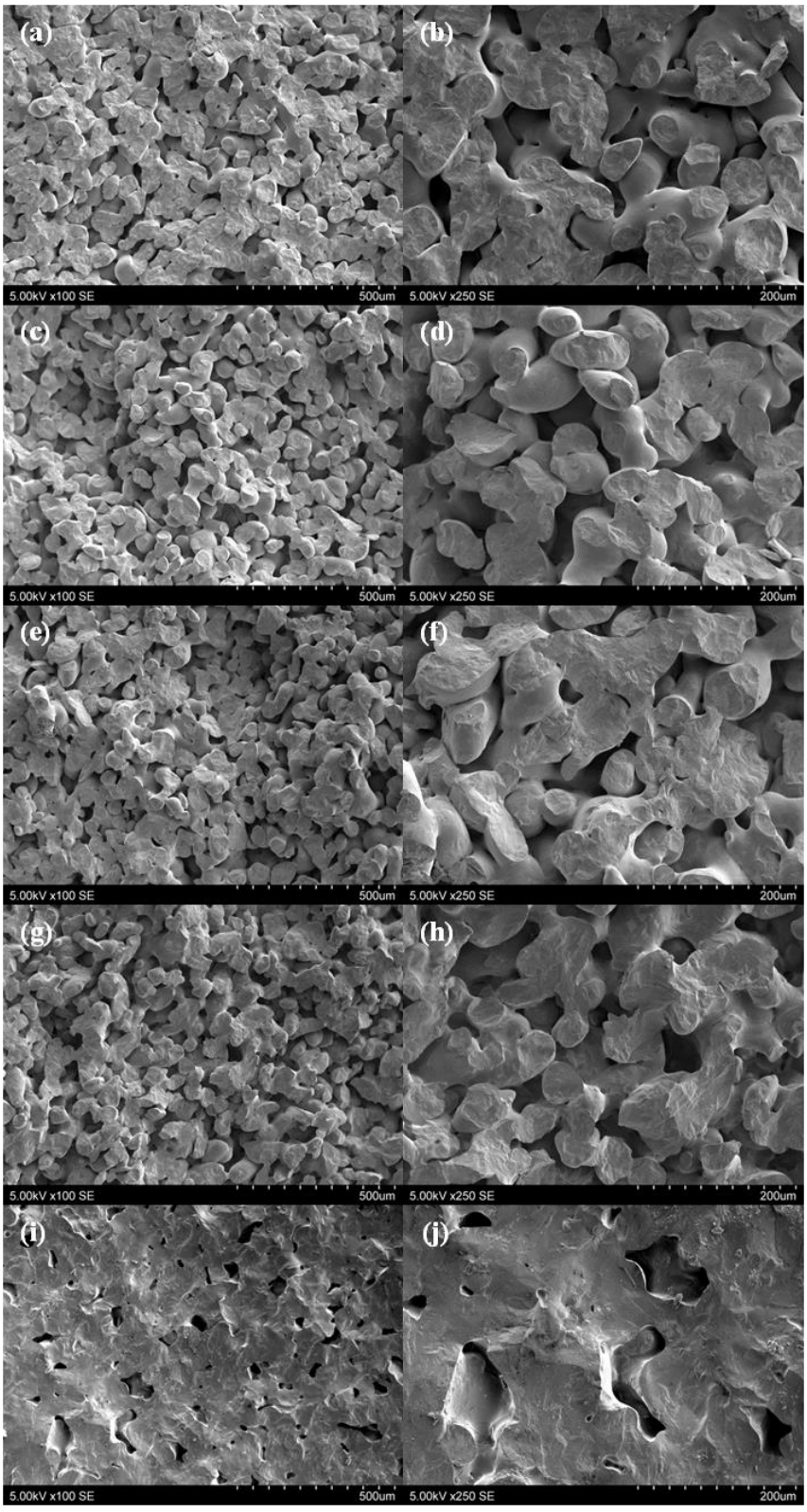

Figure 76: Secondary electron SEM images of the bar fracture surfaces taken at x100 (left) and x250 (right) magnifications. (a-b) 0 Mol % strontium (c-d) 3.12 Mol % strontium (e-f) 6.24 Mol % strontium (g-h) 9.35 Mol % strontium and (i-j) 12.47 Mol % strontium.

4.3.4.2 High Magnification SEM

High magnification images of the fracture surfaces were taken to identify any exposed crystal phases, figures 82 to 86 pages 142 to 146.

4.3.4.2.1 0 Mol % Strontium

In figure 77, it can be seen that the fracture surface is relatively flat with a small degree of roughness. There are white areas that may be individual crystals but they are too small and not exposed enough to be clearly defined.

4.3.4.2.2 3.12 Mol % Strontium

In figure 78, the surface becomes rougher and individual surface details become apparent.

4.3.4.2.3 6.24 Mol % Strontium

In figure 79, two different surfaces are visible. The majority of the fracture surfaces showed the morphology visible in figure 79 (c). These regions were similar to those observed in composition 3.12 Mol % strontium but with larger crystals. The region in figure 79 (b) contains multiple exposed crystals that are 0.5-1µm in length and appear to be a continuation of the crystals visible on the surface that were previously identified as the apatite phase.

4.3.4.2.4 9.35 Mol % Strontium

The exposed crystals in figure 80 were larger than in previous compositions. In figure 80 (b) it can be seen that as well as the areas of exposed crystals there are also smoother areas that appear to contain crystals. In figure 80 (c) it can be seen that in areas the internal crystal structures matches that on the surface but in other regions a smooth surface is aligned with the apatite crystals visible on the surface of the material.

4.3.4.2.5 12.47 Mol % Strontium

The morphologies visible in the 9.35 Mol % strontium composition are visible in 12.47 Mol % strontium composition, figure 81. There is an increase in the amount of the smooth fracture surface compared to the rough. In figure 81 (a) an internal pore is visible displaying the same features observed on the surface of the material.

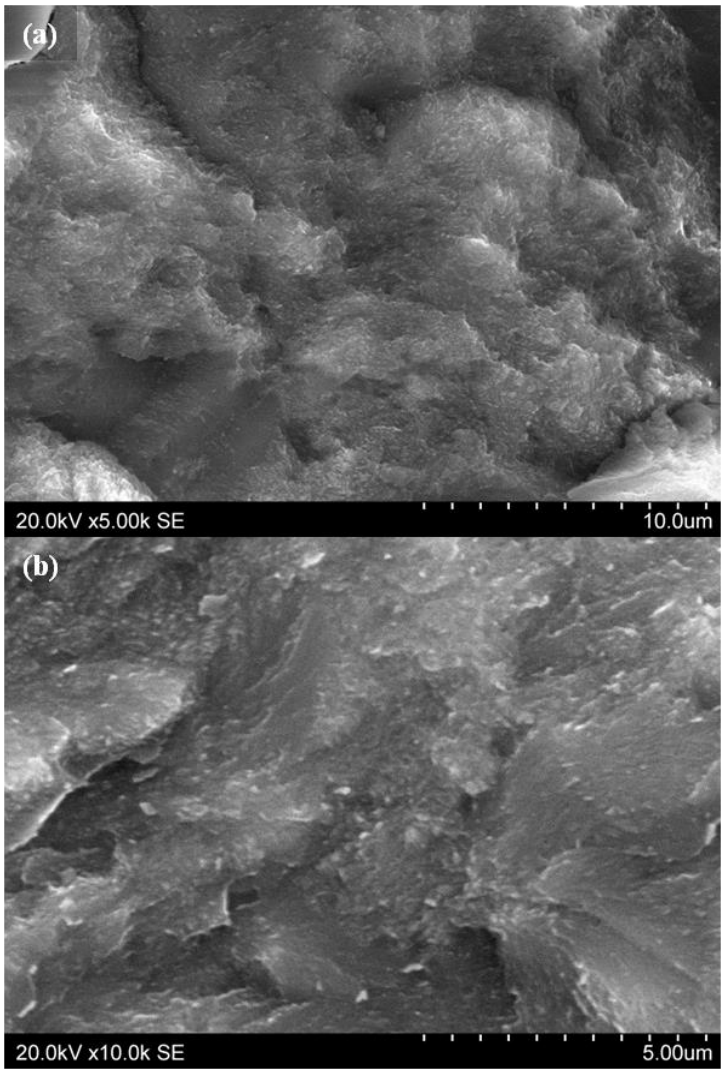

Figure 77: Secondary electron images of the fracture surface of composition 0 Mol % strontium. (a) x5,000 and (b) x10,000 magnification.

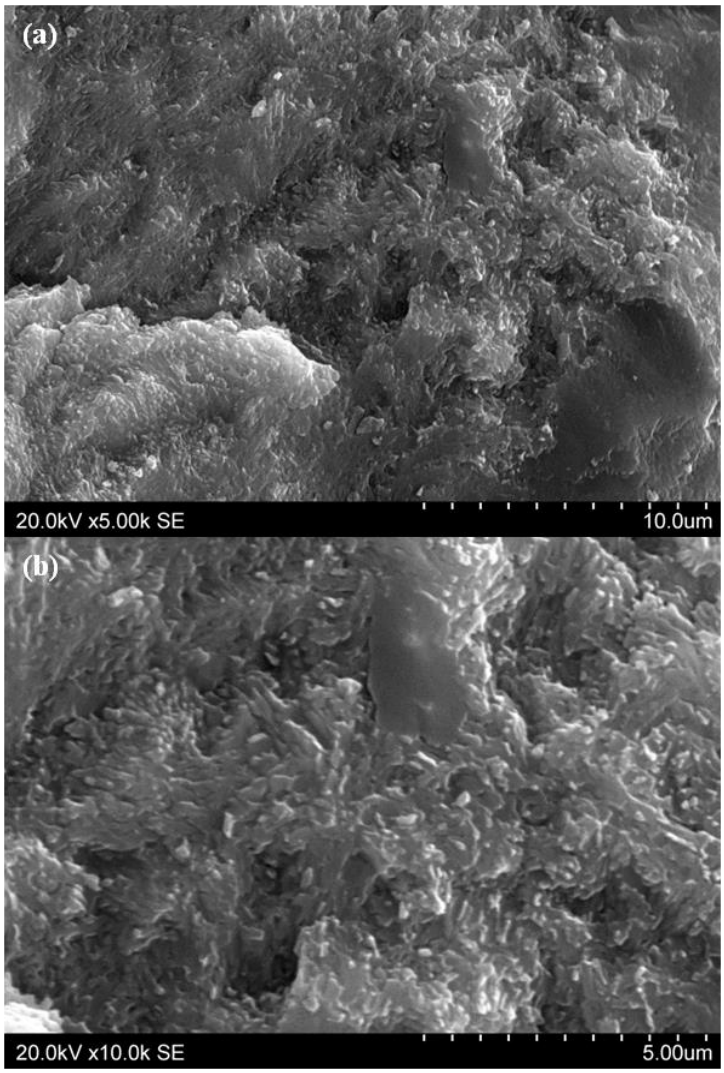

Figure 78: Secondary electron images of the fracture surface of composition 3.12 Mol % strontium. (a) x5,000 and (b) x10,000 magnification.

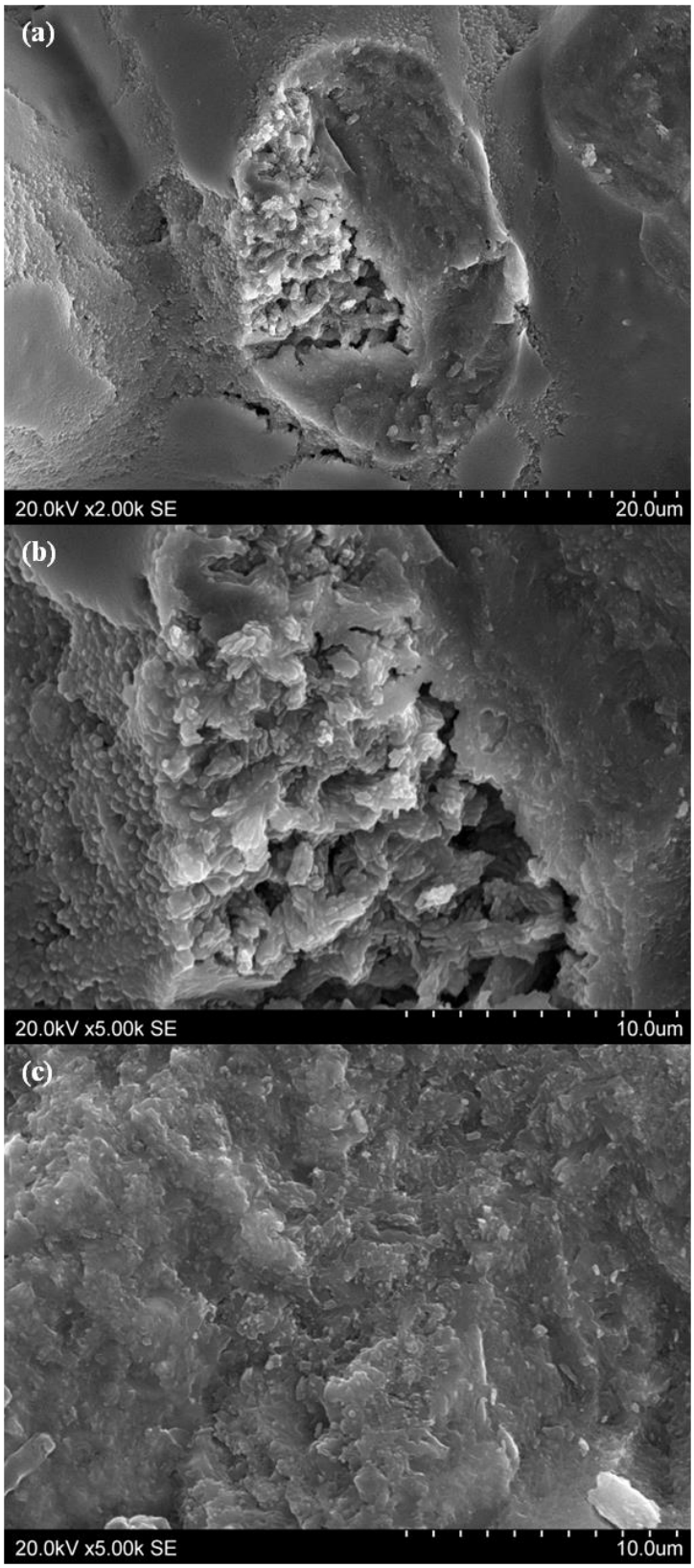

Figure 79: Secondary electron images of the fracture surface of composition 6.24 Mol % strontium. (a) x2,000 magnification and x5,000 magnification of (b) a region of exposed crystals and (c) the remaining fracture surface.

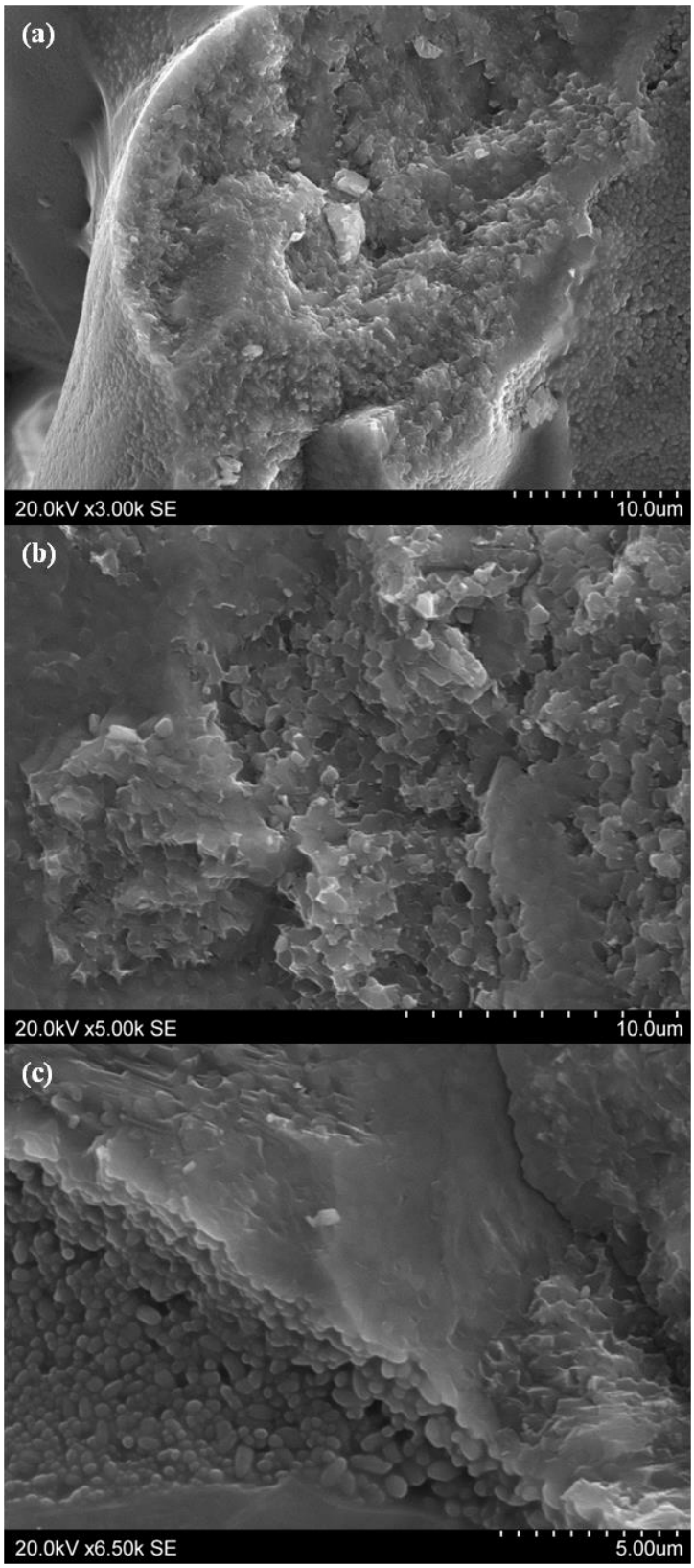

Figure 80: Secondary electron images of the fracture surface of composition9.35 Mol % strontium. (a) x2,000 magnification showing two distinct regions (b) x5,000 magnification of the fracture surface and (c) the boundary between the fracture surface and outer surface, x5,000 magnification.

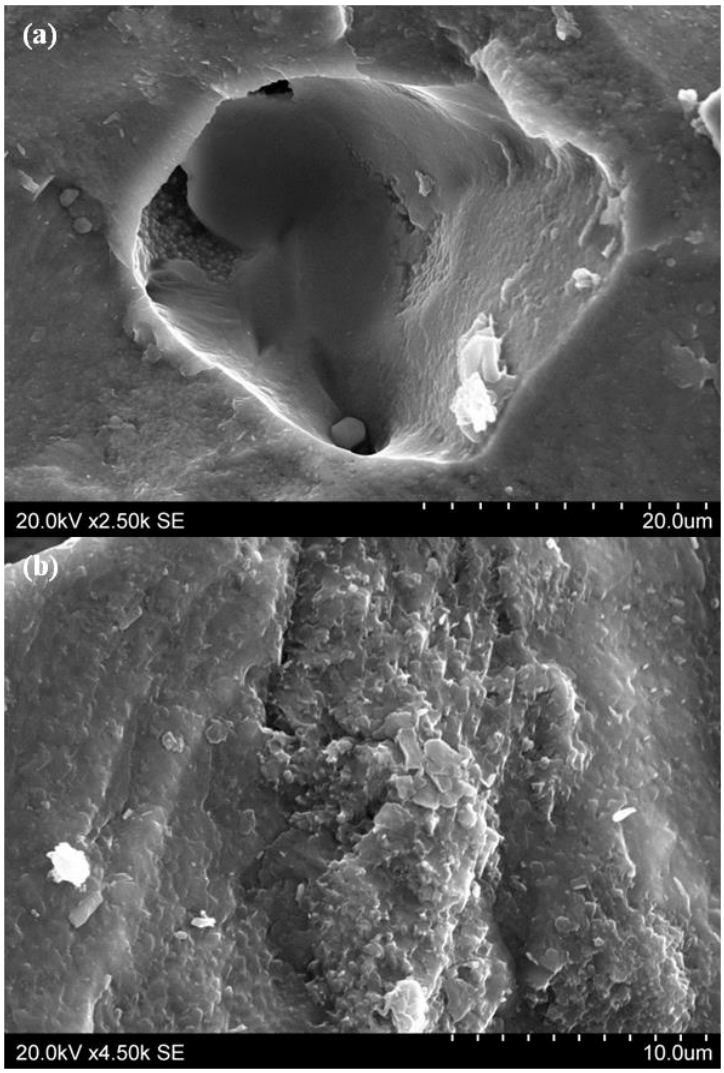

Figure 81: Secondary electron images of the fracture surface of composition 12.47 Mol % strontium. (a) x2,500 magnification of the fracture surface and an internal pore surface and (b) x4,500 magnification of the fracture surface.

4.3.4.3 EDX

The fracture surfaces were then imaged using EDX to observe any elemental distribution inhomogeneities, figures 82 to 86 on pages 149 to 153. Both oxygen and fluorine were homogenous throughout the materials, except in areas where the take-off angle inhibited their detection and so were not included in the individual maps. In all samples the distribution of magnesium was shown to vary throughout. A comparison of the calcium and magnesium maps is shown for each composition as magnesium had previously been shown to substitute for calcium into the different structures. In all compositions there were regions in the elemental maps that showed no elements present. These areas were constant between all elements and are not included when describing depleted areas.

4.3.4.3.1 0 Mol % Strontium

In composition 0 Mol % strontium, figure 82, both phosphorous and silicon were homogenously distributed across the fracture surface. Magnesium was more concentrated around the surface of the material and its location corresponded with areas that were depleted in calcium. The areas of increased magnesium were in distinct, isolated regions that occurred all around the outer boundary of the fracture and penetrated roughly 5μm into that material.

4.3.4.3.2 3.12 Mol % Strontium

The magnesium distribution was also observed in composition 3.12 Mol % strontium, figure 83. Again magnesium was more concentrated around the outer surface of the fracture cross-section. Unlike in composition 0 Mol % strontium, the magnesium in 3.12 Mol % strontium was not found all around the boundary of the cross-section and penetrated further into the material, in excess of 10μm in some instances. The magnesium regions appear smoother on overlaid SE image than the surrounding surfaces, this was observed in all subsequent compositions. An isolated magnesium rich region can also be observed in the bulk of the material. As in the previous composition, the areas of high magnesium corresponded with areas of low calcium. The magnesium rich regions appear to be depleted with respects to phosphorous and strontium, but the variation in phosphorous is minimal and it is hard to differentiate from regions that have failed to capture data.

4.3.4.3.3 6.24 Mol % Strontium

Localised increases of magnesium were also observed in composition 6.24 Mol % strontium, figure 84. Though present in regions around the periphery, isolated regions were also observed in the bulk. Depletion of strontium in the magnesium rich regions was more pronounced than in lower strontium containing samples.

4.3.4.3.4 9.35 Mol % Strontium

The magnesium rich regions are most obvious in sample 9.35 Mol % strontium, figure 85. In this sample the magnesium regions could be found throughout the material but can also be seen to propagate from the surface features, visible on the right of the material. The magnesium rich regions were depleted with respect to

strontium. Calcium depletion was not as clear due to it being substituted with strontium in the parent glass.

4.3.4.3.5 12.47 Mol % Strontium

In composition 12.47 Mol % strontium, figure 86, magnesium rich regions were visible throughout the material and corresponded to regions that were depleted in calcium. The regions were not as distinct as in previous samples and covered a much larger area. Depletion of strontium in magnesium rich regions was not observed in composition 12.47 Mol % strontium.

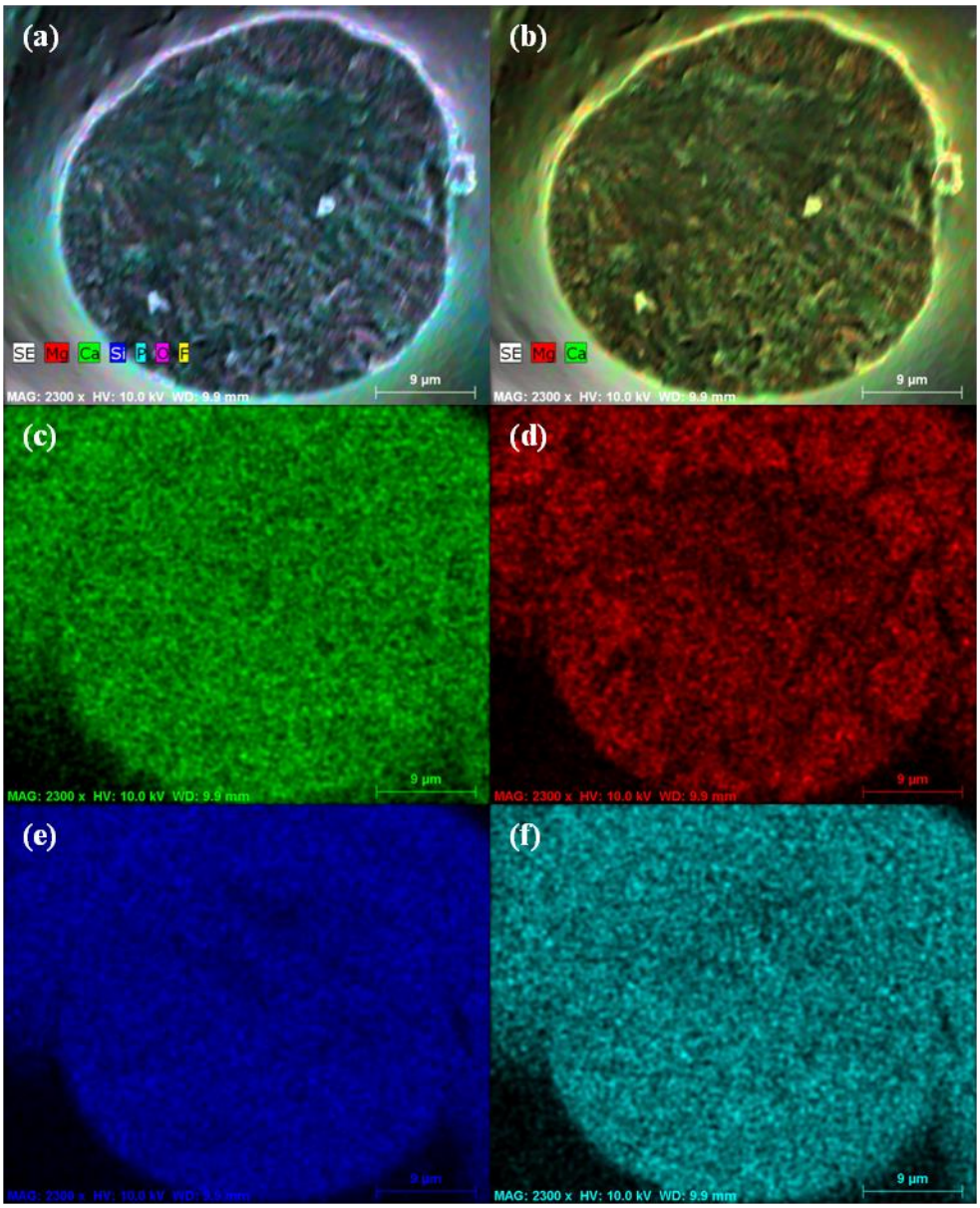

Figure 82: EDX maps of a fracture surface of composition 0 Mol % strontium (a)SE overlaid with all elements (b) SE overlaid with Ca and Mg (c) Ca (d) Mg (e) Si and (f) P.

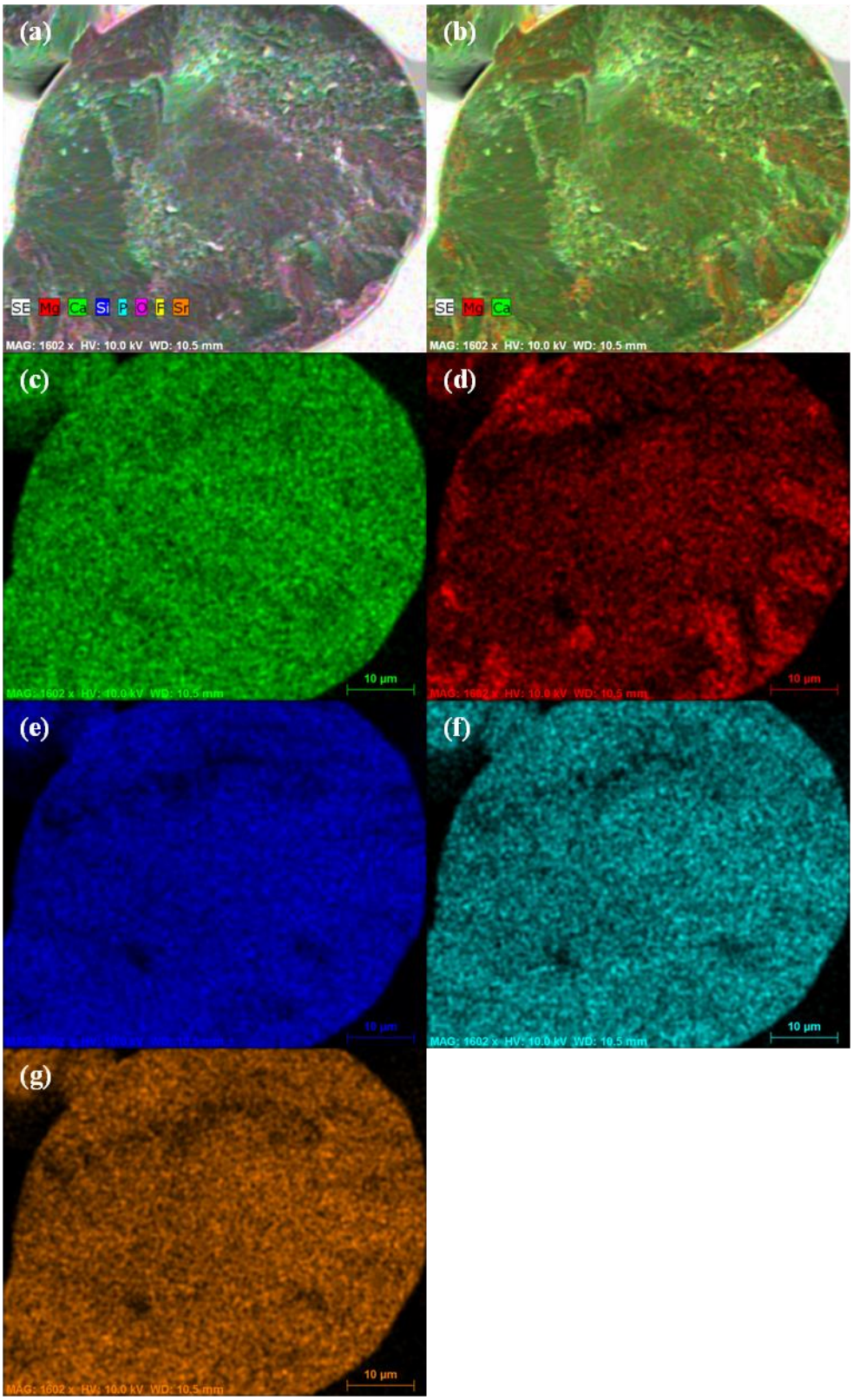

Figure 83: EDX maps of a fracture surface of composition 3.12 Mol % strontium (a)SE overlaid with all elements (b) SE overlaid with Ca and Mg (c) Ca (d) Mg (e) Si (f) P and (g) Sr.

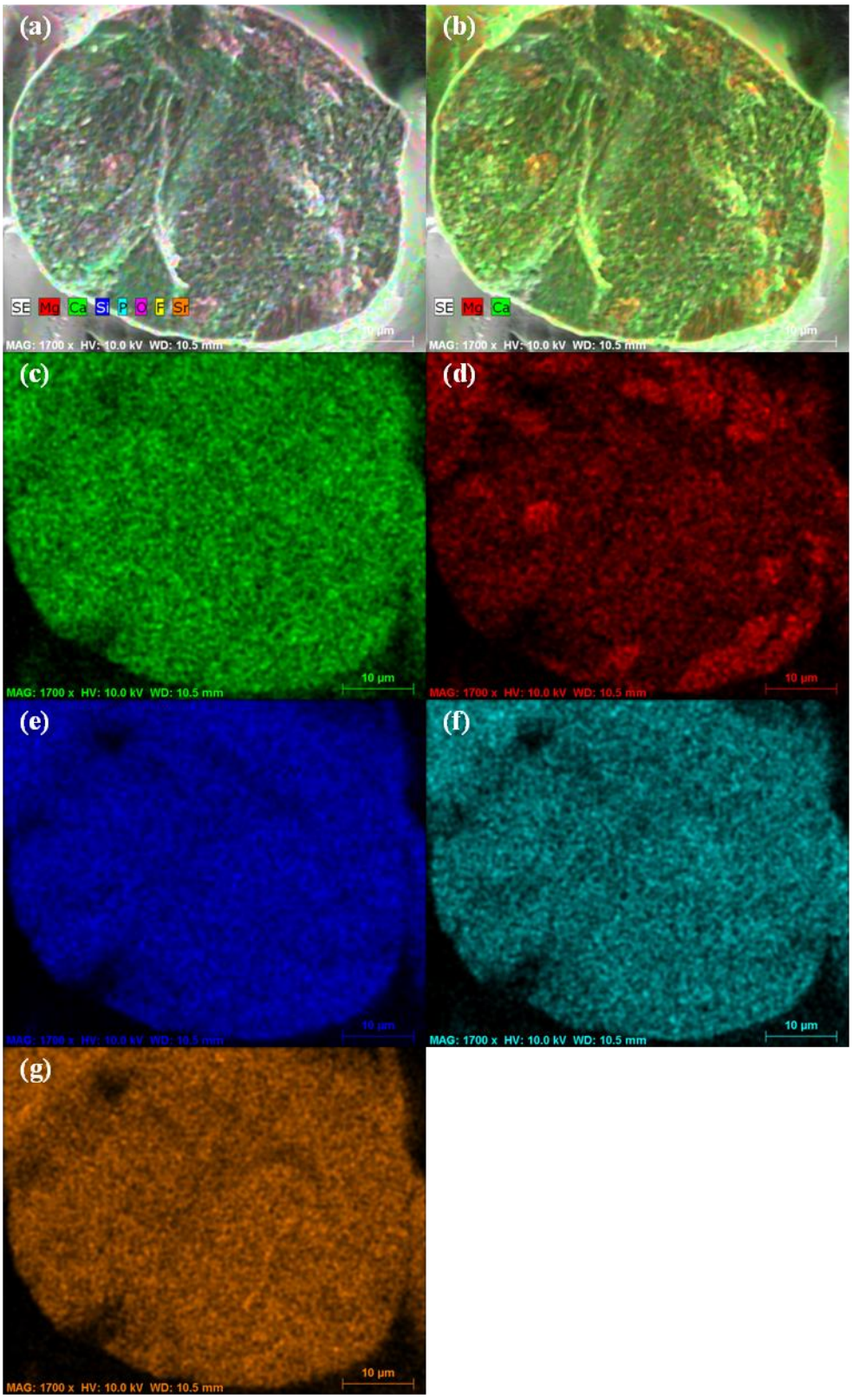

Figure 84: EDX maps of a fracture surface of composition 6.24 Mol % strontium (a)SE overlaid with all elements (b) SE overlaid with Ca and Mg (c) Ca (d) Mg (e) Si (f) P and (g) Sr.

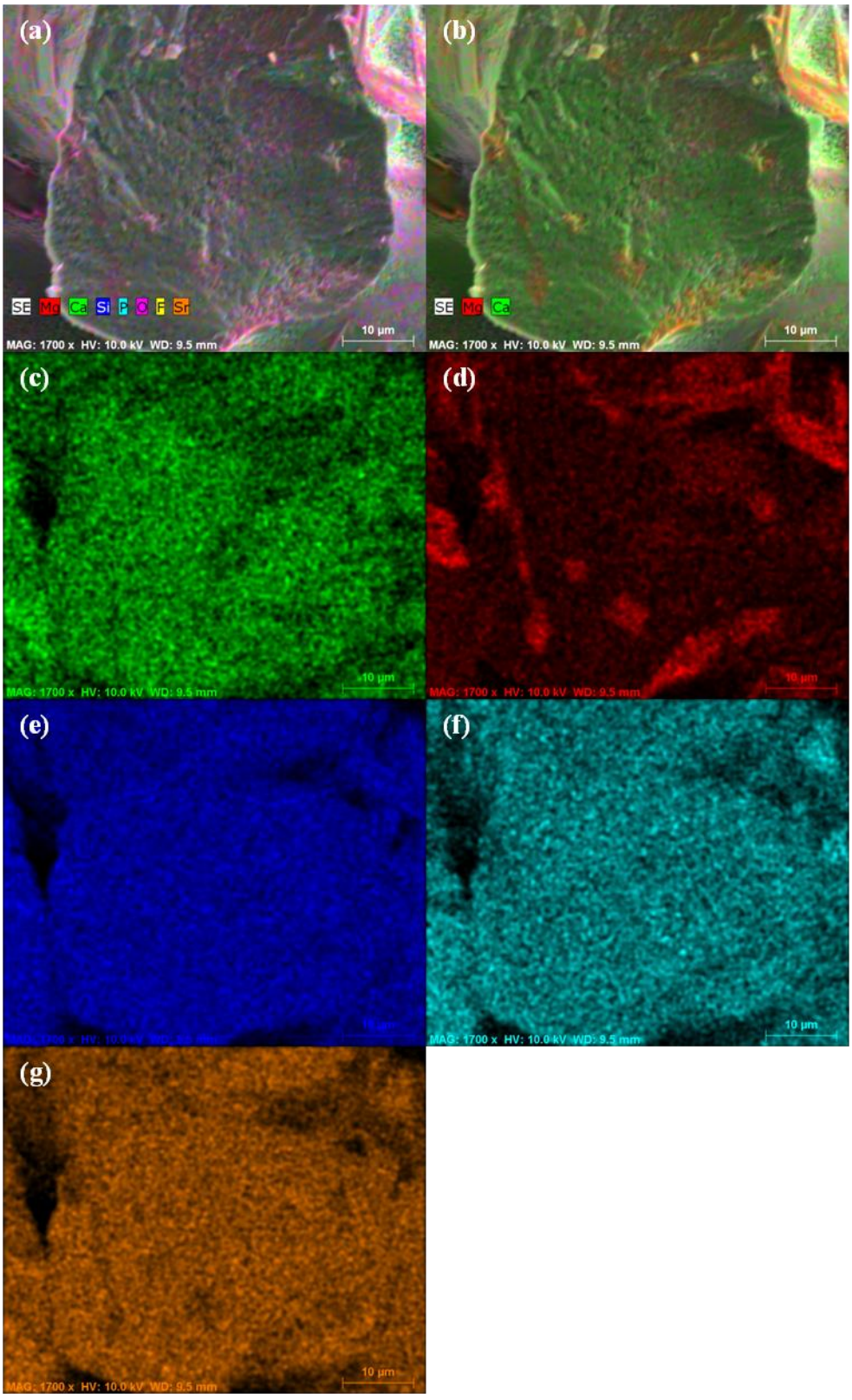

Figure 85: EDX maps of a fracture surface of composition 9.35 Mol % strontium (a)SE overlaid with all elements (b) SE overlaid with Ca and Mg (c) Ca (d) Mg (e) Si (f) P and (g) Sr.

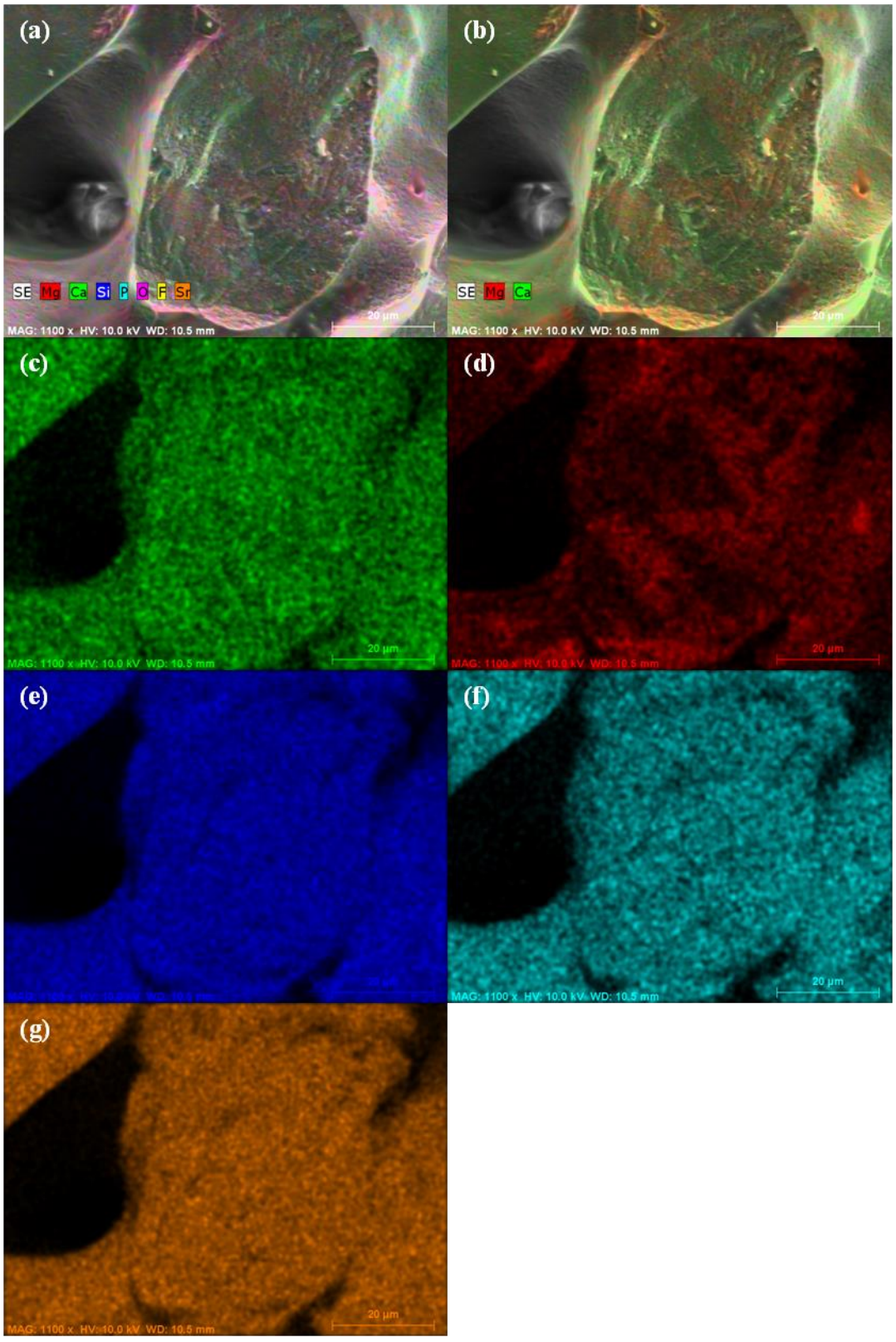

Figure 86: EDX maps of a fracture surface of composition 12.47 Mol % strontium (a)SE overlaid with all elements (b) SE overlaid with Ca and Mg (c) Ca (d) Mg (e) Si (f) P and (g) Sr.

.

4.4 Discussion

This section of work was not concerned with the optimisation of the sintering process but in observing the effect of strontium substitution on the sinterability of the new materials. As such, graphite moulds were chosen to form the bars as they offered a simple and repeatable process by which porous materials could be formed. Graphite was chosen as mould material due to its good thermal conductivity, machinability and low cost. The 45-90μm particle size fraction has previously been shown to sinter well for apatite-wollastonite and apatite-mullite glass ceramics [62, 65]. The moulds were not re-used even though the interiors appeared visibly unchanged as the outer surface had undergone some degree of combustion and re-use may have altered the thermal conductivity of the materials reducing the reproducibility of the process. It is clear from the high magnification images of the sintered materials surface that the crystals structures observed are the same as in powders sintered without moulds. This indicates that the moulds did not affect the crystallisation of the powders.

The surface of the sintered bars for all the materials tested indicated that sintering had occurred following the described processing route and that porosity, at least at the surface had been retained. The formation of necks in compositions 0-6.24 Mol % strontium indicates that sintering had occurred via a predominantly solid state mechanism. The morphology of the particles in compositions 9.35-12.47 Mol % strontium are much more rounded and necks less visible, indicating that these particles sintered by a predominantly liquid phase mechanism [65]. The change in sintering mechanism is likely due to the reduction in melting point with increasing strontium substitution as observed in chapter 3. In both mechanisms, sintering proceeds due to the drive to minimise interfaces and contact angles between particles. Solid state sintering occurs at temperatures well below the melting point and proceeds via two primary mass transport mechanisms, bulk or surface [108]. The necks are likely to have formed from a combination of the two. Bulk transport in the discussed materials is likely to have occurred via grain boundary diffusion and viscous flow mechanisms. As these mechanisms involve the transport of material from the interior of the particle they all result in densification as well as neck formation. Viscous diffusion will be the dominant mechanism for the glass phase. As the temperature increases and the viscosity of an amorphous

phase decreases, the ability of the material to flow and reduce surface tension increases. The lower the viscosity of the amorphous phase, the thicker the necks that are produced following sintering [108]. Increasing substitutions of strontium into the parent glasses reduced the glass transition temperature, indicating a reduction in connectivity and viscosity of the glass. The amorphous phase content of the samples also increased with increasing strontium substitution. Compositions containing higher levels of strontium would therefore be more susceptible to viscous flow sintering. This may explain the increase in the neck size observed in composition 6.24 Mol % strontium compared to composition 3.12 Mol % strontium. The increase in necking thickness was not observed in compositions 9.35-12.46 Mol % strontium despite a reduction in the glass transition temperature due to a change in mechanism toward liquid phase sintering. As the samples are heated they will begin to crystallise. The devitrification of the glass inhibits viscous flow sintering [151] and grain boundary diffusion and volume diffusion begin to dominate the bulk transportation mechanism. Inhomogeneities and stresses within grain boundaries allow for reduced activation energies for mass transport. Thus transport of material towards a neck can proceed along these boundaries. Grain boundary diffusion also supports crystal growth [152]. Volume diffusion is a result of vacancy transportation through a materials bulk. The most common mechanism of sintering in ceramics is surface diffusion [108]. Surface diffusion does not result in densification and is a result of mass transport from the material surface to the necking region. Previous reports of the glass ceramic system discussed show that neck formation is predominantly a result of viscous flow [127] and as such sintering and densification proceed more rapidly prior to crystallisation. The systems will however continue to sinter and densify following crystallisation, suggesting viscous flow is not the only mechanism occurring [110].

Liquid phase sintering occurs when a phase in the materials melts. It can be especially prevalent in materials that show large melting temperature ranges, such as the discussed glasses/glass ceramics. The liquid phase that forms upon melting wets the particle's surface. This surface coating, if in large enough quantities, allows for rearrangement of the solid particles. The particles are also drawn closer via capillary forces, inducing high levels of densification. Liquid phase sintering leads to the formation of liquid bridges that subsequently re-precipitate, as opposed to the necks observed in solid state sintering. In glass ceramics the glass phase is generally

less stable than the crystalline phase and has a lower melting point [65]. Thus less crystalline materials, as in the case of the higher strontium containing compositions, are more likely to undergo liquid phase sintering. From the bar cross-section it can be seen that composition 12.47 Mol % strontium has undergone the highest level of densification of all the compositions tested, further indicating that the material has undergone liquid phase sintering. This composition was also shown to contain the lowest weight percentage of the surface nucleating silicate phase. The surface nucleating phase would inhibit liquid phase sintering as it is the melting of the surface that is crucial for the mechanism to occur [153]. Though the morphology of the particles in composition 9.35 Mol % strontium appear to indicate liquid phase sintering, the lack of densification suggests that amount of liquid phase present was insufficient for re-arrangement and densification to occur. This may be due to the increased melting temperature range or increase in surface crystals compared to composition 12.47 Mol % strontium.

All the sintered bars had well dispersed porosity and dense regions were not concentrated around specific surfaces or regions indicating that sintering had not been influenced adversely by temperature gradients. Heating of samples at high rates can sometimes induce temperature gradients, leading to non-uniform densification [154, 155]. While the samples do contain areas of increased density, they are randomly distributed and are likely a result of packing of the moulds. The arrangement of the particles in the moulds prior to sintering will be highly disordered, due to their irregular shape, size range and the fact they were not compressed. While there have been many attempts to describe densification in compacted glass systems, Frenkel Mackenzie, Shuttleworth, Scherer (all summarised nicely by Prado [154]), the theory and mechanisms do not apply to uncompacted systems. It is useful to think of particle packing, for sintering purposes, in terms of connections/coordinations between neighbouring particles [108]. It is at these contact points that necks form and as a result the higher the coordination number, the greater the capacity of that material to sinter and densify. Random packing of monosized spheres produces and average coordination of around 6 or 7 [108]. Compaction and use of smaller particles can increase this value as both variables increase the density of the sample, ultimately bringing more particles into contact with each other and minimising the initial pore volume [151]. Loose particle sintering, such as reported here, with a low initial density leads to

particles forming into long chains with an open porous structure [151]. This process is essential for the described materials as it retains the open, connected, porous structure required for a successful bone replacement material.

Mechanical testing was performed on the material to assess the capacity of the material to be used in load bearing applications and also attempt to quantify the level of sintering in the materials. Densification as a result of sintering increases the mechanical strength of a material by effectively increasing the cross-sectional area [151] and as such the flexural strength should correlate with the level of sintering. Because of the effect of crystals on the solid state sintering mechanism, the ability of glasses to densify is also often assessed in terms of the size of the temperature range between the glass transition temperature and the formation of crystals in the material, often referred to as the working or sintering window, measured via DSC or DTA [125]. For this work the sintering window was defined as the difference in temperature between the glass transition temperature, T_g, and the first exotherm peak, T_{P1}. The onset of crystallisation was not used as this was not as clearly definable. Composition 0 Mol % strontium produced bars with a flexural strength that was close to those formed from apatite-wollastonite via a 2-stage selective laser sintering process [62]. A reduction in the size of the sintering window in the tested compositions coincides with a reduction in the flexural strength between 0 Mol % strontium and 3.12-69.35 Mol % strontium. Though a significant difference was not achieved, the increase in mechanical strength observed between compositions 3.12 and 6.24 Mol % strontium must be due to a factor other than the size of the sintering window. As previously discussed, this increase may be due to an increase in the amorphous content of the material, enhancing viscous flow sintering. This is supported by the reduction in both width and breadth of the bars compared to composition 3.12 Mol % strontium. There was very little increase in the amorphous phase ratio between compositions 6.24 and 9.35 Mol % strontium (though the values calculated in chapter 3 may be incorrect due to intensity mismatches, as discussed) and so the significant reduction in flexural strength may be due to the large reduction in the sintering window. It may also be due to the loss of necking due to liquid phase sintering, which was observed from the morphology of the particles. The lack of viscous flow (as a result of a small working window) and low levels of liquid phase sintering in the sample is evident in the increase in breadth and width compared to the other compositions. The increase in flexural

strength for composition 12.47 Mol % strontium compared to all other compositions correlates with the increase in densification as a result of advanced liquid phase sintering. The flexural strength of the scaffold may also be affected by the loss of the silicate phase, as previously identified via XRD, the crystallisation of fibrous wollastonite has been shown to strengthen apatite-wollastonite glass ceramics [135, 139]. Though this may contribute to the reduction in flexural strength, it does not explain the increases observed in composition 6.24 Mol % strontium compared to 3.12 Mol % strontium (though not significant) and the increase in composition 12.47 Mol % strontium compared to all other compositions. The flexural strength of glass ceramics has been shown to increase as the crystal volume percentage increase up to 40% and drops off after 60% [156]. The crystallinity of the glass ceramics tested peaks in composition 0 Mol % strontium at 60 % before dropping off. This may contribute to the reduction in flexural strength of the material.

The porosity of the sample not only determines the mechanical properties of the scaffolds, but also contributes to its ability to support neo-bone formation. Though this work was not focussed on optimising the porosity of the material, the presence of pores was still considered essential for subsequent oesteogenic potential assessment. The minimum pore size to support bone growth was originally shown to be 100µm [50, 157], though smaller pores will still form osteoid and show signs of mineralisation. What has since shown to be more important is the presence of and size of interconnected porosity [158]. The interconnection size (cross-section) should be a minimum of 100µm for the formation of new bone [159]. This is in part due to new bone formation requiring a blood supply, which requires neovascularisation which in turn requires an interconnected porosity large enough to accommodate capillaries [160]. The pores formed in compositions 0-9.35 Mol % strontium were irregular in shape but had cross sections that ranged from 45-200µm. Though most pores were smaller than 100µm in at least one dimension. This was also the case with the interconnected porosity. Although the materials were highly interconnected, the porosity was narrower than the 100µm lower limit stated in the literature. However, the materials being produced were to be used for initial assessment of the effect of the chemical/crystal composition on bone forming cells and the porosity, as stated, was not be optimised. The porosity that was achieved was suitable for *in vitro* studies where endothelial cells (capillary wall forming cells)

would not be present and as such true neobone formation would not be possible, even with an ideal porosity.

Investigation of the fracture surface revealed that all samples failed by a brittle fracture mechanism, as would be expected for a glass ceramic. In compositions 0-9.35 Mol % strontium the fracture surfaces do not lie in a single plane. This is due to the highly porous structure and irregular shape and distribution of the sintered particles. High magnification images of the fracture surfaces revealed that fracture had occurred in both the glass matrix and crystalline phases. The lack of definable structures in composition 0 Mol % strontium indicates that the phases are well distributed and interdispersed and matches the fracture surfaces reported by Kokubo [139]. However, EDX revealed a magnesium rich phase around the particle perimeter. This is likely to be the silicate phase, which was shown to take on magnesium and form via a surface nucleation mechanism. The surface nucleation mechanism was shown to reduce with increasing strontium substitution and this may explain the increase in the amount of the magnesium rich phase observed in the bulk in higher strontium containing compositions. EDX of composition 9.35 Mol % strontium revealed areas of high magnesium that were a continuation of the silicate surface crystals and showed a similar morphology when in the bulk. This was also observed in composition 6.24 Mol % strontium, but to a lesser extent. This indicates that the crystals are not limited to nucleation or growth on the surface of the material. The morphology of the magnesium rich phase was not visible via non-elemental analysis, suggesting that it lies within another phase, most likely an amorphous phase. The same morphology was not observed in compositions 0-3.12 Mol % strontium, but it was also not observed on the surface of the material.

As the strontium levels increased, crystals became visible on the fracture surface. These crystals grew in size with increasing strontium substitution. The crystals are likely to be the apatite crystals resting within a residual glass matrix. Though this was not confirmed with EDX, the highly crystalline areas did correspond to areas depleted in magnesium, suggesting that they were the apatite phase. The apatite phase was shown to take on strontium as the strontium content of the parent glass increased and it has been reported that this leads to an increase in the size of apatite crystals formed [91]. In composition 6.24 Mol % strontium, an area of crystals has been exposed at the fracture surface. This was observed only in two places on the

fracture surface, but was included as it demonstrated how the crystals of the surface continued into the bulk of the material. The crystals are a continuation of what was previously identified as the apatite phase, but may contain both the silicate phase and glass [88, 89, 135, 141]. The crystals are likely to have been exposed by flow of the amorphous phase during sintering. The formation of crystals in the glass ceramics has been shown to increase their flexural strength by deflecting a propagating crack [156]. In compositions 9.35-12.47 Mol %, there were regions of high crystallinity and also areas that appeared much smoother. The smoother areas are likely areas with a higher glass content. They display the fracture surfaces associated with a glass [156]. In composition 12.47 Mol % strontium, the smooth regions correspond with areas of high magnesium. The reduction in the weight percentage of the silicate phase in this composition would leave higher levels of magnesium in the residual amorphous phase, again indicating that the smooth regions may be areas where the glass has fractured. The increase in the amount of glass fracture sites would reduce the flexural strength of the material and so the increase that was observed is likely due to enhanced densification and reduction in porosity that was observed in the composition.

Chapter 5: Biological Assessment

5.1 Introduction

The materials developed in this work were next assessed for their biocompatibility. In order to be of use for the formation of a bone replacement device the materials investigated here must be biocompatible. With calcium phosphate glasses and ceramics this can take the form of being able to form a surface apatite layer when submerged in biologically relevant solutions. Ceramics and glasses able to form a surface apatite layer are often referred to as bioactive. The materials must also be biocompatible, in that they illicit no negative response from the body when implanted. Biocompatibility can be investigated *in vitro* by monitoring the response of cells exposed to the material. The materials may also be bioactive in that they are capable of directing the response of cells, such as their rates of proliferation, migration and differentiation down a desired lineage.

Biocompatibility testing took two forms: the ability of the materials to form a surface apatite layer following submersion in simulated body fluid and the interaction of the materials with primary human mesenchymal stem cells. Saos-2 osteosarcoma cells were used as positive controls for expression of alkaline phosphatase and of mineralisation. Soas-2 are a non-transformed cell line that display osteoblastic like properties and features and their use as a permanent cell line allows for comparison between groups and experiments. Cylindrical scaffolds were utilised and formed using the same heat treatments that were previously reported. The scaffolds were then submerged in SBF for up to 7 days and assessed via pH measurements of the reacted SBF and via SEM and EDX analysis of the scaffold surfaces. To test the interaction of cells with the scaffold, human mesenchymal stem cells were isolated from knee explants and expanded *in vitro*. The cells' ability to differentiate and their expression of known MSC markers was then assessed via flow cytometry. The method by which cells were seeded on to the scaffolds was then optimised using SEM. SEM was also used to observe the cells ability to proliferate across the scaffold surface. The ability of the cells to undergo osteogenic differentiation on the materials was assessed via pNPP alkaline phosphatase assay with the results normalised to DNA.

5.2 Experimental Methodology

5.2.1 Scaffold Formation

Porous discs were formed of dimension 2mm diameter by 3mm depth using graphite moulds (Grade EE250, Tokai Carbon) and the heat treatment reported in chapter 2.

5.2.2 Simulated Body Fluid (SBF) Analysis

5.2.2.1 SBF Preparation

Simulated body fluid solution was made up according to BS ISO 23317/2007- Implants for surgery – *in vitro* evaluation for apatite-forming ability of implant materials. The solution was made up in a 1000ml plastic beaker that had not been used for any other purpose. A stirring bar was placed in the beaker which was then set in a water bath on a heated stirring plate and covered with foil. 700ml of ion-exchanged water was added to the beaker, a temperature probe was added and the water heated to 36.5±1.5°C. The reagents shown in table 50 were then sequentially dissolved in the water.

Table 50: The reagents used in the preparation of SBF solution.

Order	Reagent	Amount (g)	Purity	Supplier
1	NaCl	8.035	99.5	Sigma-Aldrich
2	NaHCO3	0.355	99.5	Fisher Scientific
3	KCl	0.225	99.5	Sigma-Aldrich
4	K2HPO3•3H2O	0.231	99.0	Fisher Scientific
5	MgCl2•6H2O	0.311	98.0	Fisher Scientific
6	c(HCl) = 1mol/l	39 (ml)	N/A	Sigma-Aldrich
7	CaCl2	0.292	95.0	Sigma-Aldrich
8	Na2SO4	0.072	99.0	Fisher Scientific
9	TRIS	1.18	99.0	Fisher Scientific
10	c(HCl) = 1mol/l	0-5 (ml)	N/A	Fisher Scientific

Reagents were added slowly to minimise temperature or pH fluctuations. $CaCl_2$ was in granular form and each granule was added individually and allowed to dissolve before another was added. Each reagent was only added after the previous had fully dissolved. The graduated cylinder was rinsed with HCl before it was used to measure the volume of HCl. Reagents KCl, $K_2HPO_4 \cdot 3H_2O$, $MgCl_2$, $CaCl_2$ and Na_2SO_4 are hydroscopic so were measured as quickly as possible. A pH electrode was added prior to the addition of TRIS and the pH found to be 2.0±1.0. The solution was made up to 900ml and then heated to 36.5±1.5°C. TRIS was added to solution a small amount at a time whilst maintaining the temperature at 36.5±0.5. Each addition of TRIS was allowed to fully dissolve and the pH to stabilise before the next addition. TRIS was added until the pH was raised to 7.45±0.01 at 36.5±0.5. HCl was then added to lower the pH to 7.42±0.01 TRIS was then added to bring the pH to ≤7.45. The process was then repeated until all the TRIS had been dissolved. The pH of the solution was then adjusted to 7.40 at a temperature of 36.5°C using HCl. The electrode was removed and rinsed above the beaker so that the washings were added to the solution. The solution was then transferred to a 1000ml volumetric flask and ultra-pure water was added up to the mark. The solution was then allowed to cool to 20°C, at which point ultra-pure water was added to bring the final solution volume up to 1000ml. The solution was then stored at 5°C for up to 28 days before use. The solution remained clear throughout the process. Had precipitate formed, the solution would have been discarded.

5.2.2.2 Specimen Soaking

The sintered discs were rinsed with ultra pure water and dried. 15ml centrifuge tubes were then rinsed with the SBF solution. The nominal surface area of the scaffolds, S_A, calculated from the disc radius, r, and height, h, equation 26, was used to calculate the volume of SBF, V_s, to add to each sample, equation 27.

$$S_A = 2\pi r^2 + 2\pi rh$$

Equation 26

$$V_s = S_A/10$$

Equation 27

4.3ml of SBF was added to each tube and heated to 36.5°C in an incubator. The samples were then added and positioned as in figure 87. The samples were held at 36.5°C and left to soak for 0, 1, 3 and 7 days. After the desired soaking period, samples were removed and washed gently with ultra-pure water and dried in a desiccator. The pH of the SBF solutions was then measured at 36.5°C using a calibrated pH electrode. The dried samples were then attached to aluminium SEM stubs with carbon adhesive pads and imaged using a Hitachi S3400N variable pressure SEM. EDX was also performed on the surface of the scaffolds using a Bruker XFlash detector and analysed with Quantax analysis software.

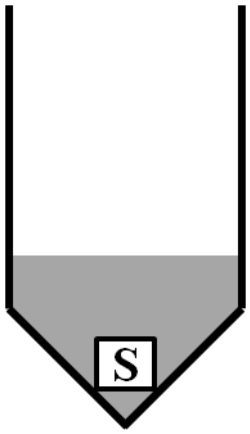

Figure 87: Sample (S) positioning for SBF soaking.

5.2.3 Cell Culture

5.2.3.1 Culture Conditions

All cell culture was performed in a sterile class II hood. All reagents used were sterile. All cultures were incubated at 37°C in a 5% CO_2 atmosphere at near 95% humidity. T175 tissue culture flasks with gas exchange lids were used for cell expansions. Basal media consisted of Dulbecco's modified eagle medium (DMEM) + 10 % FBS (unless stated) + 1 % penicillin streptomycin (all from Sigma-Aldrich). Osteogenic media consisted of basal media + 5mM β-glycerophosphate + 50µg/ml ascorbic acid + 10 nm dexamethasone (all from Sigma-Aldrich). Where osteogenic media was used, cells were first allowed to attach in basal media and osteogenic media was added after 24 hours (day 0). Harvesting of cells was done with 0.1% trypsin-ethylenediaminetetraaceticacid (trypsin-EDTA). All cell counting was done using a haemocytometer. Observation of cells during culture was done using a phase contrast microscope. Cells were passaged as they approached 75-90%

confluence and were not allowed to exceed 90% confluence. Primary cells were used up to but not exceeding passage 5. The passage of cell line Saos-2 was recorded prior to use.

5.2.3.2 Mesenchymal Stromal/Stem Cell (MSC) Isolation

Femoral condyles removed from patients undergoing total knee arthroplasty at Harrogate District Hospital were collected. They were then minced into sections roughly 20mm in diameter using a surgical clamp and scissors. The bone fragments were then placed in adherent petri dishes along with basal media containing 15% foetal bovine serum (FBS). Bone fragments were cultured for 3-4 days in an incubator, after which the fragments were removed and the cells were cultured for a further 10 days or until a confluence of 20-50% was achieved. The media was changed every 3-4 days. The cells were then harvested and seeded at a density of 1000 cells.cm^2. The donor information of the isolated cells are shown in table 51.

Table 51: Donor information for the primary mesenchymal stem cell lines.

Cell Donor Reference	Sex	DoB	BMI	Smoker	Diseased
K17	Male	03/12/49	Not Available	No	Arthritis
K28	Male	26/03/49	26.6	No	Arthritis
K41	Female	18/07/49	25.6	No	Arthritis
K56	Female	06/12/45	35.5	No	Arthritis

5.2.3.3 Osteogenic differentiation capacity via alkaline phosphatase (ALP) and von Kossa straining

MSC and Saos-2 human carcinoma cells were seeded onto adherent 24 well tissue culture plates at a density of 10,000 cells/cm^2 and cultured in basal and osteogenic media for 21 days. After 21 days culture, cells were stained for extracellular ALP using a Fast Red stain (Sigma-Aldrich) and mineralisation using a von Kossa stain (Sigma-Aldrich). The ALP mixture was made up of 0.2mg/ml naphthol in 1% N,N-dimethylformamide diluted in 0.1M Tris (Sigma-Aldrich) pH 9.2 plus 1mg/ml Fast Red TR. The solution was then filtered. A 1% silver nitrate solution was made up for the von Kossa staining by dissolving 100mg silver nitrate in 10ml distilled H_2O. Cells were washed twice with phosphate buffered saline (PBS). The filtered ALP reagent mix was then added and the cells left for 2 minutes. The cells were then washed a further two times with PBS. 4% paraformaldehyde was added to and the

cells left for 5 minutes before being washed with PBS and then with distilled H_2O. 1% silver nitrate solution was added and the samples left on a light box for 15 minutes. The samples were then washed three times with distilled H_2O. 2.5% sodium thiosulphate was added and the samples left for 5 minutes. The samples were then washed twice with distilled H_2O before being left in 20% glycerol in PBS solution. The samples were then imaged..

5.2.3.4 Flow Cytometry

Cells were analysed via flow cytometry for the surface markers shown in table 52. Media was aspirated and cells were washed twice with PBS. Cells were harvested using a 10 minute soak at 37°C in a washing buffer consisting of 0.2% bovine serum albumen (BSA) and 5mM EDTA in PBS. Cells were then centrifuged at 450g for 3 minutes and the supernatants collected. Cells were then resuspended in washing buffer and counted. An appropriate volume of cell suspension containing $50x10^5$-$1x10^6$ cells per marker was then pelleted using a 450g spin for 3 minutes. The cells were then resuspended in 100µl of washing buffer per sample. 100µl of cell suspension was then transferred to 15ml Eppendorf tubes, 1 per marker plus one marker free control, and 1ml of washing buffer was added to each tube. The tubes were the spun for 5 min at 450g at 4°C and the supernatants carefully aspirated. All cell surface markers were made up using the concentrations shown in table 52. For the fluorescein isothiocyanate (FITC)/ phycoerythrin (PE) conjugated antibodies, the pellets were resuspended in 400µl washing buffer and kept on ice in the dark until needed. For the markers requiring secondary antibodies, the cells were resuspended in 100µl washing buffer containing the PE or FITC conjugated secondary antibody (Alexa fluor 647) and incubated on ice in the dark for 30 minutes. 1ml washing buffer was then added to each Eppendorf, they were spun at 450g at 4°C for 5 minutes and the supernatants were then aspirated. Cell pellets were then resuspended in 400µl of washing buffer each and kept on ice in the dark until required. Flow cytomtery was performed on a MofLo system using the 488 nm laser with excitation/emissions at 495 nm/519 nm for FITC, 496 nm/578 nm for PE and 495 nm/519 nm for AlexaFluor. Populations were gated to exclude debris and a minimum of 10,000 cells were counted per sample.

Table 52: The markers analysed via flow cytometry.

+ve/-ve	Target	Conjugate	Concentration Used	Supplier
-	CD45	FITC	1:100/1µl	Caltag Labs
+	CD166	PE	1:50/2µl	BD Pharmagen
+	CD44	FITC	1:10/10µl	BD Pharmagen
+	CD90 Clone eBio5E10	Purified, Needs 2° Ab	1:100/1µl	ebioscience
+	CD105	Purified, Needs 2° Ab	1:100/1µl	ebioscience
+	CD29	Purified, Needs 2° Ab	1:100/1µl	BD Pharmingen
+	CD73	Purified, Needs 2° Ab	1:100/1µl	BD Pharmingen
-	CD34	FITC	1:50/2µl	Miltenyi Biotec
Secondary for use with purified antibodies				
N/A	Donkey Anti-mouse	Alexa fluor 647	1:200/0.5µl	Invitrogen

5.2.3.5 Scaffold Seeding

Scaffolds were placed in basal media and then allowed to equilibrate in an incubator at 37°C with a 5% CO_2 atmosphere. Cell cultures that were approaching but not exceeding 90% confluence were collected using a 0.1% tryspsine-EDTA solution, pelleted in a centrifuge, resuspended then counted. The volume of cell suspension, V_C, required to seed a scaffold with the required number of cells, N_C, was calculated from the cell suspension concentration, C_C, using equation 28 and the cells pelleted and resuspended in 100µL of basal media per scaffold.

$$V_C = \frac{N_C}{C_C}$$

Equation 28

The scaffolds were removed from the media and placed in individual wells of flat bottomed 96-well plates. 100µl of cell suspension, of the desired cell concentration, was then pippeted onto the surface of each scaffold, which were then placed in the incubator for 1 hour. The cell suspensions were then resuspended over the scaffold and left in the incubator for a further hour. The cell suspensions were then aspirated and the scaffolds transferred to empty wells of the 96-well plate. 200µl of fresh basal media was then added to each scaffold. Cells were cultured for 1-21 days with media changed every 3-4 days or when required. The optimum seeding density for the scaffolds was determined by seeding at concentrations $5x10^5$, $2.5x10^5$, $1x10^5$, $7.5x10^4$ and $5x10^4$. Cells were cultured on the scaffolds for 24 hours before being imaged using an SEM.

5.2.3.6 Scaffold Preparation for SEM

The media was aspirated from the constructs and they were then washed 3 times with PBS. The constructs were then fixed in 2.5% gluteraldehyde in 100mM phosphate buffer at 4°C over-night. 200mM phosphate buffer of pH 7.2-7.6 was made up from 77ml 0.2M Na_2PO_4 and 23ml 0.2M NaH_2PO_4 this was used to dilute 25% gluteraldehyde stock solution. The constructs were washed 3 times with 100mM phosphate buffer. They were then dehydrated with graded alcohol, 25, 50, 70 and 90% for 30 minutes each and then three changes of 100% for another 30 minutes each (with the last two changes utilising ultra-pure 100% ethanol). The constructs were then soaked in 100µl of hexamethyldisilazane (HMDS, Sigma-Aldrich) for 30 minutes. A fresh change of HMDS was added and the scaffolds were then left to dry overnight in a desiccator. Samples were then attached to aluminium stubs using carbon adhesive pads and sputter coated with a 6nm thick gold coating. Cells were then imaged on a S3400N variable pressure SEM.

5.2.3.7 Characterisation of MSC differentiation on the glass-ceramic scaffolds

5.2.3.7.1 Cell culture

Primary MSCs were cultured on the glass-ceramic scaffold compositions 0, 3.12 6.24 and 12.47 Mol % strontium. Cells were also seeded onto tissue culture plastic to observe if the cells were able to differentiate with the conditions used. Cells were seeded according to the seeding method previously described. Cells were cultured in 96-well plates. Cells were seeded on the scaffolds at the optimum seeding

density, $1x10^5$ cells/scaffold and on tissue culture plastic at 6400 cells per well of a 96-well plate. Sample were cultured for up to 21 days in osteogenic media. At time points 0, 7, 14 and 21 days samples were collected and the alkaline phosphatase activity and DNA content of the constructs was assessed using pNPP and PicoGreen assays, respectively. 6 scaffolds of each material were used for each time point. The experiment was repeated using 3 different donor cell lines.

5.2.3.7.2 Cell Lysis

At the desired time point, cells were washed twice with 0.2M carbonate buffer (2:1 [vol:vol] of 0.2M Na_2CO_3 to 0.2M $NaHCO_3$, pH 10.2). 150µl of the lysis buffer, (0.1% Triton-X in 0.2M carbonate buffer) was then added to each well and the samples were then treated with a freeze/thaw cycle (-80°C/37°C) three times. The samples were then pipetted up and down to fully lyse the cells. 50µl of cell solution was then added to a new 96-well plate for the pNPP assay and a further 50 µl was added to a black bottomed 96-well plate for the PicoGreen assay.

5.2.3.7.3 Alkaline Phosphatase via pNPP assay

Alkaline phosphatase activity was measured using the p-nitrophenyl phosphate (pNPP, Sigma-Aldrich) assay. This is a colourimetric assay that measures the conversion of colourless p-nitrophenyl phosphate (pNPP) to orange p-nitrophenol (pNP) in the presence of a phosphatase catalyst. The pNPP conversion is measured against a standard pNP curve. The pNP standard was made by diluting a standard solution in carbonate buffer according to table 53. 100µl of each standard concentration was added to the pNPP 96-well plate in triplicate.

Table 53: pNPP standard dilutions.

Concentration pNP	Volume Standard Solution (µl)	Volume Carbonate Buffer (µl)
0.5	20	380
0.3	12	388
0.2	8	392
0.1	4	396
0.05	2	398
0.025	1	399
0.0125	0.5	399.5
0	0	400

The working pNPP substrate was made by diluting 1 part stock solution (10mg pNPP in 9ml 0.2M carbonate buffer + 1ml 100mM $MgCl_2$) in 2 parts distilled H_2O. 50µl of the working substrate was added to each of the samples. The samples were then incubated at 37°C for up to an hour. The length of time that the substrates were incubated was noted before the absorbance of the wells was read at 405nm on a POLARstar OPTIMA microplate reader. The absorbance values were then converted to pNP levels using the standard curves and normalised to the time spent in the incubator and DNA content.

5.2.3.7.4 DNA Content via PicoGreen assay

The DNA standards were prepared using a 10µg/ml stock salmon sperm solution (Sigma-Aldrich). The solution was diluted to 100µg/ml in the lysis buffer (0.1% Triton-X in 0.2M carbonate buffer). The standards were diluted as in table 54 and 50µl of each was pipetted in triplicate into the black bottomed 96-well plate.

Table 54: PicoGreen standard dilutions.

DNA Conc. (µg/ml)	Volume of DNA (µl)	Volume of Lysis Buffer (µl)	Total Volume (µl)
8	80 (µl of 100µg/ml stock)	950	1000 (A)
4	500 of A	500	1000 (B)
2	500 of B	500	1000 (C)
1	500 of C	500	1000 (D)
0.5	500 of D	500	1000 (E)
0.25	500 of E	500	1000
0	0	500	500

A PicoGreen reagent was made up by diluting PicoGreen stock solution (Life Technologies) 1:50 in TE buffer (0.12g 10mM Tris + 0.029g 1mM EDTA made up in 100ml dH_2O and the pH set to 7.5). 50µl of the PicoGreen/TE reagent was then added to each of the samples and standards. The plate was gently shaken and then covered in foil. The plate was read at 485nm excitation and 538nm emissions on a multipurpose plate reader system. The absorbance values were then converted to DNA levels using the standard curves.

5.2.3.7.5 Statistical Analysis

Statistical analysis was performed using SPSS software. The normality of the results was first determined using a Shapiro-Wilk test. Signifcant differences were then determined using an ANOVA test for normally distributed data and a Kruskall Wallis test for non-normal data. A post-hoc Tukey test was used for multiple comparisons when a significant difference was observed.

5.3 Results

5.3.1 Simulated Body Fluid Analysis

Cylindrical; scaffolds were soaked in SBF at 36.5°C for 1, 3 and 7 days. At each time point the pH of the SBF solution after the scaffold was removed was measured using a calibrated electrode and compared to un-reacted SBF. The scaffolds that were removed were then imaged via SEM and their composition analysed via EDX.

5.3.1.1 pH

The pH of the SBF solutions following soaking of the scaffolds for 0, 1, 3 and 7 days are shown in figure 88 and table 55. All pH measurements were made at 36.5°C.

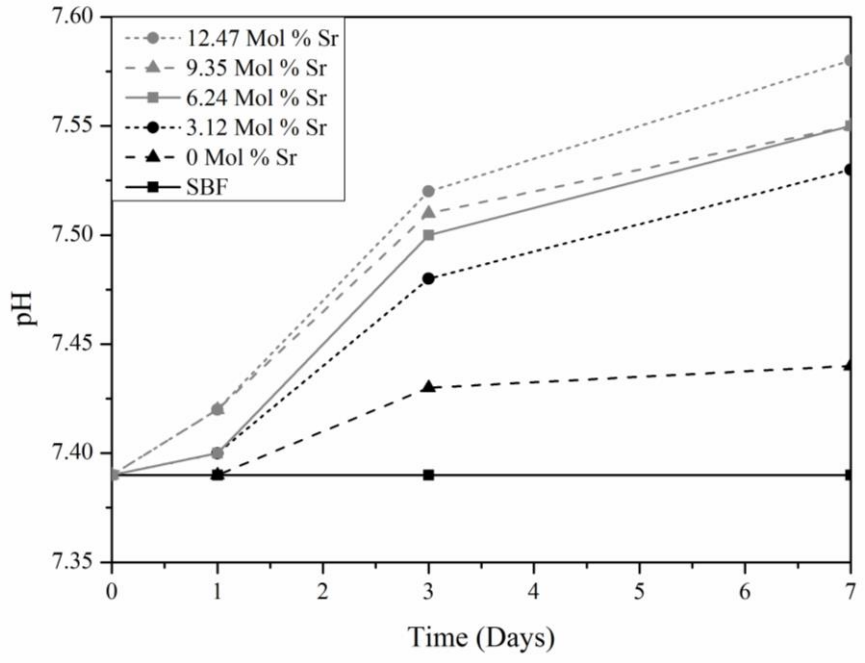

Figure 88: The pH of the SBF solution following exposure to the scaffolds for 0, 1, 3 and 7 days.

Table 55: pH of the SBF solution following soaking of glass ceramic samples.

Soaking Time (Days)	SBF	Scaffold Strontium Content (Mol %)				
		0	3.12	6.24	9.35	12.47
	pH	pH	pH	pH	pH	pH
0	7.39	7.39	7.39	7.39	7.39	7.39
1	7.39	7.39	7.4	7.4	7.42	7.42
3	7.39	7.43	7.48	7.5	7.51	7.52
7	7.39	7.44	7.53	7.55	7.55	7.58

The pH of the SBF stock solution remained constant at 7.39 for the 7 days that the experiment was run. At day 1 there was no change in the pH of the 0 Mol% strontium sample. An increase was observed in all strontium samples with a greater increase occurring in compositions 9.35-12.47 Mol % strontium. In all samples, the largest increase in pH was observed between days 1 and 3. The pH of the solution increased with increasing strontium content in the glass ceramic. By day 7 the pH of composition 0 Mol % strontium had increased by 0.04 compared to SBF alone. The pH of the strontium compositions had increased by 0.14-0.19, with a larger increase occurring with increasing strontium substitution.

5.3.1.2 SEM

SEM images of the scaffold surface following soaking in SBF for 0, 1, 3 and 7 days are shown in figures 89 to 93.

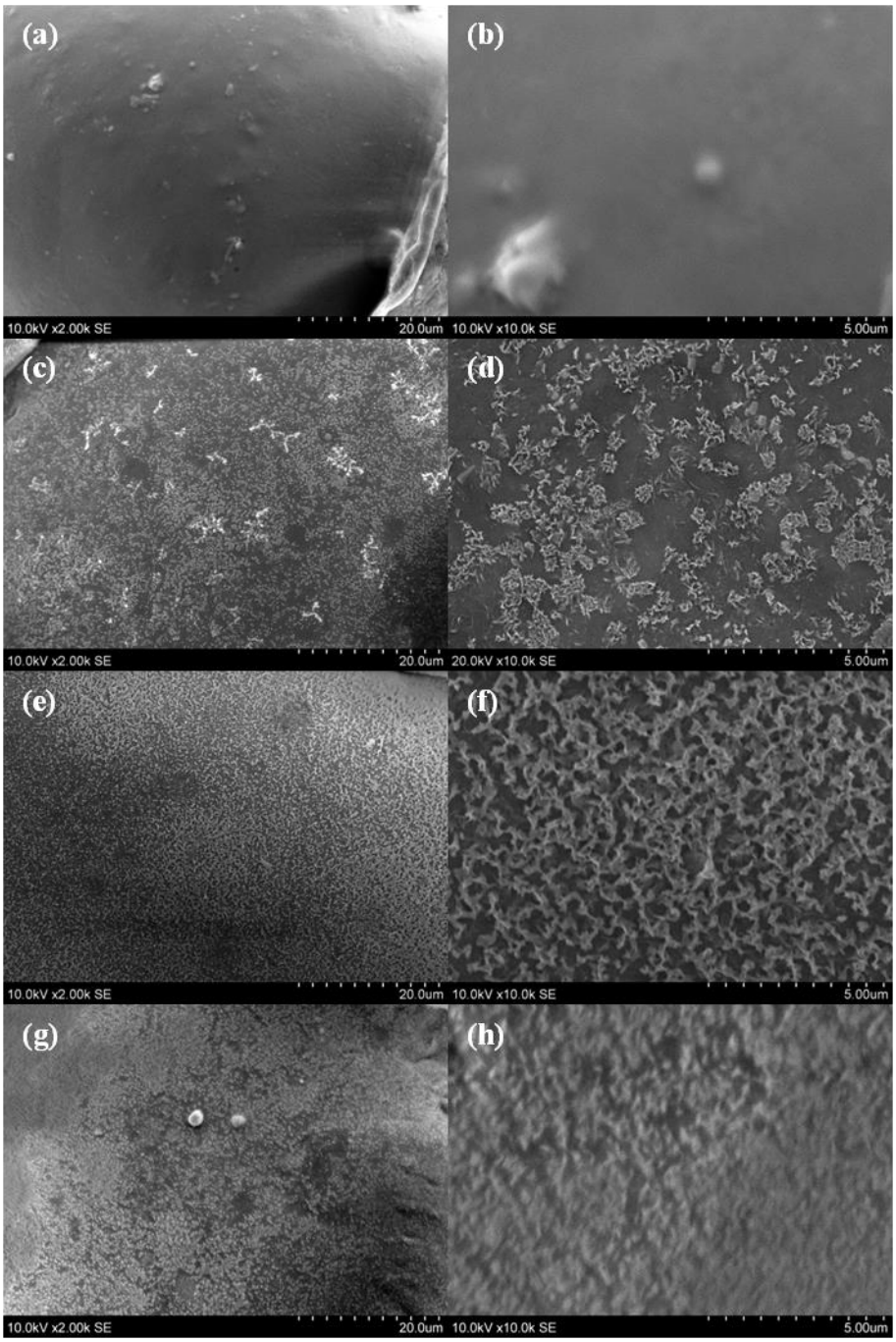

Figure 89: SEM images of the 0 Mol % strontium glass ceramic surfaces after soaking in SBF for different lengths of time. (a-b) day 0 (c-d) day 1 (e-f) day 3 and (g-h) day 7.

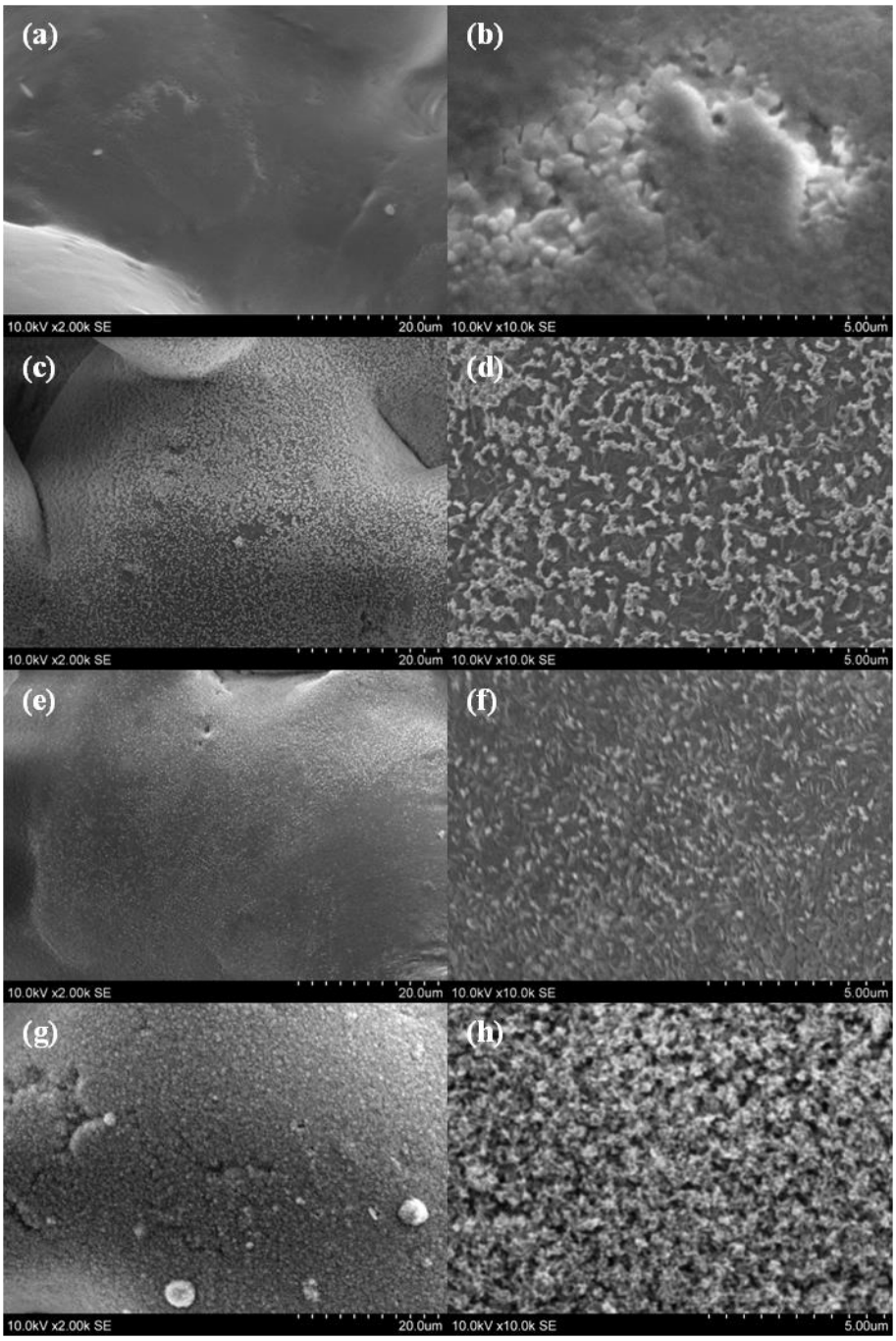

Figure 90: SEM images of the 3.12 Mol % strontium glass ceramic surfaces after soaking in SBF for different lengths of time. (a-b) day 0 (c-d) day 1 (e-f) day 3 and (g-h) day 7.

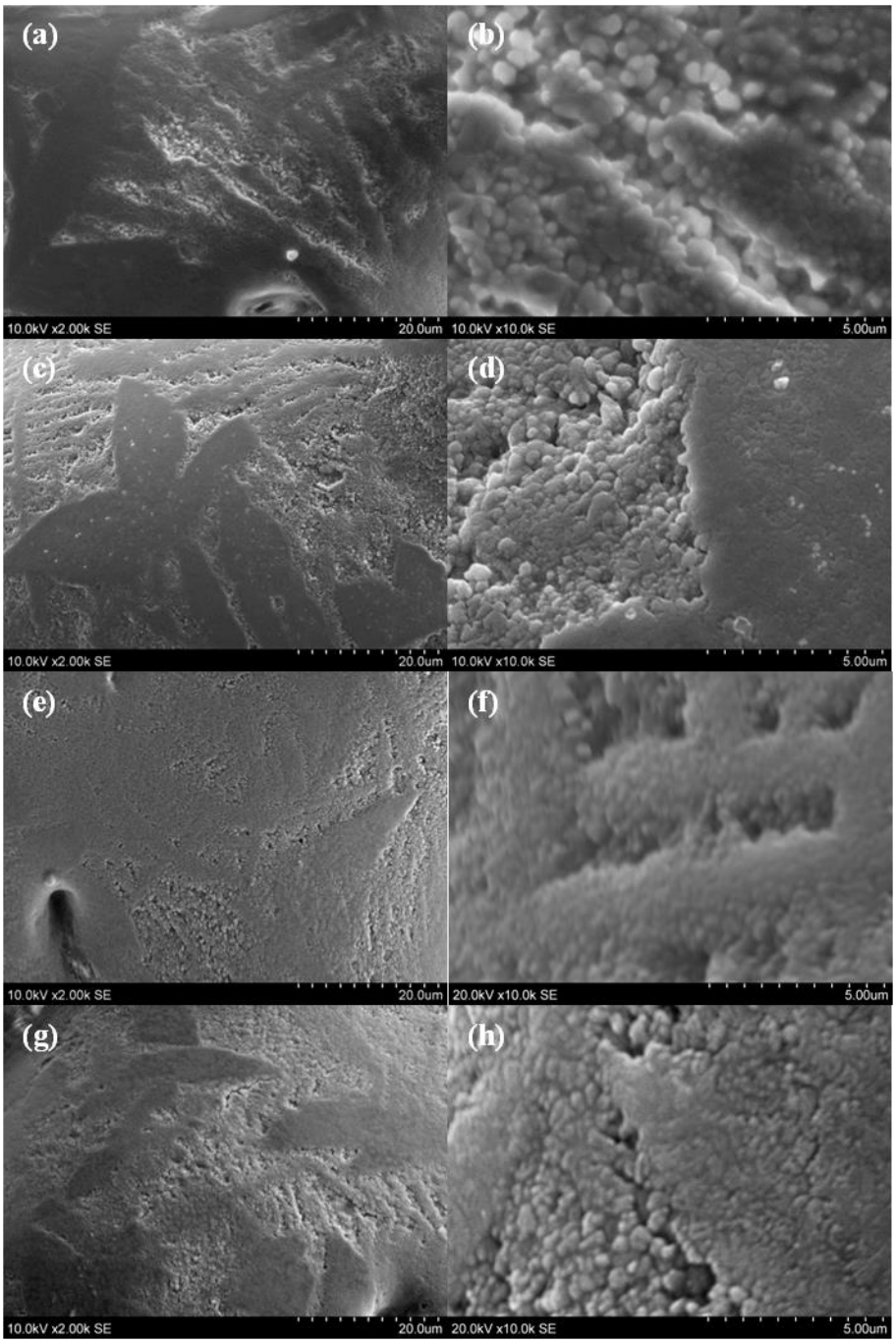

Figure 91: SEM images of the 6.24 Mol % strontium glass ceramic surfaces after soaking in SBF for different lengths of time. (a-b) day 0 (c-d) day 1 (e-f) day 3 and (g-h) day 7.

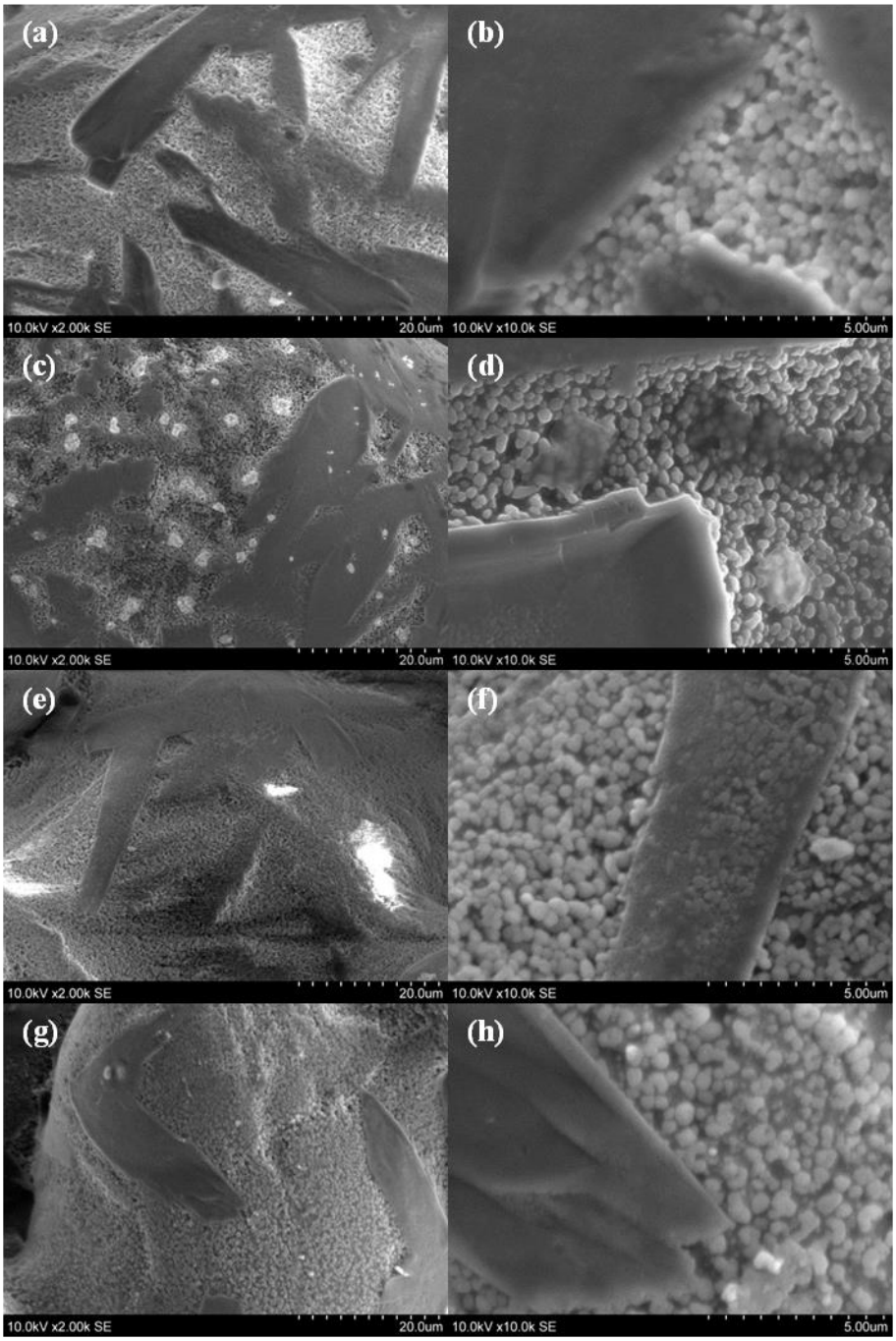

Figure 92: SEM images of the 9.35 Mol % strontium glass ceramic surfaces after soaking in SBF for different lengths of time. (a-b) day 0 (c-d) day 1 (e-f) day 3 and (g-h) day 7.

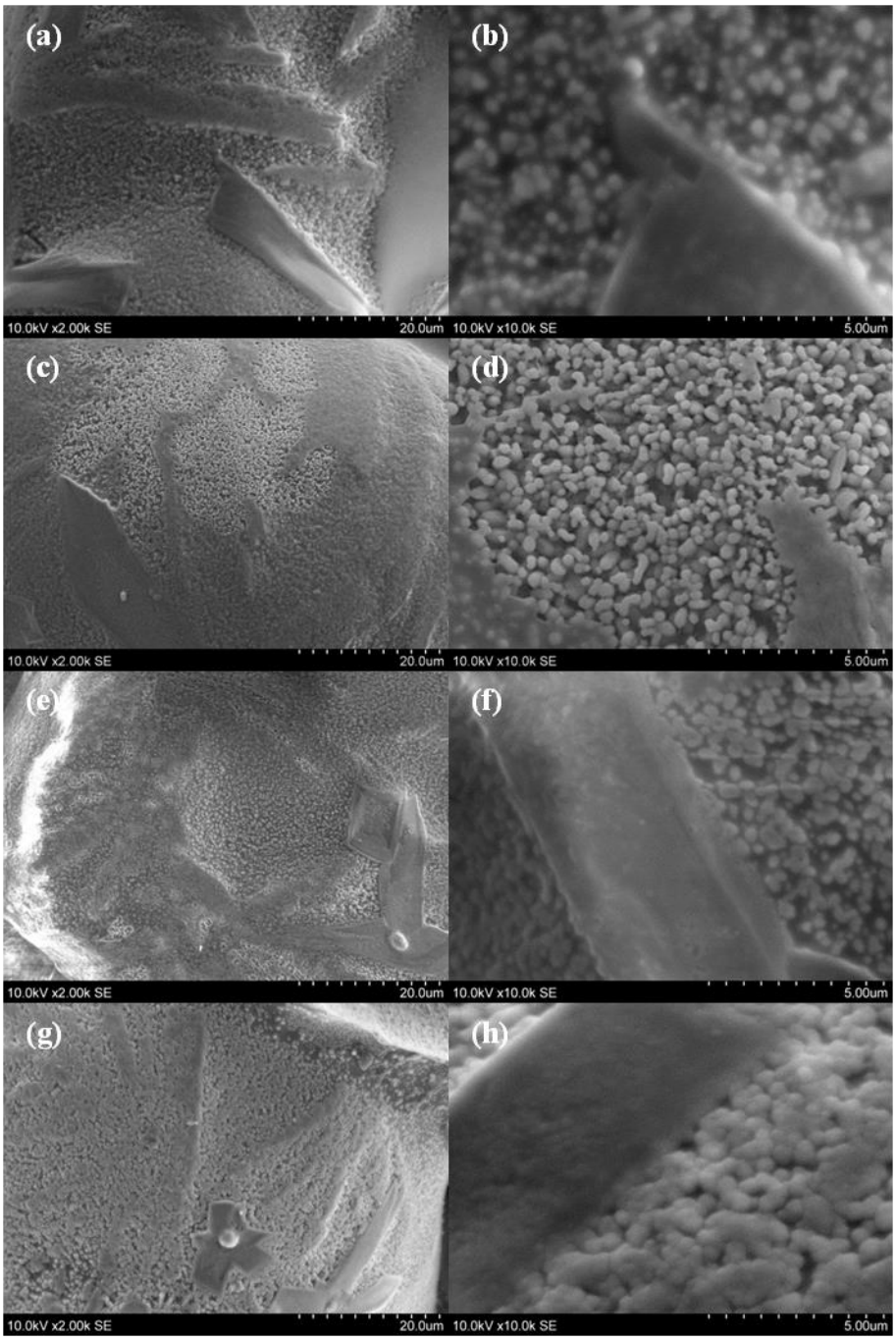

Figure 93: SEM images of the 12.47 Mol % strontium glass ceramic surfaces after soaking in SBF for different lengths of time. (a-b) day 0 (c-d) day 1 (e-f) day 3 and (g-h) day 7.

In both compositions 0 and 3.12 mol % strontium, crystals can be seen to form on the surface of the material by day 1. The crystals increase in number up to day 7 at which point they form a confluent layer on the materials surface. The crystals were not observed in compositions 6.24-12.47 Mol % strontium at any of the time points. Crystals were visible on composition 9.35 Mol % strontium at day 1 but they do not match the morphology previously observed and were not visible at any subsequent time points suggesting they are an artefact of the processing. Composition 6.24 Mol % strontium showed no change in surface morphology up to day 7. In compositions 9.25 and 12.47 Mol % strontium, the morphology of the apatite containing domains changes between days 3 and 7. The domains increase in size but no change in morphology is observed.

5.3.1.3 EDX

EDX was performed on the surface of the SBF soaked glass ceramics in order to determine any change in surface composition. The elemental ratios of silicon, phosphorous, calcium and strontium were compared as these have been shown to vary following dissolution of the surface and formation of the surface apatite layer. The results are shown in figure 94.

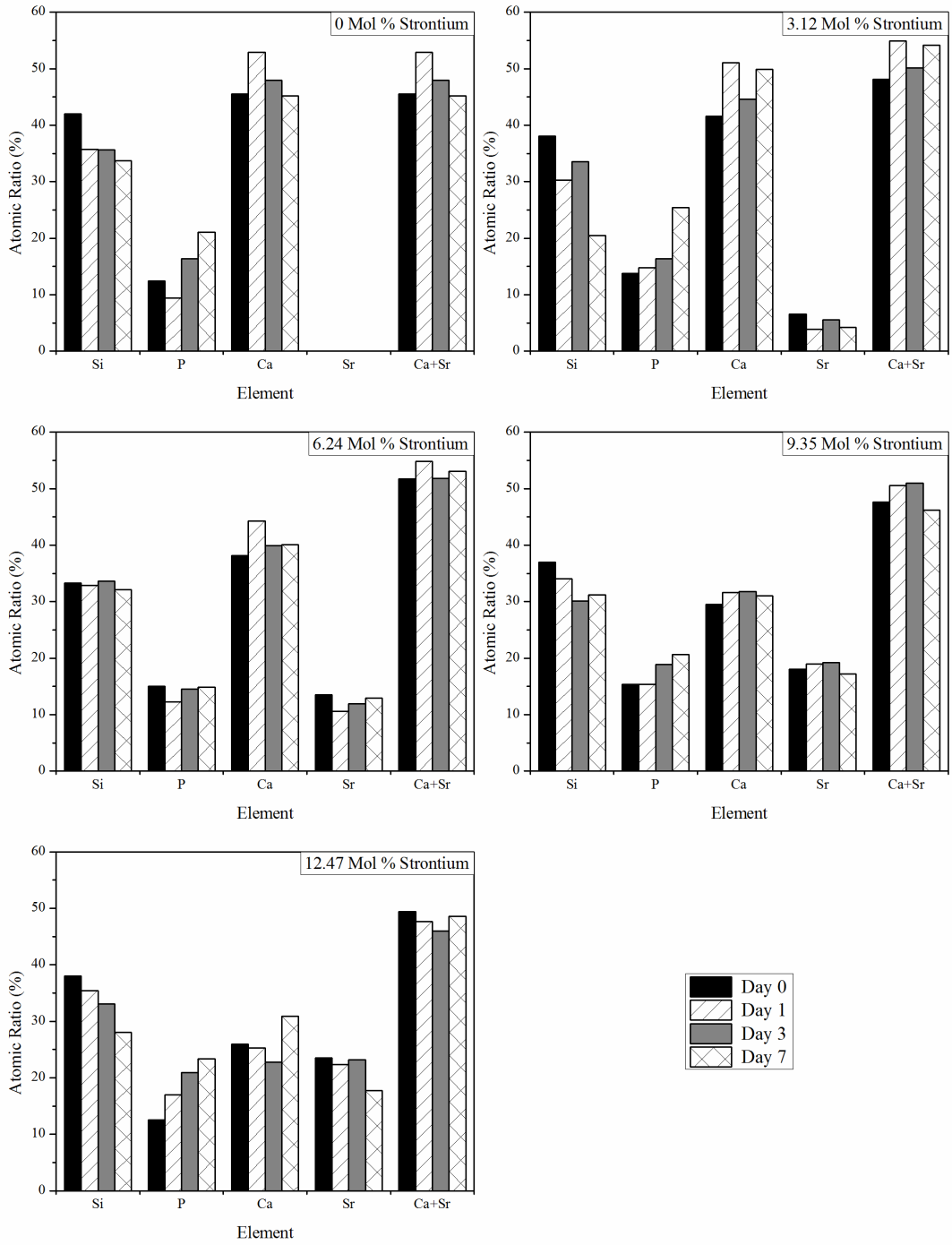

Figure 94: EDX results of the glass ceramics soaked in SBF for 0, 1, 3 and 7 days.

In all compositions except 6.24 Mol % strontium, the silicon levels decreased and the phosphorous levels increased with increasing time. In composition 6.24 Mol % strontium a small overall drop was observed in the silicon levels. A reduction in phosphorous was observed between days 0-1 followed by a gradual increase and by day 7 phosphorous levels were at the same point as day 0. Changes in the silicon and phosphorous levels were detectable from day 1. In composition 6.24 Mol %

strontium, no change was observed between the elemental ratios at different time points.The calcium and strontium levels remained relatively constant as time progressed. The ratio of calcium to strontium got smaller with increasing strontium substitution. An initial drop in the phosphorous levels was observed between days 0 and 1 in composition 0 Mol % strontium. An increase above the initial phosphorous levels was detected at days 3 and 7. In composition 3.12 Mol % strontium, an increase was observed in silicon levels between days 1 and 3 before dropping down to at day 7 to levels well below those at day 1.

5.3.2 Determination of MSC attachment and Differentiation on Strontium Containing Scaffolds

The biocompatibility of the materials was determined via observing their interactions with primary mesenchymal stem cells. To minimise the number of cells required, composition 9.35 Mol % strontium was not tested due to its low mechanical strength.

5.3.2.1 Osteogenic Differentiation

To determine the ability of the cells to undergo osteogenic differentiation, donor cell lines K28 and K17 were cultured in osteogenic media for 21 days in a static environment in 24 well tissue culture plates. MSC cell lines were compared to cells cultured in basal media and Saos-2 osteosarcoma cell lines, the results are shown in figure 95.

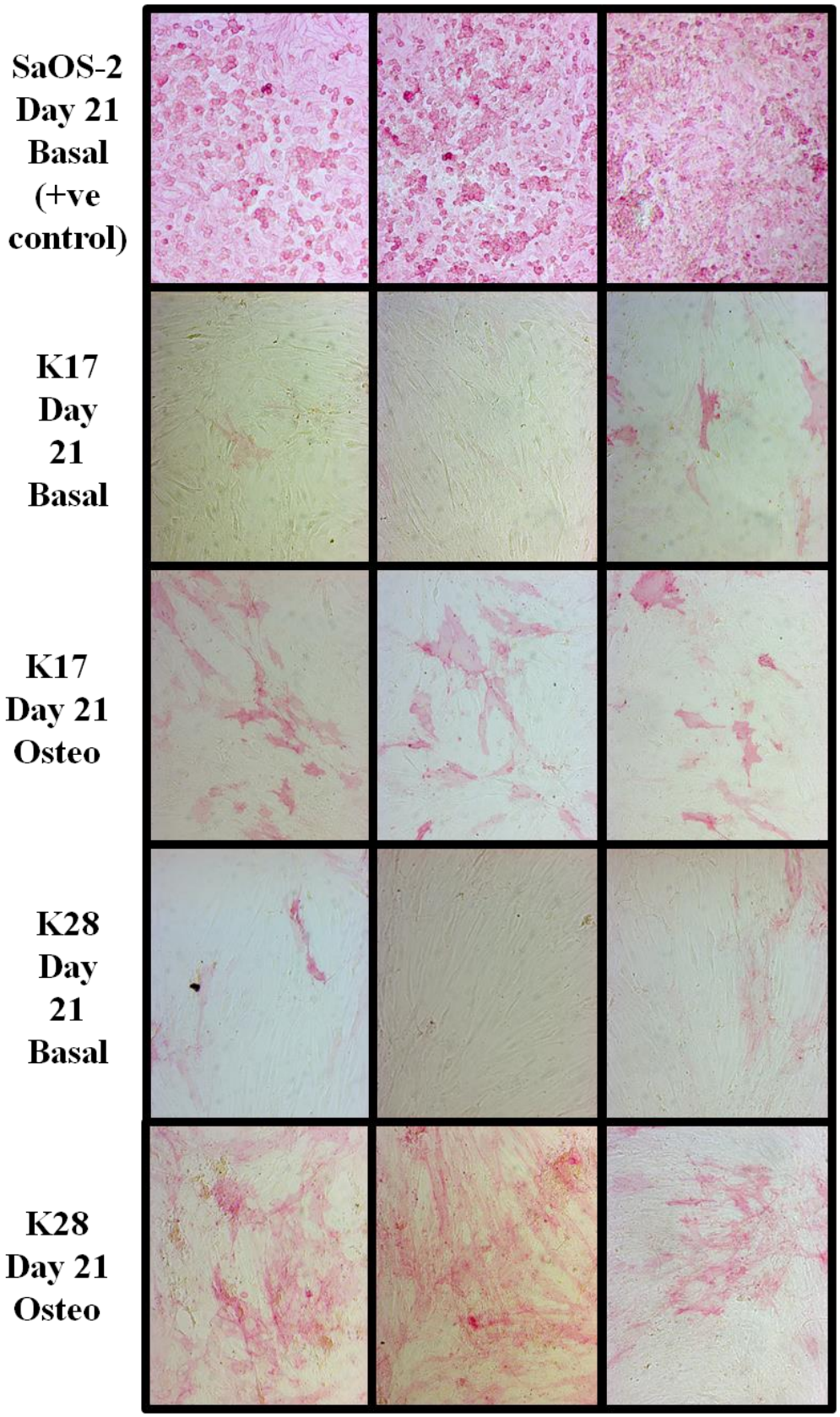

Figure 95: Alkaline phosphates (red) and von Kossa (brown) staining of MSC K28 and K17 donor lines cultured in basal and osteogenic media for21 days. Saos-2 cells are included as a positive control.

In both primary cell lines, K28 and K17, there was a small amount of red alkaline phosphatase staining following 21 days culture in basal media and very little dark von Kossa staining. The cells retained a fibroblast like morphology when cultured in basal media. In the SaOS-2 positive control there was strong alkaline phosphatase staining and very little evidence of Von Kossa staining following 21 days culture in basal media. The SaOS-2 cells had a rounded, osteoblast like morphology. An increase in alkaline phosphatase activity was observed in both primary MSC cell lines following 21 days culture in osteogenic media compared to culture in basal media. Higher alkaline phosphatase activity was detected cells K28 than K17. Small levels of von Kossa staining were observed following 21 days culture in osteogenic media.

5.3.2.2 Flow Cytometry for MSC Surface Markers

The donor cell lines that were used for subsequent biological assessment were assessed via flow cytometry for surface markers known to be present or absent on the surface of mesenchymal stem cells. The red histogram represents the control, un-labelled, population and the green the labelled population. A shift in the median to a higher value following labelling indicates the presence of the specific surface marker. The results are shown in figures 96 to 98. All cell lines were positive for CD44, CD90, CD105, CD29 and CD73 whilst being negative for CD45 and CD34. CD166 was positive in cell line K41 and 56 but negative in K28.

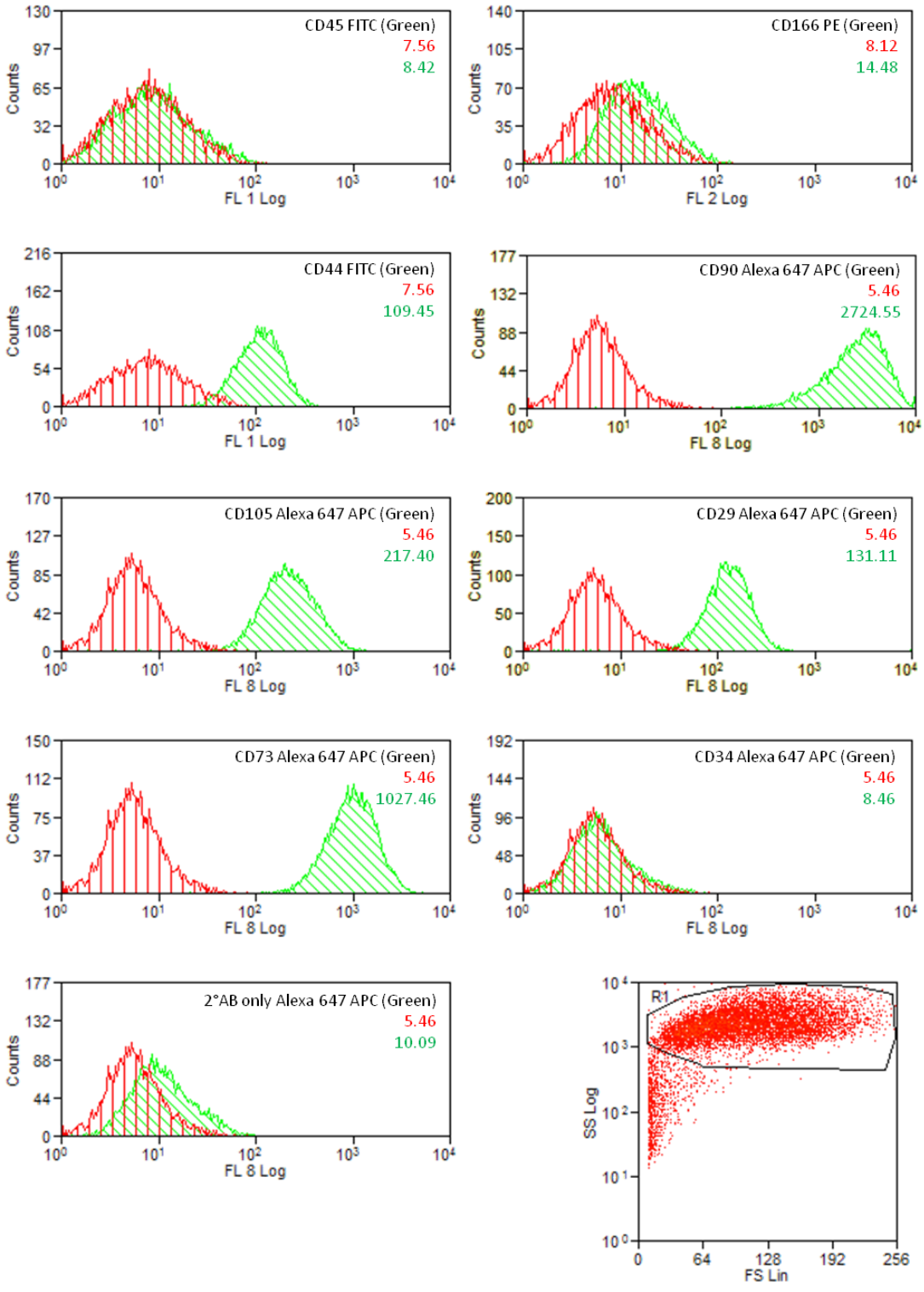

Figure 96: Flow cytometry results for donor K28. RED = control median GREEN = sample median. The surface marker and label used are also shown.

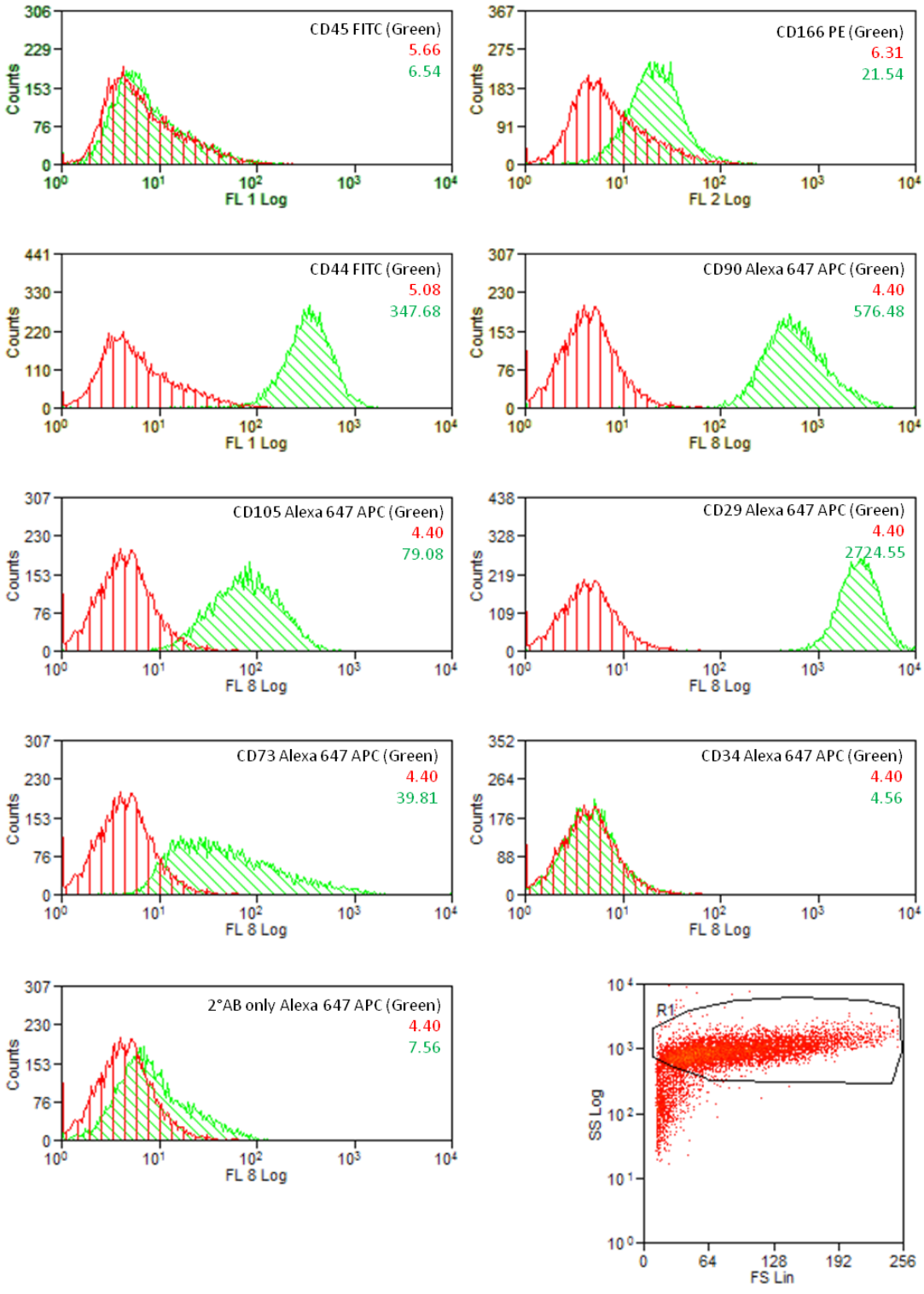

Figure 97: Flow cytometry results for donor K41. RED = control median GREEN = sample median. The surface marker and label used are also shown.

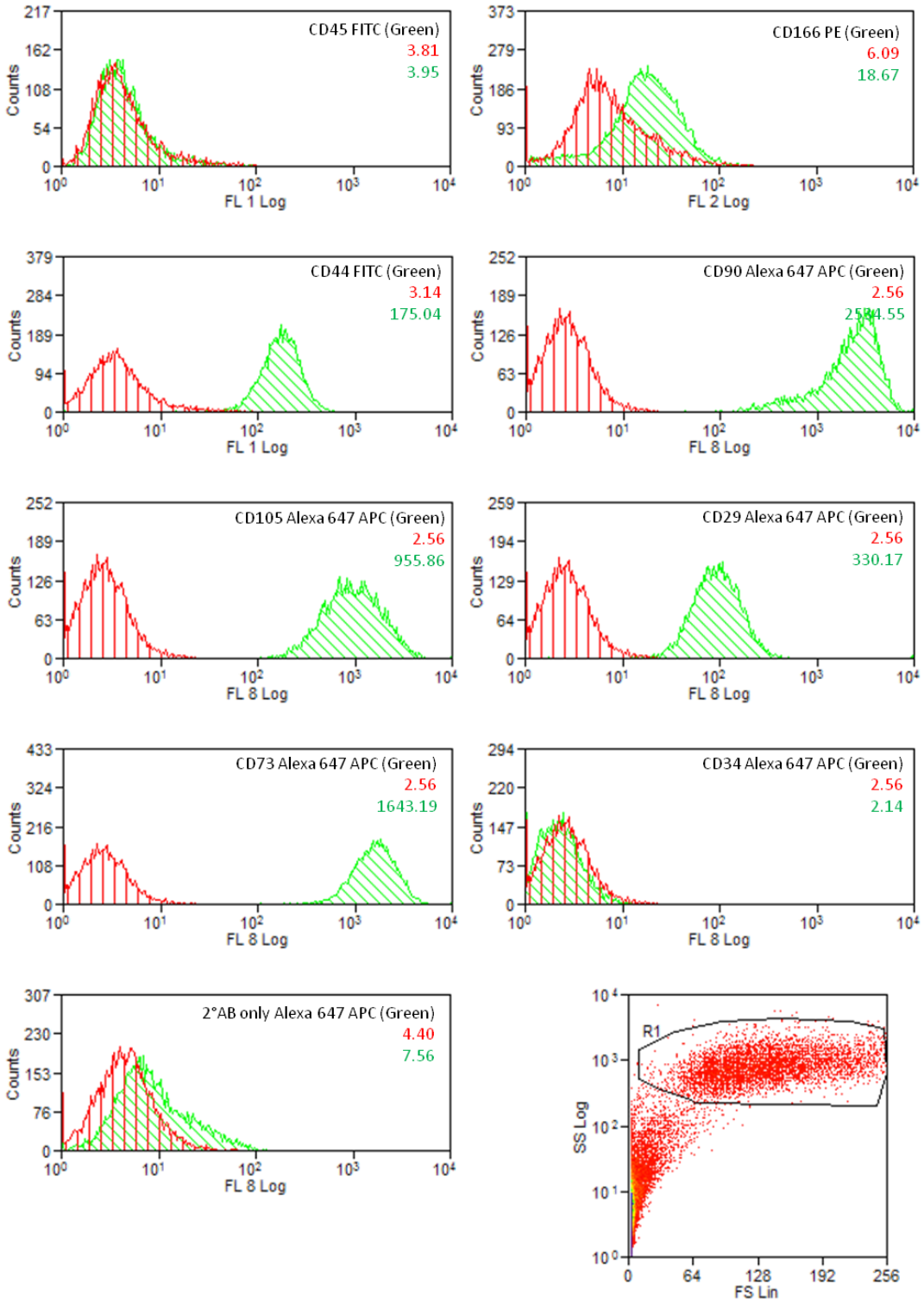

Figure 98: Flow cytometry results for donor K56. RED = control median GREEN = sample median. The surface marker and label used are also shown.

5.3.2.3 Scaffold Sterilisation

The strontium containing scaffolds were sterilised by a high temperature and pressure autoclave process. SEM imaging was used to determine if any change in surface morphology had occurred in the samples following sterilisation. Figure 99 shows that following autoclave sterilisation, all samples displayed the surface morphologies previously observed in samples that had not been treated, see 3 chapter 3.

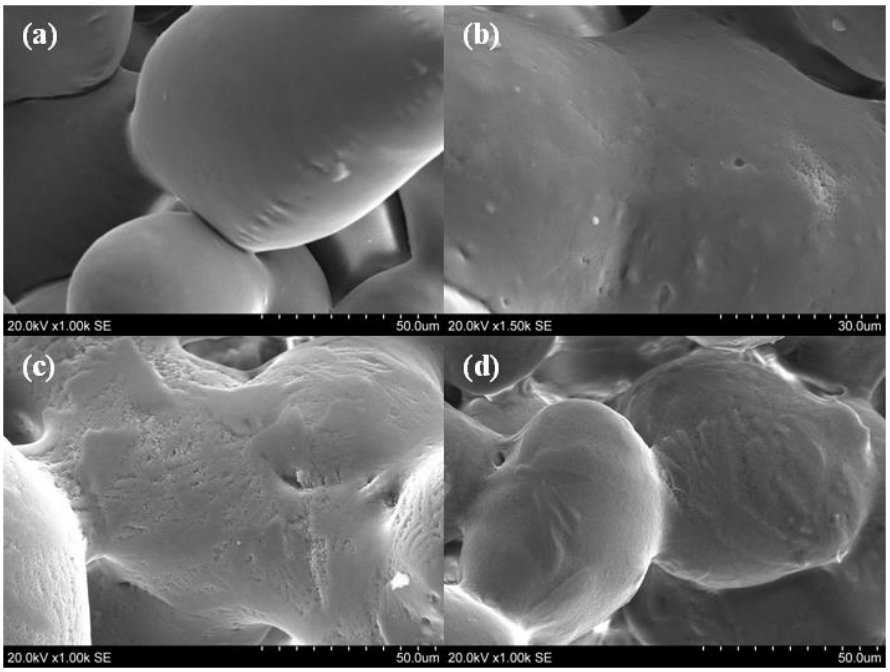

Figure 99: SEM images of the post autoclave scaffold surface (a) 0 Mol % strontium (b) 3.12 Mol % strontium (c) 6.24 Mol % strontium and (d) 12.47 Mol % strontium.

5.3.2.4 Optimum Seeding Density Determination

MSCs were seeded onto the cylindrical scaffolds of composition 0 Mol % strontium and cultured for 24 hours in basal media. Cells were seeded at $5x10^5$, $25.x10^5$, $1x10^5$, $7.5x10^4$ and $5x10^4$ cells per scaffold, see figures 100 and 101. The back scattered electron (BSE) images clearly show the dark cells contrasting the lighter scaffold. Cells were observed on the scaffold following each of the seeding densities tested. Individual cells are visible for seeding densities $5\text{-}7.5x10^4$ cells/scaffold. The individual cells are seen to bridge pores whilst making good contact with the material. As the seeding density increases the cells increase their connectivity and also begin to form sheets on the surface of the scaffold. Confluent

sheets are formed on the scaffolds for seeding densities 1-5x10^5 cells/scaffold. The sheets contain cracks induced by the dehydration process. The particles of the scaffold are visible through the cell layer. High magnification images reveal that in densities 2.5-5x10^5 cells/scaffold the confluent layer is multiple cells thick. However cells on the bottom layer can still be seen to interact directly with the scaffold. In concentration 1x10^5 cells/scaffold the confluent layer is predominantly one cell thick.

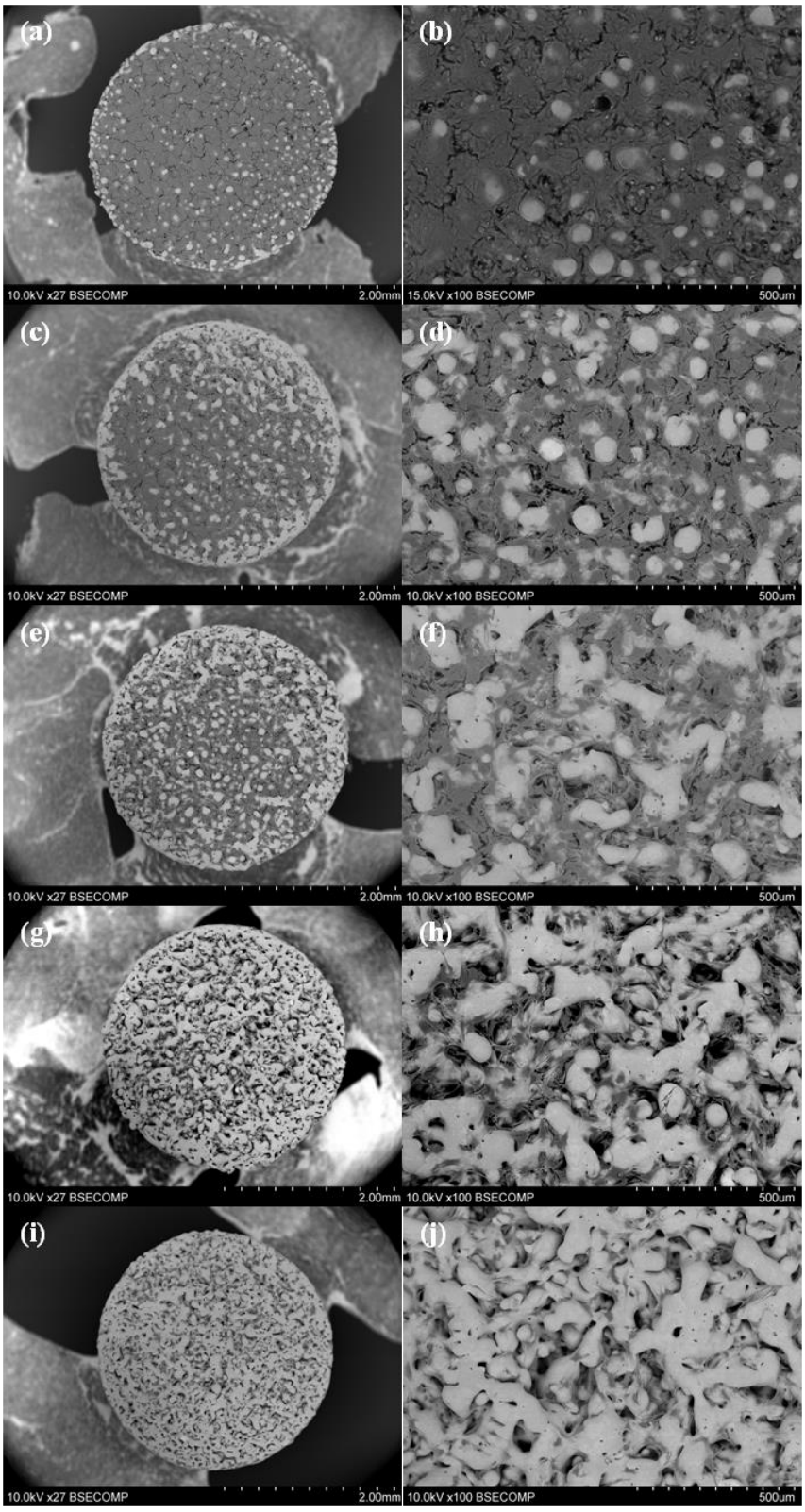

Figure 100: Optimum seeding density determination. MSCs seeded at (a-b) $5x10^5$ cells/scaffold (c-d) $2.5x10^5$ cells/scaffold (e-f) $1x10^5$ cells/scaffold (g-h) $7.5x10^4$ cells/scaffold and (i-j) $5x10^4$ cells/scaffold.

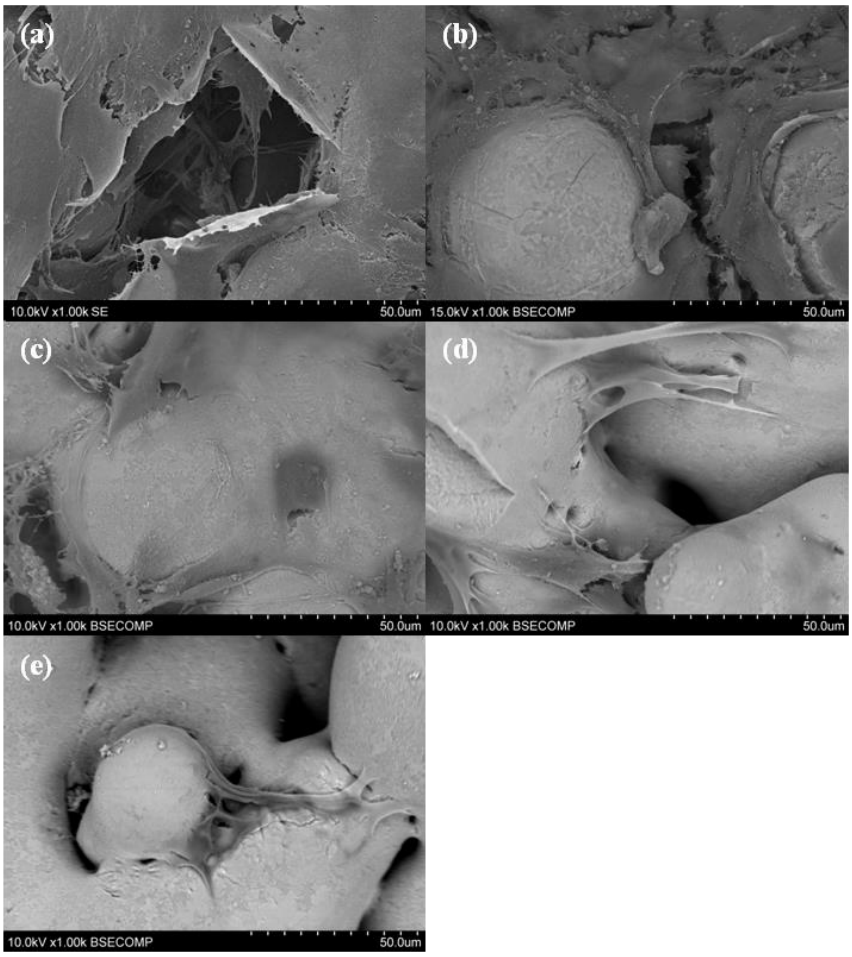

Figure 101: SE and BSE high magnification images of the optimum seeding density evaluation. (a) $5x10^5$ cells/scaffold (b) $2.5x10^5$ cells/scaffold (c) $1x10^5$ cells/scaffold (d) $7.5x10^4$ cells/scaffold and (e) $5x10^4$ cells/scaffold.

5.3.2.5 Cell Expansion on the Glass-Ceramic Scaffolds

Scaffolds were seeded at $5x10^4$ cells/scaffold (half the optimum seeding density) were cultured in basal media for up to 21 days and imaged at days 0, 7, 14 and 21 using SEM SE and EDX, figures 102 to 105. Green post analysis colouring was assigned to calcium and red to the carbon. In all samples, the calcium rich scaffolds were marked as green regions and the carbon rich cells were labelled red. The proliferation of cells across the scaffold was the same for all materials tested. Cells were isolated at day 0, residing on both the particles and within pores. At day 0 the cells can be seen to bridge pores. By day 7 the number of cells had increased. The increase in cell number also resulted in an increase in connectivity. At day 14 the cells had begun to form sheets though were not confluent. At day 21 the cells had formed near-confluent sheets. The sheets bridged pores and formed across the surface of the scaffold. Cells can be seen in the pores below the confluent sheets.

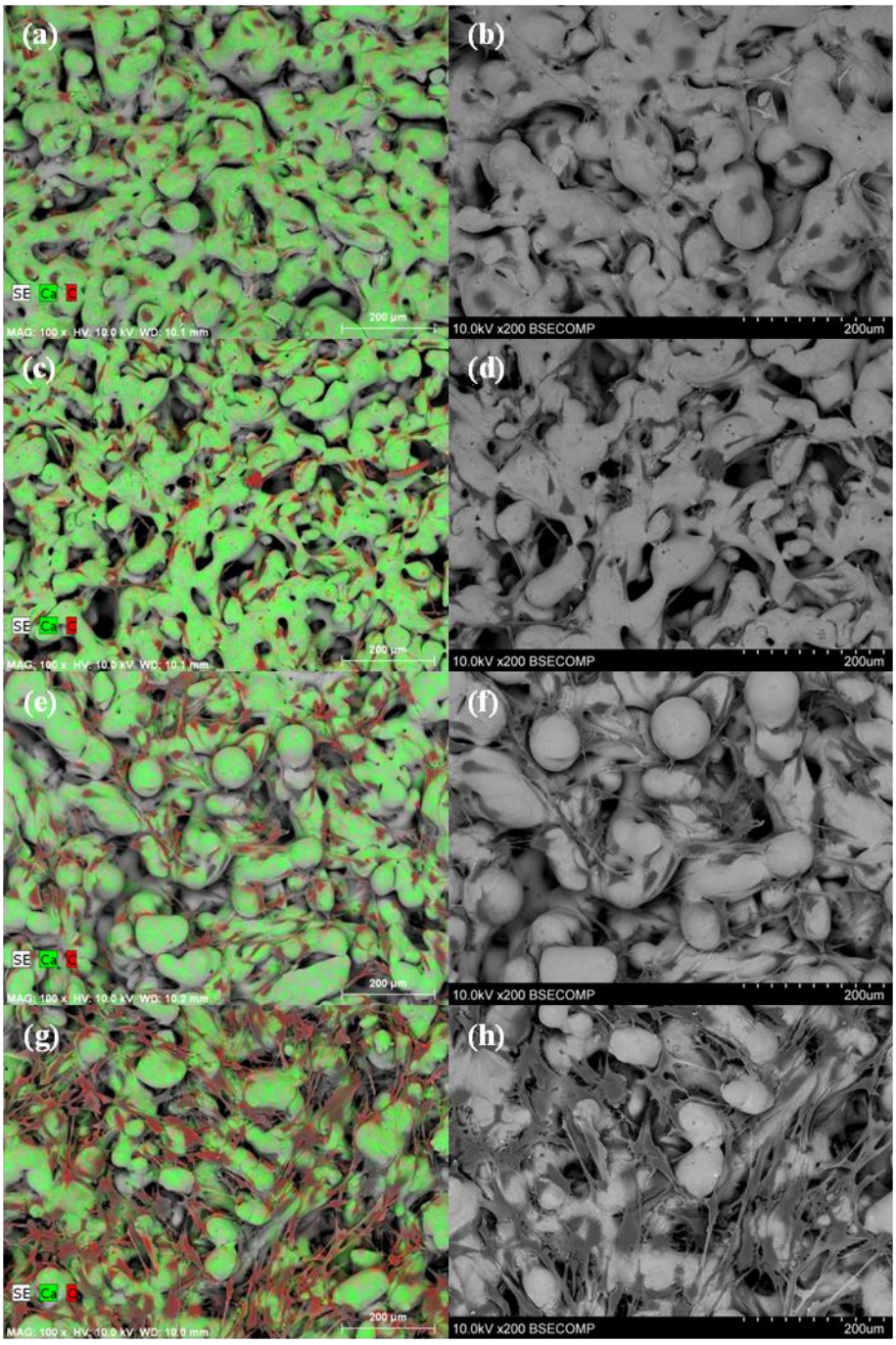

Figure 102: EDX (left) and SE (right) SEM images of the cell number expansion of MSCs seeded on composition 0 Mol % strontium at (a-b) day 0 (c-d) day 7 (e-f) day 14 and (g-h) day 21.

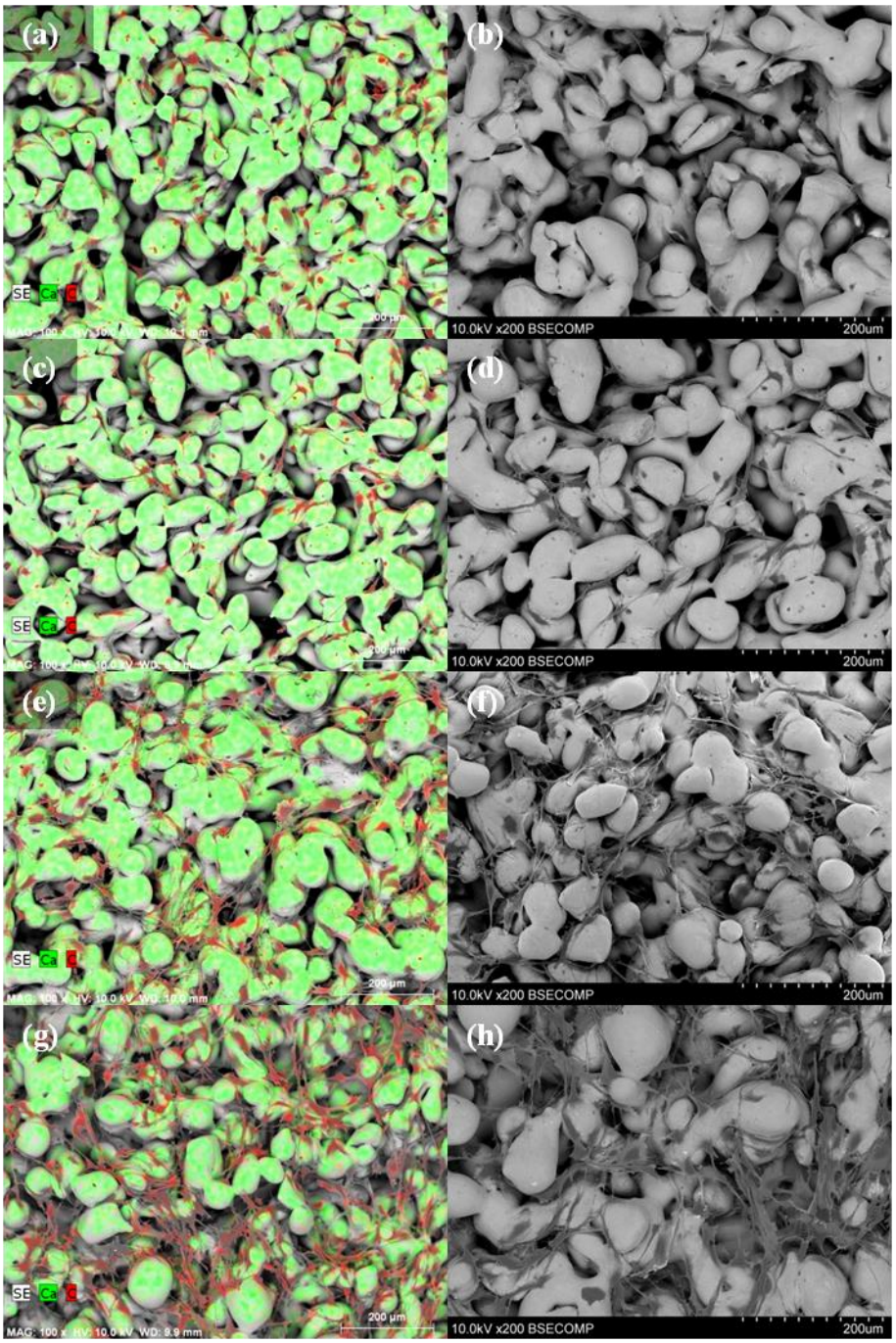

Figure 103: EDX (left) and SE (right) SEM images of the cell number expansion of MSCs seeded on composition 3.12 Mol % strontium at (a-b) day 0 (c-d) day 7 (e-f) day 14 and (g-h) day 21.

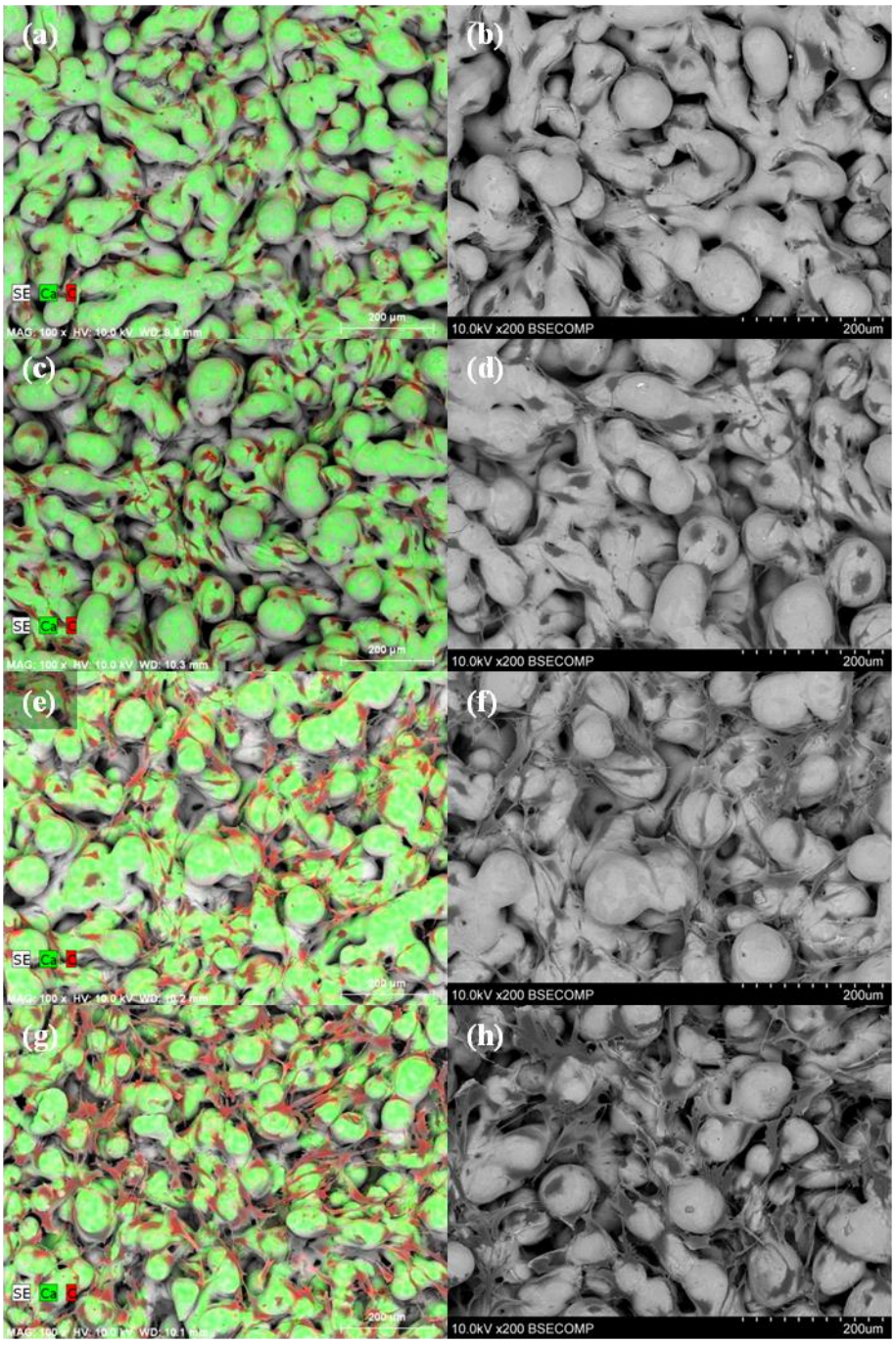

Figure 104: EDX (left) and SE (right) SEM images of the cell number expansion of MSCs seeded on composition 6.24 Mol % strontium at (a-b) day 0 (c-d) day 7 (e-f) day 14 and (g-h) day 21.

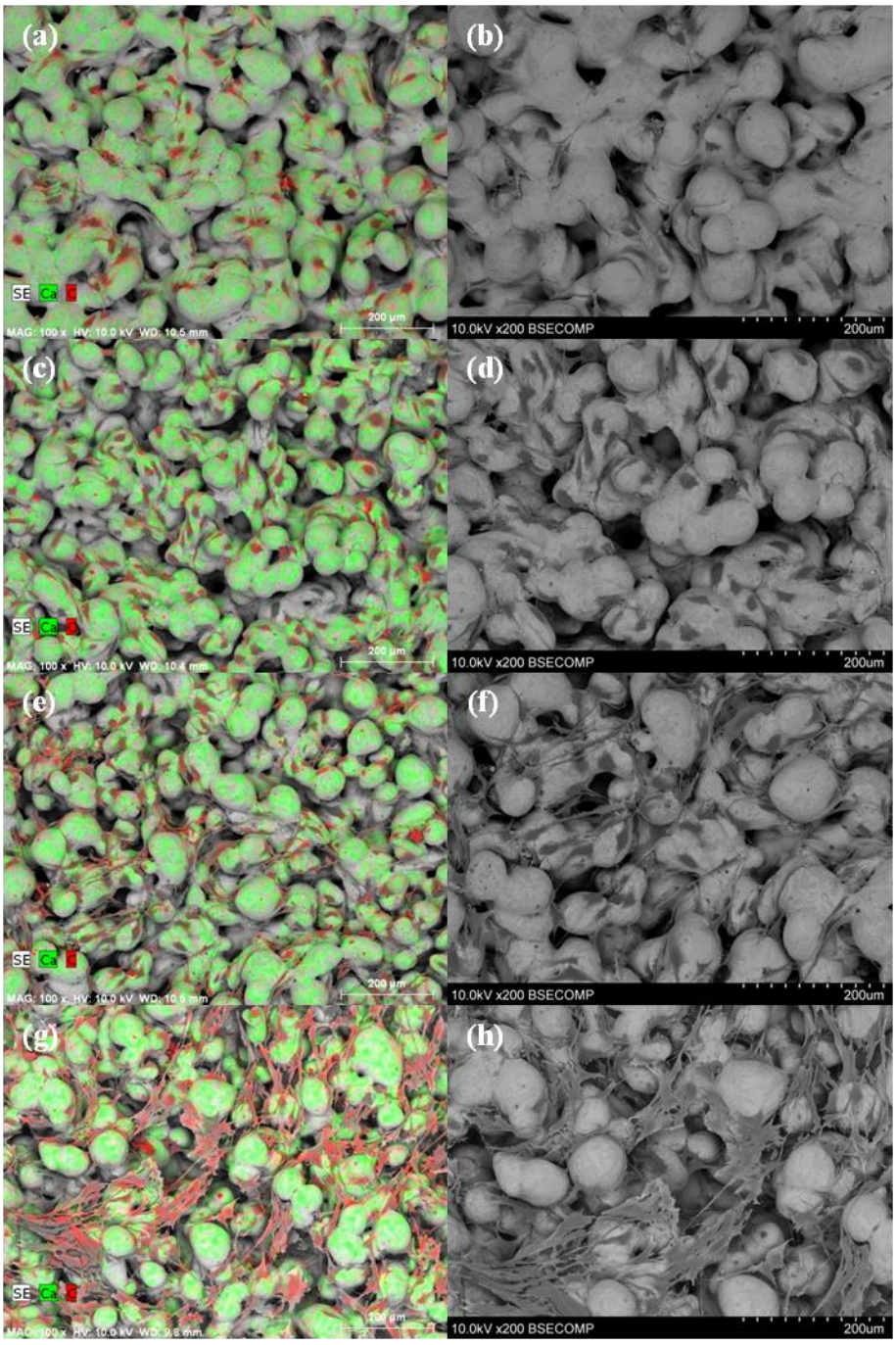

Figure 105: EDX (left) and SE (right) SEM images of the proliferation assay of MSCs seeded on composition 12.47 Mol % strontium at (a-b) day 0 (c-d) day 7 (e-f) day 14 and (g-h) day 21.

5.3.2.6 Alkaline Phosphatase Activity Via pNPP Assay

MSC primary cell lines were seeded onto the scaffolds at a concentration of $1x10^5$ cells/scaffold and cultured in osteogenic media for up to 21 days. Cells K28 and K56 were at passage 4 when seeded and K41 was at passage 5. Cell/scaffold constructs were collected at days 0, 7, 14 and 21 and the alkaline phosphatase activity of the local cells was calculated using a pNPP assay and the results normalised to DNA content using a PicoGreen assay. The results are shown in figures 106 to 111 on pages 196 to 198.

5.3.2.6.1 MSC Donor K28

For donor K28, the DNA content at day 0 was 0.28±0.025 µg/ml and increased in all samples up to day 21. Composition 0 Mol % strontium had the lowest DNA levels from day 0-14. The rate of increase got larger for composition 0 Mol % strontium between days 14 and 21 and reduced for compositions 3.12, 6.24 and 12.47 Mol % strontium. At day 21, composition 0 Mol % strontium had the highest DNA levels. The pNPP levels were highest in all compositions at day 0, though large error bars indicate a large distribution. A drop was observed at day 7, followed by an increase at day 14 and a second reduction at day 21. There was no significant difference between compositions at day 0 or day 7. By day 14 there was a significant increase ($p \leq 0.05$) in the pNPP levels of composition 3.12 Mol % strontium compared to all the other groups, which were not significantly different from each other. At day 21 composition 3.12 Mol % strontium was significantly ($p \leq 0.05$) larger than the 3 other compositions. The remaining compositions were not significantly different at $p \leq 0.05$ but at $p \leq 0.10$ composition 6.24 Mol % strontium was significantly larger than compositions 0 and 12.47 Mol % strontium, which were not significantly different.

5.3.2.6.2 MSC Donor K41

For cells K41, the initial DNA concentration was 0.35±0.015 µg/ml for all samples. In all samples an increase was observed between days 0-14. Between days 14-21 there was a small reduction for compositions 0 and 3.12 Mol % strontium, a large reduction in 6.24 Mol % strontium and an increase in composition 12.47 Mol 5 strontium. The pNPP levels increased between days 0-7 for compositions 0 and

3.12 Mol % strontium and reduced in the remaining compositions. A reduction was observed between days 7-14 for composition 0 Mol % strontium while the remaining compositions increased. Between days 14-21, a reduction was observed in composition 6.24 Mol % strontium while an increase was observed in compositions 0, 3.12 and 12.47 Mol % strontium. There was no significant difference ($p \leq 0.05$) between all compositions at day 0. At day 7 there was a significant ($p \leq 0.05$) reduction between composition 0 Mol % strontium and compositions 6.24 and 12.47 Mol % strontium. Composition 3.12 Mol % strontium was significantly ($p \leq 0.05$) larger than composition 12.47 Mol % strontium. Compositions 0 and 3.12 Mol % strontium were significantly larger than compositions 6.24 and 12.47 Mol % strontium for $p \leq 0.10$. At day 14, composition 12.47 Mol % strontium was significantly ($p \leq 0.05$) lower than the remaining compositions. Composition 3.12 Mol % strontium was significantly ($p \leq 0.05$) higher than composition 0 Mol % strontium. At day 21, compositions 0 and 3.12 Mol % strontium were significantly higher than composition 12.47 Mol % strontium.

5.3.2.6.3 MSC Donor K56

For cell line K56, the DNA concentration was 0.45±0.055µg/ml at day 0. There was a steady increase in DNA concentration between days 0-21 in all compositions tested. Composition 12.47 Mol % strontium had a lower DNA concentration at time points 7-21 days. Ther pNPP levels increased in all compositions between days 0-7. An increase was observed in compositions 0 and 3.12 Mol 5 strontium between days 7-14, compositions 6.24 Mol % strontium remained constant while composition 12.47 Mol % strontium reduced. There was a reduction in all the pNPP levels of all compositions between days 14-21. There was no significant ($p \leq 0,05$) difference between the compositions at day 0. At day 7 composition 12.47 Mol 5 strontium was significantly ($p \leq 0,05$) lower than compositions 0 and 3.12 Mol % strontium. At day 14, compositions 0 and 3.12 Mol % strontium were significantly ($p \leq 0,05$) larger than compositions 6.24 and 12.47 Mol % strontium. At day 21 composition 12.47 Mol % strontium was significantly ($p \leq 0,05$)lower than the remaining compositions. Composition 12.47 Mol % strontium was specifically higher than compositions 6.24 and 12.47 Mol % strontium.

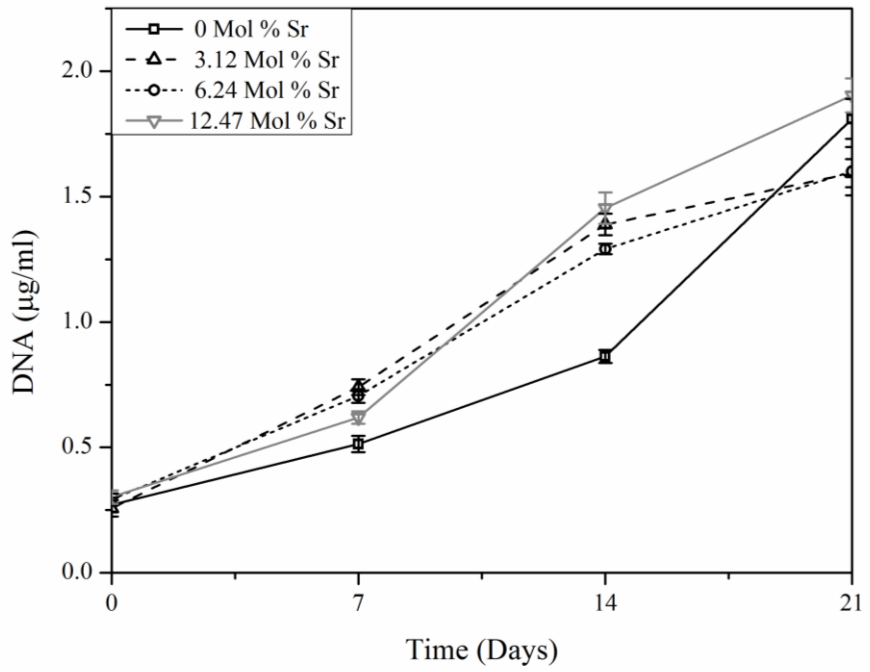

Figure 106: DNA content of the cell/scaffold constructs at different time points for donor K28 seeded at passage 4. Error bars represent the standard error.

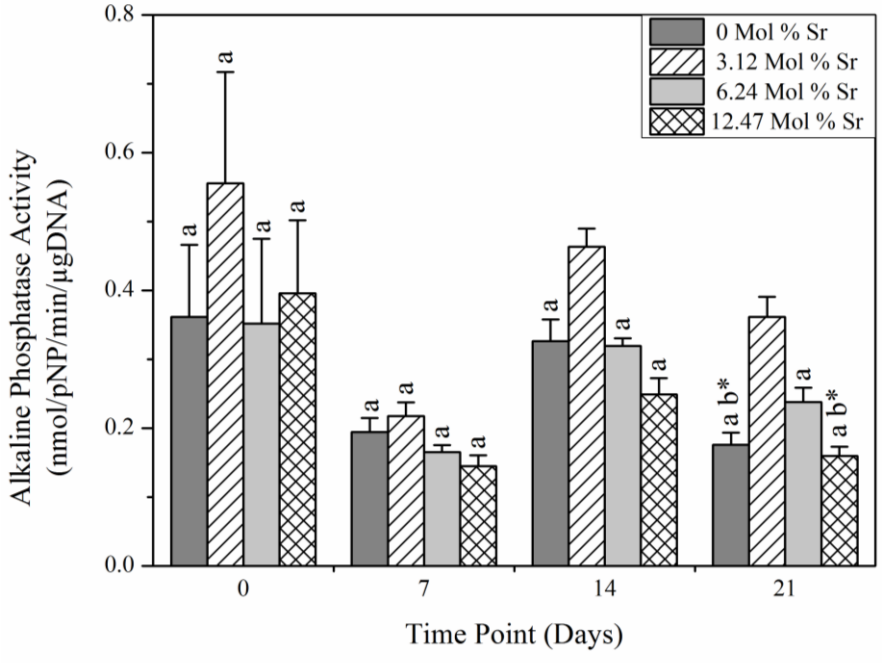

Figure 107: Alkaline phosphatase activity normalised to DNA at progressive time points for cell/scaffold constructs for donor K28 seeded at passage 4. Error bars represent standard error. Labels represent groups that were not significantly different for $p<0.05$ at a single time point, * indicates $p<0.1$.

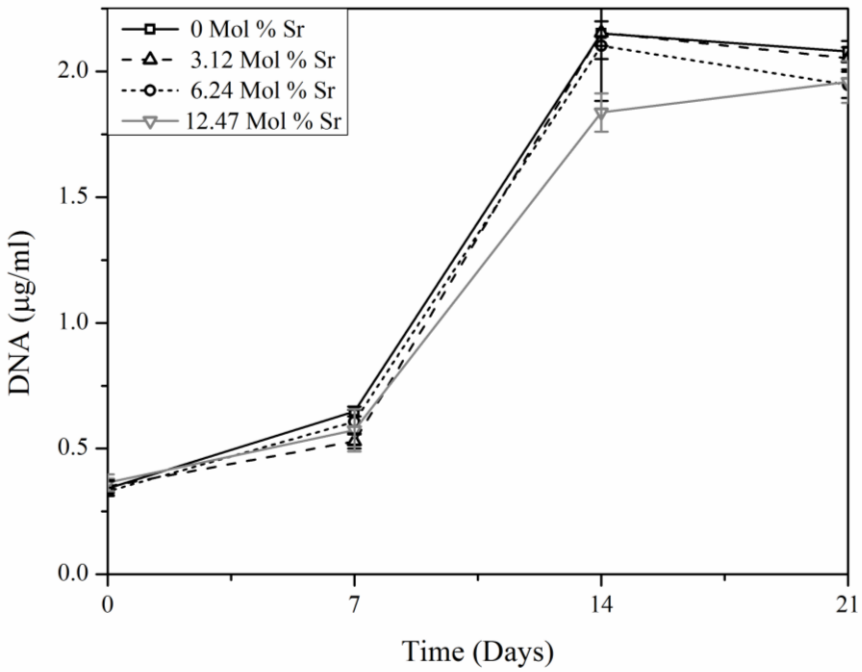

Figure 108: DNA content of the cell/scaffold constructs at different time points for donor K41 seeded at passage 5. Error bars represent the standard error.

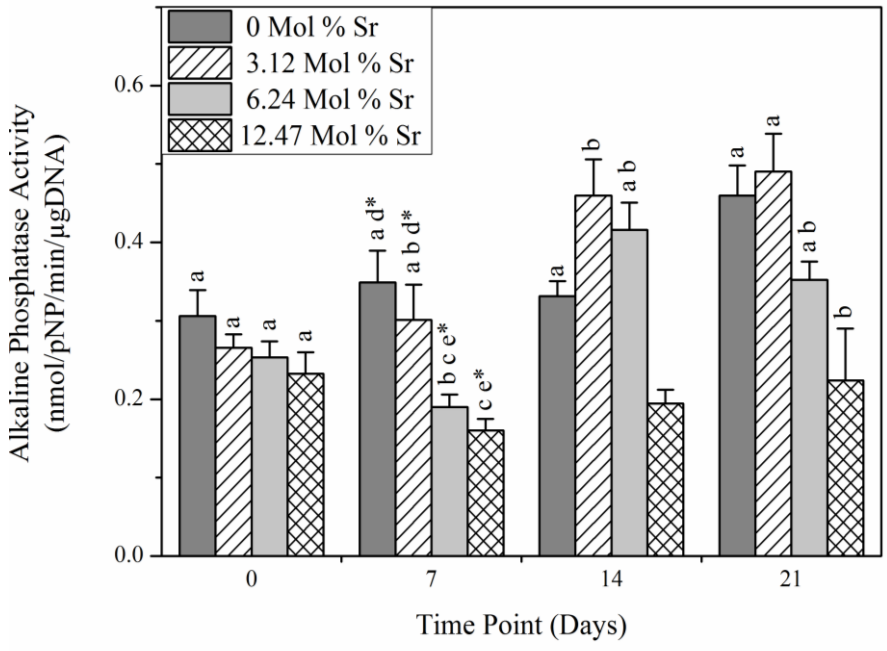

Figure 109: Alkaline phosphatase activity normalised to DNA at progressive time points for cell/scaffold constructs for donor K41 seeded at passage 5. Error bars represent standard error. Labels represent groups that were not significantly different for $p<0.05$ at a single time point, * indicates $p<0.1$.

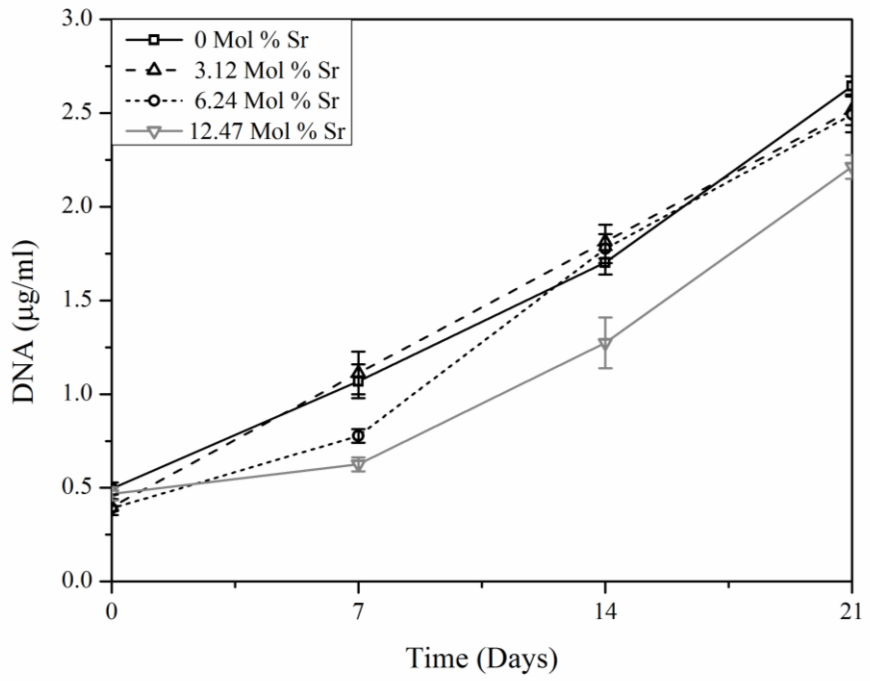

Figure 110: DNA content of the cell/scaffold constructs at different time points for donor K56 seeded at passage 4. Error bars represent the standard error.

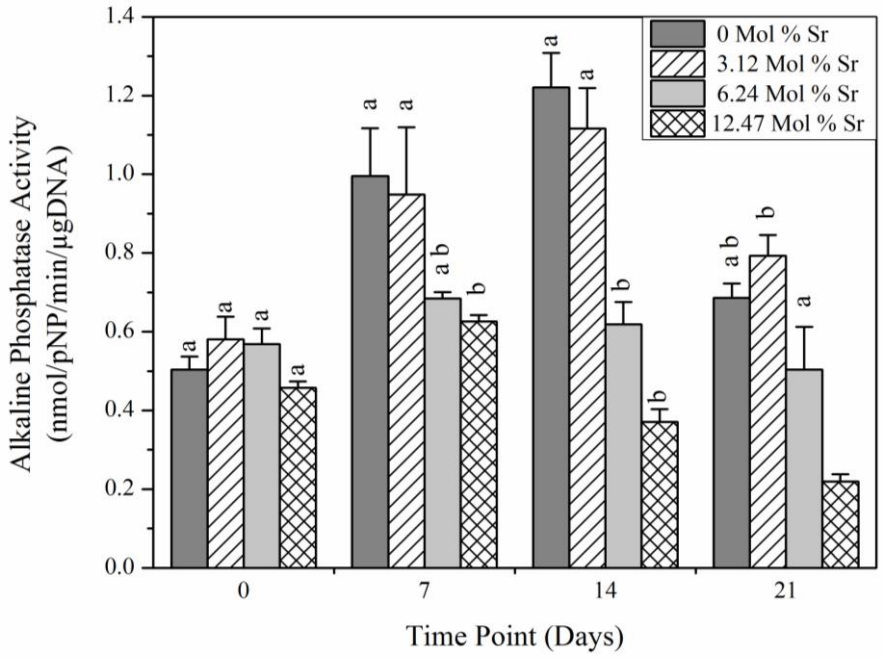

Figure 111: Alkaline phosphatase activity normalised to DNA at progressive time points for cell/scaffold constructs for donor K56 seeded at passage 4. Error bars represent standard error. Labels represent groups that were not significantly different for $p<0.05$ at a single time point.

5.3.2.6.4 Tissue Culture Plastic Control

A fifth material, tissue culture plastic, was used to ensure the MSCs were able to differentiate under the conditions used. 6 replicates were performed for each time point and for each donor, the results are shown in figure 112. DNA and normalised pNPP increased in all samples up to day 14. In donors K41 and K56 DNA increased between days 14 and 21 where as a small reduction was observed in K28. Normalised pNPP levels reduced between days 14 and 21 in all samples, with donor K28 showing the least amount of reduction.

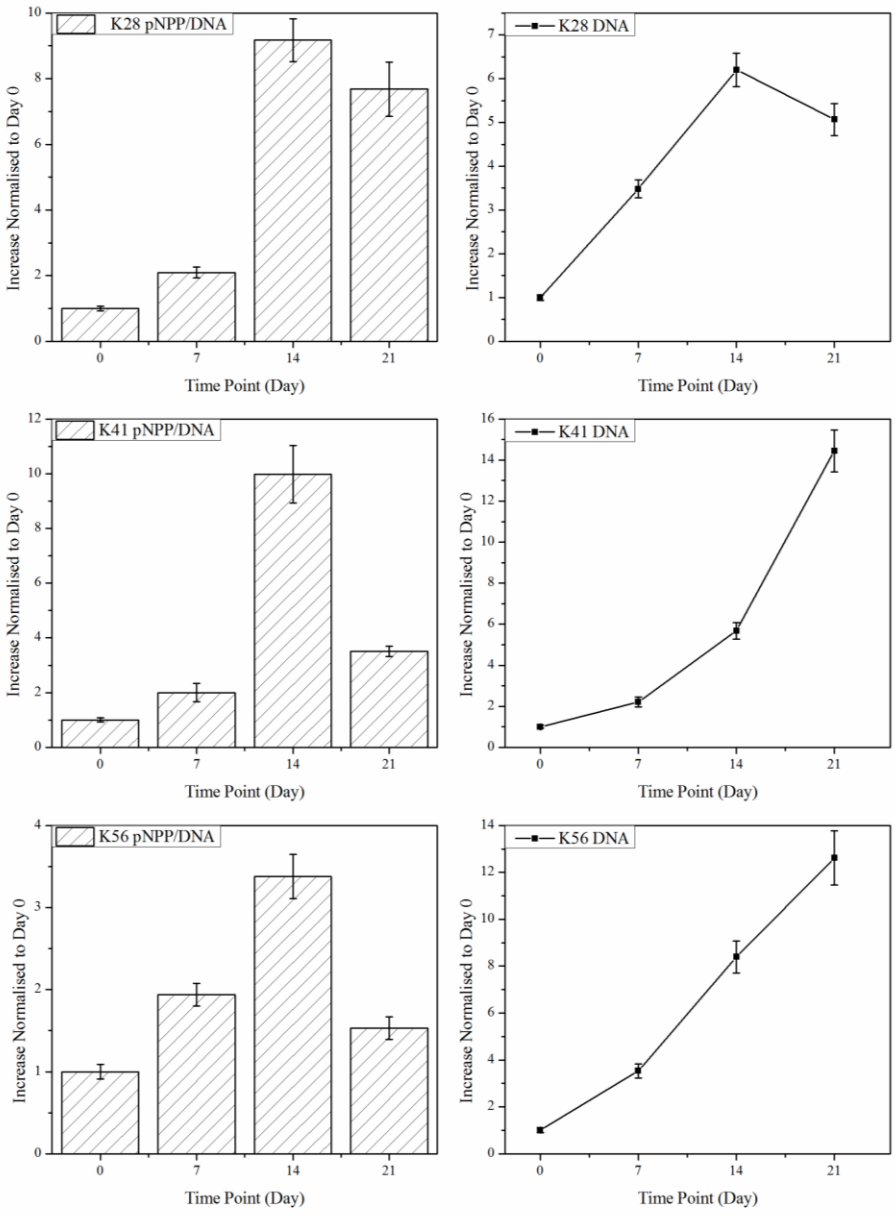

Figure 112: The pNPP normalised to DNA (left) and DNA (right) results for MSCs cultured in osteogenic media on tissue culture plastic. Donors from top to bottom are K28, K41 and K56.

5.4 Discussion

The aim of this chapter was to assess the biological compatibility of the newly developed glass ceramics. The method previously implemented for scaffold formation allowed for the rapid formation of porous glass-ceramic test specimens. The scaffolds that were used for biological testing represent an example of the application of the developed glass ceramics. To aid comparison between samples an identical heat treatment was applied to all glass compositions. The heat treatment that was chosen was that which had previously been shown to crystallise both apatite and calcium silicate phases in the glass while also forming well sintered materials that retained their porous structure. The processing that was used was not optimised for the development of individual microstructures or porosities for individual compositions. Individual scaffolds were utilised to ensure that subsequent analysis was done on the native scaffold surface as opposed to a cut surface. The scaffold size was optimised to fit within 96-well plates during subsequent cell interaction testing.

The first step that was taken in the biological assessment was the ability of the scaffolds to form a surface apatite layer when submerged in simulated body fluid. Simulated body fluid is a solution with ion concentrations nearly equal to those of blood plasma [116]. Some calcium phosphate materials will spontaneously form a surface layer of hydroxyapatite when submerged in simulated body fluid and this layer has been shown to enhance bonding of the materials to bone [161]. The formation of the surface apatite layer on the material surface varies depending on the material tested and the exact mechanism has been the subject of some debate. In all calcium phosphates the mechanism first starts with the dissolution of elements from the material surface, altering the ionic concentration of the solution and providing nucleation points for subsequent nucleation. Glass ceramic apatite-wollastonite has been shown to form a surface apatite layer following less than one day submersion in SBF [61]. The mechanism by which the layer forms has been described by Kokubo [116]. Briefly, dissolution of calcium and silica from the wollastonite and residual glass phases leads to an increase in the supersaturation of calcium in the SBF and the exposure of favourable apatite nucleation sites on the surface of the material. The different phases in the glass-ceramic have different solubilities in SBF, from most to least soluble: glass > calcium silicate > apatite phase. The

exchange of ions between the material and solution leads to variations in pH of the solution that influence subsequent dissolution of the material, formation of the surface apatite layer and also the behaviour of local cells [67]. The increase in pH of the SBF solution observed in all compositions is likely to be as result of an exchange of magnesium, calcium and strontium from the materials surface for H^+ ions in solution. The H^+ ions are produced from the dissociation of water and following their incorporation into the surface of the material leave an imbalance of OH^-, resulting in an increase in pH (a more basic solution) [162]. The increase in pH with increasing strontium content in the parent glass may be a result of an increase in the release of calcium and strontium ions from the glass due to a reduction in the connectivity and expansion of the glass matrix due to the larger strontium ion leading to a less stable glass and increased ion release, as reported by Hesaraki in CaO-SrO-SiO_2-P_2O_5 glasses [82]. O'Donnel [85] reported an increase in the pH following soaking in SBF of strontium substituted Bioglass compositions. This was also reported by Fredholm [81], who also identified an increase in strontium release with substitution into the glass but not an overall increase in strontium and calcium levels. Silicon levels were also found not to vary with strontium substitution and only an increase in phosphorous was observed. The pH change is therefore likely to be due either to the release of $HPO_4^{2-}$and PO_4^{3-} ions or the increased reactivity of strontium with water compared to calcium. The residual glass phase in the apatite-wollastonite system, as described here, is not thought to have high levels of phosphorous [135] and so will not be released to the solution and will therefore not influence the pH [89]. Lao [84] reported a reduction in dissolution with increasing strontium substitution in glasses in the CaO-SrO-SiO_2 and CaO-SrO-SiO_2-P_2O_5 systems when submerged in DMEM. This was attributed to an increase in oxygen bonding strength for strontium, compared to calcium, that was thought to inhibit exchange with H^+. It was also suggested that strontium would stabilise the glass network more than calcium due to its lower electronegativity, resulting in better charge balancing with Si-O- bonds. The inclusion of strontium into wollastonite was shown by Wu [73] to inhibit its dissolution in SBF and resulted in a lower pH following soaking. The substitution of the larger strontium ion in place of calcium into the crystal lattice was thought to inhibit diffusion through the crystal and thus limit the dissolution of the crystal. The reduction in the weight percentage of the wollastonite phase that was observed with increasing

strontium substitution into the glass-ceramics described here would limit the effect that wollastonite dissolution would have on the pH changes observed. The apatite phase is thought to be stable in SBF due to the solution already being supersaturated with respect to apatite. However, the substitution of strontium for calcium into the crystal has been shown increase its solubility [163, 164].

Analysis of the ionic composition of the SBF solution with time is required to determine the cause of the pH change. The change in pH will however have an effect of the ability of the materials to form a surface apatite layer. The dissolution of the material surface leads to an increase in calcium in the SBF, which is already supersaturated with respects to apatite. This leads to the formation of a hydroxyapatite (HA) and/or hydroxyapatite/carbonate (HCA) surface layer. The formation of the surface layer can be detected by looking at the composition and morphology of the material's surface. Crystals were detected on the surface of compositions 0 and 3.12 Mol % strontium from day 1 and its coverage of the surface increased up to day 7 when a complete covering was observed. EDX analysis revealed that the surface composition changed over time with the silicon levels reducing and phosphorous levels increasing. The phosphorous levels increased compared to calcium content suggesting that the change was due to a deposition of phosphorous and not just a reduction of silicon. This would suggest that the surface layer that was deposited was a calcium phosphate, most likely HA or HCA. The morphology of the surface layer was composed of crystals with a plate like morphology and resembled that observed previously for apatite wollastonite glass-ceramics [61, 89]. The plate like crystals were not observed on the surface of compositions 6.24-12.47 Mol % strontium. The EDX results suggest that in compositions 9.35-12.47 Mol % strontium the composition of the surface was changing in accordance with that observed for compositions 0-3.12 Mol % strontium. The morphology of the apatite phase changes between days 1-7, with the crystal domains becoming larger with less well defined boundaries. The addition of strontium to wollastonite has been shown by Wu [73] to form an apatite layer consisting of ball like crystals instead of those that resemble plates. The effect was also observed by Oliveira in strontium substituted apatite coatings. The addition of strontium has also been shown to produce a thinner HA layer, a reason why the changes in morphology observed are not as prominent in the low strontium containing compositions. The change in morphology could be due to dissolution of

the phase changing its appearance; however the EDX results indicate an increase in phosphorous, indicating deposition *is* taking place. Dissolution of phases would not only change their appearance but has been shown to influence the morphology of the deposited HA surface layer [165]. The large silicate phase in the glass ceramics reported here does not appear to show any change in morphology following soaking, suggesting an inhibitory effect on the apatite layer formation. It should be noted that the apatite rich domains may also contain residual glass and wollastonite levels that decrease with increasing strontium substitution, as previously reported. The surface of composition 6.24 Mol % strontium showed little change in morphology up to 7 days. This could be due to a combination of the mechanisms described. The reduction in solubility of the silicate phase that occurs with increasing strontium substitution would limit the material's ability to form an apatite layer. Composition 6.24 Mol % strontium has a higher calcium silicate content than the higher strontium containing compositions and fewer exposed apatite domains, therefore the reduction in solubility of the silicate phase may not have been counteracted by the increased solubility of the apatite phase. The increase in pH that was observed with increasing strontium substitution would favour apatite deposition. The formation of HA proceeds as in equation 113 [166]. A lower pH favours the dissolution of HA due to there being an increase in H^+ and a high pH at its formation [166]. This also suggests that the change in morphology of the apatite containing domains is due to deposition and not dissolution, as the higher pH would favour formation. The reduction in the rate of pH increase may be due to the formation of an apatite layer which would prevent further dissolution and also release H^+ ions into solution.

$$10Ca^{2+} + 6HPO_4^{2-} + 2H_2O \rightarrow Ca_{10}(PO_4)_6(OH)_2 + 8H^+$$

Equation 113

Subsequent biological testing was only performed on compositions 0, 3.12, 6.24 and 12.47 Mol % strontium. This was done to minimise the number of cells required. Composition 9.35 Mol % strontium was not included due to its poor formability leading to low scaffold mechanical strength. Sterilisation of the scaffold using an autoclave was shown to have no effect on the appearance of the surface features. This method of sterilisation has been reported previously for A-W glass ceramics [88, 117].

MSCs were isolated from human knee explants, removed during knee arthroplasty. The arthroplasty involved the removal of the femoral condyle, which was collected, and its replacement with a prosthesis. While the cells from different donors displayed the same fibroblast like morphology, variation was observed between their ability to differentiate down the osteogenic lineage when exposed to the osteogenic differentiation media. Large inter donor variation in properties is a known problem with MSC populations [167]. One factor affecting the variation in osteogenic capacity is the age of the donor. Cells from older donors have the same length telomeres as those from younger donors [168], maintaining their ability to divide. They do however show a reduction in their ability to differentiate, likely due to oxidative damage or senescence of supporting cells [33]. The disease state of the knee will also affect the capacity of the cells to differentiate . All the knees were being operated on due to cartilage and eventual bone degradation due to osteoarthritis. The severity of the disease state of the knees was not reported. The use of cells from the diseased joint for the testing of the material reported here may better replicate the environment in which it will be used. The number of population doublings that the cells undergo in culture affects their ability to proliferate and differentiate [169]. The differentiation ability of *in vitro* cultured bone MSCs drops from the 6^{th} passage on, due to a reduction in telomere length leading to senescence and cycle blocking [170]. Tissue derived and marrow derived MSCs have been shown to retain similar growth kinetics up to passage 8 [169]. Both cell lines that were used in the osteogenic assay were at passage 3.

Flow cytometry results show that the populations were all positive for markers CD29, CD44, CD73, CD90 and CD105 while being negative for CD34 and CD45. The positive and negative cell markers reported are all in line with the most frequently reported MSC markers [171]. A small increase in the histogram median was observed for CD166. The reduction in CD166 has previously been reported in cells that were extracted from the bone and cartilage as opposed to the bone marrow, which expressed CD166 at high levels [169]. Cells grown from trabecular bone and cartilage expressed CD29, CD90 and CD105 and were negative for CD45 and CD90 but showed a large reduction in the expression of CD166 than populations of bone marrow derived mesenchymal cells. The cells were still shown to proliferate and differentiate, but with a reduced capacity [169]. A systematic review by Mafi on the most commonly reported markers indicated some inconsistencies between the

reports of different research groups [171], highlighting the difficulties in assigning specific surface markers to this group of cells.

The scaffold seeding protocol was modified from the method utilised by Dyson [117]. The optimum seeding density was chosen to provide a confluent monolayer in as short a time as possible. Seeding of bone marrow derived cells at higher densities has been shown to enhance mineralisation [172]. Too high a seeding density resulted in the formation of layer which was multiple cells thick, reducing the contact which the cells had with the scaffold. Too low a seeding density and the cells would not undergo osteogenic differentiation within the time frame of the experiment. On A-W scaffolds with a similar structure, Dyson reported that when using scaffolds that were 3x3x3mm a seeding density of $5x10^5$ cells/scaffold allowed cells to attach after 6 hours and form a confluent sheet by 24 hours [117], a similar value to that reported here. Dyson achieved a seeding density of 28.4±2.6% [117], the efficiency of static seeding has been shown to be around 25% [172]. The seeding efficiency can be increased by using a dynamic seeding method, with the methods used reviewed by Yeatts [173]. The SEM/EDX proliferation study does however show that cells seeded at half the optimum seeding density are still capable of forming a confluent layer on the material. Magallanes-Perdomo [88] reported that individual cells were able to proliferate and migrate on A-W discs and formed a confluent sheet by day 14 with calcium phosphate depositions observed by day 21. Bone derived MSCs have previously been shown to attach to and proliferate on A-W glass ceramics [88, 117] but the proliferation study shows that the novel strontium containing glass ceramics were also able to support cell attachment and proliferation to ultimately form a confluent cell layer by day 21. No difference was observed between the ability of the different scaffolds to support cell attachment and expansion. This was also verified using the pico green DNA assay where all compositions showed a similar rate of DNA increase. Strontium incorporated into Bioglass has previously been shown to not influence cell proliferation [85].

Three donors were used for the quantitative assay to help minimise the effect of inter donor variation. the pNPP levels of day 0 for donor K28 were the highest reported but also had the largest error bars. This was in part due to initially low DNA levels. An increase was observed in pNPP levels between days 7 and 14 in all samples but

donor K56 compositions 6.24 and 12.47 Mol % strontium. The pNPP levels remained constant or decreased between days 14 and 21. This was also observed in the cells cultured on tissue culture plastic, who's normalised pNPP levels all peaked at day 14. This behaviour has been observed previously in rat osteoblasts [174] and human MSCs [117] when cultured on A-W. It was clear that by day 21 compositions 0, 3.12 and 6.24 Mol % strontium were better able to support osteogenic differentiation than composition 12.47 Mol % strontium. Composition 3.12 Mol % strontium had the highest pNPP levels at day 21 in all donor groups but was only significantly larger than composition 0 Mol % strontium for donor K28. A significant increase was observed for composition 3.12 Mol % strontium compared to composition 0 Mol % strontium at day 14 for donors K28 and K41. It is clear from the results that strontium incorporation into the scaffolds is having an effect on the ability of the scaffolds to support osteogenic differentiation. The lowest level of strontium substitution investigated was able to increase osteogenic differentiation while composition 6.24 Mol % strontium had no significant effect and composition 12.47 Mol % inhibited osteogenic differentiation. The mechanisms by which strontium has induced these effects will now be discussed.

The release of strontium ions from the material's surface may be responsible for the fluctuations in osteogenicity of the materials. Orally administered strontium salt (strontium renate) has been shown to have a beneficial effect on bone mass in patients with osteoporosis [175, 176]. Part of the reason for this is that it has been shown to enhance osteoprogenitor differentiation into osteoblasts and enhance their proliferation [176]. Strontium substitution for calcium into Bioglass was shown to increase ALP levels with increasing substitution up to 100 % strontium [90]. Strontium substitution into sol-gel derived CaO-SrO-SiO_2-P_2O_5 glasses showed an increase in ALP with an optimum value at 5 Mol %. Substitutions larger than this produced a reduction in ALP but also a reduction in proliferation resulting in a ALP normalised to DNA level not significantly different from 0 Mol % substitution. The value of 5 Mol % strontium is close to the optimum (3.12 Mol %) composition developed here. Substitution of strontium for calcium into hydroxyapatite, up to 10% substitution, increased ALP levels in rat osteoblasts that were exposed to media conditioned with the apatites [71]. This was also shown in human osteoblast cell line MG-63 exposed to of strontium substituted hydroxyapatite conditioned media, substitutions greater than 10 % strontium produced no change in ALP [91]. The

same cell line increased ALP levels when exposed to strontium containing wollastonite, up to 20 % substitution [91]. It should be noted that optimum composition, 3.12 Mol % strontium, was a 12.5% strontium substitution for calcium, a close match to the optimum values reported in the literature. These results from the literature clearly show that the dissolution products of strontium containing materials can influence the bone forming ability of osteoblasts and their progenitors.

In the experiments reported here cells were put into direct contact with the scaffolds. The surface morphology of the material has been shown to influence the behaviour of cells [48, 177, 178]. The inclusion of strontium into the parent glass was shown to influence the morphology and ratio of phases that formed in the material, causing the surface topography of the material to change. Changing in patterning of the surface has been shown to influence MSC differentiation and can be used to osteogenically differentiate human bone MSCs without the use of osteogenic factors in the media [178]. Though not investigated here, the change in materials stiffness and elasticity that would likely result with substitution of strontium will also influence the cells ability to differentiate into osteoblasts [48]. The surface of the materials will also spontaneously change upon immersion in the media. DMEM [179]. The change in morphology of the surface and the surface apatite layer will influence the surface that the cells are exposed to. A-W preconditioned with a surface apatite layer was shown to enhance ALP expression compared to non-conditioned A-W in rat osteoblasts following 23 days culture [174]. Unlike when standard SBF is used, the use of DMEM and also FCS will incorporate proteins into the surface, most likely fibronectin and vitronectin, which will enhance the osteoblast adhesion and interaction with the material [180]. The surface morphology and phase composition of 3.12 Mol % strontium was the most similar to composition 0 Mol % strontium (compared to the other strontium containing compositions). This suggests that the changes in surface morphology and phase composition were having a negative effect on the osteogenic differentiation of the MSCs that were counteracting the enhancing effects of strontium ion release. Exposure of the cells to media conditioned with the materials would confirm if the observed effect was a result of the chemical dissolution products or the physical interactions with the material surface.

Chapter 6: General Discussion

Replacement materials are required when spontaneous healing of a bone defect does not occur. Healing of bone requires a combination of cells, extra cellular matrix (ECM) and environmental factors such as chemical signalling or mechanical stimulus. A suitable replacement material should act as an ECM by mechanically supporting and protecting local cells while providing the correct environment to assist, accelerate or induce the formation of new bone. Calcium phosphate bioactive glasses and glass-ceramics have found favour as bone replacement materials due to their ability to bond to native bone via a surface apatite layer and also to support and direct cell attachment, proliferation and differentiation [114]. This is done via modification of the material's chemistry and processing to engineer a device that has the bulk and intrinsic mechanical strength, surface chemistry and topography and macro and micro structure that is optimised for bone formation. One such modification is the substitution of strontium for calcium in glasses and ceramics to enhance their bone forming ability [68, 71, 73, 81, 85-87, 90, 136]. Strontium has the same charge as calcium (Sr^{2+}/Ca^{2+}) and so can be readily substituted in both crystalline and amorphous materials. Strontium treatments have been shown to upregulate osteoblast activity and downregulate resorption by osteoclasts leading to an increase in bone mass [175, 176]. The substitution has been shown to have an effect on a material's solubility and ion release [67, 68, 71, 73, 81, 84-86, 90], mechanical properties [181], formability [86, 125] and crystalline composition and morphology [71, 72, 86, 91, 125, 176, 182], all of which will influence how the material performs in bone replacement applications. The aim of this work was to develop a new strontium containing glass-ceramic based on the apatite-wollastonite (A-W) system for use as a bioactive bone replacement material. Apatite-wollastonite was chosen as the starting material as it has high mechanical strength compared to the bioactive glasses [139], such as Bioglass 45S, while remaining highly bioactive and capable of bonding to native bone [161]. A-W is a polycrystalline glass-ceramic formed primarily of apatite and wollastonite crystals that lie within a residual glass matrix. It is the combination of ordered and disordered phases in the material that allow it to share both the high mechanical strength of a ceramic with the bioactivity of a glass [116]. A range of novel compositions were formed based on the molar substitution of strontium for calcium.

The effect of these substitutions on the amorphous, crystalline and bulk properties of the material were investigated along with what influence these changing parameters had on the processing of the material, its ability to be formed into a bone replacement device and ultimately its ability to promote bone healing.

The synthesis and processing of the material will determine the properties of a device formed from it and so this will be discussed first. The final material was required to consist of a glass that was capable of partial devitrifying to form biocompatible crystalline and residual amorphous phases following a post processing heat treatment. Devitrification of the A-W parent glass has been shown to be highly sensitive to composition [111, 140], particle size [150] and heating rate [60]. The particle size and heating rate were thus maintained between compositions while the composition was varied to observe its effect on the final material. Fibrous wollastonite forms in the A-W parent glass via a heterogeneous nucleation process and the growth of crystals from the periphery leads to cracking of large monolithic blocks [183]. As such A-W must be processed from a ground glass powder of smaller particle sizes that must both crystallise and sinter to form a bulk material. The 45-90μm particle size fraction was chosen for devitrification studies as it could subsequently be used for the formation of porous materials without the use of a template, foaming or leaching agent or post processing machining. A melt quench route was chosen as this has previously been shown to be a successful method to produce the A-W parent glass and allows for relatively large batch sizes (≈200g) [62]. Laser diffraction determined that the 45-90μm particle fractions all had the same size distribution and so were suitable for subsequent analysis. The addition of strontium into the glass network was shown to produce x-ray amorphous materials with a network that expanded with increasing strontium substitution. The successful substitution was also confirmed by an increasing density and x-ray attenuation with increasing strontium. The substitution had a marked effect on the thermodynamic effects that occurred in the glasses following heating. A reduction in the glass transition temperature was observed with increasing strontium substitution, possibly as a result of the expanded network. There was also a reduction in the peak crystallisation of the first phase to form, the apatite phase, and an increase in that of the second phase, a calcium silicate. The change in peak position was shown to influence the ratio of the crystalline phases in the bulk material, with increasing strontium producing a reduction in the weight percentage

of the calcium silicate phase. The first phase to crystallise was identified as non-stoichiometric fluorapatite the unit cell of which expanded with strontium substitution, indicating its uptake into the phase. The second phase was identified as monoclinic β-wollastonite, the unit cell of which also expanded with strontium addition and at higher substitutions partially transformed into pseudowollastonite. The inclusion of strontium into the crystalline phases and the weight ratios of the phases to each other plays a key role in the application of the final material as a bone replacement material [116]. The changes that occurred were shown to influence the materials mechanical strength, surface chemistry and topography and ability to form a surface apatite layer when exposed to biological conditions. The premature crystallisation of the apatite phase counteracted the reduction of the glass temperature, reducing the size of the sintering window with increasing strontium substitution, this reduced the ability of the material to sinter. Combined with the reduction in the wollastonite content of the glass, this produced scaffolds that had significantly lower flexural strengths than A-W. This was not the case in the highest strontium containing composition, 12.47 Mol % strontium, where a lack of wollastonite and a reduction in glass connectivity allowed the material to melt at a lower temperature. This induced liquid phase sintering upon heating, leading to increased densification and mechanical strength of the porous material, despite loss of the calcium silicate, which is known to reinforce the material [135]. Though the increase in strength is desirable, it was done so at the loss of porosity which should be avoided to ensure new bone growth within the material [160]. The wollastonite phase is also proven to be crucial in the ability of A-W to form a surface apatite layer and so its loss from the glass-ceramic should be avoided [116]. A balance between the materials sinterability, bulk mechanical strength and its retention of the wollastonite phase is therefore crucial to ensure a successful bone replacement material.

Increasing strontium substitution caused the formation of different structures on the material's surface compared to A-W. A-W had a homogenous surface composed of small interlocking domains that have previously been identified as apatite and wollastonite crystals sitting within a residual glass matrix. As the strontium content of the parent glass increased, separate regions formed that were identified as strontium containing apatite, a magnesium rich calcium silicate, a magnesium depleted calcium silicate and the residual glass phase. The loss of wollastonite

exposed the apatite and glass domains and its partial transformation to pseudowollastonite resulted in the formation of distinct crystals. All the phases were also present in the bulk of the material. The change in ratio and morphology of the crystalline phases altered the surface chemistry and topography of the glass ceramics. The result of this is modification of the environment that is presented to cells and body fluids when the material is placed in a biological setting. This was highlighted via simulated body fluid testing and *in vitro* testing with mesenchymal stem cells (MSCs). A coherent surface apatite layer of plate like crystals was formed on the surface of composition 0 Mol % strontium (A-W) following 7 days of immersion, this coincided with a reduction in silicon and calcium and an increase in phosphorous levels at the surface. This behaviour was observed only in the lowest strontium composition tested, 3.12 Mol % strontium. Very little change was observed in composition 6.24 Mol % strontium and although there was a change in the morphology and surface chemistry of 9.35 and 12.47 Mol % strontium, the change in the surface features did not resemble that which was observed in A-W. This suggests that these strontium substituted materials may be less able to bond to native bone but this could only be confirmed with *in vivo* tests. A change in the pH of the SBF was observed between all samples suggesting a change in the dissolution of the samples and varied ion release. SBF testing provides simplified insight into the ability of the scaffold to induce new bone formation. One of the key components missing from the fluid is proteins. Upon implantation *in vivo* the material surface will be coated with proteins, these proteins will direct any subsequent cell adhesion and also help to nucleate apatite on the materials surface [180]. The change in surface topography effects the material's apparent surface area that is presented for protein attachment. Immersion in a more biologically active medium such as cell culture medium containing serum will deposit proteins such as fibronectin and vitronectin on the material's surface and, though this wasn't directly investigated, cells were able to attach to all the compositions tested, suggesting protein incorporation onto the surface [180]. The effect of the change in the material's surface following strontium incorporation had a significant effect on the ability of bone marrow derived mesenchymal stem cells to differentiate down an osteogenic lineage. While MSCs were shown to attach and increase in number on all the compositions tested, their ability to undergo osteogenic differentiation was enhanced, compared to all other samples, on composition

3.12 Mol % strontium with the difference being significant ($p \leq 0.05$) for one of the donors. In composition 12.47 Mol % strontium, osteogenic differentiation was significantly reduced ($p \leq 0.05$) compared to A-W in two of the three donors. As discussed, the materials did not just vary in chemical composition but also in their crystalline makeup, surface features and also porosity. While compositions 0-6.24 Mol % strontium had comparable porosities, composition 12.47 Mol % strontium showed a reduction in pore size and interconnectivity. This may have contributed to the cells lack of osteogenic differentiation but would be expected to play less of a role *in vitro* than *in vivo* [50, 157, 158] where an interconnected porosity is required for the formation of a vascular network [160]. The change in osteogenic capacity is thus down to the change in the surface presented to the cells which would influence signalling to the cells both directly through their attachment site [184] and also through local ion release and pH levels [185, 186]. The effect on the cells of ion release from the scaffolds could be tested using media conditioned with the material following a set soaking period, this was not however investigated in this work. The enhanced osteogenic differentiation in osteogenic media induced by the scaffolds and their ability to form a surface apatite layer indicates that they have the capacity to be osteoconductive when implanted into the body [187]. This means that they are able to direct the growth and formation of new bone onto the material's surface. The ability of the scaffolds to direct osteogenic differentiation without the addition of osteogenic supplements is known as osteoinduction. Osteoinduction is thought to be strongly influenced by ion release but also the deposition of bone morphogenic proteins onto the material's surface [187-189] and so can only truly be investigated *in vivo* [189].

The glass-ceramics that were tested represent only a single processing route. The properties of the final material can not only be controlled by changing the composition of the parent glass but also by changing the particle size, heat treatment and post processing treatments.

As was shown, the position of the wollastonite peak shifted to lower temperatures when smaller particle sizes were used, though this effect got smaller with increasing strontium substitution. This does however mean that use of a smaller particle size would result in an increase in the wollastonite content of the glass-ceramic, potentially increasing the materials intrinsic strength and ability to form a surface

apatite layer. The use of small, large or mixed particle sizes can also be used to modify the bulk materials porosity following sintering [108]. The green part packing, brown part density and neck formation decreases with increasing particle size, producing larger pores. A range of particle sizes can be used to reduce the porosity and increase the networking of particles and number of necks formed following sintering, increasing the bulk mechanical strength of a material [114]. However, *in vivo* bone formation favours more porous structures with large, interconnected porosities [158, 159] and so is often optimised at the expense of mechanical strength. The sinterability and phase ratio will also be influenced by the heating rate used. As the heating rate increased the temperature of both the apatite and wollastonite peaks increased while the glass transition temperature showed little variation. This would delay the onset of crystallisation during heating, allowing viscous flow sintering of the glass phase to proceed further and enhance neck formation and mechanical strength of the porous material. However, the wollastonite peak temperature increase with increasing temperature was greater than the apatite peak which would result in a reduced final weight percentage of wollastonite in the final glass ceramic. A change in heating rate could be coupled with multiple dwells at different temperatures. Temperature holds during heating can be used to optimise sintering and crystal nucleation and growth. Viscous flow sintering can be enhanced by holding the material at a temperature between the glass transition region and the onset of crystallisation. However in this work apatite was found to form in all materials 15°C bellow the DSC-determined onset of crystallisation. The optimum nucleation and growth temperatures can be determined via DSC/DTA for the different phases and used to control crystal size and phase ratios [61] which in turn contribute to directing the cellular response to the scaffolds. Control of the crystalline content of the material will also influence its degradation rate. Incorporation of strontium into both crystalline [73, 163, 164] and amorphous phases [84] will affect the rate at which it dissolves in the body. Also, as the glass, wollastonite and apatite phases have different solubilities [116] so control of the ratio of the phases to each other can be used to control the resorption of the material. This would allow for the rate of resorption to be matched to the rate of new bone deposition, ensuring structural integrity of the defect site throughout healing [190]. The increased radiodensity of the strontium containing materials would make their

degradation in the body easier to track using x-ray radiography and computed tomography [130].

Scaffolds were formed using a simple no-compression sintering route in a mould. This method was chosen as it provided a fast route through which a porous bulk material could be formed from the powders and was shown to produce consistent results. The method also allowed for the formation of different size geometries to match the application which, in the case of this work, was the production of bars for flexural strength analysis and cylinders to fit within a 96-well plate. Different mould sizes and dimensions could be utilised to produce scaffolds for different surgical interventions [191]. Applications where glass-ceramic bone replacement materials have previously been used include maxillofacial reconstruction, iliac crest prosthesis, vertebral prosthesis devices and dental implants [192]. Patient specific implants can be designed using accurate 3D models formed from computed tomography x-ray images of the defect gathered pre-operatively [193]. Bespoke implants reduce the time of the implantation surgery as the defect site and device are already matched with respect to geometry [194]. 3D models can be used to form moulds or direct the milling of sintered blocks. These methods are however limited in that they cannot control the internal geometry of a device and so cannot be used to introduce features such as channels to promote the in growth of vasculature. Additive manufacturing methods such as stereolithography, fused deposition moulding, selective laser sintering (SLS) and 3D printing [195] allow for the manufacture of bespoke geometries with controlled internal structures. SLS has previously been used for the formation of porous A-W scaffolds [61, 117]. An indirect method was used whereby a binder is added to the glass powder which is subsequently melted via SLS, bonding the powders in the desired shape. Subsequent sintering and devitrification preserves the shape and forms the mechanically strong glass-ceramic. The prefabricated scaffolds are useful for load bearing applications where immediate induction of structural integrity is required for bone healing. In non-load bearing applications a loose powder may be used in combination an organic matrix. Apatite-wollastonite glass-ceramic powders used in combination with fibrin glue or a bisphenol-a-glycidyl methacylate resin were shown to accelerate the healing of rabbit tibia defects [196, 197] and when processed properly can be injected to fill irregular voids or overly porous bone[198].

The developed materials have shown promise as bone replacement materials and the knowledge gained through this work will allow for their optimisation to a range of bone replacement applications.

Chapter 7: Conclusions

This work investigated the effects of strontium substitution for calcium into apatite-wollastonite glass ceramic. The work focussed on the substitution of strontium into the glass, the influence strontium has on the thermodynamic evolution of crystal phases and the morphology and composition of the phases formed. The new materials were then formed into porous scaffolds and their biological properties investigated with respect to their ability to form a surface apatite layer in biological conditions and their effect on the growth and osteogenic differentiation of human mesenchymal stem cells. To summarise the findings:

- Strontium was successfully substituted for calcium on a molar ratio up to a 1 SrCO:1 CaCO ratio. All compositions formed via the melt quench route formed x-ray amorphous glasses with the intended final compositions.

- The substitution of strontium for calcium produced an increase in the radio density of the material in line with theoretical models. This would allow for a greater ease in post operative x-ray imaging of the materials if used in a bone replacement device.

- When heated, all the parent glasses devitrified to form apatite and wollastonite phases and a residual glass phase. Strontium was taken up into both the apatite and wollastonite phases with an increase in unit cell dimensions observed with subsequent substitutions. At higher strontium levels, pseudowollastonite began to form alongside the monoclinc β-wollastonite.

- Electron microscopy of the glass-ceramics revealed the materials to be composed of interlocked phases sitting within a residual glass matrix. The apatite crystals were found to form in small domains that also contained residual glass. Two silicate phases were observed, definable by their morphology and varying magnesium content. The surface phases were more pronounced at higher strontium contents.

- The temperature at which the wollastonite phase formed increased with increasing strontium substitution and its relative phase contribution to the

glass ceramic decreased accordingly. The temperature at which the apatite phase formed showed a small decrease with increasing strontium substitution while the glass transition temperature showed a small increase, reducing the working window of the materials.

- The reduction in the size of the working windows led to a reduction in sintering and mechanical strength, apart from in composition 12.47 Mol % strontium where a shift from solid to liquid phase sintering produced an increase in densification and mechanical strength.

- Scaffolds formed from the materials retained an interconnected porosity, apart from composition 12.47 Mol % strontium, where densification led to the occlusion of pores.

- Compositions 0 and 3.12 Mol % strontium formed a surface apatite layer after 7 days immersion in simulated body fluid. Composition 6.24 Mol % strontium showed no change following 7 days soaking. The apatite surface domains increased in size in compositions 9.35-12.47 Mol % strontium between days 3 and 7 but no change on morphology was observed. Energy dispersive x-ray analysis revealed that the calcium, phosphorous and silicon levels of the materials surfaces varied with soaking time, suggesting ion exchange with the solution. Increasing strontium substitution produced an increase in the solution pH.

- The interaction of compositions 0, 3.12, 6.24 and 12.47 Mol % strontium with human bone marrow mesenchymal stem cells was investigated. All compositions were able to support cell attachment and expansion up to day 21. Composition 12.47 Mol % strontium inhibited osteogenic differentiation compared to apatite-wollastonite (composition 0 Mol % strontium) where-as composition 3.12 mol % strontium enhanced osteogenic differentiation; this was significant for one donor.

In conclusion, glass-ceramics were successfully formed following the substitution of strontium into the apatite-wollastonite parent glass. The materials were shown to support mesenchymal stem cell growth and differentiation and thus show promise as bone replacement materials.

Chapter 8: Future Work

The complex nature of the glass-ceramics produced in this piece of work provides a large scope for future work. Though it was shown that strontium could be substituted for calcium into the apatite-wollastonite glass-ceramic, the processing was not fully optimised for the ultimate goal of producing a bone replacement device from the materials. While the devitrification of the material was characterised in terms of the thermodynamics and phase formation in the glass, the effect of different heat treatments on the final glass-ceramics was not determined. This would involve characterisation of the material's physical properties and also its biological interactions with simulated body fluid, bone forming cells and also *in vivo* animal and human studies.

To aid comparison between samples, all materials were exposed to the same heat treatment. The materials were found to crystallise at different temperatures and so heating regimes specific to each material could be used to control the phase content of the glass-ceramics. Subsequent testing with mesenchymal stem cells (MSCs) would allow for a better understanding of how each phase contributes to the effects that were observed in this work. For example, a heat treatment that does not nucleate the calcium silicate phase would allow for a better understanding of how the apatite phase influences both the ability of the material to form a surface apatite layer in simulated body fluid (SBF) and also how it directs the fate of MSCs. Testing could be performed using a matrix setup, comparing the biological response to different heat treatments and thus different phase compositions. The heating rate and particle size used influenced the temperature at which the phases formed in the material, and so a varied heating rate would also allow for the control of the glass-ceramic's final crystal composition. This would not only influence the environment exposed to the body if implanted but also the mechanical properties of the material including mechanical strength, porosity and solubility.

Only one method of forming a porous material was investigated in this work. Further work should focus on the formation of more biologically relevant architectures. This would focus on both the pore structure of the material, matching it to the application eg. cancellous or cortical bone, and also the bulk architecture, matching the size and shape of the scaffold to the defect site. The application of the

material for a range of free form fabrication methods, such as selective laser sintering and 3D-printing, should be investigated to achieve the goal of producing a controlled architecture.

The dissolution of the material within a biologically relevant environment should be examined. Analysis of the ion levels of simulated body fluid following specimen soaking would help to understand the degradation of the materials, this could be done using inductively coupled plasma atomic absorption or optical emission spectroscopy. The rate of degradation and its effect on the mechanical properties of the material should also be investigated to allow for the formation of a device which degrades at the same rate as new tissue formation, thus maintaining structural integrity of the implant site during healing.

Biological testing should be furthered through *in vivo* testing in animal models and subsequent human testing. Though the *in vitro* tests reported provide an insight into the potential of the materials as bone replacement devices, they fail to simulate the complex environment found in the body. Subcutaneous implantation of the materials would allow for the osteoinductive nature of the materials to be properly assessed as *in vitro* testing lacks the local proteins, fluctuations in serum compositions and variety of cell types that are found in the body. Implantation into a defect in an animal model would allow for investigation of the ability of the material to bond to bone and also the time taken for resorption. *In vivo* animal studies would first have to be performed before human clinical tries could be conducted in order to assess the efficacy of the material as the basis of a bone replacement device.

Chapter 9: References

1. Greenwald, A.S., et al., *Bone-Graft Substitutes: Facts, Fictions, and Applications.* J Bone Joint Surg Am, 2001. **83**(2_suppl_2): p. S98-103.
2. Urabe, K., et al., *Current trends in bone grafting and the issue of banked bone allografts based on the fourth nationwide survey of bone grafting status from 2000 to 2004.* Journal of Orthopaedic Science, 2007. **12**(6): p. 520-525.
3. Laurencin, C.T., et al., *Tissue engineering: Orthopedic applications.* Annual Review of Biomedical Engineering, 1999. **1**: p. 19-46.
4. Handoll, H.H.G. and A.C. Watts, *Bone grafts and bone substitutes for treating distal radial fractures in adults.* Cochrane Database of Systematic Reviews, 2008(2).
5. Langer, R. and J.P. Vacanti, *Tissue engineering.* Science, 1993. **260**(5110): p. 920-926.
6. Weiner, S. and H.D. Wagner, *The material bone: Structure mechanical function relations.* Annual Review of Materials Science, 1998. **28**: p. 271-298.
7. Kokubo, T., *Bioceramics and Their Clinical Applications*. First ed. 2008: Woodhead Publishing Limited.
8. Xian, C.J., et al., *Intramembranous ossification mechanism for bone bridge formation at the growth plate cartilage injury site.* Journal of Orthopaedic Research, 2004. **22**(2): p. 417-426.
9. Sommer, B., et al., *Expression of matrix proteins during the development of mineralized tissues.* Bone, 1996. **19**(4): p. 371-380.
10. Ziv, V. and S. Weiner, *Bone Crystal Sizes - a comparison of transmission electron microscopic and x-ray-diffraction line-width broadening techniques.* Connective Tissue Research, 1994. **30**(3): p. 165-175.
11. Fritsch, A. and C. Hellmich, *'Universal' microstructural patterns in cortical and trabecular, extracellular and extravascular bone materials: Micromechanics-based prediction of anisotropic elasticity.* Journal of Theoretical Biology, 2007. **244**(4): p. 597-620.
12. web-books.com. *Compact Bone and Spongy (Cancelous) Bone*. 2013 [cited 2013 02/07/2013]; Available from: <**http://www.web-books.com/eLibrary/Medicine/Physiology/Skeletal/compact_spongy_bone.jpg**>.
13. Vaananen, K., *Mechanism of osteoclast mediated bone resorption - rationale for the design of new therapeutics.* Advanced Drug Delivery Reviews, 2005. **57**(7): p. 959-971.
14. Long, M.W., et al., *Regulation of human bone-marrow-derived osteoprogenitor cells by osteogenic growth-factors.* Journal of Clinical Investigation, 1995. **95**(2): p. 881-887.
15. Whitson, S.W., *Tight junction formation in osteon.* Clinical Orthopaedics and Related Research, 1972(86): p. 206-&.
16. Winkler, D.G., et al., *Osteocyte control of bone formation via sclerostin, a novel BMP antagonist.* Embo Journal, 2003. **22**(23): p. 6267-6276.
17. Choi, K., et al., *The Elastic-Moduli Of Human Subchondral, Trabecular, And Cortical Bone Tissue And The Size-Dependency Of Cortical Bone Modulus.* Journal of Biomechanics, 1990. **23**(11): p. 1103-1113.

18. Yaszemski, M.J., et al., *Evolution of bone transplantation: Molecular, cellular and tissue strategies to engineer human bone.* Biomaterials, 1996. **17**(2): p. 175-185.
19. Yamamuro, T., *Clinical Application of Bioactive Glass-Ceramics*, in *Bioceramics and Their Clinical Applications*, T. Kokubo, Editor. 2008, Woodhead Publishing, Ltd.: Cambridge, England.
20. Hoc, T., et al., *Effect of microstructure on the mechanical properties of Haversian cortical bone.* Bone, 2006. **38**(4): p. 466-474.
21. Weiner, S., W. Traub, and H.D. Wagner, *Lamellar bone: Structure-function relations.* Journal of Structural Biology, 1999. **126**(3): p. 241-255.
22. Alberts, *Molecular Biology of the Cell*. Fourth Edition ed. 2002: Garland Science.
23. Brighton, C.T. and R.M. Hunt, *Early Histological And Ultrastructural-Changes In Medullary Fracture Callus.* Journal of Bone and Joint Surgery-American Volume, 1991. **73A**(6): p. 832-847.
24. Martini, F.H., *Fundamentals of Anatomy & Physiology*. Third ed. 1995: Prentice Hall, Inc.
25. Martin, T.J. and E. Seeman, *Bone remodelling: its local regulation and the emergence of bone fragility.* Best Practice & Research Clinical Endocrinology & Metabolism, 2008. **22**(5): p. 701-722.
26. Parfitt, A.M., et al., *Structural and cellular changes during bone growth in healthy children.* Bone, 2000. **27**(4): p. 487-494.
27. Hadjidakis, D.J. and I.I. Androulakis, *Bone Remodeling.* Annals of the New York Academy of Sciences, 2006. **1092**(Women's Health and Disease: Gynecologic, Endocrine, and Reproductive Issues): p. 385-396.
28. Doblaré, M., J.M. García, and M.J. Gómez, *Modelling bone tissue fracture and healing: a review.* Engineering Fracture Mechanics, 2004. **71**(13-14): p. 1809-1840.
29. van Oers, R.F.M., et al., *A unified theory for osteonal and hemi-osteonal remodeling.* Bone, 2008. **42**(2): p. 250-259.
30. Baroli, B., *From Natural Bone Grafts to Tissue Engineering Therapeutics: Brainstorming on Pharmaceutical Formulative Requirements and Challenges.* Journal of Pharmaceutical Sciences, 2009. **98**(4): p. 1317-1375.
31. Pittenger, M.F., et al., *Multilineage Potential of Adult Human Mesenchymal Stem Cells.* Science, 1999. **284**(5411): p. 143-147.
32. Awad, H.A., et al., *Autologous Mesenchymal Stem Cell-Mediated Repair of Tendon.* Tissue Engineering, 1999. **5**(3): p. 267-277.
33. Sethe, S., A. Scutt, and A. Stolzing, *Aging of mesenchymal stem cells.* Ageing Research Reviews, 2006. **5**(1): p. 91-116.
34. d'Aquino, R., et al., *Dental pulp stem cells: A promising tool for bone regeneration.* Stem Cell Reviews, 2008. **4**(1): p. 21-26.
35. Montelatici, E., et al. *Characterization, expression analysis and differentiation of human adipose-derived mesenchymal stem cells*. in *34th Annual Meeting of the International-Society-for-Experimental-Hematology*. 2005. Glasgow, SCOTLAND.
36. Toma, J.G., et al., *Isolation of multipotent adult stem cells from the dermis of mammalian skin.* Nature Cell Biology, 2001. **3**(9): p. 778-784.
37. Wada, M.R., et al., *Generation of different fates from multipotent muscle stem cells.* Development, 2002. **129**(12): p. 2987-2995.

38. Rosada, C., et al., *The human umbilical cord blood: A potential source for osteoblast progenitor cells.* Calcified Tissue International, 2003. **72**(2): p. 135-142.
39. Erices, A., P. Conget, and J.J. Minguell, *Mesenchymal progenitor cells in human umbilical cord blood.* British Journal of Haematology, 2000. **109**(1): p. 235-242.
40. Kassem, M., et al., *Demonstration of cellular aging and senescence in serially passaged long-term cultures of human trabecular osteoblasts.* Osteoporosis International, 1997. **7**(6): p. 514-524.
41. Simonsen, J.L., et al., *Telomerase expression extends the proliferative life-span and maintains the osteogenic potential of human bone marrow stromal cells.* Nature Biotechnology, 2002. **20**(6): p. 592-596.
42. Buehring, H.-J., et al., *Novel markers for the prospective isolation of human MSC,* in *Hematopoietic Stem Cells Vi*, L. Kanz, et al., Editors. 2007. p. 262-271.
43. Lennon, D.P. and A.I. Caplan, *Mesenchymal Stem Cells for Tissue Engineering,* in *Culture of Cells for Tissue Engineering*, R.I. Freshney, Editor. 2006, John Wiley & Sons, Inc.
44. Roura, S., et al., *Effect of aging on the pluripotential capacity of human CD105+ mesenchymal stem cells.* Eur J Heart Fail, 2006. **8**(6): p. 555-563.
45. Crapnell, K., et al., *Growth, differentiation capacity, and function of mesenchymal stem cells expanded in serum-free medium developed via combinatorial screening.* Experimental Cell Research, 2013. **319**(10): p. 1409-1418.
46. Tasso, R. and G. Pennesi, *When stem cells meet immunoregulation.* International Immunopharmacology, 2009. **9**(5): p. 596-598.
47. Tasso, R., et al., *Development of sarcomas in mice implanted with mesenchymal stem cells seeded onto bioscaffolds.* Carcinogenesis, 2009. **30**(1): p. 150-157.
48. Engler, A.J., et al., *Matrix elasticity directs stem cell lineage specification.* Cell, 2006. **126**(4): p. 677-689.
49. Even-Ram, S., V. Artym, and K.M. Yamada, *Matrix Control of Stem Cell Fate.* Cell, 2006. **126**(4): p. 645-647.
50. Hulbert, S.F., et al., *Potential of ceramic materials as permanently implantable skeletal prostheses.* Journal of Biomedical Materials Research, 1970. **4**(3): p. 433-456.
51. Itala, A.I., et al., *Pore diameter of more than 100 mu m is not requisite for bone ingrowth in rabbits.* Journal of Biomedical Materials Research, 2001. **58**(6): p. 679-683.
52. Karageorgiou, V. and D. Kaplan, *Porosity of 3D biornaterial scaffolds and osteogenesis.* Biomaterials, 2005. **26**(27): p. 5474-5491.
53. Habibovic, P., et al., *Osteoinduction by biomaterials - Physicochemical and structural influences.* Journal of Biomedical Materials Research Part A, 2006. **77A**(4): p. 747-762.
54. Habibovic, P., et al., *3D microenvironment as essential element for osteoinduction by biomaterials.* Biomaterials, 2005. **26**(17): p. 3565-3575.
55. Heymer, A., et al., *Multiphasic collagen fibre-PLA composites seeded with human mesenchymal stem cells for osteochondral defect repair: an in vitro study.* Journal of Tissue Engineering and Regenerative Medicine, 2009. **3**(5): p. 389-397.

56. Cheung, H.Y., et al., *A critical review on polymer-based bio-engineered materials for scaffold development.* Composites Part B-Engineering, 2007. **38**(3): p. 291-300.
57. Yoshimi, R., et al., *Self-Assembling Peptide Nanofiber Scaffolds, Platelet-Rich Plasma, and Mesenchymal Stem Cells for Injectable Bone Regeneration With Tissue Engineering.* Journal of Craniofacial Surgery, 2009. **20**(5): p. 1523-1530.
58. Lee, K., et al., *Cell Therapy for Bone Regeneration-Bench to Bedside.* Journal of Biomedical Materials Research Part B-Applied Biomaterials, 2009. **89B**(1): p. 252-263.
59. Hench, L.L., et al., *Analysis of bioglass fixation of hip prostheses.* Journal of Biomedical Materials Research, 1977. **11**(2): p. 267-282.
60. Likitvanichkul, S. and W.C. Lacourse, *Apatite-wollastonite glass-ceramics part I - Crystallization kinetics by differential thermal analysis.* Journal of Materials Science, 1998. **33**(24): p. 5901-5904.
61. Xiao, K., *Indirect Selective Laser Sintering Of Apatite-Wollastonite Glass Ceramic*, in *School of Mechanical Engineering*. 2007, University of Leeds: Leeds, UK.
62. Xiao, K., et al., *Indirect selective laser sintering of apatite-wollostonite glass-ceramic.* Proceedings of the Institution of Mechanical Engineers Part H-Journal of Engineering in Medicine, 2008. **222**(H7): p. 1107-1114.
63. Bogdanov, B.I., et al., *Bioactive fluorapatite-containing glass ceramics.* Ceramics International, 2009. **35**(4): p. 1651-1655.
64. Magallanes-Perdomo, M., et al., *In vitro study of the proliferation and growth of human bone marrow cells on apatite-wollastonite-2M glass ceramics.* Acta Biomaterialia, 2010. **In Press, Corrected Proof**.
65. Goodridge, R.D., K.W. Dalgarno, and D.J. Wood, *Indirect selective laser sintering of an apatite-mullite glass-ceramic for potential use in bone replacement applications.* Proceedings of the Institution of Mechanical Engineers Part H-Journal of Engineering in Medicine, 2006. **220**(H1): p. 57-68.
66. Kokubo, T., *Bioactive glass-ceramics*, in *Bioceramics and Their Clinical Applications*, T. Kokubo, Editor. 2008, Woodhead Publishing, Ltd.: Cambridge, England.
67. Fredholm, Y.C., et al., *Influence of strontium for calcium substitution in bioactive glasses on degradation, ion release and apatite formation.* Journal of the Royal Society Interface, 2012. **9**(70): p. 880-889.
68. Fujikura, K., et al., *Influence of strontium substitution on structure and crystallisation of Bioglass (R) 45S5.* Journal of Materials Chemistry, 2012. **22**(15): p. 7395-7402.
69. O'Donnell, M.D., et al., *Materials characterisation and cytotoxic assessment of strontium-substituted bioactive glasses for bone regeneration.* Journal of Materials Chemistry, 2012. **20**(40): p. 8934-8941.
70. Salman, S.M., S.N. Salama, and H.A. Abo-Mosallam, *The role of strontium and potassium on crystallization and bioactivity of Na2O-CaO-P2O5-SiO2 glasses.* Ceramics International, 2012. **38**(1): p. 55-63.
71. Ni, G.-X., et al., *The effect of strontium incorporation into hydroxyapatites on their physical and biological properties.* Journal of Biomedical Materials Research Part B-Applied Biomaterials, 2011. **100B**(2): p. 562-568.
72. O'Donnell, M.D., et al., *Structural analysis of a series of strontium-substituted apatites.* Acta Biomaterialia, 2008. **4**(5): p. 1455-1464.

73. Wu, C., et al., *The effect of strontium incorporation into CaSiO3 ceramics on their physical and biological properties.* Biomaterials, 2007. **28**(21): p. 3171-3181.
74. Marie, P.J., D. Felsenberg, and M.L. Brandi, *How strontium ranelate, via opposite effects on bone resorption and formation, prevents osteoporosis.* Osteoporosis International, 2011. **22**(6): p. 1659-1667.
75. Marie, P.J., et al., *An Uncoupling Agent Containing Strontium Prevents Bone Loss By Depressing Bone-Resorption And Maintaining Bone-Formation In Estrogen-Deficient Rats.* Journal of Bone and Mineral Research, 1993. **8**(5): p. 607-615.
76. Brennan, T.C., et al., *Osteoblasts play key roles in the mechanisms of action of strontium ranelate.* British Journal of Pharmacology, 2009. **157**(7): p. 1291-1300.
77. Brown, E., *Is the calcium receptor a molecular target for the actions of strontium on bone?* Osteoporosis International, 2003. **14**(3): p. 25-34.
78. Hurtel-Lemaire, A.S., et al., *The Calcium-sensing Receptor Is Involved in Strontium Ranelate-induced Osteoclast Apoptosis: NEW INSIGHTS INTO THE ASSOCIATED SIGNALING PATHWAYS.* Journal of Biological Chemistry, 2009. **284**(1): p. 575-584.
79. Chattopadhyay, N., et al., *The calcium-sensing receptor (CaR) is involved in strontium ranelate-induced osteoblast proliferation.* Biochemical Pharmacology, 2007. **74**(3): p. 438-447.
80. Fromigue, O., *Essential Role of Nuclear Factor of Activated T Cells (NFAT)-mediated Wnt Signaling in Osteoblast Differentiation Induced by Strontium Ranelate.* Journal of Biological Chemistry, 2010. **285**(33): p. 25251-25258.
81. Fredholm, Y.C., et al., *Strontium Containing Bioactive Glasses: Glass Structure And Physical Properties.* Journal of Non-Crystalline Solids, 2010. **356**(44-49): p. 2546-2551.
82. Hesaraki, S., et al., *The effect of Sr concentration on bioactivity and biocompatibility of sol-gel derived glasses based on CaO-SrO-SiO2-P2O5 quaternary system.* Materials Science & Engineering C-Materials for Biological Applications, 2010. **30**(3): p. 383-390.
83. Shannon, R.D., *Revised Effective Ionic-Radii And Systematic Studies Of Interatomic Distances In Halides And Chalcogenides.* Acta Crystallographica Section A, 1976. **32**(SEP1): p. 751-767.
84. Lao, J., J.M. Nedelec, and E. Jallot, *New strontium-based bioactive glasses: physicochemical reactivity and delivering capability of biologically active dissolution products.* Journal of Materials Chemistry, 2009. **19**(19): p. 2940-2949.
85. O'Donnell, M.D., et al., *Materials characterisation and cytotoxic assessment of strontium-substituted bioactive glasses for bone regeneration.* Journal of Materials Chemistry, 2010. **20**(40): p. 8934-8941.
86. Goel, A., R.R. Rajagopal, and J.M.F. Ferreira, *Influence of strontium on structure, sintering and biodegradation behaviour of CaO-MgO-SrO-SiO2-P2O5-CaF2 glasses.* Acta Biomaterialia, 2011. **7**(11): p. 4071-4080.
87. Hill, R.G., et al., *The influence of strontium substitution in fluorapatite glasses and glass-ceramics.* Journal of Non-Crystalline Solids, 2004. **336**(3): p. 223-229.
88. Magallanes-Perdomo, M., et al., *In vitro study of the proliferation and growth of human bone marrow cells on apatite-wollastonite-2M glass ceramics.* Acta Biomaterialia, 2010. **6**(6): p. 2254-2263.

89. Magallanes-Perdomo, M., et al., *Bone-like forming ability of apatite-wollastonite glass ceramic.* Journal of the European Ceramic Society, 2011. **31**(9): p. 1549-1561.
90. Gentleman, E., et al., *The effects of strontium-substituted bioactive glasses on osteoblasts and osteoclasts in vitro.* Biomaterials, 2010. **31**(14): p. 3949-3956.
91. Zhang, W., et al., *Effects of strontium in modified biomaterials.* Acta Biomaterialia, 2011. **7**(2): p. 800-808.
92. Zanotto, E.D., *Crsytalistion of liquids and glasses: a kinetic approach*, in *Glass-Ceramic Materials: Fundamentals and Applications*, J. Rincon, Editor. 1997, Mucchi Editore: Madrid, Spain. p. 25-39.
93. Beadle, J., *Glass*. Design Engineering Series. 1969, London: Morgan-Grampian Ltd.
94. Rawlings, R.D., *Bioactive glasses and glass-ceramics.* Clinical Materials, 1993. **14**(2): p. 155-179.
95. Rawlings, R.D., *General principles of glass-ceramic production*, in *Glass-ceramic materials: Fundamentals and Applications*, J. Rincon, Editor. 1997, Mucchi Editore: Madrid, Spain. p. 77-92.
96. Balta, P., Balta, E., *Introduction to the physical chemistry of the vitrous state*. 1976, Tumbridge Wells,: Abacus Press.
97. Rincon, J., *Glass-ceramic materials: Fundamentals and Applications*. 1997: Mucchi Editore.
98. Stoch, L., *Crystal-chemistry of chrystallization phenomena in glass-ceramics*, in *Glass-ceramic materials: Fundementals and applicaions*, J. Rincon, Editor. 1997, Mucchi Editore: Madrid, Spain. p. 41-64.
99. Holand, W., Beall, G., *Glass-ceramic technology*. 2002, Westerville: The American Ceramic Society.
100. James, P.F., *Nucleation in glass-forming systems - a review*, in *Advances in Ceramics*. 1982, The American Ceramic Society, Inc.: Washington, D.C.
101. James, P.F., *Volume nucleation in silicate glasses*, in *Glasses and glass ceramics*, M.H. Lewis, Editor. 1989, Chapman and Hall: Coventry, UK.
102. Dupree, R., Holland, D., *MAS NMR: a new spectroscopic technique for structure determination in glasses and ceramics*, in *Glasses and Glass-Ceramics*, M.H. Lewis, Editor. 1989, Chapman and Hall: Coventry, UK.
103. Leite, E. and C. Ribeiro, *Introduction*, in *Crystallization and Growth of Colloidal Nanocrystals*. 2012, Springer New York. p. 1-6.
104. Hu, A.-M., et al., *Effect of nucleation temperatures and time on crystallization behavior and properties of Li2O-Al2O3-SiO2 glasses.* Materials Chemistry and Physics, 2006. **98**(2-3): p. 430-433.
105. Holand, W., V. Rheinberger, and M. Schweiger, *Control of nucleation in glass ceramics.* Philosophical Transactions of the Royal Society of London Series a-Mathematical Physical and Engineering Sciences, 2003. **361**(1804): p. 575-588.
106. Clifford, A., et al., *The influence of calcium to phosphate ratio on the nucleation and crystallization of apatite glass-ceramics.* Journal of Materials Science-Materials in Medicine, 2001. **12**(5): p. 461-469.
107. German, R., P. Suri, and S. Park, *Review: liquid phase sintering.* Journal of Materials Science, 2009. **44**(1): p. 1-39.
108. German, R.M., *Sintering Theory and Practice*. 1986.
109. Goel, A., et al., *Alkali-free bioactive glasses for bone tissue engineering: A preliminary investigation.* Acta Biomaterialia, 2012. **8**(1): p. 361-372.

110. Cannillo, V., et al., *Thermal and physical characterisation of apatite/wollastonite bioactive glass-ceramics.* Journal of the European Ceramic Society, 2009. **29**(4): p. 611-619.
111. Chang, C.K., D.L. Mao, and J.S. Wu, *Characteristics of crystals precipitated in sintered apatite/wollastonite glass ceramics.* Ceramics International, 2000. **26**(7): p. 779-785.
112. Standard, B., *Methods of test for dense shaped refractory products - Part 1: Determination of bulk density, apparent porosity and true porosity*. 1995, BSI Group: Brittish Standards Online.
113. Bertoldi, S., S. Fare, and M.C. Tanzi, *Assessment of scaffold porosity: the new route of micro-CT.* Journal of Applied Biomaterials & Biomechanics, 2011. **9**(3): p. 165-175.
114. Gerhardt, L.-C. and A.R. Boccaccini, *Bioactive Glass and Glass-Ceramic Scaffolds for Bone Tissue Engineering.* Materials, 2010. **3**(7): p. 3867-3910.
115. Standard, B., *Dentistry - Ceramic materials*. 2008, BSI Group: Brittish Standards Online.
116. Kokubo, T., *Bioactive glass ceramics: properties and applications.* Biomaterials, 1991. **12**(2): p. 155-163.
117. Dyson, J.A., et al., *Development of custom-built bone scaffolds using mesenchymal stem cells and apatite-wollastonite glass-ceramics.* Tissue Engineering, 2007. **13**(12): p. 2891-2901.
118. Bushberg, J.T., et al., *X-Ray Production, X-Ray Tubes, and Generators*, in *The Essential Physics of Medical Imaging*, J.T. Bushberg, Editor. 2002, Lippincott Williams & Wilkins: Philadelphia, USA. p. 95-144.
119. Shimadzu. *Volume Standard and Number Standard in Particle Size Distribution*. [Web Page] 2013 [cited 2013 16/01/2013]; Available from: http://www.shimadzu.com/an/powder/support/practice/p01/lesson17.html.
120. Hubble, J.H. and S. S.M. *Tables of X-Ray Mass Attenuation Coefficients and Mass Energy-Absorption Coefficients from 1 keV to 20 MeV for Elements Z = 1 to 92and 48 Additional Substances of Dosimetric Interest*. 1996 23/01/12]; Available from: http://www.nist.gov/pml/data/xraycoef/index.cfm.
121. Malvern, I.L., *Getting Started: Mastersizer Manual*. 1997, Malvern Instruments Ltd,. p. 3.1-3.7.
122. Malvern, I.L. *Analyzing Irregular Particles*. 2013 28/01/13]; Available from: http://www.malvern.com/LabEng/technology/laser_diffraction/irregular_particles.htm.
123. Goldstein, J., et al., *Special Topics in Electron Beam X-Ray Microanalysis*, in *Scanning Electron Microscopy and X-Ray Microanalysis*, J. Goldstein, Editor. 2003, Springer Scienece and Business Media, Inc.: New York, USA. p. 462-470.
124. Hill, R. and M. Stevens, *Bioactive Glass*, W.I.P. Organization, Editor. 2007: Great Britain.
125. Lotfibakhshaiesh, N., D.S. Brauer, and R.G. Hill, *Bioactive Glass Engineered Coatings For Ti6Al4V Alloys: Influence Of Strontium Substitution For Calcium On Sintering Behaviour.* Journal of Non-Crystalline Solids, 2010. **356**(44-49): p. 2583-2590.
126. Galliano, P.G., A.L. Cavalieri, and J.M.P. Lopez, *A Study By Density-Measurements And Indentation Tests Of A Calcium Silicophosphate*

Bioactive Glass With Different Mgo Or Sro Contents. Journal of Non-Crystalline Solids, 1995. **191**(3): p. 311-320.
127. Kansal, I., et al., *Structural Analysis And Thermal Behavior Of Diopside-Fluorapatite-Wollastonite-Based Glasses And Glass-Ceramics.* Acta Biomaterialia, 2010. **6**(11): p. 4380-4388.
128. Whaites, E., *Radiation Physics and Equipment*, in *Essential of Dental Radiography and Radiology*, E. Whaites, Editor. 2007, Churchill Linvingstone Elsevier: London, UK. p. 13-66.
129. Poludniowski, G.G., *Calculation Of X-Ray Spectra Emerging From An X-Ray Tube. Part II. X-Ray Production And Filtration In X-Ray Targets.* Medical Physics, 2007. **34**(6): p. 2175-2186.
130. Beaman, F.D., et al., *Imaging characteristics of bone graft materials.* Radiographics, 2006. **26**(2): p. 373-U5.
131. Haramati, N., et al., *CT Scans Through Metal Scanning Technique Versus Hardware Composition.* Computerized Medical Imaging and Graphics, 1994. **18**(6): p. 429-434.
132. Bushberg, J.T., et al., *Computed Tomography*, in *The Essential Physics of Medical Imaging*, J.T. Bushberg, Editor. 2002, Lippincott Williams & Wilkins: Philadelphia, USA. p. 369-372.
133. Link, T.M., et al., *CT Of Metal Implants: Reduction Of Artifacts Using An Extended CT Scale Technique.* Journal of Computer Assisted Tomography, 2000. **24**(1): p. 165-172.
134. Augis, J.A. and J.E. Bennett, *Calculation Of The Avrami Parameters For Heterogeneous Solid State Reactions Using A Modification Of The Kissinger Method.* Journal of Thermal Analysis and Calorimetry, 1978. **13**(2): p. 283-292.
135. Kokubo, T., et al., *Formation of a high-strength bioactive glass-ceramic in the system MgO-CaO-SiO2-P2O5.* Journal of Materials Science, 1986. **21**(2): p. 536-540.
136. O'Donnell, M.D. and R.G. Hill, *Influence of strontium and the importance of glass chemistry and structure when designing bioactive glasses for bone regeneration.* Acta Biomaterialia, 2010. **6**(7): p. 2382-2385.
137. Ray, N.H., *Compositionâ€"property relationships in inorganic oxide glasses.* Journal of Non-Crystalline Solids, 1974. **15**(3): p. 423-434.
138. Doweidar, H., *The density of alkali silicate glasses in relation to the microstructure.* Journal of Non-Crystalline Solids, 1996. **194**(1â€“2): p. 155-162.
139. Kokubo, T., et al., *Mechanical-Properties Of A New Type Of Apatite-Containing Glass Ceramic For Prosthetic Application.* Journal of Materials Science, 1985. **20**(6): p. 2001-2004.
140. Calver, A., R.G. Hill, and A. Stamboulis, *Influence of fluorine content on the crystallization behavior of apatite-wollastonite glass-ceramics.* Journal of Materials Science, 2004. **39**(7): p. 2601-2603.
141. Magallanes-Perdomo, M., et al., *Devitrification studies of wollastonite-tricalcium phosphate eutectic glass.* Acta Biomaterialia, 2009. **5**(8): p. 3057-3066.
142. van Dooren, A.A. and B.W. MÃ¼ller, *Influence of experimental variables on curves in differential scanning calorimetry. Part III. Effects on peak height, peak width, shape index and baseline displacement.* Thermochimica Acta, 1981. **49**(2â€“3): p. 175-183.

143. Fernandez-Pradas, J.M., et al., *Pulsed laser deposition of pseudowollastonite coatings.* Biomaterials, 2002. **23**(9): p. 2057-2061.
144. de Aza, P.N., et al., *Morphological and structural study of pseudowollastonite implants in bone.* Journal of Microscopy (Oxford), 2000. **197**(1): p. 60-67.
145. Carrodeguas, R.G., et al., *Assessment of natural and synthetic wollastonite as source for bioceramics preparation.* Journal of Biomedical Materials Research Part A, 2007. **83A**(2): p. 484-495.
146. Yang, H.X. and C.T. Prewitt, *On the crystal structure of pseudowollastonite (CaSiO3).* American Mineralogist, 1999. **84**(5-6): p. 929-932.
147. Fokin, V.M., et al., *Critical assessment of DTA-DSC methods for the study of nucleation kinetics in glasses.* Journal of Non-Crystalline Solids, 2010. **356**(6-8): p. 358-367.
148. Galliano, P.G. and J.M.P. Lopez, *Thermal-Behavior Of Bioactive Alkaline-Earth Silicophosphate Glasses.* Journal of Materials Science-Materials in Medicine, 1995. **6**(6): p. 353-359.
149. Cabral, A.A., V.M. Fokin, and E.D. Zanotto, *On the Determination of Nucleation Rates in Glasses by Nonisothermal Methods.* Journal of the American Ceramic Society, 2010. **93**(9): p. 2438-2440.
150. Illesova, L., *Determination of avrami parameters of hydroxyapatite and Î²-wollastonite in bioactive phosphorâ€"Silica glasses.* Journal of thermal analysis, 1995. **44**(3): p. 589-595.
151. Prado, M.O. and E.D. Zanotto, *Glass sintering with concurrent crystallization.* Comptes Rendus Chimie, 2002. **5**(11): p. 773-786.
152. Chen, I.W. and X.H. Wang, *Sintering dense nanocrystalline ceramics without final-stage grain growth.* Nature, 2000. **404**(6774): p. 168-171.
153. Prado, M.O., C. Fredericci, and E.D. Zanotto, *Glass sintering with concurrent crystallisation. Part 2. Nonisothermal sintering of jagged polydispersed particles.* Physics and Chemistry of Glasses, 2002. **43**(5): p. 215-223.
154. Prado, M.O., E.B. Ferreira, and E.D. Zanotto, *Sintering kinetics of crystallizing glass particles - A review*, in *Melt Chemistry, Relaxation, and Solidification Kinetics of Glasses*, H. Li, et al., Editors. 2005. p. 163-179.
155. Prado, M.O., E.D. Zanotto, and R. MÃ¼ller, *Model for sintering polydispersed glass particles.* Journal of Non-Crystalline Solids, 2001. **279**(2â€“3): p. 169-178.
156. Peitl, O., et al., *Compositional and microstructural design of highly bioactive P2O5-Na2O-CaO-SiO2 glass-ceramics.* Acta Biomaterialia, 2012. **8**(1): p. 321-332.
157. Klawitter, J.J., et al., *Evaluation Of Bone-Growth Into Porous High-Density Polyethylene.* Journal of Biomedical Materials Research, 1976. **10**(2): p. 311-323.
158. Eggli, P.S., W. Muller, and R.K. Schenk, *Porous Hydroxyapatite And Tricalcium Phosphate Cylinders With 2 Different Pore-Size Ranges Implanted In The Cancellous Bone Of Rabbits - A Comparative Histomorphometric And Histologic-Study Of Bony Ingrowth And Implant Substitution.* Clinical Orthopaedics and Related Research, 1988(232): p. 127-138.
159. Klawitter, J.J. and S.F. Hulbert, *Application Of Porous Ceramics For The Attachment Of Load Bearing Internal Orthopedic Applications.* Journal of

Biomedical Materials Research Biomedical Materials Symposium, 1972. **2**: p. 161-229.
160. Karageorgiou, V. and D. Kaplan, *Porosity of 3D biomaterial scaffolds and osteogenesis.* Biomaterials, 2005. **26**(27): p. 5474-5491.
161. Kokubo, T., *Surface-Chemistry Of Bioactive Glass-Ceramics.* Journal of Non-Crystalline Solids, 1990. **120**(1-3): p. 138-151.
162. Brauer, D.S., et al., *Fluoride-containing bioactive glasses: Effect of glass design and structure on degradation, pH and apatite formation in simulated body fluid.* Acta Biomaterialia, 2010. **6**(8): p. 3275-3282.
163. Pan, H.B., et al., *Solubility of strontium-substituted apatite by solid titration.* Acta Biomaterialia, 2009. **5**(5): p. 1678-1685.
164. Landi, E., et al., *Sr-substituted hydroxyapatites for osteoporotic bone replacement.* Acta Biomaterialia, 2007. **3**(6): p. 961-969.
165. Sainz, M.A., et al., *Influence of design on bioactivity of novel CaSiO3â€“CaMg(SiO3)2 bioceramics: In vitro simulated body fluid test and thermodynamic simulation.* Acta Biomaterialia, 2010. **6**(7): p. 2797-2807.
166. Samachso, J., *Basic requirements for calcification.* Nature, 1969. **221**(5187): p. 1247-&.
167. Castromalaspina, H., et al., *Characterization Of Human-Bone Marrow Fibroblast Colony-Forming Cells (Cfu-F) And Their Progeny.* Blood, 1980. **56**(2): p. 289-301.
168. Roura, S., et al., *Effect of aging on the pluripotential capacity of human CD105(+) mesenchymal stem cells.* European Journal of Heart Failure, 2006. **8**(6): p. 555-563.
169. Yameen, Z., et al., *Multilineage differentiation potential of bone and cartilage cells derived from explant culture.* The Open Stem Cell Journal, 2009. **1**: p. 10-19.
170. Bonab, M.M., et al., *Aging of mesenchymal stem cell in vitro.* Bmc Cell Biology, 2006. **7**.
171. Mafi, P., et al., *Adult mesenchymal stem cells and cell surface characterization - a systematic review of the literature.* The open orthopaedics journal, 2011. **5**(Suppl 2): p. 253-60.
172. Holy, C.E., M.S. Shoichet, and J.E. Davies, *Engineering three-dimensional bone tissue in vitro using biodegradable scaffolds: Investigating initial cell-seeding density and culture period.* Journal of Biomedical Materials Research, 2000. **51**(3): p. 376-382.
173. Yeatts, A.B. and J.P. Fisher, *Bone tissue engineering bioreactors: Dynamic culture and the influence of shear stress.* Bone. **48**(2): p. 171-181.
174. Loty, C., et al., *The biomimetics of bone: Engineered glass-ceramics a paradigm for in vitro biomineralization studies.* Connective Tissue Research, 2002. **43**(2-3): p. 524-528.
175. Boivin, G., et al., *Strontium distribution and interactions with bone mineral in monkey iliac bone after strontium salt (S 12911) administration.* Journal of Bone and Mineral Research, 1996. **11**(9): p. 1302-1311.
176. Marie, P.J., et al., *Mechanisms of action and therapeutic potential of strontium in bone.* Calcified Tissue International, 2001. **69**(3): p. 121-129.
177. Wan, Y.Q., et al., *Adhesion and proliferation of OCT-1 osteoblast-like cells on micro- and nano-scale topography structured pply(L-lactide).* Biomaterials, 2005. **26**(21): p. 4453-4459.

178. Dalby, M.J., et al., *The control of human mesenchymal cell differentiation using nanoscale symmetry and disorder.* Nature Materials, 2007. **6**(12): p. 997-1003.
179. Lusvardi, G., et al., *Fluoride-containing bioactive glasses: Surface reactivity in simulated body fluids solutions.* Acta Biomaterialia, 2009. **5**(9): p. 3548-3562.
180. Webster, T.J., et al., *Specific proteins mediate enhanced osteoblast adhesion on nanophase ceramics.* Journal of Biomedical Materials Research, 2000. **51**(3): p. 475-483.
181. Barbeeri, L., et al., *The microstructure and mechanical properties of sintered celsian and strontium-celsian glass-ceramics.* Materials Research Bulletin, 1995. **30**(1): p. 27-41.
182. Renaudin, G., E. Jallot, and J.M. Nedelec, *Effect of strontium substitution on the composition and microstructure of sol-gel derived calcium phosphates.* Journal of Sol-Gel Science and Technology, 2009. **51**(3): p. 287-294.
183. Kokubo, T., et al., *Mechanical properties of a new type of apatite-containing glass-ceramic for prosthetic application.* Journal of Materials Science, 1985. **20**(6): p. 2001-2004.
184. Rea, S.M., S.M. Best, and W. Bonfield, *Bioactivity of ceramic-polymer composites with varied composition and surface topography.* Journal of Materials Science-Materials in Medicine, 2004. **15**(9): p. 997-1005.
185. Jell, G. and M.M. Stevens, *Gene activation by bioactive glasses.* Journal of Materials Science-Materials in Medicine, 2006. **17**(11): p. 997-1002.
186. Kaysinger, K.K. and W.K. Ramp, *Extracellular pH modulates the activity of cultured human osteoblasts.* Journal of Cellular Biochemistry, 1998. **68**(1): p. 83-89.
187. Barradas, A.M.C., et al., *Osteoinductive Biomaterials: Current Knowledge Of Properties, Experimental Models And Biological Mechanisms.* European Cells & Materials, 2011. **21**: p. 407-429.
188. Yuan, H.P., et al., *A preliminary study on osteoinduction of two kinds of calcium phosphate ceramics.* Biomaterials, 1999. **20**(19): p. 1799-1806.
189. de Bruijn, J.D., et al., *Osteoinduction and its evaluation*. Bioceramics and Their Clinical Applications, ed. T. Kokubo. 2008. 199-219.
190. Ohsawa, K., et al., *In vivo absorption of porous apatite- and wollastonite-containing glass-ceramic.* Journal of Materials Science-Materials in Medicine, 2004. **15**(8): p. 859-864.
191. Ito, M., et al., *Iliac crest reconstruction with a bioactive ceramic spacer.* European Spine Journal, 2005. **14**(1): p. 99-102.
192. De Aza, P.N., et al., *Bioactive glasses and glass-ceramics.* Boletin De La Sociedad Espanola De Ceramica Y Vidrio, 2007. **46**(2): p. 45-55.
193. Berry, E., et al., *Preliminary experience with medical applications of rapid prototyping by selective laser sintering.* Medical Engineering & Physics, 1997. **19**(1): p. 90-96.
194. Salmi, M., et al., *Patient-specific reconstruction with 3D modeling and DMLS additive manufacturing.* Rapid Prototyping Journal, 2012. **18**(3): p. 209-214.
195. Seitz, H., et al., *Three-dimensional printing of porous ceramic scaffolds for bone tissue engineering.* Journal of Biomedical Materials Research Part B-Applied Biomaterials, 2005. **74B**(2): p. 782-788.

196. Ono, K., et al., *Apatite Wollastonite Containing Glass Ceramic Fibrin Mixture As A Bone Defect Filler.* Journal of Biomedical Materials Research, 1988. **22**(10): p. 869-885.
197. Kobayashi, M., et al., *Bioactive bone cement: Comparison of apatite and wollastonite containing glass-ceramic, hydroxyapatite, and β-tricalcium phosphate fillers on bone-bonding strength.* Journal of Biomedical Materials Research, 1998. **42**(2): p. 223-237.
198. Wong, C.T., et al., *In vivo cancellous bone remodeling on a strontium-containing hydroxyapatite (Sr-HA) bioactive cement.* Journal of Biomedical Materials Research Part A, 2004. **68A**(3): p. 513-521.

Appendix A
License Numbers for Re-Print Permissions

Figure 1: National Cancer Institute, free to use or share

Figure 2: 3198880286380

Figure 3: 3199450772357

Figure 4: 3198880106136

Figure 5: 3198880106136

Figure 6: 3198880106136

Figure 7: 3198880106136

Figure 8: 3205951030101

Figure 9: 3205951276294

Figure 10: 3198871443484

Figure 11: 3205941243679

Figure 12: 3205950043817

Figure 13: 3205950531733

Appendix B
Silicon Standard Rietveld Refinement

The Rietveld refinement of the silicon standard matched to PDF 04-016-4861.

B.I Rietveld refinement of the silicon standard

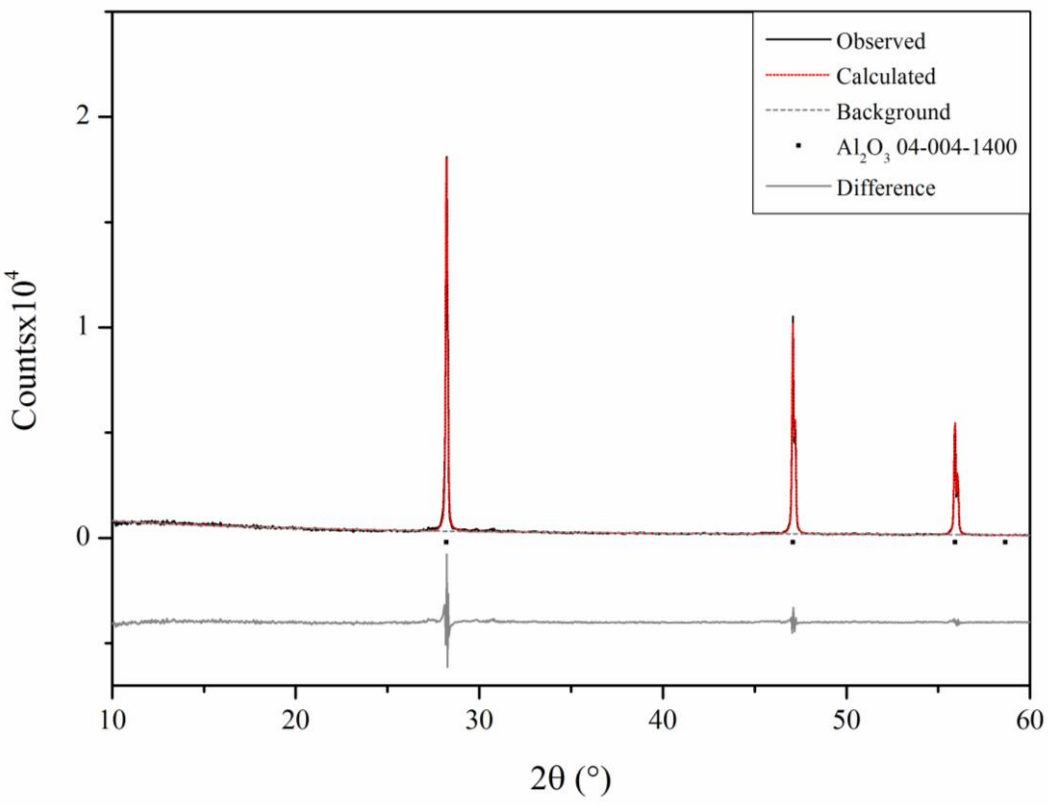

Figure B.I.a: The Si standard experimental and refined x-ray diffraction patterns.

Table B.I.a: The results of the Si standard Rietveld refinement.

Phase	Refinement Factors			
	U	σ	W	σ
Si	0.0091	0.0023	0.0065	0.0004

Appendix C
SPSS Statistical Output of the 3-Point Flexural Test

The SPSS statistical output of the 3-point flexural test, figure 75 and tables 48 and 49.

C.I SPSS statistical output for 3-point flexural test

Table C.I.a: Test of normality.

Tests of Normality

	1	Kolmogorov-Smirnov[a]			Shapiro-Wilk		
		Statistic	df	Sig.	Statistic	df	Sig.
flexural strength	0	.176	11	.200*	.900	11	.183
	3.12	.133	11	.200*	.968	11	.861
	6.24	.223	11	.133	.895	11	.160
	9.35	.195	11	.200*	.928	11	.394
	12.47	.132	11	.200*	.985	11	.987

Table C.I.b: ANOVA test of normally distributed samples.

ANOVA
flexural strength

	Sum of Squares	df	Mean Square	F	Sig.
Between Groups	4217.411	4	1054.353	214.622	.000
Within Groups	245.631	50	4.913		
Total	4463.041	54			

Table C.I.c: Post hok Tukey test for normally distributed samples.

Multiple Comparisons
Dependent Variable: flexural strength
Tukey HSD

(I) 1	(J) 1	Mean Difference (I-J)	Std. Error	Sig.	95% Confidence Interval	
					Lower Bound	Upper Bound
0	3.12	13.06628*	.94509	.000	10.3918	15.7407
	6.24	11.21400*	.94509	.000	8.5396	13.8884
	9.35	15.86014*	.94509	.000	13.1857	18.5346
	12.47	-7.21992*	.94509	.000	-9.8944	-4.5455
3.12	0	-13.06628*	.94509	.000	-15.7407	-10.3918
	6.24	-1.85227	.94509	.300	-4.5267	.8222
	9.35	2.79387*	.94509	.037	.1194	5.4683
	12.47	-20.28620*	.94509	.000	-22.9606	-17.6118
6.24	0	-11.21400*	.94509	.000	-13.8884	-8.5396
	3.12	1.85227	.94509	.300	-.8222	4.5267
	9.35	4.64614*	.94509	.000	1.9717	7.3206
	12.47	-18.43392*	.94509	.000	-21.1084	-15.7595
9.35	0	-15.86014*	.94509	.000	-18.5346	-13.1857
	3.12	-2.79387*	.94509	.037	-5.4683	-.1194
	6.24	-4.64614*	.94509	.000	-7.3206	-1.9717
	12.47	-23.08006*	.94509	.000	-25.7545	-20.4056
12.47	0	7.21992*	.94509	.000	4.5455	9.8944
	3.12	20.28620*	.94509	.000	17.6118	22.9606
	6.24	18.43392*	.94509	.000	15.7595	21.1084
	9.35	23.08006*	.94509	.000	20.4056	25.7545

Appendix D
SPSS Statistical Output for pNPP Results

SPSS statistical output for pNPP results, figures 107 to 111.

D.I Donor K21

D.I.1 Day 0

Table D.I.1.a: Test of normality.

Tests of Normality

VAR00002	Kolmogorov-Smirnov[a]			Shapiro-Wilk		
	Statistic	df	Sig.	Statistic	df	Sig.
.00	.192	6	.200*	.972	6	.903
1.00	.256	6	.200*	.931	6	.584
2.00	.287	6	.133	.728	6	.012
3.00	.244	6	.200*	.930	6	.583

*. This is a lower bound of the true significance.
a. Lilliefors Significance Correction

Table D.I.1.b: Kruskal-Wallis test of not normally distributed data.

Test Statistics[a,b]

	VAR00001
Chi-Square	1.767
df	3
Asymp. Sig.	.622

a. Kruskal Wallis Test
b. Grouping Variable: VAR00002

D.I.2 Day 7

Table D.I.2.a: Test of normality.

Tests of Normality

	VAR00002	Kolmogorov-Smirnov[a]			Shapiro-Wilk		
		Statistic	df	Sig.	Statistic	df	Sig.
VAR00001	10.00	.284	6	.141	.862	6	.196
	11.00	.193	6	.200*	.924	6	.533
	12.00	.223	6	.200*	.941	6	.668
	13.00	.206	6	.200*	.893	6	.333

*. This is a lower bound of the true significance.
a. Lilliefors Significance Correction

Table D.I.2.b: ANOVA analysis of normally distributed data.

ANOVA
VAR00001

	Sum of Squares	df	Mean Square	F	Sig.
Between Groups	.018	3	.006	3.559	.033
Within Groups	.034	20	.002		
Total	.053	23			

D.I.3 Day 14

Table D.I.3.a: Test of normality.

Tests of Normality

	VAR00002	Kolmogorov-Smirnov[a]			Shapiro-Wilk		
		Statistic	df	Sig.	Statistic	df	Sig.
VAR00001	20.00	.227	6	.200*	.917	6	.481
	21.00	.154	6	.200*	.952	6	.760
	22.00	.131	6	.200*	.994	6	.997
	23.00	.184	6	.200*	.913	6	.455

*. This is a lower bound of the true significance.
a. Lilliefors Significance Correction

Table D.I.3.b: ANOVA analysis of normally distributed data.

ANOVA
VAR00001

	Sum of Squares	df	Mean Square	F	Sig.
Between Groups	.145	3	.048	13.902	.000
Within Groups	.069	20	.003		
Total	.214	23			

Table D.I.3.c: Tukey post hoc analysis.

Multiple Comparisons
Dependent Variable: VAR00001
Tukey HSD

(I) VAR00002	(J) VAR00002	Mean Difference (I-J)	Std. Error	Sig.	95% Confidence Interval	
					Lower Bound	Upper Bound
20.00	21.00	-.137*	.034	.003	-.232	-.042
	22.00	.007	.034	.997	-.088	.102
	23.00	.077	.034	.138	-.018	.172
21.00	20.00	.137*	.034	.003	.042	.232
	22.00	.144*	.034	.002	.049	.239
	23.00	.214*	.034	.000	.119	.309
22.00	20.00	-.007	.034	.997	-.102	.088
	21.00	-.144*	.034	.002	-.239	-.049
	23.00	.070	.034	.198	-.025	.165
23.00	20.00	-.077	.034	.138	-.172	.018
	21.00	-.214*	.034	.000	-.309	-.119
	22.00	-.070	.034	.198	-.165	.025

*. The mean difference is significant at the 0.05 level.

D.I.4 Day 21

Table D.I.4.a: Test of normality.

Tests of Normality

	VAR00002	Kolmogorov-Smirnov[a]			Shapiro-Wilk		
		Statistic	df	Sig.	Statistic	df	Sig.
VAR00001	30.00	.194	6	.200*	.918	6	.491
	31.00	.159	6	.200*	.973	6	.914
	32.00	.167	6	.200*	.984	6	.968
	33.00	.232	6	.200*	.935	6	.619

*. This is a lower bound of the true significance.
a. Lilliefors Significance Correction

Table D.I.4.b: ANOVA analysis of normally distributed data.

ANOVA
VAR00001

	Sum of Squares	df	Mean Square	F	Sig.
Between Groups	.160	3	.053	20.183	.000
Within Groups	.053	20	.003		
Total	.213	23			

Table D.I.4.c: Tukey post hoc analysis.

Multiple Comparisons
Dependent Variable: VAR00001
Tukey HSD

(I) VAR00002	(J) VAR00002	Mean Difference (I-J)	Std. Error	Sig.	95% Confidence Interval	
					Lower Bound	Upper Bound
	31.00	-.197*	.030	.000	-.280	-.114
30.00	32.00	-.073	.030	.096	-.156	.010
	33.00	.005	.030	.998	-.078	.088
	30.00	.197*	.030	.000	.114	.280
31.00	32.00	.124*	.030	.002	.041	.207
	33.00	.202*	.030	.000	.119	.285
	30.00	.073	.030	.096	-.010	.156
32.00	31.00	-.124*	.030	.002	-.207	-.041
	33.00	.078	.030	.068	-.005	.161
	30.00	-.005	.030	.998	-.088	.078
33.00	31.00	-.202*	.030	.000	-.285	-.119
	32.00	-.078	.030	.068	-.161	.005

*. The mean difference is significant at the 0.05 level.

D.II. Donor K41

D.II.1 Day 0

Table D.II.1.a: Test of normality.

Tests of Normality

	VAR00002	Kolmogorov-Smirnov[a]			Shapiro-Wilk		
		Statistic	df	Sig.	Statistic	df	Sig.
VAR00001	.00	.208	6	.200*	.913	6	.455
	1.00	.187	6	.200*	.911	6	.444
	2.00	.285	6	.140	.840	6	.130
	3.00	.276	6	.173	.795	6	.053

*. This is a lower bound of the true significance.
a. Lilliefors Significance Correction

Table D.II.1.b: ANOVA analysis of normal data.

ANOVA
VAR00001

	Sum of Squares	df	Mean Square	F	Sig.
Between Groups	.017	3	.006	1.517	.241
Within Groups	.076	20	.004		
Total	.094	23			

D.II.2 Day 7

Table D.II.2.a: Test of normality.

Tests of Normality

	VAR00002	Kolmogorov-Smirnov[a]			Shapiro-Wilk		
		Statistic	df	Sig.	Statistic	df	Sig.
VAR00001	10.00	.288	6	.131	.823	6	.094
	11.00	.197	6	.200*	.965	6	.855
	12.00	.221	6	.200*	.930	6	.580
	13.00	.195	6	.200*	.956	6	.790

*. This is a lower bound of the true significance.
a. Lilliefors Significance Correction

Table D.II.2.b: ANOVA analysis of normally distributed data.

ANOVA
VAR00001

	Sum of Squares	df	Mean Square	F	Sig.
Between Groups	.145	3	.048	7.799	.001
Within Groups	.124	20	.006		
Total	.269	23			

Table D.II.2.c: Tukey post hoc analysis.

Multiple Comparisons
Dependent Variable: VAR00001
Tukey HSD

(I) VAR00002	(J) VAR00002	Mean Difference (I-J)	Std. Error	Sig.	95% Confidence Interval	
					Lower Bound	Upper Bound
10.00	11.00	.048	.045	.719	-.079	.175
	12.00	.159*	.045	.011	.032	.287
	13.00	.189*	.045	.003	.062	.316
11.00	10.00	-.048	.045	.719	-.175	.079
	12.00	.111	.045	.100	-.016	.239
	13.00	.141*	.045	.026	.014	.268
12.00	10.00	-.159*	.045	.011	-.287	-.032
	11.00	-.111	.045	.100	-.239	.016
	13.00	.030	.045	.912	-.097	.157
13.00	10.00	-.189*	.045	.003	-.316	-.062
	11.00	-.141*	.045	.026	-.268	-.014
	12.00	-.030	.045	.912	-.157	.097

*. The mean difference is significant at the 0.05 level.

D.II.3 Day 14

Table D.II.3.a: Test of normality.

Tests of Normality

	VAR00002	Kolmogorov-Smirnov[a]			Shapiro-Wilk		
		Statistic	df	Sig.	Statistic	df	Sig.
VAR00001	20.00	.184	6	.200*	.943	6	.687
	21.00	.200	6	.200*	.926	6	.550
	22.00	.203	6	.200*	.911	6	.441
	23.00	.175	6	.200*	.918	6	.491

*. This is a lower bound of the true significance.
a. Lilliefors Significance Correction

Table D.II.3.b: ANOV analysis of normally distributed data.

ANOVA
VAR00001

	Sum of Squares	df	Mean Square	F	Sig.
Between Groups	.246	3	.082	13.577	.000
Within Groups	.121	20	.006		
Total	.366	23			

Table D.II.3.c: Tukey post hoc analysis.

Multiple Comparisons
Dependent Variable: VAR00001
Tukey HSD

(I) VAR00002	(J) VAR00002	Mean Difference (I-J)	Std. Error	Sig.	95% Confidence Interval	
					Lower Bound	Upper Bound
20.00	21.00	-.128*	.045	.044	-.254	-.003
	22.00	-.084	.045	.268	-.210	.041
	23.00	.137*	.045	.029	.012	.263
21.00	20.00	.128*	.045	.044	.003	.254
	22.00	.044	.045	.762	-.082	.169
	23.00	.265*	.045	.000	.140	.391
22.00	20.00	.084	.045	.268	-.041	.210
	21.00	-.044	.045	.762	-.169	.082
	23.00	.221*	.045	.000	.096	.347
23.00	20.00	-.137*	.045	.029	-.263	-.012
	21.00	-.265*	.045	.000	-.391	-.140
	22.00	-.221*	.045	.000	-.347	-.096

*. The mean difference is significant at the 0.05 level.

D.II.4 Day 21

Table D.II.4.a: Test of normality.

Tests of Normality

	VAR00002	Kolmogorov-Smirnov[a]			Shapiro-Wilk		
		Statistic	df	Sig.	Statistic	df	Sig.
VAR00001	30.00	.296	6	.108	.804	6	.064
	31.00	.273	6	.185	.799	6	.057
	32.00	.235	6	.200*	.906	6	.408
	33.00	.311	6	.071	.723	6	.011

*. This is a lower bound of the true significance.
a. Lilliefors Significance Correction

Table D.II.4.b: Kruskal-Wallis analysis of not normally distributed data.

Test Statistics[a,b]

	VAR00001
Chi-Square	10.607
df	3
Asymp. Sig.	.014

a. Kruskal Wallis Test
b. Grouping Variable: VAR00002

Table D.II.4.c: Bonferroni post hoc analysis.

Multiple Comparisons
Dependent Variable: VAR00001
Bonferroni

(I) VAR00002	(J) VAR00002	Mean Difference (I-J)	Std. Error	Sig.	95% Confidence Interval	
					Lower Bound	Upper Bound
30.00	31.00	-.031	.066	1.000	-.224	.163
	32.00	.108	.066	.712	-.086	.301
	33.00	.236*	.066	.011	.043	.429
31.00	30.00	.031	.066	1.000	-.163	.224
	32.00	.138	.066	.296	-.055	.332
	33.00	.267*	.066	.004	.073	.460
32.00	30.00	-.108	.066	.712	-.301	.086
	31.00	-.138	.066	.296	-.332	.055
	33.00	.128	.066	.398	-.065	.322
33.00	30.00	-.236*	.066	.011	-.429	-.043
	31.00	-.267*	.066	.004	-.460	-.073
	32.00	-.128	.066	.398	-.322	.065

*. The mean difference is significant at the 0.05 level.

D.III Donor K56

D.III.1 Day 0

Table D.III.1.a: Test of normality.

Tests of Normality

	VAR00002	Kolmogorov-Smirnov[a]			Shapiro-Wilk		
		Statistic	df	Sig.	Statistic	df	Sig.
VAR00001	.00	.169	6	.200*	.933	6	.604
	1.00	.303	6	.090	.858	6	.181
	2.00	.255	6	.200*	.874	6	.244
	3.00	.221	6	.200*	.935	6	.617

*. This is a lower bound of the true significance.
a. Lilliefors Significance Correction

Table D.III.1.b: ANOVA analysis of normally distributed data.

ANOVA
VAR00001

	Sum of Squares	df	Mean Square	F	Sig.
Between Groups	.060	3	.020	2.144	.127
Within Groups	.186	20	.009		
Total	.246	23			

D.III.2 Day 7

Table D.III.2.a: Test of normality.

Tests of Normality

	VAR00002	Kolmogorov-Smirnov[a]			Shapiro-Wilk		
		Statistic	df	Sig.	Statistic	df	Sig.
VAR00001	10.00	.321	6	.052	.820	6	.088
	11.00	.259	6	.200*	.883	6	.284
	12.00	.230	6	.200*	.874	6	.241
	13.00	.367	6	.011	.736	6	.014

*. This is a lower bound of the true significance.
a. Lilliefors Significance Correction

Table D.III.2.b: Kruskal-Wallis analysis of not normally distributed data.

Test Statistics[a,b]

	VAR00001
Chi-Square	14.287
df	3
Asymp. Sig.	.003

a. Kruskal Wallis Test
b. Grouping Variable: VAR00002

Table D.III.2.c: Bonferroni post hoc analysis.

Multiple Comparisons
Dependent Variable: VAR00001
Bonferroni

(I) VAR00002	(J) VAR00002	Mean Difference (I-J)	Std. Error	Sig.	95% Confidence Interval	
					Lower Bound	Upper Bound
10.00	11.00	.047	.155	1.000	-.407	.501
	12.00	.377	.155	.148	-.077	.832
	13.00	.625*	.155	.004	.170	1.079
11.00	10.00	-.047	.155	1.000	-.501	.407
	12.00	.330	.155	.276	-.124	.785
	13.00	.578*	.155	.008	.123	1.032
12.00	10.00	-.377	.155	.148	-.832	.077
	11.00	-.330	.155	.276	-.785	.124
	13.00	.247	.155	.759	-.207	.702
13.00	10.00	-.625*	.155	.004	-1.079	-.170
	11.00	-.578*	.155	.008	-1.032	-.123
	12.00	-.247	.155	.759	-.702	.207

*. The mean difference is significant at the 0.05 level.

D.III.3 Day 14

Table D.III.3.a: Test of normality.

Tests of Normality

	VAR00002	Kolmogorov-Smirnov[a]			Shapiro-Wilk		
		Statistic	df	Sig.	Statistic	df	Sig.
VAR00001	20.00	.206	6	.200*	.900	6	.374
	21.00	.242	6	.200*	.904	6	.397
	22.00	.230	6	.200*	.874	6	.241
	23.00	.367	6	.011	.736	6	.014

*. This is a lower bound of the true significance.
a. Lilliefors Significance Correction

Table D.III.3.b: Kruskal-Wallis analysis of not normally distributed data.

Test Statistics[a,b]

	VAR00001
Chi-Square	19.227
df	3
Asymp. Sig.	.000

a. Kruskal Wallis Test
b. Grouping Variable: VAR00002

Table D.III.3.c: Bonferroni post hoc analysis.

Multiple Comparisons
Dependent Variable: VAR00001
Bonferroni

(I) VAR00002	(J) VAR00002	Mean Difference (I-J)	Std. Error	Sig.	95% Confidence Interval	
					Lower Bound	Upper Bound
20.00	21.00	.104	.106	1.000	-.205	.414
	22.00	.602*	.106	.000	.292	.912
	23.00	.850*	.106	.000	.540	1.160
21.00	20.00	-.104	.106	1.000	-.414	.205
	22.00	.498*	.106	.001	.188	.808
	23.00	.745*	.106	.000	.435	1.055
22.00	20.00	-.602*	.106	.000	-.912	-.292
	21.00	-.498*	.106	.001	-.808	-.188
	23.00	.247	.106	.179	-.062	.557
23.00	20.00	-.850*	.106	.000	-1.160	-.540
	21.00	-.745*	.106	.000	-1.055	-.435
	22.00	-.247	.106	.179	-.557	.062

*. The mean difference is significant at the 0.05 level.

D.III.4 Day 21

Table D.III.4.a: Test of normality.

Tests of Normality

	VAR00002	Kolmogorov-Smirnov[a]			Shapiro-Wilk		
		Statistic	df	Sig.	Statistic	df	Sig.
VAR00001	30.00	.161	6	.200*	.962	6	.835
	31.00	.217	6	.200*	.892	6	.329
	32.00	.350	6	.020	.788	6	.045
	33.00	.288	6	.130	.884	6	.288

*. This is a lower bound of the true significance.
a. Lilliefors Significance Correction

Table D.III.4.b: Kruskal-Wallis analysis of not normally distributed data.

Test Statistics[a,b]

	VAR00001
Chi-Square	16.333
df	3
Asymp. Sig.	.001

a. Kruskal Wallis Test
b. Grouping Variable: VAR00002

Table D.III.4.c: Bonferroni post hoc analysis.

Multiple Comparisons
Dependent Variable: VAR00001
Bonferroni

(I) VAR00002	(J) VAR00002	Mean Difference (I-J)	Std. Error	Sig.	95% Confidence Interval	
					Lower Bound	Upper Bound
30.00	31.00	-.138	.090	.844	-.402	.125
	32.00	.151	.090	.648	-.112	.415
	33.00	.436*	.090	.001	.173	.700
31.00	30.00	.138	.090	.844	-.125	.402
	32.00	.290*	.090	.026	.026	.553
	33.00	.574*	.090	.000	.311	.838
32.00	30.00	-.151	.090	.648	-.415	.112
	31.00	-.290*	.090	.026	-.553	-.026
	33.00	.285*	.090	.029	.021	.548
33.00	30.00	-.436*	.090	.001	-.700	-.173
	31.00	-.574*	.090	.000	-.838	-.311
	32.00	-.285*	.090	.029	-.548	-.021

*. The mean difference is significant at the 0.05 level.